sciendo

DFT studies of camptothecins cytotoxicity IV — active and inactive forms of irinotecan

Marek Šteklář, Martin Breza

Department of Physical Chemistry, Faculty of Chemical and Food Technology STU,
Radlinského 9, SK-81237, Bratislava, Slovakia
martin.breza@stuba.sk

Dedicated to Assoc. Prof. Jozef Kožíšek on the occasion of his 70th birthday.

Abstract: Structures of irinotecan (CPT-11) in neutral lactone, neutral carboxyl, and anionic carboxylate forms in singlet ground states and of their complexes with Cu(II) in doublet ground states are optimized using B3LYP/6-311G* treatment. Metal ion affinities (MIA), Cu charges and Laplacians of Cu-ligand bond critical points of possible CPT active sites are evaluated. The formation of Cu(II) complexes with the anionic carboxylate ligand leads to the release of CO_2 that can cause a decrease in the concentration of the active lactone form due to equilibria between all forms of the drug. MIA values and electron density transfer to Cu increase in the sequence lactone < neutral carboxyl < anionic carboxylate. Both neutral forms of irinotecan exhibit lower MIA values than those of camptothecin, unlike the anionic carboxylate form.

Keywords: copper(II), cytotoxicity, DFT calculations, electron structure, molecular modelling

Introduction

The semisynthetic anticancer drug irinotecan (CPT-11), (4*S*)-4,11-diethyl-3,4,12,14-tetrahydro-4-hydroxy-3,14-dioxo-1*H*-pyrano[3',4':6,7]-indolizino[1,2-b]quinolin-9-yl-[1,4'-bipiperidine]-1'-carboxylate was approved for cancer treatment in 1994 (Bailly, 2019). It is obtained by chemical modification of camptothecin with the aim to increase its low water solubility (Sawada et al., 1991). After enzymatic cleavage of the bispiperidine side chain, its minor metabolite SN-38, (4*S*)-4,11-diethyl-4,9-dihydroxy-1,4-dihydro-3*H*,14*H*-pyrano[3',4':6,7] indolizino[1,2-*b*]quinolone-3,14-dione is obtained, which is an even more potent anticancer drug (Tanizawa et al., 1994). In aqueous solutions, the lactone ring of irinotecan is hydrated to the inactive carboxylate form, which is favored under neutral and alkaline conditions, whereas the active lactone form **I** prevails in acidic solutions (Fassberg and Stella, 1992; DiNunzio et al., 2018). Structure of the irinotecan lactone form has been determined by single crystal X-ray diffraction (Sawada et al., 1991), NMR measurements in DMSO solution (D'Amelio et al., 2012), and quantum-chemical model studies (Babu et al., 2012; Ivanova and Spiteller, 2012; Hussain et al., 2016).

Relative cytotoxicity of various forms of camptothecin and lactone forms of irinotecan and SN-38 have been investigated in a series of studies (Steklac and Breza, 2018, 2021, 2022, 2022a) by means of quantum chemistry. This treatment was originally developed for antioxidants (Alagona and Ghio, 2009, 2009a; Mammino, 2013; Kabanda et al., 2014; Tsiepe et al., 2015; Serobatse et al., 2016, 2016a; Puskarova and Breza, 2016, 2017; Jelemenska and Breza, 2021; Breza and Jelemenska, 2022) and is based on the complexation ability of their various active sites to Cu(II) with subsequent electron density transfer (ligand oxidation and metal reduction). Metal ion affinity (*MIA*) data for the ligand active sites in hypothetical complexes can be obtained by DFT treatment. However, inclusion of the solvent effect decreases the *MIA* values and thus, vacuum model studies are more suitable for cytotoxicity studies (Alagona and Ghio, 2009, 2009a; Mammino, 2013).

This method has been successfully applied to rutile nanoparticles (Breza and Simon, 2019, 2020; Breza, 2021), substituted phenols (Steklac and Breza, 2021a, 2021b) and benzoquinones (Steklac and Breza, 2021c) revealing linear relations between the degree of electron density transfer to Cu, Cu-phenol interaction energy and experimental toxicity data, which were evaluated as $\log(1/IC_{50})$ where IC_{50} is the concentration of substituted phenol/benzoquinone that causes 50 % inhibition of cell growth.

The generally accepted paradigm that the purpose of quantum-chemical modelling is to explain the properties of real systems is usually interpreted so that only real systems should be modelled. This is a very restricted interpretation. Our method of modelling hypothetical complexes to compare the complexation ability and the extent of electron density transfer for individual active sites of the compound under study is an example of extended interpretation of this paradigm. In our case, the

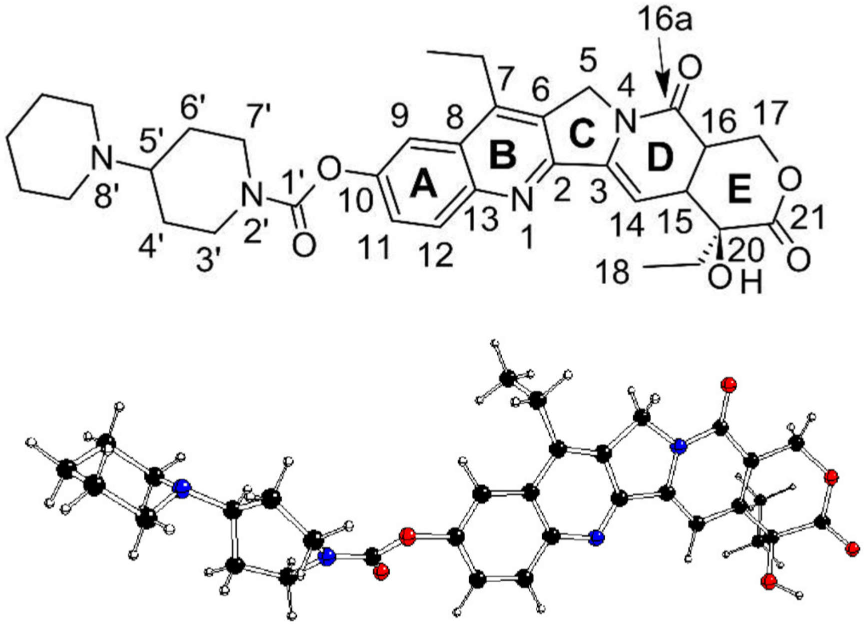

Fig. 1. Atom and ring notation of the irinotecan (CPT-11) lactone (top) and the DFT structure (bottom) of its neutral form **I** (carbon — black, hydrogen — white, nitrogen — blue, oxygen — red) studies (Steklac and Breza, 2022a).

Cu^{2+} ion serves only as a probe to measure properties of the complexes and to rationalize the electronic structure factors of cytotoxicity. This is of practical importance as experiments cannot distinguish between pharmacokinetics and electronic structure factors of the drug action.

In our studies (Steklac and Breza, 2021, 2022), we have explained why the carboxylate and protonated lactone forms of camptothecin are not suitable as anticancer drugs. In our previous comparative study (Steklac and Breza, 2022a), cytotoxicity of lactone forms was found to decrease in the sequence irinotecan > SN-38 > camptothecin. The discrepancy with the least relative *in vitro* irinotecan cytotoxicity is probably due to their different pharmacokinetics. The aim of our recent study is to compare the cytotoxicity of the neutral lactone, neutral carboxyl, and anionic carboxylate forms of irinotecan, which coexist in aqueous solutions. In agreement with our previous cytotoxicity studies, all calculations were performed *in vacuo* because of more palpable trends compared to solutions (see above).

Method

Geometries of three forms of irinotecan (neutral lactone and carboxyl, anionic carboxylate) in singlet ground states, as well as of their Cu(II) complexes in doublet ground state, were optimized using the B3LYP hybrid functional (Becke, 1993). Standard 6-311G* basis sets from the Gaussian library (Frisch et al., 2013) were used for all atoms. Optimized geometries were checked for the absence of imaginary vibrations by vibrational analysis. The charges and spin populations of copper atoms were evaluated using the Mulliken population analysis (MPA) (Mulliken, 1955, 1955a). Gaussian09 software was used for all quantum-chemical calculations (Frisch et al., 2013).

Alternatively, the charge and spin population of copper was evaluated in terms of Quantum Theory of Atoms-in-Molecules (QTAIM) (Bader, 1990). Irinotecan → Cu electron density transfer was estimated as the Laplacian of the electron density ($\nabla^2\rho$) at bond critical points (BCP) using the AIMAll software (Keith, 2017). The MOLDRAW software (Ugliengo, 2006) was used for geometry manipulation and visualization purposes. QTAIM molecular graphs were drawn using the AIM2000 software (Biegler-Konig et al., 2001).

Metal-ion affinity (*MIA*) was evaluated as the interaction energy

$$E_{\mathrm{int}} = E_{\mathrm{complex}} - E_{\mathrm{Cu(II)}} - E_{\mathrm{L}} \qquad (1)$$

where E_{complex} is the DFT energy of the $^{2}[\mathrm{L}\ldots\mathrm{Cu}]^{2+q}$ complex, $E_{\mathrm{Cu(II)}}$ is the DFT energy of the copper(II) ion and E_{L} is the DFT energy of the L ligand, i.e., the neutral lactone ($q = 0$), neutral carboxyl ($q = 0$) or anionic carboxylate ($q = -1$) form of irinotecan.

Results and discussion

In the first step, structures of neutral lactone (**I**), neutral carboxyl (II), and three possible anionic carboxylate (**III**) forms of irinotecan were optimized. After hydration of the lactone ring (Fig. 1), the C_{21}—O_{17} bond is split, the O_{21} site is formally doubled, and the O_{17} site is protonated to the neutral carboxyl form **II** (Fig. 2). Subsequently, this form can be deprotonated at the O_{17}, O_{20}, or O_{21} sites. Our results show that the most probable deprotonation site is at O_{21} (see Table 1) and that only this isomer should be present in real systems. Therefore, only this structure will be denoted as form **III** (Fig. 3) and considered in our further studies.

Tab. 1. Absolute (G_{298}) and relative (ΔG_{298}) Gibbs energies at 298 K of the deprotonated irinotecan carboxylate forms (**III**) at various sites and their relative abundance (P_i) based on Boltzmann statistical distribution.

Site	G_{298} [Hartree]	ΔG_{298} [kJ/mol]	P_i
O_{17}	–2026.46179	218.42	5.41×10^{-39}
O_{20}	–2026.50356	108.75	8.85×10^{-20}
O_{21}	–2026.54498	0.00	1.00

In the next step, a Cu^{2+} ion was placed in the vicinity of heteroatoms (ca 1.7 Å distance) of the above mentioned molecules, i.e., N_1 (**a**), N_4 (**b**), O_{16a} (**c**), O_{20} (**d**), O_{21} (**e**), O_{17} (**f**), O_{10} (**g**), $O_{1'}$(**h**), $N_{2'}$(**i**) or $N_{8'}$(**j**) sites in model complexes with ligands **I**, **II** and **III** in agreement with our previous studies (Steklac and Breza, 2021, 2022, 2022a). Thus obtained geometry optimization of the $^2[L...Cu]^q$ complexes leads to stable structures with QTAIM molecular graphs presented in (Steklac and Breza, 2022a) for L being the neutral lactone **I** ligand (q = +2), in Figs. 4—5 for L being the neutral carboxyl ligand **II** (q = +2), and in Figs. 6—7 for L being the anionic carboxylate ligand **III** (q = +1). Notation of these complexes (see Table 2) is related to the Cu-bond sites mentioned above.

No model complexes with Cu bound to the N_4 site have been found. Similarly as in the case of camptothecin (Steklac and Breza, 2021), the Cu—O_{17} bonding is absent in case of neutral lactone ligand **I** and the formation of Cu(II) complexes with carboxylate form **III** leads to the release of CO_2 (except for models **IIIe** and **IIIef** with Cu—O_{21} bonding, see Table 2 and Figs. 6—7). Interactions with neighboring electron-accepting molecules can decrease electron density at the relevant active sites of carboxylate forms of camptothecins and cause their decarboxylation (and decay) and therefore contribute to the decrease in the concentrations of the active lactone form (Steklac and Breza, 2021).

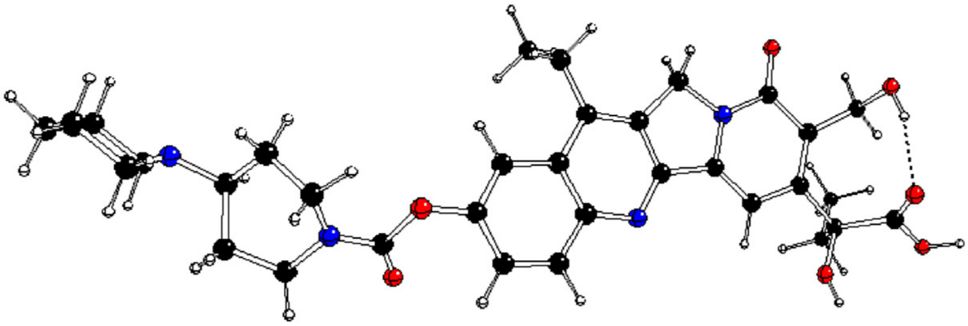

Fig. 2. DFT structure of neutral irinotecan carboxyl **II** (carbon — black, hydrogen — white, nitrogen — blue, oxygen — red).

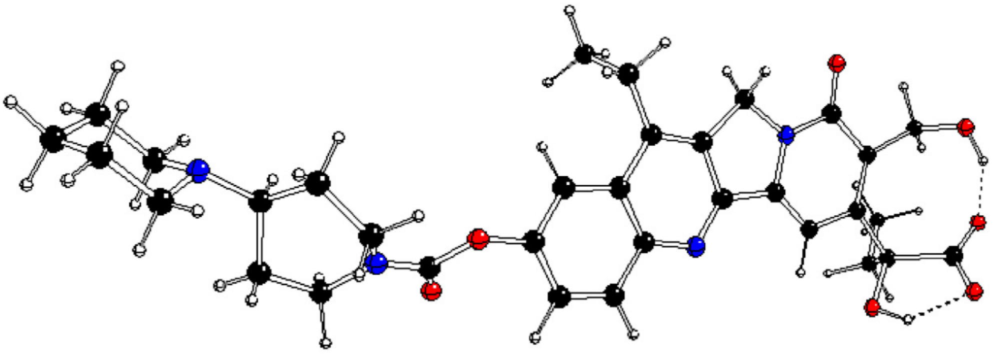

Fig. 3. DFT structure of anionic irinotecan carboxylate **II** (carbon — black, hydrogen — white, nitrogen — blue, oxygen — red).

If the Cu atom is bound to a single atom only, the extent of the corresponding electron density transfer from the active site to Cu can be accurately evaluated. Unfortunately, such cases are rare, and the Cu atom is often bound to two atoms. The H atom basis sets were not augmented with any polarization and diffusion functions in order to weaken the undesirable Cu—H bonds (collateral with desired Cu—O or Cu—N bonds), their lengths are greater than 2.2 Å (except for the **Ig** and **IIg** systems) and so the H contribution to the complete electron density transfer to Cu are usually very small (compare (Steklac and Breza, 2021, 2022, 2022a)). Unfortunately, undesirable Cu—C bonding (collateral with desired Cu—O bonding) with shorter bond lengths (comparable to the Cu—O ones) and a relevant C → Cu electron density transfer (compare (Steklac and Breza, 2021, 2022, 2022a)) is problematic and pure contributions of the active O sites to complete electron density transfer to Cu cannot be distinguished. Therefore, the **Id**, **IIId**, **Ih**, **IIh**, **IIIh** and **Ief**2 systems are hardly usable for our purpose. Even though in the systems with Cu bound to two or three O sites (**IIcf**, **IIIcf**, **IIef1,** and **IIIef**), their pure contributions cannot be separated, they can at least be used for mutual comparisons of carboxyl and carboxylate ligands.

In our studies on the cytotoxicity of substituted phenols (Steklac and Breza, 2021a, 2021b, 2021c),

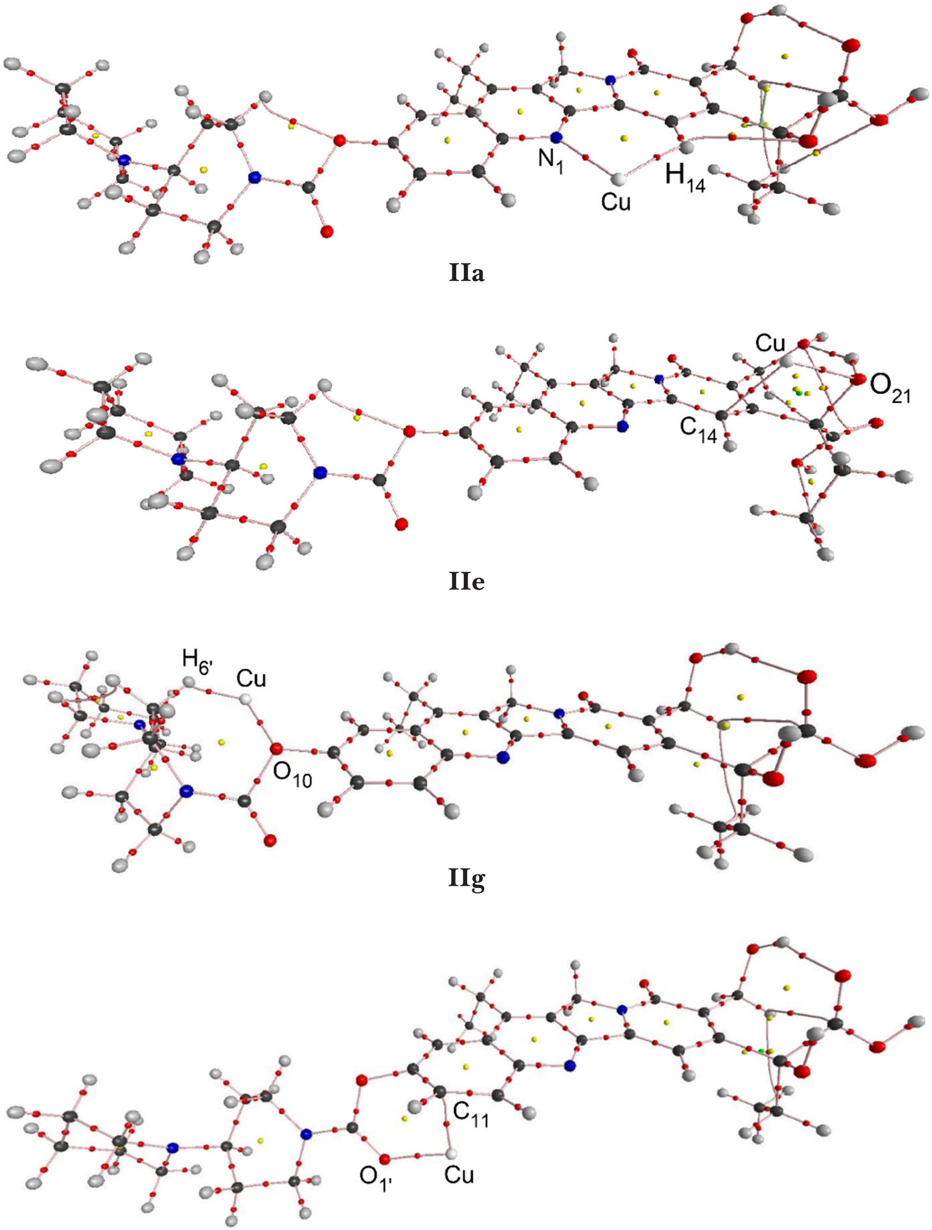

IIa

IIe

IIg

IIh

Fig. 4. Bond paths and critical points of electron density in **IIa**, **IIe**, **IIg**, and **IIh** model systems (carbon – black, hydrogen – white, nitrogen – blue, oxygen – red, bond critical point – small red, ring critical points – yellow, cage critical point – green).

higher toxicity was shown to be connected with more negative interaction energies E_{int}. According to our results (Table 3), E_{int} values for the neutral irinotecan carboxyl ligand **II** are more negative than for the neutral lactone ligand **I**, but significantly less negative than for the anionic carboxylate ligand **III**. An analogous relation has been observed for camptothecin (Steklac and Breza, 2021). Both neutral forms of camptothecin exhibit less negative E_{int} values than irinotecan, unlike the negative carboxylate form. As expected, bonding to two O sites is connected with more negative E_{int} values than in

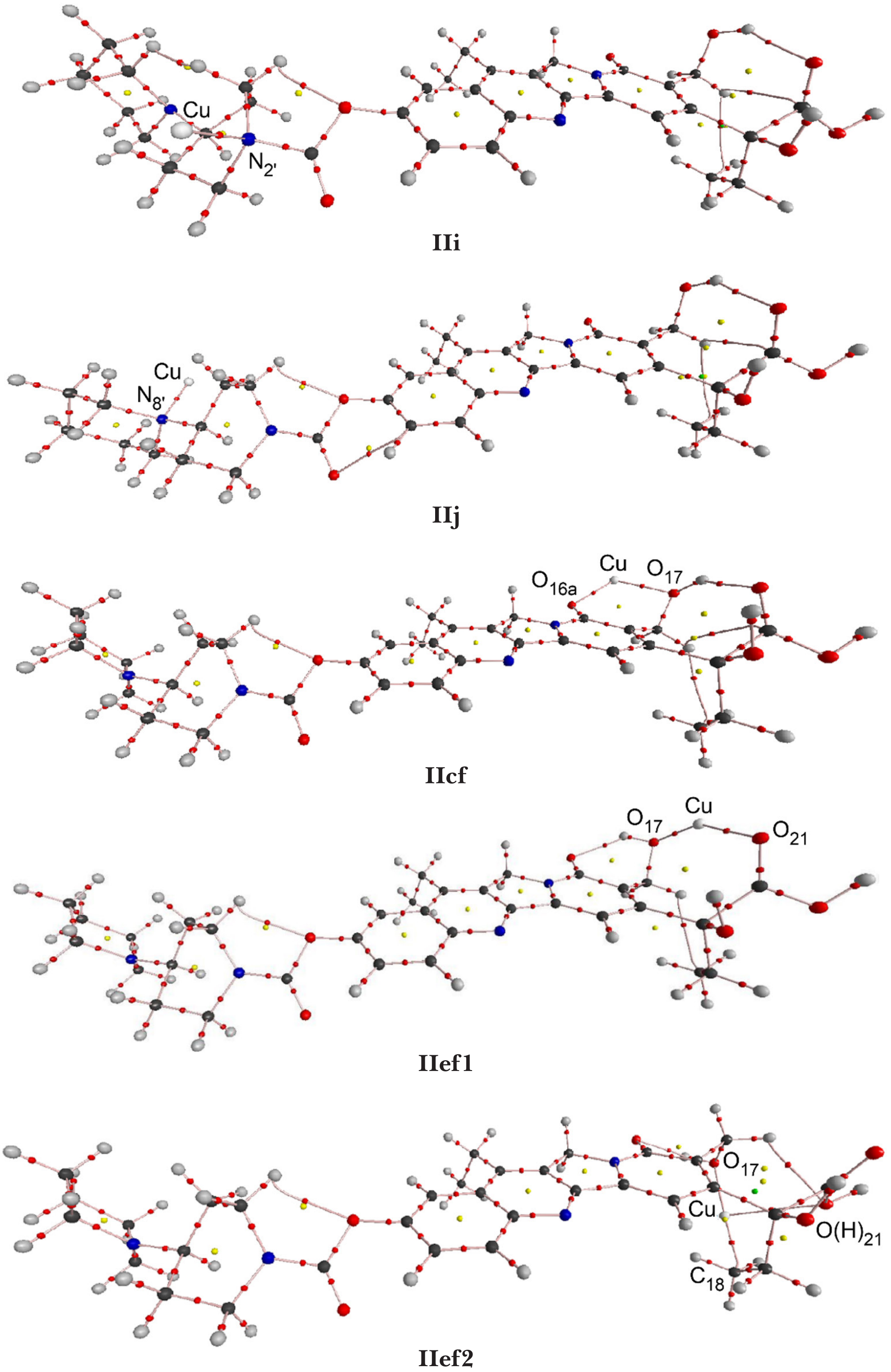

IIi

IIj

IIcf

IIef1

IIef2

Fig. 5. Bond paths and critical points of electron density in **IIi**, **IIj**, **IIcf**, **IIef1**, and **IIef2** model systems (carbon – black, hydrogen – white, nitrogen – blue, oxygen – red, bond critical point – small red, ring critical points – yellow, cage critical point – green).

the case of bonding to a single O site only. The least negative E_{int} values were found for Cu—O_{10} and Cu—$N_{2'}$ bonds, which are missing in analogous camptothecin systems (Steklac and Breza, 2021).

Positive QTAIM charges of copper atoms in the Cu(II) complexes with substituted phenols decrease with their cytotoxicity due to increasing ligand → Cu electron density transfer (Steklac and Breza, 2021a, 2021b, 2021c). Analogously to our previous study on camptothecin (Steklac and Breza, 2021), average Cu charges in the complexes with the anionic irinotecan carboxylate ligand **III** are lower than in case of neutral irinotecan lactone **I** and carboxyl **II** ligands (Table 4). Nevertheless, the lowest Cu charges correspond to **IIIi** and **IIIj** systems (missing in camptothecin complexes), whereas the most positive Cu charges are found in **IIId** and **IIIef** complexes. Unlike camptothecin complexes, non-vanishing Cu spin populations can be found only in anionic irinotecan carboxylate complexes **IIId**, **IIIi**, **IIIj**, and **IIIef**.

BCP Laplacians of Cu-ligand bonds in Cu complexes of substituted phenols (Steklac and Breza, 2021a, 2021b, 2021c) increase with their toxicity. Their values for Cu—H bond paths are very low (Table 5)

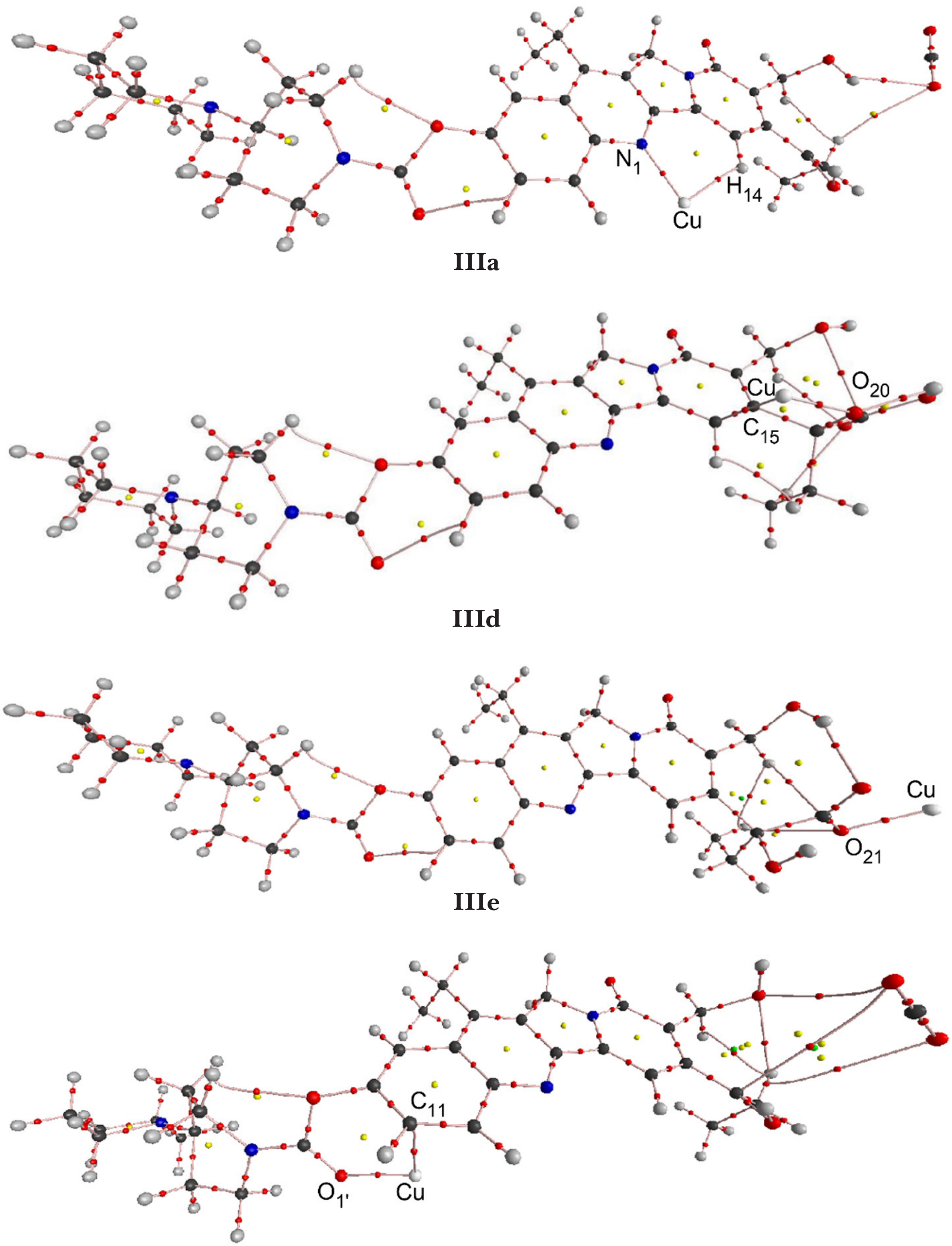

IIIa

IIId

IIIe

IIIh

Fig. 6. Bond paths and critical points of electron density in **IIIa**, **IIId**, **IIIe**, and **IIIh** model systems (carbon — black, hydrogen — white, nitrogen — blue, oxygen — red, bond critical point — small red, ring critical points — yellow, cage critical point — green).

except for **Ig** and **IIg** complexes with too short bond lengths. BCP Laplacians of Cu—C bonds are relatively high in comparison with the Cu—O ones, restricting the use of the **Id**, **IIId**, **II**e, **Ih**, **II**h, **IIIh** and **IIef**2 complexes for our purpose. Our results indicate the highest electron density transfer from the O_{21} and O_{16a} sites, while the lowest one from $N_{2'}$, $N_{8'}$, and O_{10} sites.

Similarly to camptothecin (Steklac and Breza, 2021), most trends of MPA charges of Cu atoms in Cu(II) complexes of various forms of irinotecan (Table 6) are similar to those of QTAIM. Cu charges of anionic carboxylate **III** complexes are lower than those of the complexes with neutral ligands **I** and **II**. Except for the **IIIef** system, the highest Cu charges are found in the complexes with Cu—C bonds. The lowest Cu charges are observed for **IIIi** and **IIIj** complexes with Cu—N bonds to piperidine rings. Non-vanishing Cu spin populations are again observed in **IIId**, **IIIi**, **IIIj** and **IIIef** complexes of the

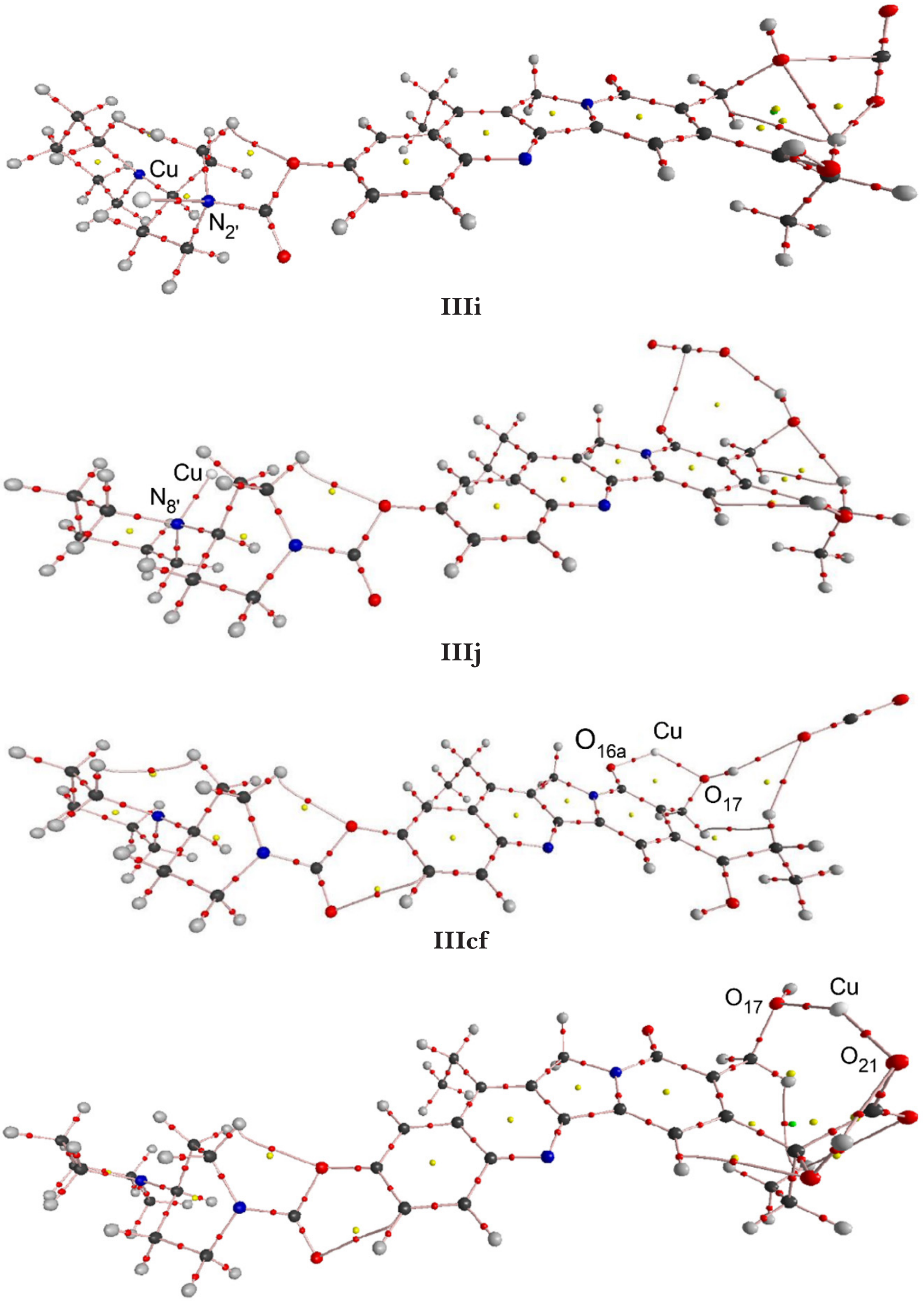

Fig. 7. Bond paths and critical points of electron density in **IIIi**, **IIIj**, **IIIcf**, and **IIIef** model systems (carbon – black, hydrogen – white, nitrogen – blue, oxygen – red, bond critical point – small red, ring critical points – yellow, cage critical point – green).

Tab. 2. Description of Cu model complexes with lactone (**I**), carboxyl (**II**), and carboxylate (**III**) ligands (see Fig. 1 for atom notation).

	I (Steklac and Breza, 2022)			**II**			**III**		
Site	Model	Bond path	Distance [Å]	Model	Bond path	Distance [Å]	Model	Bond path	Distance [Å]
N_1	**Ia**	Cu—N_1 Cu—H_{14}	1.879 2.223	**IIa**	Cu—N_1 Cu—H_{14}	1.877 2.208	**IIIa** a)	Cu—N_1 Cu—H_{14}	1.867 2.288
O_{16a}	**Ic**	Cu—O_{16a} Cu—H_5	1.830 2.542	–	–	–	–	–	–
O_{20}	**Id**	Cu—O_{20} Cu—C_{14}	2.061 1.988	–	–	–	**IIId** a)	Cu—O_{20} Cu—C_{15}	1.839 2.020
O_{21}	**Ie**	Cu—O_{21}	1.865	**IIe**	Cu—O_{21} Cu—C_{14}	2.081 2.031	**IIIe**	Cu—O_{21}	1.848
O_{10}	**Ig**	Cu—O_{10} Cu—$H_{6'}$	1.954 1.674	**IIg**	Cu—O_{10} Cu—$H_{6'}$	1.954 2.066	–	–	–
$O_{1'}$	**Ih**	Cu—$O_{1'}$ Cu—C_{11}	1.977 1.982	**IIh**	Cu—$O_{1'}$ Cu—C_{11}	1.970 1.981	**IIIh** a)	Cu—$O_{1'}$ Cu—C_{11}	1.956 1.986
$N_{2'}$	**Ii**	Cu—$N_{2'}$	1.925	**IIi**	Cu—$N_{2'}$	1.923	**IIIi** a)	Cu—$N_{2'}$	1.965
$N_{8'}$	**Ij**	Cu—$N_{8'}$	1.927	**IIj**	Cu—$N_{8'}$	1.927	**IIIj** a)	Cu—$N_{8'}$	1.952
O_{16a}, O_{17}	–	–	–	**IIcf**	Cu—O_{16a} Cu—O_{17}	1.909 1.962	**IIIcf** a)	Cu—O_{16a} Cu—O_{17}	1.885 1.945
O_{17}, O_{21}	–	–	–	**IIef1**	Cu—O_{17} Cu—O_{21}	1.906 1.870	**IIIef**	Cu—O_{17} Cu—O_{21}	1.895 1.832
	–	–	–	**IIef2**	Cu—O_{17} Cu—O(H)$_{21}$ Cu—C_{18}	1.926 2.597 2.128	–	–	–

a) CO_2 release

Tab. 3. Interaction energies in model complexes of Cu with lactone (**I**), carboxyl (**II**) and carboxylate (**III**) ligands (see Fig. 1 for atom notation).

	I (Steklac and Breza, 2022)		**II**		**III**	
Site	Model	E_{int} [kJ/mol]	Model	E_{int} [kJ/mol]	Model	E_{int} [kJ/mol]
N_1	**Ia**	–1368	**IIa**	–1378	**IIIa** a)	–1975
O_{16a}	**Ic**	–1338	–	–	–	–
O_{20}	**Id**	–1369	–	–	**IIId** a)	–1890
O_{21}	**Ie**	–1353	**IIe**	–1404	**IIIe**	–1905
O_{10}	**Ig**	–1219	**IIg**	–1255	–	–
$O_{1'}$	**Ih**	–1376	**IIh**	–1397	**IIIh** a)	–2040
$N_{2'}$	**Ii**	–1225	**IIi**	–1255	**IIIi** a)	–1901
$N_{8'}$	**Ij**	–1364	**IIj**	–1395	**IIIj** a)	–1997
O_{16a}, O_{17}	–	–	**IIcf**	–1464	**IIIcf** a)	–2060
O_{17}, O_{21}	–	–	**IIef1**	–1479	**IIIef**	–1976
	–	–	**IIef2**	–1461	–	–
Average	–	–1326		–1388		–1968

a) CO_2 release

Tab. 4. QTAIM charges and spin populations of Cu atoms in model complexes of Cu with lactone (**I**), carboxyl (**II**) and carboxylate (**III**) ligands (see Fig. 1 for atom notation).

	I (Steklac and Breza, 2022)			**II**			**III**		
Site	Model	Charge	Spin	Model	Charge	Spin	Model	Charge	Spin
N_1	**Ia**	0.744	0.000	**IIa**	0.739	0.000	**IIIa**$^{a)}$	0.719	0.000
O_{16a}	**Ic**	0.780	0.000	–	–	–	–	–	–
O_{20}	**Id**	0.742	0.001	–	–	–	**IIId**$^{a)}$	0.902	0.343
O_{21}	**Ie**	0.815	0.000	**IIe**	0.740	0.001	**IIIe**	0.727	0.000
O_{10}	**Ig**	0.764	0.000	**IIg**	0.821	0.000	–	–	–
$O_{1'}$	**Ih**	0.800	0.002	**IIh**	0.800	0.002	**IIIh**$^{a)}$	0.782	0.001
$N_{2'}$	**Ii**	0.750	-0.001	**IIi**	0.747	-0.001	**IIIi**$^{a)}$	0.496	0.288
$N_{8'}$	**Ij**	0.678	0.000	**IIj**	0.677	0.000	**IIIj**$^{a)}$	0.491	0.222
O_{16a}, O_{17}	–	–	–	**IIcf**	0.797	0.028	**IIIcf** $^{a)}$	0.756	0.010
O_{17}, O_{21}	–	–	–	**IIef1**	0.770	0.001	**IIIef**	0.857	0.188
	–	–	–	**IIef2**	0.727	0.000	–	–	–
Average	–	0.759	0.000	–	0.758	0.003	–	0.716	0.132

$^{a)}CO_2$ release

Tab. 5. Laplacians of BCP electron density of Cu-ligand bonds in model complexes of Cu with lactone (**I**), carboxyl (**II**) or carboxylate (**III**) ligands (see Fig. 1 for atom notation).

	I (Steklac and Breza, 2022)			**II**			**III**		
Site	Model	Bond path	$\nabla^2\rho$ [e/bohr^5]	Model	Bond path	$\nabla^2\rho$ [e/bohr^5]	Model	Bond path	$\nabla^2\rho$ [e/bohr^5]
N_1	**Ia**	Cu—N_1 Cu—H_{14}	0.513 0.068	**IIa**	Cu—N_1 Cu—H_{14}	0.515 0.070	**IIIa**$^{a)}$	Cu—N_1 Cu—H_{14}	0.521 0.060
O_{16a}	**Ic**	Cu—O_{16a} Cu—H_5	0.664 0.040	–	–	–	–	–	–
O_{20}	**Id**	Cu—O_{20} Cu—C_{14}	0.346 0.192	–	–	–	**IIId**$^{a)}$	Cu—O_{20} Cu—C_{15}	0.599 0.163
O_{21}	**Ie**	Cu—O_{21}	0.627	**IIe**	Cu—O_{21} Cu—C_{14}	0.563 0.327	**IIIe**	Cu—O_{21}	0.636
O_{10}	**Ig**	Cu—O_{10} Cu—$H_{6'}$	0.492 0.256	**IIg**	Cu—O_{10} Cu—$H_{6'}$	0.492 0.262	–	–	–
$O_{1'}$	**Ih**	Cu—$O_{1'}$ Cu—C_{11}	0.449 0.215	**IIh**	Cu—$O_{1'}$ Cu—C_{11}	0.460 0.215	**IIIh**$^{a)}$	Cu—$O_{1'}$ Cu—C_{11}	0.480 0.221
$N_{2'}$	**Ii**	Cu—$N_{2'}$	0.423	**IIi**	Cu—$N_{2'}$	0.439	**IIIi**$^{a)}$	Cu—$N_{2'}$	0.366
$N_{8'}$	**Ij**	Cu—$N_{8'}$	0.430	**IIj**	Cu—$N_{8'}$	0.434	**IIIj**$^{a)}$	Cu—$N_{8'}$	0.415
O_{16a}, O_{17}	–	–	–	**IIcf**	Cu—O_{16a} Cu—O_{17}	0.562 0.489	**IIIcf** $^{a)}$	Cu—O_{16a} Cu—O_{17}	0.610 0.518
O_{17}, O_{21}	–	–	–	**IIef1**	Cu—O_{17} Cu—O_{21}	0.584 0.603	**IIIef**	Cu—O_{17} Cu—O_{21}	0.608 0.679
	–	–		**IIef2**	Cu—O_{17} Cu—$O(H)_{21}$ Cu—C_{18}	0.540 0.084 0.230	–	–	–

$^{a)}CO_2$ release

Tab. 6. MPA charges and spin populations of Cu atoms in model complexes of Cu with lactone (**I**), carboxyl (**II**) and carboxylate (**III**) ligands (see Fig. 1 for atom notation).

	I (Steklac and Breza, 2022)			**II**			**III**$^{-}$		
Site	Model	Charge	Spin	Model	Charge	Spin	Model	Charge	Spin
N_1	**Ia**	0.863	0.000	**IIa**	0.857	0.000	**IIIa**[a)]	0.836	0.000
O_{16a}	**Ic**	0.816	0.000	–	–	–	–	–	–
O_{20}	**Id**	0.918	0.001	–	–	–	**IIId**[a)]	1.040	0.315
O_{21}	**Ie**	0.821	0.000	**IIe**	0.934	0.001	**IIIe**	0.715	0.000
O_{10}	**Ig**	0.881	0.000	**IIg**	0.879	0.000	–	–	–
$O_{1'}$	**Ih**	0.999	0.002	**IIh**	0.999	0.000	**IIIh**[a)]	0.977	0.002
$N_{2'}$	**Ii**	0.846	-0.001	**IIi**	0.843	-0.001	**IIIi**[a)]	0.553	0.337
$N_{8'}$	**Ij**	0.803	0.000	**IIj**	0.802	0.000	**IIIj**[a)]	0.573	0.273
O_{16a}, O_{17}	–	–	–	**IIcf**	0.864	0.028	**IIIcf**[a)]	0.816	0.007
O_{17}, O_{21}	–	–	–	**IIef1**	0.829	0.001	**IIIef**	0.900	0.179
	–	–	–	**IIef2**	0.836	0.000	–	–	–
Average	–	0.878	0.000		0.871	0.003		0.801	0.139

[a)] CO_2 release

anionic carboxylate ligand, which is in agreement with the QTAIM data. Average MPA Cu charges are lower than in analogous forms of camptothecin (Steklac and Breza, 2021).

Conclusions

Our results indicate high similarity between active and inactive forms of camptothecin (Steklac and Breza, 2021) and irinotecan. In both cases, no Cu—N_4 bonds were found and the Cu—O_{17} bond is absent in the complexes of the neutral lactone ligand. The formation of Cu(II) complexes with the anionic carboxylate ligand leads to the release of CO_2 in both cases. This corresponds to the interaction with electron acceptors in real solutions and the decrease in the concentration of lactone forms because of the equilibria between all forms of the drug. Absolute values of interaction energies and electron density transfer to Cu increase in the sequence lactone < neutral carboxyl < anionic carboxylate. In analogy with our studies on substituted phenols and quinones (Steklac and Breza, 2021a, 2021b, 2021c), cytotoxicity should exhibit the same trend. Both neutral forms of irinotecan exhibit more negative interaction energies than those of camptothecin, unlike the anionic carboxylate form. The lowest electron density transfer irinotecan → Cu is from $N_{2'}$, $N_{8'}$, and O_{10} sites which are not present in camptothecin.

We plan to extend the above studies to other camptothecin derivatives and their forms to contribute to better understanding the electronic structure factors of drug cytotoxicity that cannot be distinguished from pharmacokinetic factors in the experimental data.

Acknowledgments

This work was supported by the Slovak Grant Agency VEGA (contract No. 1/0139/20) and by the Slovak Science and Technology Assistance Agency (contract no. APVV-20-0213). The authors thank the HPC center at the Slovak University of Technology in Bratislava, which is a part of the Slovak Infrastructure of High Performance Computing (SIVVP Project No. 26230120002, funded by the European Region Development Funds), for computing facilities. M.B. thanks the Ministry of Education, Science, Research and Sport of the Slovak Republic for funding within the scheme 'Excellent research teams'.

References

Alagona G, Ghio C (2009) J Phys Chem A 113: 15206–15216.

Alagona G, Ghio C (2009a) Phys Chem Chem Phys 11: 776–790.

Babu PC, Sundaraganesan N, Sudha S, Aroulmoji V, Murano E (2012) Spectrochim Acta A 98: 1–6.

Bader RFW (1990) Atoms in Molecules: A Quantum Theory. Claredon Press, Oxford.

Bailly Ch (2019) Pharmacol Res 148: 104398.

Becke AD (1993) J Chem Phys 98: 5648–5652.

Biegler-Konig F, Schonbohm J, Bayles D (2001) J Comput Chem 22: 545–559.

Breza M (2021) Acta Chim Slovaca 14: 38–50.

Breza M, Jelemenska I (2022) J Vinyl Addit Technol 28: 352–366.

Breza M, Simon P (2019) Acta Chim Slovaca 12: 168–174.

Breza M, Simon P (2020) J Nanopart Res 22: 0058.

D'Amelio N, Aroulmoji V, Toraldo A, Sundaraganesan N, Anbarasan PM (2012) J Mol Struct 1013: 26–35.

DiNunzio MR, Douhal Y, Organero JAG, Douhal A (2018) Phys Chem Chem Phys 20: 14182–14191.

Fassberg J, Stella VJ (1992) J Pharm Sci 81: 676–684.

Frisch MJ, Trucks GW, Schlegel HB, Scuseria GE, Robb MA, Cheeseman JR et al. (2013) Gaussian 09, Revision D.01, Gaussian, Inc., Wallingford, CT.

Hussain I, Bania KK, Gour NK, Deka RC (2016) ChemistrySelect 1: 4973–4978.

Ivanova B, Spiteller M (2012) J Mol Struct 1012: 189–197.

Jelemenska I, Breza M (2021) Polym Degrad Stab 183: 109438.

Kabanda MM, Tran VT, Seema KM, Serobatse KRN, Tsiepe TJ, Tran QT, Ebenso EE (2014) Mol Phys 113: 683–697.

Keith TA (2017) AIMAll, Version 17.11.14, TK Gristmill Software Overland Park, KS. Available from aim.tkgristmill.com.

Mammino L (2013) J Mol Model 19: 2127–2142.

Mulliken RS (1955) J Phys Chem 23: 1833–1840.

Mulliken RS (1955a) J Phys Chem 23: 1841–1846.

Puskarova I, Breza M (2016) Polym Degrad Stab 128: 15–21.

Puskarova I, Breza M (2017) Chem Phys Let 680: 78–82.

Sawada S, Okajima S, Aiyama R, Nokata K-I, Furuta T, Yokokura T, Sugino E, Yamaguchi K, Miyasaka T (1991) Chem Pharm Bull 39: 1446–1454.

Serobatse KRN, Kabanda MM (2016) Eur Food Res Technol 242: 71–90.

Serobatse KRN, Kabanda MM (2016a) J Theor Comput Chem 15: 1650048.

Steklac M, Breza M (2018) Acta Chim Slovaca 11: 6–10.

Steklac M, Breza M (2021) Comput Theor Chem 1206: 113461.

Steklac M, Breza M (2021a) Polyhedron 207: 115360.

Steklac M, Breza M (2021b) ChemistrySelect 6: 7049–7055.

Steklac M, Breza M (2021c) Polyhedron 210: 115532.

Steklac M, Breza M (2022) Comput Theor Chem 1211: 113677.

Steklac M, Breza M (2022a) Acta Chim Slovaca 15: 72–84.

Tanizawa A, Fujimori A, Fujimori Y, Pommier Y (1994) J Natl Cancer Inst 86: 836–842.

Tsiepe TJ, Kabanda MM, Serobatse KRN (2015) Food Biophys 10: 342–359.

Ugliengo P (2006) MOLDRAW: A Program to Display and Manipulate Molecular and Crystal Structures. University Torino, Torino. Available from: www.moldraw.software.informer.com.

sciendo

Study on secondary metabolites of *Trichoderma atroviride* F742 and their role in antibiosis

Tomáš Pagáč, Zuzana Kubová, Ján Víglaš,
Zuzana Kavalová, Petra Olejníková

Institute of Biochemistry and Microbiology, Faculty of Food and Chemical Technology,
Slovak University of Technology in Bratislava, Radlinského 9, 812 37, Bratislava, Slovakia
tomaspagac1@gmail.com, petra.olejnikova@stuba.sk

Abstract: Soil-borne pathogenic fungi responsible for serious damage in agriculture are widely distributed. Traditional approach to control these pathogens leads to the use of chemical fungicides, many of which have proven harmful side effects on the environment. Mycoparasitic fungi of the genus *Trichoderma* have been used for pathogens biocontrol as well as for their ability to promote plant growth. As increased mycoparasitic activity of mutant strain *Trichoderma atroviride* F742 has been observed, its use as a biocontrol agent might be considered. In this work, we focused on mycoparasitic activity of the strain *T. atroviride* F742 prepared by UV mutagenesis (from parental strain *T. atroviride* F534) and the physiological role of *T. atroviride* metabolites in antibiosis.
T. atroviride F742 shows remarkable mycoparasitic activity attacking and colonizing phytopathogens (*Alternaria alternata*, *Botrytis cinerea*, *Fusarium culmorum*). Its isolated metabolites inhibit the growth of bacteria, yeasts, and fungi *Candida albicans, A. alternata* and *F. culmorum.* As different expression patterns in the secondary metabolites production of ABC transporters have been observed, we suggest their role in transport of secondary metabolites produced by *T. atroviride* F742.

Keywords: *Trichoderma* sp., secondary metabolites, mycoparasitism, ABC transporters, antimicrobial potential of produced metabolites

Introduction

Soil pathogenic fungi can cause serious damage in agriculture (Yu et al., 2021). Traditional approach to pathogen eradication involves the use of chemical fungicides, which have often been shown to have harmful side effects on the environment. An attractive way of reducing the concentration of chemical fungicides in agriculture is their combination with biocontrol strains (Howell, 2003; Sood et al., 2020). One of the possibilities for biocontrol are mycoparasitic fungi of the genus *Trichoderma* (Mukherjee et al., 2012; Poveda et al., 2020) which, apart from their mycoparasitic activity, protect plants and promote their growth (Raaijmakers et al., 2009; Aime et al., 2013).

Trichoderma sp. **mycoparasitism** is a result of combined processes including the production of antifungal secondary metabolites (Dennis and Webster, 1971; Claydon et al., 1987; Schirmböck et al., 1994; Lorito et al., 1996; Vinale et al., 2008), competition of nutrients (Chet, 1987), changes in morphological structure such as coiling, curling, and formation of appresorium-like structures (Elad et al., 1983; Lu et al., 2004).

Fungal antibiosis is strongly connected to the secretion of enzymes, antibiotics, and various secondary metabolites. Studies on suppression of plant pathogens have identified many different molecules involved in this process (Vey et al., 2001; Benitez et al., 2004; Khan et al., 2020), including peptaibols, 6-pentyl-α-pyrone, viridin, gliovirin, glisoprenins, gliotoxin, and various others. Apart from being toxic to pathogens (Pascale et al., 2020; Raaijmakers et al., 2009), these compounds are also involved in the promotion of plant growth (Lee et al., 2016). **Polyketides,** including polyphenols, anthraquinones, macrolides, polyenes, enediynes and polyethers, represent a highly diverse group of molecules with carbon skeletons. Considering the structural and functional diversity of polyketides, their synthesis is a result of controlled assembly of acetate and propionate. *Trichoderma* sp. genome contains more orthologues of polyketide synthase (PKS) genes with polyketide playing an important role in the fungus biology. Genomes of *T. atroviride* and *T. virens* contain 18 PKSs while the *T. reesei* genome has 11 PKSs (Baker et al., 2012). However, insufficient knowledge of secondary metabolites and their involvement in the antagonism has to be considered. A possible role in the antagonism is indicated by the expression of two *T. atroviride* PKS genes during the confrontation with plant pathogen *Rhizoctonia solani* (Mukherjee et al., 2012; Roveda et al., 2020).

While the production and secretion of antimicrobial compounds is an important factor of fungal antagonism, natural ability to protect themselves against toxins must be considered. The expression of ABC transporters enables protection against various phytopathogen toxins. Their detoxification function is well known, but their other physiological functions need to be further investigated. It is known that ABC transporters are not restricted to one particular substrate/s (Higgins, 2001). This diversity of substance specificity is reflected in the variety of physiological roles played by ABC transporters in the cell. There is a significant role of each ABC transporter in the export of a variety of secondary metabolites (including those participating in antagonistic interactions), waste products or toxins from the cell. For example, deletion mutants of *T. atroviride Taabc2* (G family ABC transporter) showed decreased resistance to fungal inhibitory compounds and their ability to protect tomato plants from *Pythium ultimum* and *R. solani* was impaired (Alfiky et al., 2021; Ruocco et al., 2009). In addition, null mutation of gene *CrabcG5 Clonostachys rosea* decreased the antagonism action against *Fusarium graminearum*, which resulted in unsuccessful protection of barley seedlings from foot rot diseases (Dubey et al., 2014a).

In this work, we focused on mycoparasitic activity of the strain *T. atroviride* F742 prepared by UV mutagenesis in confrontation with three different phytopathogens (*Alternaria alternata*, *Botrytis cinerea*, *Fusarium culmorum*). Secondary metabolites were isolated to determine their role in antibiosis and to design their possible transport mechanism via ABC transporters.

Materials and methods

Microorganisms and culture conditions

Fungal strains of *T. atroviride* CCM F534, *T. atroviride* CCM F742, *A. alternata* CCM F128, *B. cinerea* CCM F16, and *F. culmorum* CCM F21 were maintained on potato/dextrose/agar (PDA, Biolife, Italy) plates at 25 °C prior to their use in the experimental procedures. Bacteria (*Escherichia coli* CCM 3988, *Pseudomonas aeruginosa* CCM 1955, *Proteus vulgaris* CCM 1955, *Enterobacter cloacae* CCM 1903, *Staphylococcus aureus* CCM 3953, *S. epidermidis* CCM 4505) were maintained on Mueller-Hinton/Agar (MHA, Biolife, Italy) plates at 37 °C prior to their use in the experiments. All fungal and bacterial strains were obtained from the Czech Collection of Microorganisms. Model yeast *Candida albicans* SC 5314/ATCC MYA-2876 and *Candida parapsilosis* ATCC 22019 were obtained from the American Type Culture Collection and were maintained on Sabouraud agar (SDA, Biolife Italy) at 30 °C prior to their use in the experiments.

Dual culture assay

To examine the antagonistic activity of *T. atroviride* F742 against three phytopathogenic fungi, a dual culture assay was performed. Mycelial discs (5 mm diam.) of both mycoparasite (*T. atroviride* F742) and phytopathogen cultures were taken from the edge of actively growing colonies (48 h) and placed on the opposite site of fresh PDA 1.5 cm from the edge of the Petri dish. Fungal colonies were incubated for ten days in dual culture. After the confrontation of filamentous fungi, the antagonistic interaction was evaluated in terms of the mycoparasite growth over the phytopathogen (i), conidiation of the mycoparasitic fungus (ii) as well as conidiation on the phytopathogen colony (iii), according to Bell et al. (1982). To determine the microbistatic or microbicidal effect on phytopathogens, discs were taken from the confrontation zone after ten days of cultivation and placed on fresh PDA growth medium with benomyl (5 $\mu g \cdot mL^{-1}$, blocking any *Trichoderma* sp. growth, but not the phytopathogen; MIC of benomyl = 1 $\mu g \cdot mL^{-1}$ with microbistatic effect on *Trichoderma* sp., data not shown). If the growth of the phytopathogen was not observed after four days of cultivation, a disc of mycelium was taken and placed into 1 mL of Tween 80 solution, briefly shaken on vortex to release conidia and 250 µL was spread onto PDA plates. After 48 hours, the colonies of fungi grown from conidia were counted.

Transcriptomic analysis of ABC transporters during the production of secondary metabolites

During the secondary metabolites production on PDA growth medium covered with cellophane, the mycelium was harvested after 1st, 2nd and 3rd week. After being frozen in liquid nitrogen, 100 mg of mycelium was homogenized to powder. RNA was then extracted using the TRI reagent method (Sigma Aldrich, USA). After DNAase treatment (Qiaqen, USA) RNA was used for cDNA synthesis with the Masterscript RT-PCR System (5 Prime, USA). cDNA was subsequently used for the PCR reaction (PerfectTaq Plus DNA Polymerase kit, 5 Prime, Germany) with cycling procedure as follows: initial denaturation at 94 °C for 2 min; 30 cycles of denaturation at 94 °C for 30 s; appropriate annealing temperature for each primer set (Tab. 1) for 30 s; synthesis at 68 °C for 1 min; and further final synthesis of 10 min at 68 °C. The obtained PCR products were subjected to electrophoresis in 1.3 % agarose gel and visually shown under UV light (UVP Cambridge, UK).

Secondary metabolites extraction

Secondary metabolites *T. atroviride* F742 were isolated after cultivation on PDA growth medium inoculated on cellophane and cultivated for 21 days. Metabolites produced in the growth medium were then extracted with ethyl acetate. The organic fraction was dried

(Na_2SO_4), vaccum-concentrated at 40 °C to get a solid/oil-like residue, which was then diluted in 1 mL of ethyl acetate. The metabolites were visualized using thin layer chromatography (200 µm thick aluminum TLC plates, Silica gel 60F254; Merck Schüchardt, Germany), with 5 µL of metabolite extract. The plates were developed in a solvent system containing benzene and acetone (3:1). The secondary metabolites were then visualized in a visible spectrum and under UV light. Metabolite extract was then transferred into a microtube, dried under reduced pressure at 40 °C, weighed and diluted in 1 mL of DMSO, and used for the detection of antimicrobial activity.

Antimicrobial activity of isolated secondary metabolites

Sensitivity of bacterial strains and yeasts was determined by the broth micro-dilution method (CLSI, 1996; 2014). Antifungal activity (filamentous fungi) was evaluated by the macrodillution method (Dudová et al., 2002).

Biofilm formation in vitro

Biofilm formation was assayed by crystal violet staining in a 96-well polystyrene microtiter plate. In short, *C. albicans* was cultivated for 16 h (overnight inoculum) in Sabouraud broth (SB, Biolife Italy) supplemented with 2 % glucose under shaking (200 rpm). The culture was diluted to cell density of 10^7/mL into SB and 198 µL aliquots of fresh diluted cells were added into wells of a 96-flat bottom well polystyrene microplate (Sarstedt, Nümbrecht, Germany). For the biofilm inhibition assay, 2 µL of secondary metabolites (final concentration of 2.5—10 $\mu L \cdot mL^{-1}$) were added to 198 µL of inoculated SB medium. As the control, DMSO (1 %) treated cells were used. First, cells were cultivated without shaking at 37 °C for 2 h (phase of adherence). After 2 h, the culture medium was replaced by a fresh one (supplemented with metabolites), so only the cells that adhered to the plate surface formed the biofilm. The plates were then incubated without shaking at 37 °C for 48 h. The biofilm-coated wells were washed twice with 200 µL of PBS and then air dried for 15 min. Washed wells were stained with 110 µL of 0.4 % aqueous crystal violet solution for 15 min. Afterwards, each well was washed four times with 350 µL of sterile distilled water and immediately washed with 200 µL of 95 % ethanol. After 15 min of washing, 100 µL of the washing solution were transferred to a new well and the amount of the crystal violet stain in the washing solution was measured with a microtiter plate reader at 570 nm. Biofilm intensity was evaluated according to the observed absorbance values as weak, medium, or strong — [A570 <0.1—0.29> weak biofilm formation; A570 <0.3—0.5> medium biofilm formation; A570 >0.5 strong biofilm formation]. All experiments were performed in six parallel measurements.

Results

The model strain *T. atroviride* F742 was gained by UV mutagenesis from the parental strain *T. atroviride* F534 (Betina et al., 1986) and is characterized by brown conidia and the production of brown-red pigment (Fig. 1, Fig. 2) consisting of 1-acetyl-2,4,5,7-tetrahydroxyanthraquinone which is characterized by Rf = 0.32 (Betina et al., 1986).

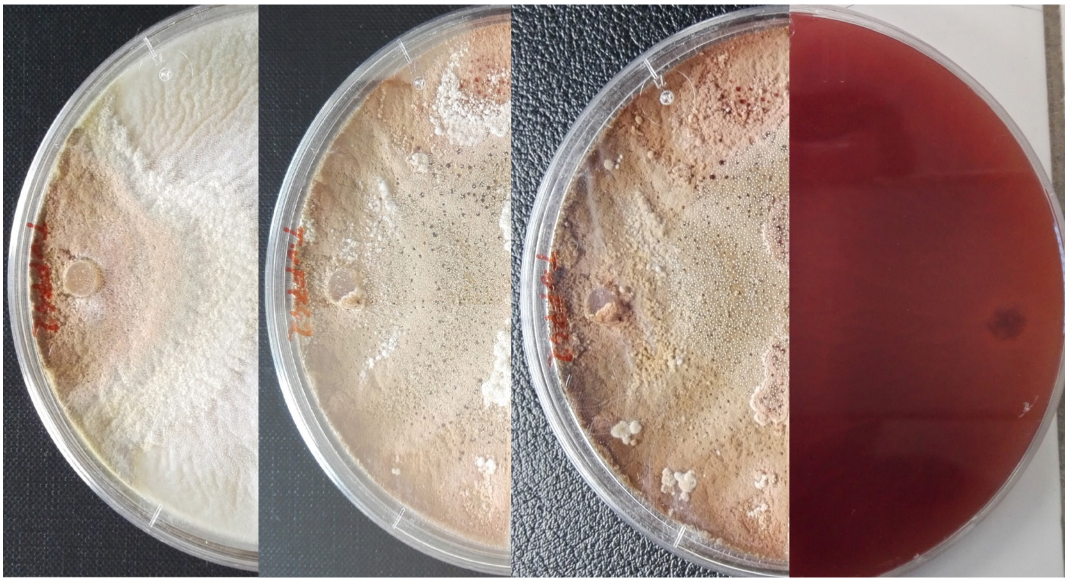

Fig. 1. Production of brown-red pigment during three weeks of *T. atroviride* F742 cultivation on PDA growth medium.

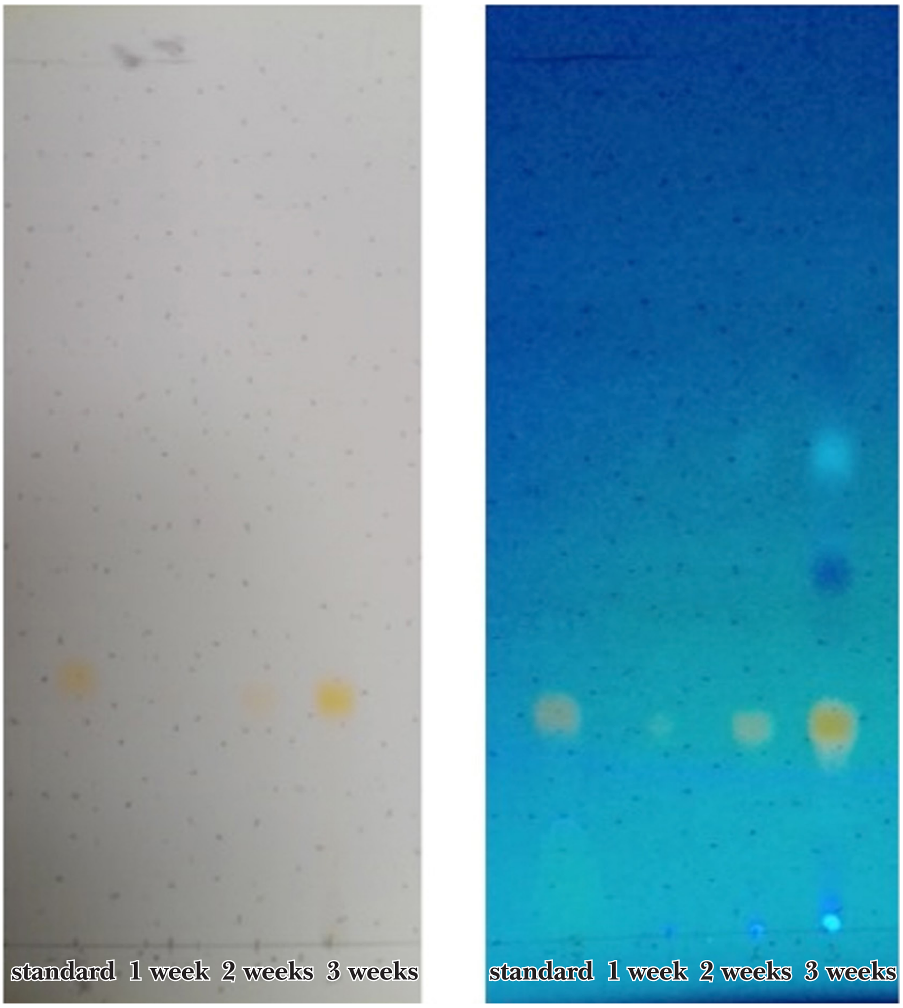

Fig. 2. Production of brown-red pigment – 1-acetyl-2,4,5,7-tetrahydroxyanthraquinone and other secondary metabolites, by *Trichoderma atroviride* F742 on PDA growth medium visualized on TLC plates under VIS light (left) and UV light (right).

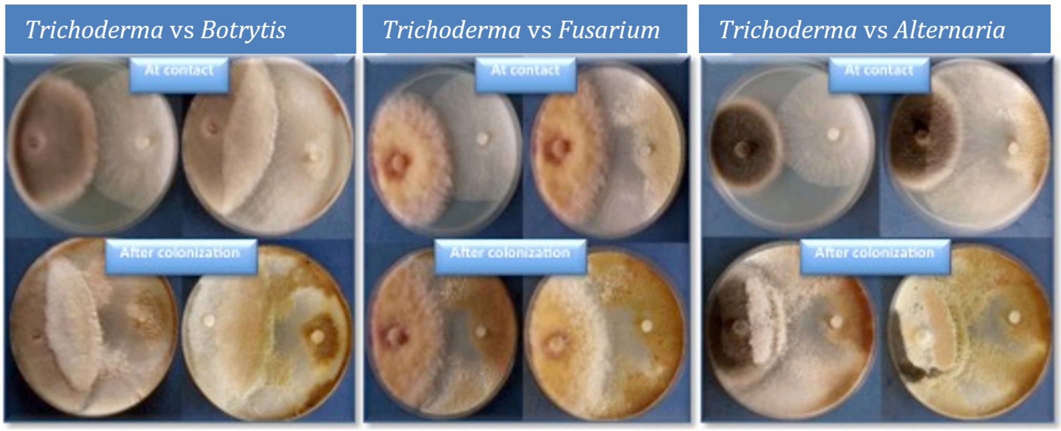

Fig. 3. Mycoparasitic activity of *Trichoderma atroviride* F742 against phytopathogens. At contact – the first picture shows the primary contact of model fungi, while the second picture shows slight overgrowth of phytopathogen. After colonization – the first picture shows overgrowth of the phytopathogen and the second picture manifest full colonization of model fungus.

In this work, increased mycoparasitic activity of *T. atroviride* F742 has been observed when compared to that of the parental strain *T. atroviride* F534 (Fig. 3). Parental strain *T. atroviride* F534 is able to inhibit the growth of all model phytopathogens but it is not able to overgrow them. On the other hand, as it is shown in Fig. 3, *T. atroviride* F742 is able to attack and colonize all model phytopathogens.

The results of mycoparasitic interaction and conidiation of the mycoparasite on the phytopathogen colony are summarized in Tab. 1. Phytopathogens were intensively colonized by *T. atroviride* F742, with intense conidiation on the phytopathogen surface. The effect of mycoparasite on phytopathogens was estimated as lethal – there was no growth of phytopathogen observed after the mycelium disk was taken from the overgrown area and placed on the PDA growth medium supplemented with benomyl (5 $\mu g \cdot mL^{-1}$). The benomyl concentration of 5 $\mu g \cdot mL^{-1}$ is fungistatic for *Trichoderma* sp. (including *T. atroviride* F742) but does not inhibit the growth of the phytopathogen. The fungistatic benomyl concentration for phytopathogens is above 10 $\mu g \cdot mL^{-1}$ (Kubová et al., 2022). The phenotype difference between the mutant and the parental strain is mainly in the different conidial color followed by the spectra of secondary metabolites (Fig. 2) with Rf factors of 0.32 (1-acetyl-2,4,5,7-tetrahydroxyanthraquinone), 0.4 and 0.516. In this work, the physiological role of secondary metabolites reflecting their role in antibiosis as well as the potential transport system for secondary metabolites, the ABC transporters, were investigated.

The transcriptomic profile of ABC transporters type G (Taabc2–Taabc9) and MDR transporters (MDR1–MDR8) (Kubová et al., 2022) were determined together with anthraquinone and other secondary metabolites production. Induction of PDR genes expression was observed for Taabc9, Taabc2, and Taabc7 after the first week of cultivation (Fig. 5), while the expression of MDR genes MDR6, MDR4, MDR2, MDR1, and MDR5 (Fig. 6) was observed at a later exponential phase, the highest gene expression was observed during the stationary phase (after 2nd and 3rd week), which correlates with the production of secondary metabolites (Fig. 2).

As the synergy of the produced secondary metabolites may contribute to antibiosis with other microorganisms, antimicrobial potential of *T. atroviride* F742 metabolites is also shown in our study. Antimicrobial activity was assayed on model bacteria, yeasts, and phytopathogenic fungi. Inhibition of *E. coli*, *S. aureus* and *S. epidermidis* were observed (Tab. 2), with the highest susceptibility of *E. coli* (58 % growth inhibition). Growth inhibition of three phytopathogens, *B. cinerea*, *A. alternata,* and *F. culmorum,* in the presence of isolated metabolites was monitored via the macrodilution method. The growth of *B. cinerea* was not affected, but partial inhibition (30 %) of *A. alternata* and *F. culmorum* was observed after three days. Model yeast *C. albicans* was also inhibited (40 %) by the sum of metabolites (Tab. 3). As candidiasis is often followed by biofilm formation, the potential of *C. albicans* biofilm eradication by the sum of secondary metabolites was studied. The biofilm was partially eradicated by the sum of secondary metabolites as shown in Tab. 4. In comparison with the control (no metabolites,

Tab. 1. Mycoparasitic activity of *Trichoderma atroviride* F534 and *Trichoderma atroviride* F742 in dual culture assay.

Strain	*B. cinerea*	*A. alternata*	*F. culmorum*
Pathogen colonization[a]			
T. atroviride F534	1	1	1
***T. atroviride* F742**	3	3	3
Conidiation on plate[b]			
T. atroviride F534	1	1	1
***T. atroviride* F742**	3	3	3
Conidiation on pathogen colony[c]			
T. atroviride F534	1	1	1
***T. atroviride* F742**	3	3	3

[a] 0 – Mycoparasite does not grow over the phytopathogen colony. 1 – mycoparasite partly grows over the phytopathogen colony (5–20 mm from the zone of contact of both micromycetes). 2 – mycoparasite grows over the phytopathogen colony (21–40 mm from the zone of contact). 3 – mycoparasite intensely colonizes the surface of the phytopathogen (41–60 mm from the zone of contact).

[b] 0 – Mycoparasite does not form conidia outside the phytopathogen colonies. 1 – weak conidiation of the mycoparasite outside the phytopathogen colonies (10–100 conidia per cm^2), 2 – conidiation of the mycoparasite outside the phytopathogen colonies (10^3–10^4 conidia per cm^2), 3 – intense conidiation of the mycoparasite beyond the phytopathogen (10^5–10^6 conidia per cm^2).

[c] 0 – Mycoparasite does not form conidia outside the phytopathogen colonies. 1 – weak conidiation of the mycoparasite outside the phytopathogen colonies (10–100 conidia per cm^2), 2 – conidiation of the mycoparasite outside the phytopathogen colonies (10^3–10^4 conidia per cm^2), 3 – intense conidiation of the mycoparasite beyond that of the phytopathogen (10^5–10^6 conidia per cm^2).

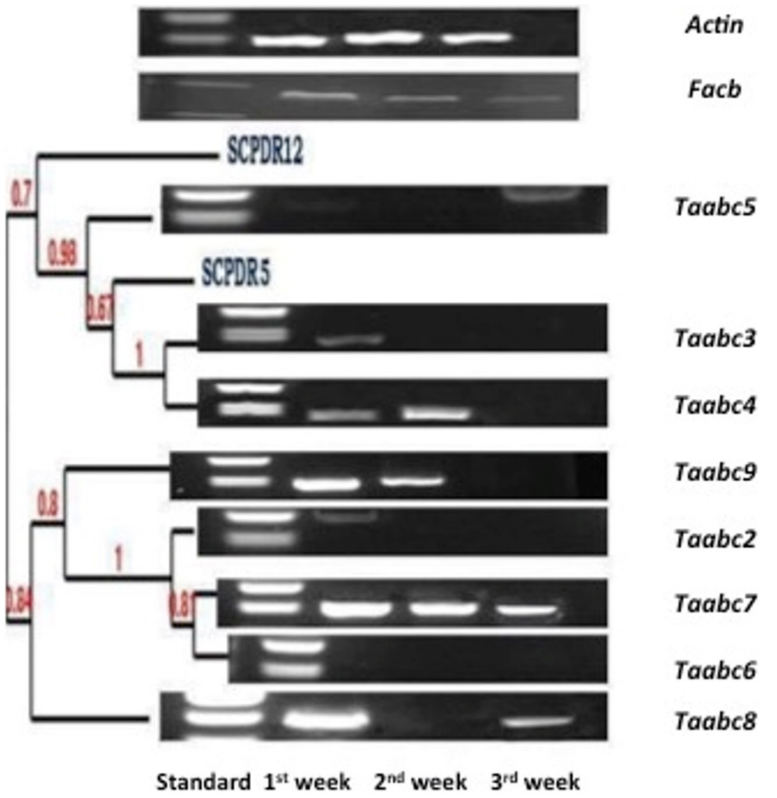

Fig. 5 Transcriptomic analysis of ABC transporter (ABC G-family) genes Taabc2—Taabc9 of *T. atroviride* F742 during three-week cultivation on PDA growth medium.

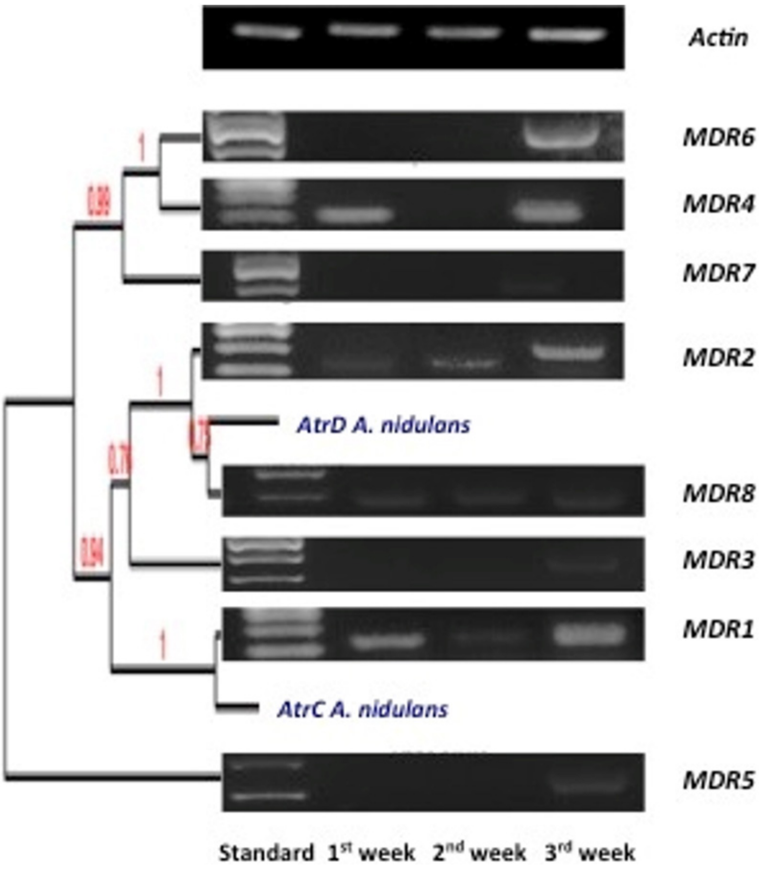

Fig. 6 Transcriptomic analysis of MDR transporter (ABC B-family) genes MDR1—MDR8 of *T. atroviride* F742 during three-week cultivation on PDA growth medium.

1 % DMSO), the intensity of biofilm formation decreased from strong to weak. Apart from their mycoparasitic activity, fungal strain *T. atroviride* F742 is also a potential source of new antimicrobial compounds as it is shown in this study.

Tab. 2. Antibacterial activity of extracted secondary metabolites (10 $\mu L \cdot mL^{-1}$).

Microorganism	Growth (%)
Escherichia coli CCM 3988	42
Proteus vulgaris CCM 3955	100
Enterobacter cloacae CCM 1903	100
Staphylococcus aureus CCM 3953	50
Staphylococcus epidermidis CCM 4505	65

Tab. 3. Antifungal activity of extracted secondary metabolites (10 $\mu L \cdot mL^{-1}$).

Microorganism	Growth (%)
Candida albicans SC 5314	60
Candida parapsilosis ATCC 22019	100
Alternaria alternata CCM F397	70
Fusarium culmorum CCM F21	70
Botrytis cinerea CCM F314	100

Tab. 4. Intensity of *C. albicans* biofilm in the presence of the sum of secondary metabolites of *T. atroviride* F742.

Metabolites	Intensity of formed biofilm	A_{570}
10 $\mu L \cdot mL^{-1}$	Weak	0.298
5 $\mu L \cdot mL^{-1}$	Medium	0.320
2.5 $\mu L \cdot mL^{-1}$	Medium	0.421
Control (1 % DMSO)	Strong	1.394

Discussion

Management of fungal diseases of food crops and fruits attracts more and more attention as soil-borne pathogenic fungi are widely distributed and are responsible for serious damages in agriculture (Rossman, 2009; Yu et al., 2021). Phytopathogenic fungi are not only responsible for plant diseases, but some representatives of *Fusarium* sp., *Aspergillus* sp., *Penicillium* sp., are able to produce mycotoxins while growing on plants, which can seriously endanger consumers' health. The fight against phytopathogenic fungi is based on traditional approach – the use of chemical fungicides, which have been a very effective "weapon in the fight" against soil-borne fungal pathogens.

In recent years, environmental hazards caused by excessive use of pesticides have been widely discussed; therefore, scientists in the agricultural field are searching for alternative measures against pesticides. Furthermore, shortly after the introduction of site-specific fungicides into the plant protection management, resistance development in the pathogen populations was observed, leading to the loss of primary active fungicides (McBeath et al., 2010; Su et al., 2021). These findings strongly support more eco-friendly approach with the use of biological control as a potential tool to minimize the risk on human health and environment.

Mycoparasitic fungi of the genus *Trichoderma* have been used for biocontrol of pathogens like *Rhizoctonia solani*, *Sclerotium rolfsii* and *Botrytis cinerea* (Mukherjee et al., 2012; Roveda et al., 2020). Apart from their mycoparasitic activity, they protect plants by inducing a plant defensive system and promoting plant growth (Raaijmakers et al., 2009; Aime et al., 2013; Pascale et al., 2020). Our study has focused on the fungal strain *T. atroviride* F742 prepared by UV mutagenesis as a potential biocontrol agent for its use in environmentally friendly crops protection. In comparison with the parental strain, the characteristic feature of mutant strain *T. atroviride* F742 is brown-colored conidia followed by the production of brown-red pigment consisting of 1-acetyl-2,4,5,7-tetrahydroxyanthraquinone (Betina et al., 1986).

As increased mycoparasitic activity of *T. atroviride* F742 has been observed, its potential use in biocontrol is in play. The parental strain *T. atroviride* F534 was also able to inhibit the growth of phytopathogens but complete colonization has not been observed (Olejníkova et al., 2010). On the other hand, our mutant strain easily colonized all three model phytopathogens with intense conidiation on the surface of the phytopathogen colony. The effect of the mycoparasite on the phytopathogens was estimated as lethal – there was no growth observed after mycelium was taken from the overgrown area.

As secondary metabolites play an important role in antibiosis, the physiological role of secondary metabolites of *T. atroviride* F742 was investigated. Also, fungal tools for transport of secondary metabolites were studied. Production of the most secondary metabolites of *Trichoderma* sp. is bound to the end of exponential and stationary growth phase, as documented by TLC (Fig. 2), which clearly shows that other secondary metabolites are produced together with anthraquinones. Anthraquinones are red-brown colored metabolites and as it is easy to follow their production; they have been chosen as an indicator of secondary metabolism initialization and progress. There is limited knowledge about the transport mechanisms of secondary metabolites into the environment. Some studies indicate that the role of fungal ABC transporters is not limited only to the detoxification mechanisms.

Fungal MFS and ABC transporters are closely associated with the transport of host-specific or non-specific toxic metabolites by toxinogenic fungal phytopathogens (del Sobro et al., 2000; Jeandet et al., 2021). As mycotoxins produced by fungal strains are classified as secondary metabolites, the role of efflux pumps in secondary metabolites transport is thus confirmed. Moreover, the organization of gene clusters supports the physiological function of ABC transporters in secondary metabolite transport as these are clustered with gene coding PKS (polyketide synthesis), enzymes involved in synthesis of secondary metabolites (Andrade et al., 2000, Dohren et al., 2009). To determine the ABC transporters as transport systems for secondary metabolites produced by *Trichoderma* sp., the profile of ABC transporters – G family and ABC transporters of family B (MDR) were expressed in correlation with the production of anthraquinones and other secondary metabolites. Anthraquinones are in general synthesized from acetyl-CoA and malonyl-CoA via the Claisen condensation by PKS type I, which results in the formation of poly-β-ketide chain (Fig. 4). ABC transporters possess a binding site for Facb (transcription factor of acetate metabolism in fungi) as acetyl CoA is the precursor of polyketides and other secondary metabolites. The presence of the Facb site in regulation regions indicates their potential role in the transport of secondary metabolites. Bioinformatic analysis of the *Trichoderma* sp. genome (http://genome.jgi.doe.gov/Triat2/Triat2.home.html) has shown eight full and two half ABC-G transporters with high homology to yeast transporters PDR12 and PDR5 (*Saccharomyces cerevisiae*) and eight MDR transporters with high homology to AtrC and AtrD (*Aspergillus nidulans*) (Kubová et al., 2022). The transcriptomic profile of ABC transporters type G (Taabc2–Taabc9) and MDR transporters (MDR1–MDR8) genes were determined in correlation with anthraquinone and other secondary metabolites production. The expression of MDR genes MDR6, MDR4, MDR2, MDR1 and MDR5 (Fig. 6) was observed at later exponential phase (after two weeks) and at stationary phase (after three weeks) in correlation with secondary metabolites production. Thus, it can be assumed that MDR transporters have a role in the transport of secondary metabolites as their expression correlates with anthraquinones and other secondary metabolites production (Fig. 2).

Many microorganisms isolated from soil and plant-associated environments produce secondary metabolites that adversely affect the growth or metabolic activity of other microorganisms (Harman et al., 2021; Fravel, 1988). The production of secondary metabolites often favors its producer in the environment since many metabolites are toxic to other competing microorganisms in the same environment. Secondary metabolites are often the sources of rare antimicrobial active compounds (del Sorbo et al., 2000, Schoonbeek et al., 2002). While *Trichoderma* sp. are soil-born fungi related to plant rhizosphere, and their offensive and defensive strategies are well developed, they present a potential source of antimicrobial active compounds. In this work, we have shown how the whole sum of produced secondary metabolites contributes to antibiosis with other microorganisms via the antimicrobial potential of metabolites produces by *Trichoderma* sp. Antimicrobial effect on bacteria, yeasts, and phytopathogenic fungi has been observed. Antifungal potential was observed only when the whole sum of metabolites was present, which mirrors the synergism of metabolites produced in the environment. As it has been shown, *T. atroviride* F742 is a successful antagonistic

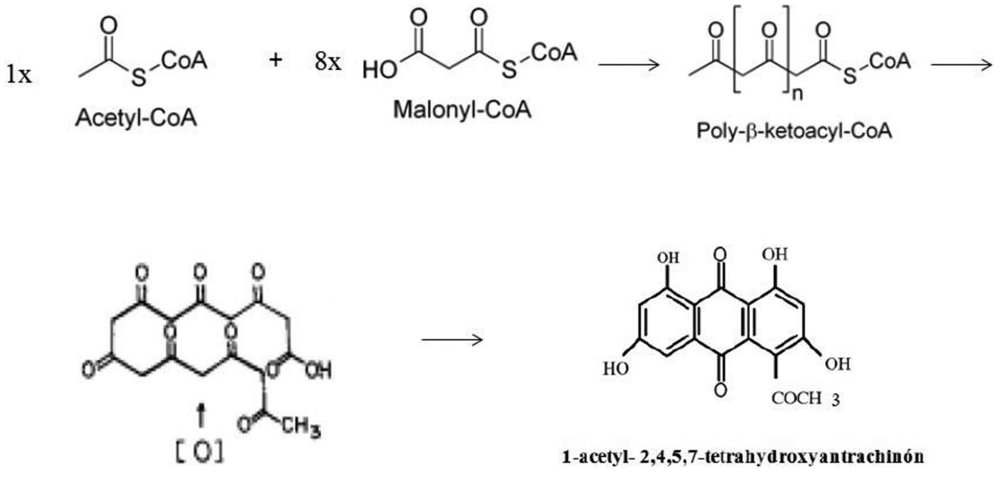

Fig. 4. Proposed synthesis of 1-acetyl-2,4,5,7-tetrahydroxyanthraquinone (Betina et al., 1986).

fungus and antifungal activity of its secondary metabolites can also contribute to its mycoparasitic properties by partial inhibition of phytopathogens growth. Its main contribution to mycoparasitic activity is considered to be the activity of hydrolytic enzymes degrading cell walls of phytopathogens (Druzhinina et al., 2011; Tyśkiewicz et al., 2022).

Conclusion

In this work, mycoparasitic activity of the strain *Trichoderma atroviride* F742 prepared by UV mutagenesis was confronted with three different phytopathogens. Specifically, secondary metabolites were isolated to determine its antimicrobial activity and possible transport system via ABC transporters MDR6, MDR4, MDR2, MDR1 and MDR5. The mutant strain *T. atroviride* F742 was able to attack and colonize all model phytopathogens with lethal effect on phytopathogenic fungi, while the parental strain *T. atroviride* F534 only inhibits the growth of model phytopathogens but is not able to colonize them. As different expression patterns of various ABC transporters have been observed, potential role of MDR in the transport of isolated secondary metabolites has been suggested. Antimicrobial testing of secondary metabolites showed the highest inhibition of *E. coli* and *S. aureus* among model bacteria. Phytopathogenic fungi (*A. alternata* and *F. culmorum*) were partially (30 %) inhibited suggesting that secondary metabolites produced by *T. atroviride* F742 can also contribute to its mycoparasitic activity. Even though the main contribution to their mycoparasitic activity is still considered to be the activity of hydrolytic enzymes degrading cell walls of phytopathogens, it is important to consider the contribution of other mechanisms, taking in account that mycoparasitic interaction is the synergy of several mechanisms. However, further and more detailed investigation is needed to study the increased mycoparasitic activity of *T. atroviride* F742.

Acknowledgement

This work was supported by the Grant Agency of Ministry of Education, Science, Research and Sport of the Slovak Republic, research project No. VEGA 1/0388/22 and by the Slovak Research and Development Agency, under the Contract No. APVV-19-0-0094.

References

Aimé S, Alabouvette C, Steinberg C, Olivain C (2013) Molecular Plant-Microbe Interactions 26: 918–926.

Alfiky A, Weisskopf L (2021) Journal of Fungi, 7(1), 61.

Andrade AC, Van Nistelrooy JGM, Peery RB, Skatrud PL, De Waard MA (2000) Molecular and General Genetics MGG 263: 966–977.

Baker SE, Perrone G, Richardson NM, Gallo A, Kubicek CP (2012) Microbiology 158: 147–154.

Bell DK, Wells HD, Markham CR (1982) Phytopathology 72: 379–382.

Benítez T, Rincón AM, Limón MC, Codón AC (2004) International microbiology 7: 249–260.

Betina V, Sedmera P, Vokoun J, Podojil M (1986) Cellular and Molecular Life Sciences 42: 196–197.

Chet I (1987) Innovative approaches to plant disease control. Wiley.

Claydon N, Allan M, Hanson JR, Avent AG (1987) Transactions of the British Mycological Society, 88: 503–513.

Clinical and Laboratory Standards Institute (CLSI). Approved standard—Eight edition, CLSI M7-A9, USA; 2014.

Clinical and Laboratory Standards Institute (CLSI). NCCLS document M27-A, 15, 10, VA Medical Center, Tucson; 1996.

Del Sorbo G, Schoonbeek HJ, De Waard MA (2000) Fungal genetics and biology, 30(1), 1–15.

Dennis C, Webster J (1971) Transactions of the British Mycological Society 57: 41IN4-48.

Druzhinina IS, Seidl-Seiboth V, Herrera-Estrella A, Horwitz BA, Kenerley CM, Monte E, Kubicek CP (2011) Nature Reviews Microbiology 9: 749–759.

Dubey MK, Jensen DF, Karlsson M (2014) Molecular Plant-Microbe Interactions 27: 725–732.

Dudová B, Hudecová D, Pokorný R, Mičková M, Palicová M, Segľa P, Melník M (2002) Folia microbiologica 47: 225–229.

Elad Y, Barak R, Chet I (1983) Journal of Bacteriology 154: 1431–1435.

Fravel, Deborah R. Annual Review of Phytopathology 26.1 (1988): 75–91.

Harman G, Khadka R, Doni F, Uphoff N (2021) Frontiers in Plant Science, 11, 610065.

Higgins CF (2001) Research in microbiology 152: 205–210.

Hjeljord L, Tronsmo A (1998) Trichoderma and Gliocladium 2: 131–151.

Howell CR (2003) Plant disease 87: 4–10.

Inbar J, Chet I (1992) Journal of Bacteriology 174: 1055–1059.

Jeandet P, Vannozzi A, Sobarzo-Sánchez E, Uddin MS, Bru R, Martínez-Márquez A, Nabavi SM (2021) Natural product reports, 38(7), 1282–1329.

Khan RAA, Najeeb S, Hussain S, Xie B, Li Y (2020) Microorganisms, 8(6), 817.

Kubová Z, Pagáč T, Víglaš J, Olejníková P (2022) Acta Chimica Slovaca, 15(1), 85–96.

Lee S, Yap M, Behringer G, Hung R, Bennett JW (2016) Fungal Biology and Biotechnology 3: 7.

Lorito M, Woo SL, D'ambrosio M, Harman GE, Hayes CK, Kubicek CP, Scala F (1996) MPMI-Molecular Plant Microbe Interactions 9: 206–213.

Lu Z, Tombolini R, Woo S, Zeilinger S, Lorito M, Jansson JK (2004) Applied and Environmental Microbiology 70: 3073–3081.

Mukherjee M, Mukherjee PK, Horwitz BA, Zachow C, Berg G, Zeilinger S (2012) Indian journal of microbiology 52: 522–529.

Olejnikova P et al. (2010) Folia microbiologica 55.1: 102–104.

Pascale A, Proietti S, Pantelides IS, Stringlis IA (2020) Frontiers in plant science, 10, 1741.

Pavlovičová R (1998) Chem. Listy, 92: 406–414.

Poveda J, Abril-Urias P, Escobar C (2020) Frontiers in Microbiology, 11, 992.

Raaijmakers JM, Paulitz TC, Steinberg C, Alabouvette C, Moënne-Loccoz Y (2009) Plant and soil 321: 341–361.

Rossman AY (2009) Biological Invasions 11: 97–107.

Ruocco M, Lanzuise S, Vinale F, Marra R, Turrŕ D, Woo SL, Lorito M (2009) Molecular Plant-Microbe Interactions 22: 291–301.

Schirmböck M, Lorito M, Wang YL, Hayes CK, Arisan-Atac I, Scala F, Kubicek CP (1994) Applied and Environmental Microbiology 60: 4364–4370.

Sood M, Kapoor D, Kumar V, Sheteiwy MS, Ramakrishnan M, Landi M, Sharma A (2020) Plants, 9(6), 762.

Su J, Zhao J, Zhao S, Li M, Pang S, Kang Z, Wang X (2021) Frontiers in Genetics, 12, 699342.

Tyśkiewicz R, Nowak A, Ozimek E, Jaroszuk-Ściseł J (2022) International Journal of Molecular Sciences, 23(4), 2329.

Vey A, Hoagland RE, Butt TM (2001) 12 Fungi as biocontrol agents 311.

Vinale F, Sivasithamparam K, Ghisalberti EL, Marra R, Woo SL, Lorito M (2008) Soil Biology and Biochemistry, 40(1), 1–10.

von Döhren H (2009) Fungal Genetics and Biology 46: 45–52.

Yu J, Wang D, Geetha N, Khawar KM, Jogaiah S, Mujtaba M (2021) Carbohydrate Polymers, 261, 117904.

Zeilinger S, Galhaup C, Payer K, Woo SL, Mach, RL, Fekete C, Kubicek CP (1999) Fungal Genetics and Biology 26: 131–140.

sciendo

Thermal- and light-induced SCO effect in Fe(II) complexes and coordination polymers

Alexandra Šagátová[1], **Barbora Brachňaková**[1], **Ivan Šalitroš** [1, 2]

1Department of Inorganic Chemistry, Faculty of Chemical and Food Technology,
Slovak University of Technology in Bratislava. Bratislava SK-81237, Slovakia.
2Central European Institute of Technology, Brno University of Technology,
Purkyňova 123, 61200 Brno, Czech Republic.
alexandra.sagatova@stuba.sk

Abstract: The review presents several families of spin crossover (SCO) active Fe(II) coordination compounds with photoactive N-donor heterocyclic ligands, in which the photoinduced structural changes can activate reversible change of spin state and thus control magnetic properties under isothermal conditions. Detailed description of structural, spectral, and magnetic behavior for selected examples of photoisomerizable coordination compounds are provided. From the application point of view, light is an excellent tool to control SCO properties. The first and best known approach called Light Induced Excited Spin State Trapping (LIESST) has a significant technological limitation due to low temperatures (< 120 K) required for the trapping and existence of photoexcited metastable states. The second and more elegant approach known as Ligand-Driven Light-Induced Spin Crossover (LD-LISC) seems to be a very suitable strategy utilizing light-induced structural changes to control the spin. Isomerization of photoswitchable groups, such as azobenzenes or stilbenes, can cause reversible transformation between two isomeric forms after exposition to selective wavelengths at ambient temperature. A very recent third approach, the Guest-Driven Light-Induced Spin Crossover (GD-LISC) effect employing the photoisomerizable guest molecules to control the spin state has also been introduced.

Keywords: spin crossover, isomerization, light-excited spin-state trapping effect, ligand-driven light-induced spin crossover, molecular switches, guest-driven light-induced spin crossover.

Introduction

Based on the crystal field theory, octahedral symmetry of Fe(II) complexes has the valence *d*-orbitals split into two energy levels. Energy difference between the lower energy triply degenerate t_{2g} and higher energy doubly degenerate e_g orbitals is a parameter of crystal field strength Δ. Its value is balanced by other natural parameter representing spin-pairing energy P of the Fe(II) electrons. The Δ magnitude is inversely dependent on distances between the metal and ligand donor atoms and it varies systematically according to the electron nature of the ligands (König, 1991). Electron effects of ligand influence the spin state of Fe(II) ions, which are either diamagnetic low-spin (LS) or paramagnetic high-spin (HS) at given temperature (Hauser, 2004). If Δ is higher than P, the valence d-electrons of Fe(II) occupies the t_{2g} levels. If the σ-donor and π-acceptor properties prevail, the ligands produce the strong ligand field and the LS state of Fe(II) ions is reached. No intrinsic magnetic moment of Fe(II) electron pairs is produced upon external magnetic field resulting in negative magnetic susceptibility χ. On the other hand, if Δ is lower than P, the Fe(II) valence d-electrons reach energy based on the Hund's maximum multiplicity rule. Unpaired electrons cause a change in the magnetism; thus, external magnetic field induces magnetic moment μ resulting in positive value of magnetic susceptibility χ. Coordinated ligands have weaker π-back donation effect thus, they have weaker ligand field, and the HS state is reached. Ligand field strength of aromatic N-donor ligands is often classified into intermediate range and the energy parameters Δ and P are similar. Reversible transition between the LS and HS states can be induced by external stimuli, such as temperature (T), pressure (p), light ($h\nu$), magnetic field induction (B), or electric field strength (E); these coordination compounds exhibit so-called "spin crossover" effect (Brachňaková and Šalitroš, 2018; Gütlich et al., 1994; Šalitroš et al., 2009). One of the most important parameters of the temperature-induced SCO effect is the transition temperature ($T_{1/2}$) at which half of both HS and LS fraction coexist together. The HS mole fraction γ_{HS}, evaluated in the μ_{eff} or $\chi_M T$ form, shows quantitative information on total induced intrinsic magnetic moment. Another basic SCO characteristic is the shape of the conversion curve, which can be gradual, incomplete, abrupt, hysteretic, or multi-step. In addition, thermal hysteresis is also characterized by the width of loop $\Delta T_{1/2}$ given as a difference between cooling $T_{1/2}(\downarrow)$ and heating cycle $T_{1/2}(\uparrow)$. The conversion curve can be divided into three parts: LS and HS plateaus and active SCO section (Gütlich and Goodwin, 2004).

SCO is accompanied by a change in magnetic values. In case of the HS state of the Fe(II) center, the compounds contain unpaired electrons ($S = 2$) and they show paramagnetic behavior. Since there are no unpaired electrons in the LS ($S = 0$), they are diamagnetic at the corresponding temperature. SCO is also associated with changes in the structural parameters. Bond distances between the central atom and donor atom of the ligand are longer and weaker for the HS electronic configuration due to occupied e_g orbitals with the antibonding character. This leads to the expansion of the molecular volume (between 1 % and 10 %), and the change of the angles of coordination polyhedron and unit cell parameters (a, b, c, α, β, γ, V). Vibrational spectroscopic measurements (FT-IR and Raman spectroscopy) are often used to characterize SCO systems. Bond strength between the central atom and ligands changes significantly upon the spin transition and the vibrational modes. SCO compounds have different color in the HS and LS state; thus their electronic transition properties depend on the actual spin state. Therefore, the SCO event can be detected by electronic spectroscopy, where LS and HS *d-d* and metal-to-ligand charge transfer transitions can be recognized in visible and IR regions, respectively. For instance, Fe(II) HS complexes have one single transition, $^5T_{2g}\rightarrow{}^5E_g$, localized in near-infrared area (figure 1 is LIESST effect) and the LS configuration shows two absorption bands assigned to spin-allowed $^1A_{1g}\rightarrow{}^1T_{1g}$ and $^1A_{1g}\rightarrow{}^1T_{2g}$ transitions. Electron spectra of the SCO active Fe(II) complex above and below $T_{1/2}$ should also clearly reflect the temperature-induced t_{2g}^6 ($^1A_{1g}$) ↔ $t_{2g}^4\ e_g^2$ ($^5T_{2g}$) conversion (Gütlich et al., 2000). The LS → HS conversion reaches thermodynamic equilibrium at $T_{1/2}$ presenting zero Gibbs energy difference ΔG. Entropy ΔS between the fractions is higher and thus, the $T\Delta S$ contribution dominates over that of ΔH, which is identified to be positive in this process. Hence, the SCO phenomenon is entropically controlled and the variation of its free ΔG becomes negative. In the lower temperature interval $T < T_{1/2}$, the LS state with lower entropy is thermodynamically more stable while the HS configuration is preferred in SCO complexes up to above $T_{1/2}$ (Halcrow, 2011).

In general, the SCO phenomenon has molecular origin, however, the shape of the $\gamma_{HS} = f(T)$ curve is strongly dependent on intermolecular interactions. The stronger these interactions are, the more intense is the cooperation of neighboring SCO molecules in the crystal lattice and the SCO curve is steeper (Boukheddaden et al., 2007; Bousseksou et al., 2011). Magnetic hysteresis related to the intermolecular interactions (e.g., hydrogen bonding, π-π interactions, or π-system interactions with a free electron pair) is caused by elastic stress and its loop width is related to the strength of the cooperative interactions. Uncoordinated anions or solvent molecules involved in the crystal lattice may also affect an intermolecular pressure in the lattice and create intermolecular interactions between SCO active complex units (Murray and Kepert, 2004; Real et al., 2005). Some complexes have different magnetic properties due to different arrangements of molecules in the crystal lattice, thus, the polymorphs may show different SCO behavior. Such magnetic diversity in SCO complexes is caused by different internal pressure within the crystal lattice (Šalitroš et al., 2012; Šalitroš et al., 2014; Tao et al., 2012).

Light-induced spin crossover

One of two principles of light-induced SCO between the LS ($^1A_{1g}$) ↔ HS ($^5T_{2g}$) states is the **L**ight-**I**nduced **E**xcited **S**pin **S**tate **T**rapping (LIESST) effect (Decurtins et al., 1984; Decurtins et al., 1985). In this case, Fe(II) complexes are irradiated by light with wavelength typical for the **M**etal-to-**L**igand **C**harge-**T**ransfer (MLCT) and d-d transitions (usually 400–800 nm) and the LS electrons are excited into metastable HS state. At sufficiently low temperatures (mostly below 30 K), the lifetime of

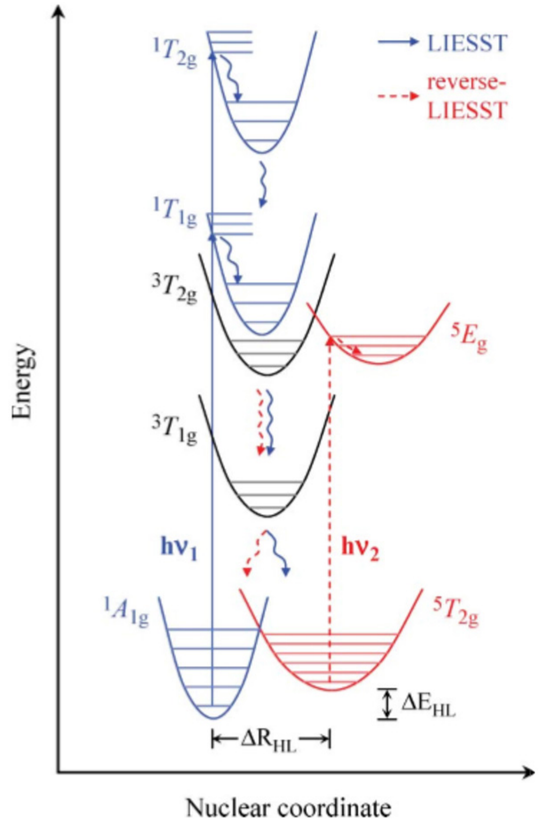

Fig. 1. Jablonski diagram of the mechanism of LIESST and *reverse*-LIESST effect for Fe(II) SCO complexes (Ando et al., 2010).

trapped metastable state can reach several hours or days (Šalitroš and Pavlik, 2018). Mechanism of the LIESST effect (Fig. 1) is proposed so that excited singlet states ($^1T_{1g}$, $^1T_{2g}$) can relax to triplet states ($^3T_{1g}$, $^3T_{2g}$) by **I**nter**s**ystem **C**rossing and subsequently either to the LS ($^1A_{1g}$) or HS ($^5T_{2g}$) state (Hauser, 1991; Bertoni et al., 2015). Back-relaxation of the metastable HS phase to ground LS state is activated by heat, where T(LIESST) parameter characterizes the critical temperature above which the LS → HS photoexcitation cannot be observed anymore. This temperature follows the trend of inverse energy gap, which is given by equation 1 (Létard, 2005). Thus, T(LIESST) and $T_{1/2}$ temperatures of the photoinduced and temperature induced SCO effect are inversely proportional to each other based on the inverse gap effect in the given empirical equation (1) (Capes et al., 2000).

$$T(\text{LIESST}) = T_0 - 0.3T_{1/2} \qquad (1)$$

Another situation occurs when the HS compound is irradiated with light typical for its d-d transitions (usually near IR region, 800–1200 nm) and the same, but reversed mechanism, the so-called *reverse*-LIESST occurs (Hauser and Adler, 1991). Excited HS electrons of the central atom's configuration preferentially relax to the singlet LS ground state $^1A_{1g}$. To achieve a long-lived metastable state, the potential energy barrier between the LS and HS states should be sufficiently separated to suppress the thermal relaxation and tunnelling phenomenon. By analyzing the potential curves, feasibility of LIESST and *reverse*-LIESST effects can be predicted according to the relative position and energy of a reaction coordinate of an **i**ntermediate **s**tate compared to the HS and LS reaction coordinates (Fig. 2). In the same complex, both LIESST and *reverse*-LIESST can be induced only if intermediate states are localized between the LS and HS minima (Case 1). Moreover, if the intermediate state acquires energy in the range of the HS reaction coordinate, the LIESST effect can be achieved but not the *reverse*-LIESST (Case 2). Conversely, if the intermediate states minimum is shifted to the LS potential curve, the *reverse*-LIESST is achieved instead of the LIESST effect (Case 3). In the end, the intermediate state reaction coordinate energy is localized below the HS state, hence neither LIESST nor *reverse*-LIESST effect occur (Case 4) (Ando et al., 2010).

However, the fact that a complex exhibits temperature-induced SCO does not immediately imply the attainability of the LIESST effect as the LIESST effect has not been observed in many compounds with temperature-induced SCO. Light-induced SCO effect is also accompanied by structural changes, which greatly determine the stability of the metastable spin state. For example, lifetime of the excited HS state depends mainly on the change of the coordination bond lengths. If the difference in bond lengths between the LS and HS state is small, the energy barrier is small too. Coordination bond lengths vary in the range of 0.2 Å–0.4 Å for the LIESST active Fe(II) complexes. Up to now, the light-excited metastable HS state has been reached only at cryogenic temperatures (T(LIESST) < 130 K). Therefore, this effect shows significant application limits (Sheu et al., 2009).

Second approach of light-induced SCO effect is described for compounds coordinated by ligands with incorporated photoactive moiety. A photoreaction on the ligand skeleton via absorption of radiation λ causes isothermal spin transition of Fe(II) electrons, the so-called **L**igand **D**riven – **L**ight-**I**nduced **S**pin **C**hange (LD-LISC) effect (Roux et al., 1994; Zarembowitch et al., 1993). Photoinduced structural changes of the light-sensitive moiety lead to the ligand field change which results into SCO switching of the corresponding coordination compound (Boillot et al., 1996; Boillot et al., 2009; Rösner et al., 2015; Šalitroš et al., 2017). For example, the Fe(II) compound, which differs only in an isomeric moiety of coordinated ligand, has a photosensitive group in the *trans*- configuration for C_A and this complex shows to be SCO active with $T_{1/2,1}$. However, complex C_B with *cis*- configuration

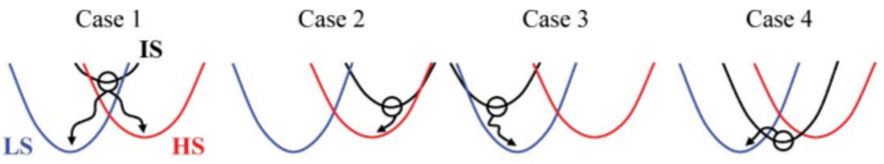

LIESST	Yes	Yes	No	No
reverse-LIESST	Yes	No	Yes	No

Fig. 2. Prediction of LIESST and reverse-LIESST effect from the relative positions of potential energies of LS, HS and IS states. IS state is described by the minimum of the potential energy (black circle) and its intersystem crossing process (arrows) (Ando et al., 2010).

of ligand is determined in permanent HS configuration over the whole temperature region. Changes in the magnetic properties of C_A can be induced from the LS ($\gamma_{HS} = 0$) to the HS state ($\gamma_{HS} = 1$) by light exposure at working temperatures (T_{wA1}) lower than $T_{1/2,1}$, while the LS → HS conversion is accompanied by structural transformation of the coordinated ligand induced by λ_A wavelength. At the same temperature, reverse photoreaction can be induced in C_B by λ_B radiation accompanied by the HS → LS conversion (Fig. 3a). Another case of the LD-LISC effect may be complex C_A, which is SCO active, while C_B is stable in the LS configuration over the whole temperature region. Photoinduced reversible SCO is localized at T_{wA2}, which is higher than $T_{1/2,2}$ and the LS → HS and HS → LS conversions are induced by two selective λ_B and λ_A wavelengths, respectively (Fig. 3b). In the last case, both C_A and C_B complexes are SCO active with defined $T_{1/2,A3}$ and $T_{1/2,B3}$. Spin transition based on the LD-LISC effect is feasible only inside the temperature region at certain T_{w3} while conversion is induced by λ_B or λ_A wavelengths (Fig. 3c). To achieve feasibility and applicability of the LD-LISC effect, necessary conditions such as large energy barrier between the isomers of the ligand moiety, long lifetime of photoisomers at given temperature, existence of different spin states in the temperature range based on the photosensitive part of the ligand, and high quantum yield of photoisomerization must be met (Boillot et al., 2004; Roux et al., 1994; Zarembowitch et al., 1993).

Azobenzene and stilbenes are archetypal examples of photoisomerzable molecules capable of changing their geometric and/or electronic properties upon irradiation which makes them very promising switchable moieties of ligands for Fe(II) coordination compounds and the study of LD LISC activity. In general, the bent structure of the *cis*- isomer restricts the π-conjugation of the ligand and induces a decrease of the π-acceptor character, which is a major contribution to the ligand field strength. Thus, the *cis*- configuration of the ligand moiety exhibits weaker ligand field to the Fe(II) ions (Brachňaková and Šalitroš, 2018). For azobenzene derivatives, the isomerization mechanism is comparable to that of stilbenes and thus inversion around the single —N—Car— bond or rotation around the double —N═N— bond is assumed (Merino and Ribagorda, 2012). The *trans*-isomers of azobenzene (or stilbene) easily isomerizes to the *cis*- configuration by irradiation with a wavelength within the UV region. The reaction is reversible, and the *trans*- isomer is recovered when the *cis*- isomer is irradiated with light within the VIS region for azobenzene (or UV for stilbene) or by heating. The UV-VIS absorption spectrum of *trans*-azobenzene presents two characteristic absorption bands corresponding to more pronounced π → π* and weak n → π* electronic transitions (Figure 5a, black line). The π → π* absorption band of *cis*-azobenzene shows a hypsochromic shift and the n → π* band becomes more intensive (in the 380—520 nm region) (Fig. 4a, red line). In the UV-VIS spectrum of *trans*-stilbene, only a very intense π → π* band (in the 240—340 region) is shown, which is blue-shifted and decreases in intensity in *cis*-stilbene (Fig. 4b). Obviously, when going from the *trans*- to the *cis*- configuration in azobenzene (resp. stilbene), isomerization distance between two para carbon atoms varies from 9.0 Å (resp. 9.4 Å) to 6.3 Å (resp. 6.3 Å). The *cis*- or *trans*- arrangement of the aromatic rings is also reflected in the proton nuclear magnetic resonance spectrum ^{1}H-NMR. Signals of the *cis*- isomer appear in higher region than those corresponding to the *trans*- isomer due to the anisotropic effect of the π cloud of the aromatic ring as well as their geometry.

In addition to the stilbene or azobenzene molecules, very promising ligands for Fe(II) coordination are those comprising a diarylethene moiety, which provides LD-LISC active complexes. The molecule

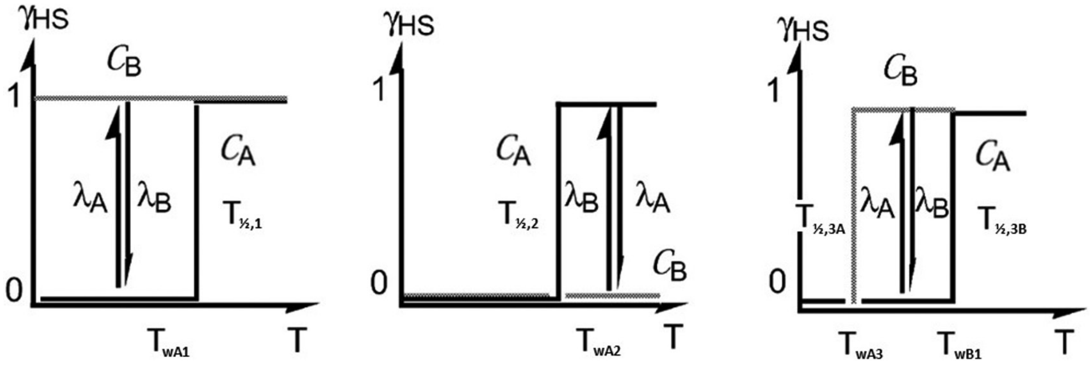

a) b) c)

Fig. 3. LD-LISC effect if a) complex C_A is SCO active and C_B is in permanent HS state, b) C_A is SCO active and C_B is in permanent LS state, c) C_A and C_B are SCO active (Boillot et al., 2004).

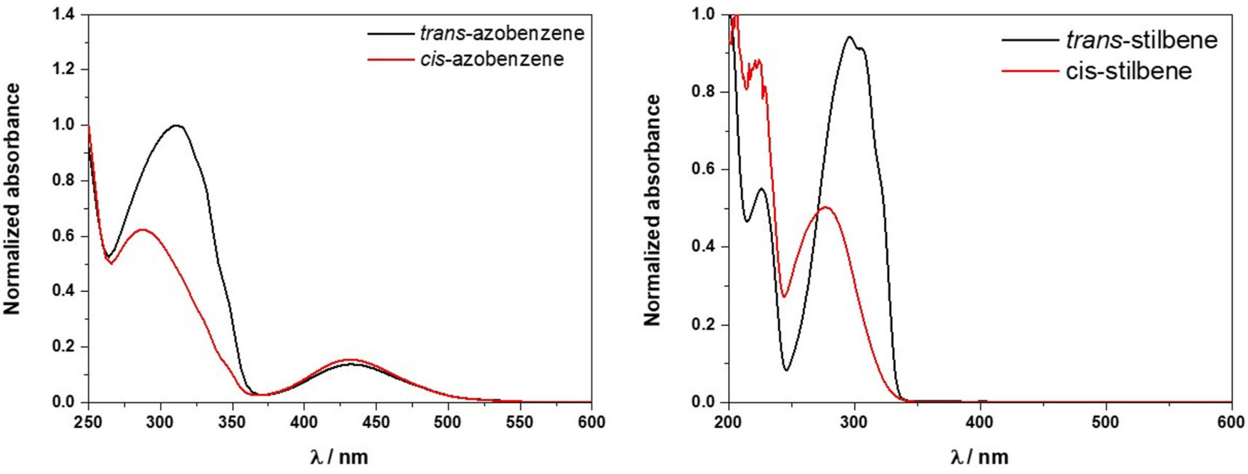

a) b)

Fig. 4. UV-VIS spectra of a) *trans*-azobenzene (black line), *cis*-azobenzene (red line) and b) *trans*-stilbene (black line), *cis*-stilbene (red line).

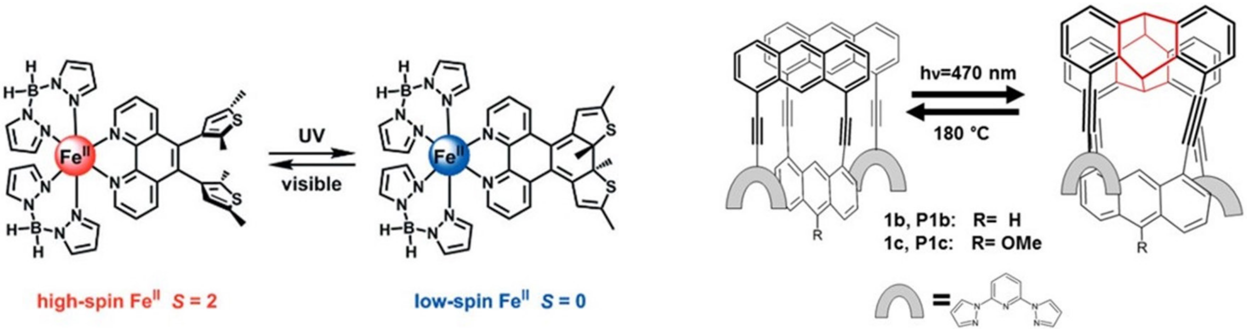

a) b)

Fig. 5. a) Ring closing and opening photoreactions of diarylethene moiety causing different spin state of Fe(II) induced by UV and visible light, respectively (Rösner et al., 2015). b) [4+4] photocycloaddition of anthracenes. (Šalitroš et. al., 2017).

is opening and closing its cycles upon light irradiation by a selected wavelength. Ring opening conversion of the aromatic systems is usually activated by UV light and conversely, visible light can induce photocyclic reversion (Fig. 5a, Rösner et al., 2015). Reversible photocyclization leads to changes in the electronic structures of the coordinated ligands and therefore, the isomers may exhibit different spin states of the metal center under isothermal conditions. Anthracene derivatives also appear to be promising LD-LISC ligands due to their reversible [4+4] photocycloaddition. Irradiation of the solid phase or solution by 400—450 nm wavelengths was used to link two anthracene rings through the formation of new bonds between the 9-9' and 10-10' carbon atoms of anthracene (Fig. 5b; Šalitroš, et. al., 2017). However, only one copper complex was prepared, where magnetic properties were successfully controlled by photocyclization (Castallano et al., 2011).

Photoactive Fe(II) complexes

Monodentate N-donor heterocyclic ligands such as the isomers of 4-styrylpyridine (*cis*-L1 and *trans*-L1) were used to synthesize $[Fe(L1)_4(NCS)_2]$ complexes, which are an amazing example of the LD-LISC activity. The *trans*- complex $[Fe(trans\text{-}L1)_4(NCS)_2]$ was prepared as red crystals and purple-red powder while the $[Fe(cis\text{-}L1)_4(NCS)_2]$ one was prepared as a yellow powder and orange crystals. Chromophore $[FeN_6]$ of the complexes showed pseudo-octahedral geometry and shorter Fe—N bond distances of isothiocyanate donors (~0.013 Å) compared to those of 4-styrylpyridine moieties. This reflects different ligand field strength of coordinated isomers in the corresponding complexes. Based on the $\chi_M T$ vs. T plot, $[Fe(cis\text{-}L1)_4(NCS)_2]$ was in permanent HS state in the whole temperature region (~3.67 $cm^3 \cdot mol^{-1} \cdot K$) because *cis*-L1 had weaker ligand field compared to the SCO active $[Fe(trans\text{-}L1)_4(NCS)_2]$ with abrupt transition centered at 108 K (Fig. 6a). The almost planar structure of *trans*-L1 caused stronger ligand field in [Fe(*trans*-L1)$_4$(NCS)$_2$] due to efficient electronic delocalization and significant stabilization of its π and π* orbitals. Working temperature T_w, at which complexes were irradiated, was allocated below 90 K, where [Fe(*trans*-L1)$_4$(NCS)$_2$] was fully LS and [Fe(*cis*-L1)$_4$(NCS)$_2$] was fully HS. Unfortunately, LD LISC was not detected due to technical obstructions of the electron absorbance spectroscopy measurements. (Roux et al., 1994). Exchange of axial terminal ligands to NCSe$^-$ shifted $T_{1/2}$ as well as T_w to higher temperature region. Complex [Fe(*trans*-L1)$_4$(NCSe)$_2$] displayed shortened Fe—N bond lengths (~0.20 Å) and contraction of the cell (~2 %) upon cooling from 293 K to 104 K. Complete SCO is in the range of 130–200 K and $T_{1/2}$ was determined to be 163 K, The $\chi_M T$ vs. T curve of [Fe(*cis*-L1)$_4$(NCSe)$_2$] stayed constant upon cooling with values characteristic for the HS state species of hexacoordinated Fe(II) ions ($\chi_M T \sim 3.63\ \mathrm{cm^3 \cdot mol^{-1} \cdot K}$, Fig. 6b).

For the detection of LD LISC via UVVIS spectroscopy, both complexes were separately dispersed into 5 % PMMA thin films. First, temperature dependence of magnetization was measured in the dark and constant magnetic curves were established at a negative value due to diamagnetic contribution of the PMMA polymer. Irradiation temperature of [Fe(*trans-L1*)$_4$(NCSe)$_2$] was chosen to be 130 K as the diluted complex showed SCO around $T_{1/2}$ = = 132 ±25 K, lower compared to the transition temperature of the bulk sample ($T_{1/2}$ = 163 K). Data collected by *in situ* UV (355 nm) light irradiation showed increased or decreased negative magnetization based on the *cis* → *trans* or *trans* → *cis* isomerization in [Fe(*cis-L1*)$_4$(NCSe)$_2$] or [Fe(*trans-L1*)$_4$(NCSe)$_2$], respectively. In the dark, the HS isomer [Fe(*cis-L1*)$_4$(NCSe)$_2$] showed a temperature invariant (Fig. 7a, red squares) curve. Upon irradiation of 355 nm, a decrease of the magnetization was observed suggesting *cis* → *trans* isomerization accompanied by HS → LS conversion. The value stayed constant up to 250 K (Fig. 7a, black triangles). On the other hand, the PMMA thin film of [Fe(*trans-L1*)$_4$(NCSe)$_2$] displayed an increase of the magnetization at low temperatures ~70 K and the value slowly decreased upon heating (Fig. 7d, black rhombus) indicating *trans* → *cis* phototransformation accompanied by LS → HS conversion. Time-dependent magnetization was measured upon continual UV irradiation at 130 K and [Fe(*trans-L1*)$_4$(NCSe)$_2$] *trans* → *cis* isomerization was saturated after ~400 min (Fig. 7e), while [Fe(*cis-L1*)$_4$(NCSe)$_2$] was saturated after 80 minutes of light exposure (Fig. 7b). Thin PMMA films of both [Fe(L1)$_4$(NCSe)$_2$] complexes were also characterized by UV-VIS absorption spectroscopy at 120 K. The complexes showed absorption maximum at 254 nm and 313 nm for [Fe(*cis-L1*)$_4$(NCSe)$_2$] and [Fe(*trans-L1*)$_4$(NCSe)$_2$], respectively, which can be attributed to the intra-ligand π → π* transitions. Maximum of [Fe(*trans-L1*)$_4$(NCSe)$_2$] was slightly shifted toward lower wavelengths with a significant intensity decrease upon 313 nm light irradiation (Fig. 7f). On the other hand, the π → π* band of [Fe(*cis-L1*)$_4$(NCSe)$_2$] was red shifted (above 300 nm) upon 254 nm irradiation with significant intensity increase (Fig. 7c). Bidirectional *cis* ↔ *trans*

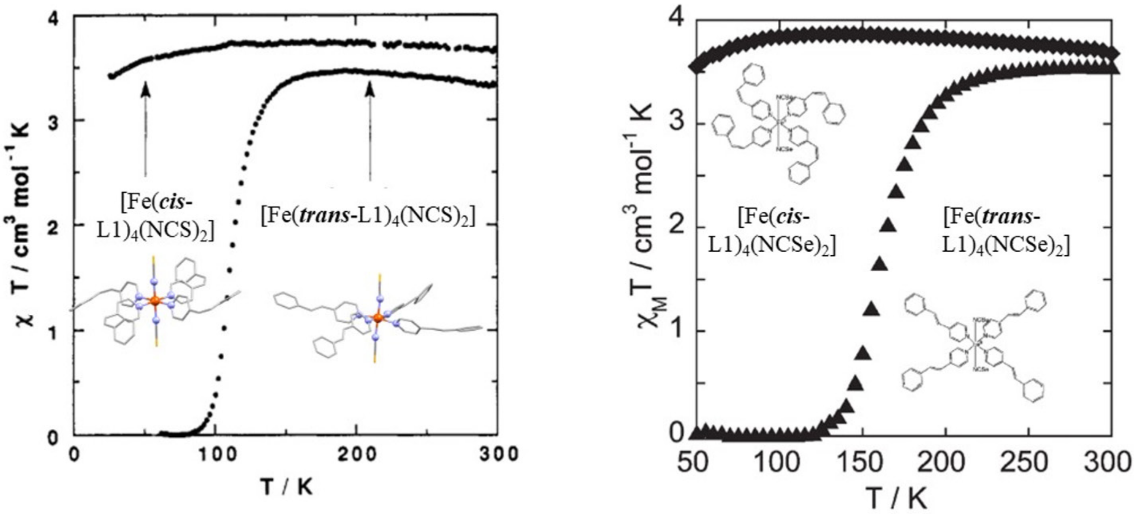

a) b)

Fig. 6. Magnetic properties in χ_MT vs. T form of a) [Fe(cis-L1)$_4$(NCS)$_2$] and SCO active [Fe(trans-L1)$_4$(NCS)$_2$] complex (Roux et al., 1994), and b) permanent HS [Fe(cis-L1)$_4$(NCSe)$_2$] (squares) and SCO active [Fe(trans-L1)$_4$(NCSe)$_2$] (triangles) complex (Boillot et al., 2009).

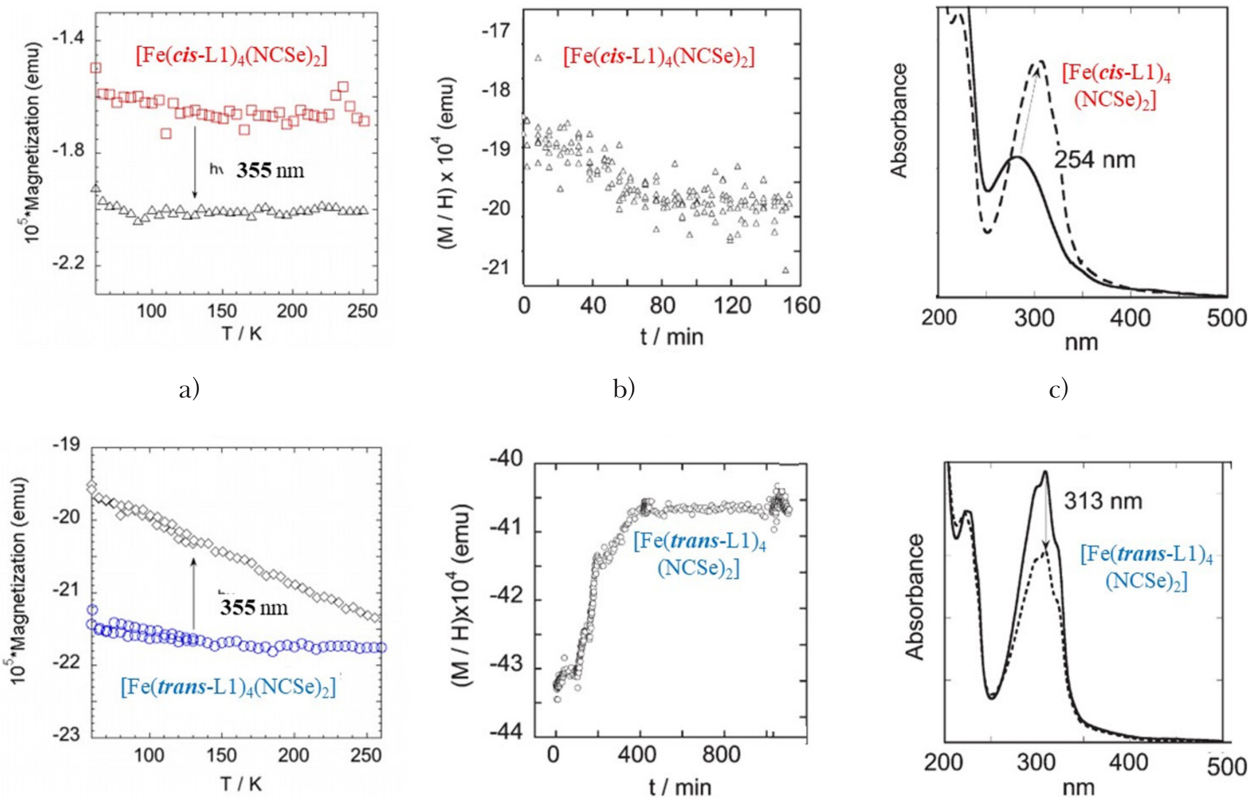

a) b) c)

d) e) f)

Fig. 7. Magnetization variation (M.10^5 vs. T) upon in-situ irradiation (130 K, 355 nm) for 5 % PMMA thin film of a) [Fe(cis-L1)$_4$(NCSe)$_2$] before (red squares) and after light exposure (black tringles), b) [Fe(trans-L1)$_4$(NCSe)$_2$] before (blue squares) and after light exposure (black rhombus). M/H vs. time of irradiation (355 nm, 130 K) of the thin film of c) [Fe(cis-L1)$_4$(NCSe)$_2$] (H = 1000 Oe) and d) [Fe(trans-L1)$_4$(NCSe)$_2$] (H = 5000 Oe). UV-VIS spectra at 120 K for e) [Fe(cis-L1)$_4$(NCSe)$_2$] (initial (-) sample and its photostationary state (--) reached upon 254 nm irradiation) and the thin film of f) [Fe(trans-L1)$_4$(NCSe)$_2$] (initial (-) sample and its photostationary state (--) reached upon 313 nm irradiation) (Boillot et al., 2009).

isomerization of styryl moieties at 120 K was determined by comparing the absorption spectra, measured before and after UV light irradiation of both [Fe(L1)$_4$(NCSe)$_2$] PMMA thin films (Boillot et al., 2009).

Pellets of ~0.1 mm thickness made from microcrystalline powders of both [Fe(L1)$_4$(NCSe)$_2$] complexes were analyzed at room temperature upon 532 nm irradiation. The *cis* ↔ *trans* isomerization occurred through the MLCT excitation pathway instead of the LD-LISC principle. The triplet mechanism of *cis* → *trans* conversion can occur *via* the ^{5}MLCT excited state further converted into energy of intraligand ^{3}IL(L1) excited state through inter-system crossing transition and non-radiative deactivation from the excited states. Geometry transformation of the *cis* → *trans* conversion (293 K, 532 nm) based on the singlet pathway was investigated by DFT calculations for both isomeric forms showing that asymmetrical [Fe(*trans-L1*)$_4$(NCSe)$_2$] complex produces different excited states, pathways, and energy barriers with respect to MLCT activation and isomerization has only unidirectional character. No impact on the spin state change of Fe(II) occurred as both complexes were in the HS configuration at room temperature. The *cis* → *trans* conversion of the styryl moiety resulted in an amorphous photoproduct associated with orange-to-red color change. Spectroscopic ellipsometry showed that the intensity of π → π* (~310 nm) increased and of the MLCT (~435 nm) band decreased during the *cis* → *trans* conversion induced by green light at room temperature (Fig. 8a). For the highly diluted thin films or solutions of [Fe(*cis*-L1)$_4$(NCSe)$_2$], a broader, less intense π → π* band (~280 nm) is typical. In this case, unusually intense red-shifted band at 313 nm was reached due to the asymmetrical distribution of void cavities, which resulted in contacts between pyridyl, phenyl, and ethylenic groups. Investigation of the isomerization by FT-IR spectroscopy was based on increasing ethylenic *ν*(C=C) stretching vibration at ~1600 cm^{-1} and the C—H out-of-plane bending vibration at 957 cm^{-1}. Conversion in the photoproduct was determined *via* the peak at ~950 cm^{-1} because it is characteristic only for *trans*-L1 ligand and ~66 % of new [Fe(*trans-L1*)$_4$(NCSe)$_2$] phase was produced in the photoproduct (Fig. 8b). Transmittance spectra obtained during UV light (365 nm) irradiation at 293 K showed to be more like the parent spectrum, intensity of the peak at ~950 cm^{-1} was three times lower compared to that in the photoproduct's spectrum produced after irradiation at 532 nm. It means that a six-fold penetration depth of visible light occurred, and thus UV light caused minor alternation in the recorded FT-IR transmittance spectra. The *cis* → *trans* isomerization in [Fe(*cis*-L1)$_4$(NCSe)$_2$] powder induced by 532 nm light at 293 K was investigated by X-ray diffraction analysis. Laser exposure time dependence of the unit-cell volume showed an increase of the volume of 49 Å^3 upon the irradiation; thus, the isomerization was assumed to be related to the ~1 % expansion of the unit cell. Crystal packing of [Fe(*cis*-L1)$_4$(NCSe)$_2$] and [Fe(*trans*-L1)$_4$(NCSe)$_2$] contained a large fraction of void spaces. The cavities were present in *ca.* 11 % of the crystal lattice volume and were defined as the regions of unit-cell spheres of r = 0.8 Å radius not entering the van der Waals surfaces of neighboring atoms. The crystal structure topology did not favor single-crystal-to-single-crystal photoisomerization because of the non-systematic distribution of the cavities around the phenyl rings of L1 ligands. This may be a reason phototransformation resulted in amorphous solid. Amorphization was also further confirmed by pictures of the crystal using a polarized microscope. Isomerization monitored by reflectivity measurements revealed a variation of reflectivity ~0.13 between 220 K and 130 K in the SCO active [Fe(*trans-L1*)$_4$(NCSe)$_2$] complex.

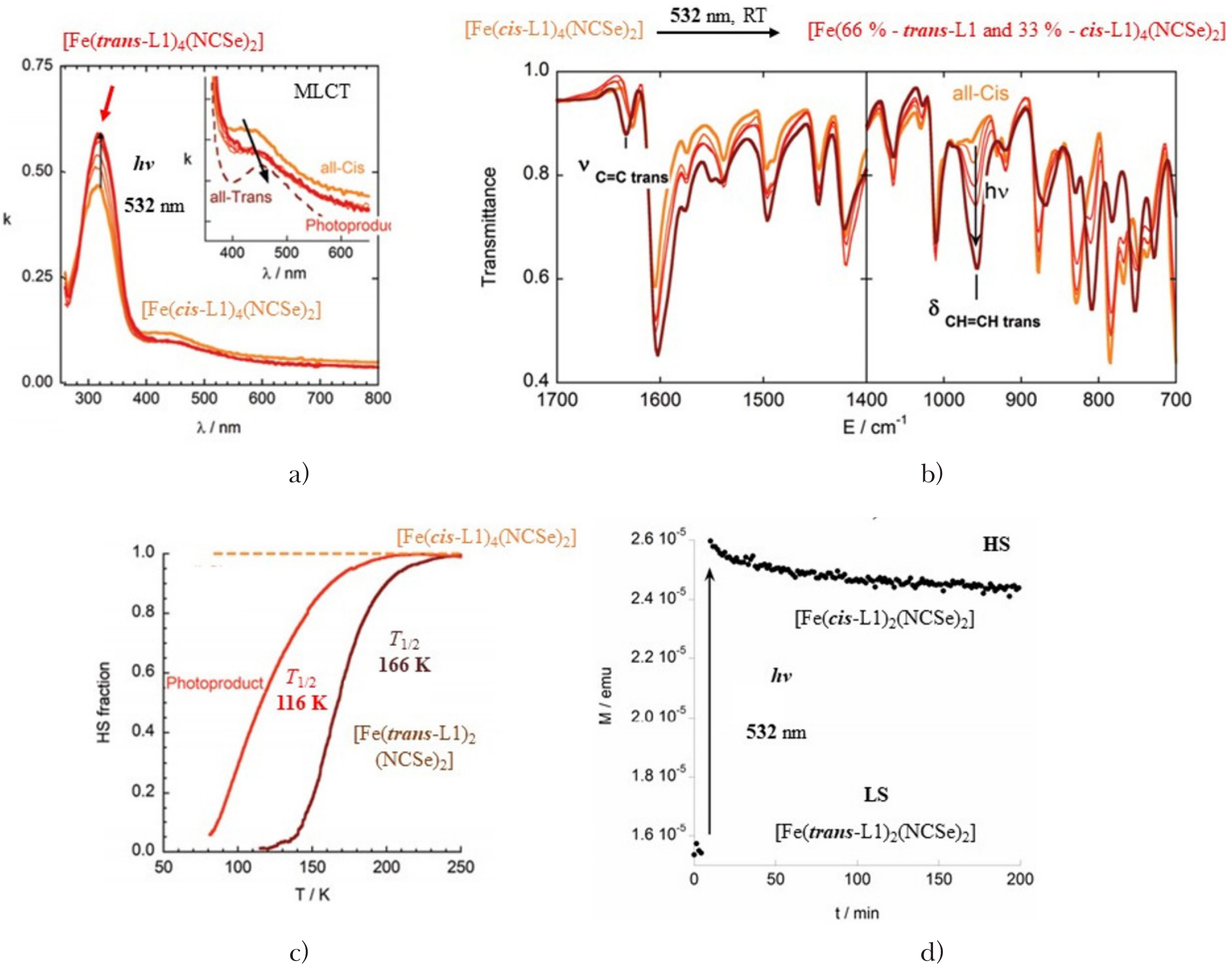

a) b)

c) d)

Fig. 8. a) Ellipsometric spectra of [Fe(cis-L1)$_4$(NCSe)$_2$] pellet (orange line) and its photoproduct (red line) (532 nm, 293 K). Insert plot represents expansions of the curves in the 350–600 nm range (MLCT region). b) ATR FT-IR spectra of [Fe(cis-L1)$_4$(NCSe)$_2$] complex (orange) in the pellet form and its photoproduct (532 nm, 293 K) (red spectrum). c) HS fraction vs. T extracted from diffuse reflectivity measurements of [Fe(cis-L1)$_4$(NCSe)$_2$] (broken yellow line), its photoproduct (532 nm) (red), and [Fe(trans-L1)$_4$(NCSe)$_2$] (dark-red line), d) LIESST effect probed at 10 K by in situ photoexcitation (532 nm) of [Fe(cis-L1)$_4$(NCSe)$_2$] photoproduct (Tissot et al., 2010).

The resulting gradual curve of the photoproduct's HS fraction was centered at $T_{1/2} \sim 116$ K and then was shifted down by about 47 K compared to $T_{1/2}$ determined for bulk [Fe(*trans-L1*)$_4$(NCSe)$_2$] (Fig. 8c). As expected for permanent HS species, reflectivity of [Fe(*cis-L1*)$_4$(NCSe)$_2$] varied very slightly (0.76—0.78) in the whole temperature region. The LIESST effect (10 K, 532 nm) of the photoproduct produced from [Fe(*cis-L1*)$_4$(NCSe)$_2$] was also studied. First, the fresh complex was irradiated by green light at 293 K until the C—H out-of-plane deformation ethylenic vibration ($\sim$950 cm^{-1}) reached saturation. Subsequently, the irradiated sample with a significant amount of the [Fe(*trans-L1*)$_4$(NCSe)$_2$] phase was cooled down to 10 K in a magnetometer forming the new LS phase. Time depending on magnetization of the photoproduct was first determined in the dark until it reached a constant value. The 532 nm light exposure caused the excitation of Fe(II) electrons into metastable HS state and the photoinduced SCO effect at 10 K was accompanied by positive magnetization variation representing the LS → HS conversion (Fig. 8d). This process has a reversible character because the magnetization slowly decreased in the dark back to the initial value (Tissot et al., 2010).

The family of homoleptic Fe(II) coordination compounds with bidentate 2-(2'-pyridyl)benzimidazole ligand (L2) and their derivatives often exhibit temperature-induced SCO effect (Brachňaková et al., 2020). Structural modification of L2 by introducing photoactive azophenyl moiety onto benzimidazole core (L3 = phenyl-(2-pyridine-2-yl-3*H*-benzoimidazol-5-yl)-*trans*-diazene) offers an interesting possibility for LD-LISC investigation (Fig. 9a). Thermal SCO of [Fe(*trans*-L3)$_3$](BF$_4$)$_2 \cdot 3$H$_2$O was analyzed in the solid phase and in acetone-d_6 solution. First, magnetic measurements were carried out for the bulk compound (Fig. 9b). Complete and gradual SCO is situated at 279 K, which is in good agreement with the temperature-dependent ^{1}H-NMR measurements. The *trans/cis* ratio was estimated by ^{1}H-NMR spectroscopy, which showed that the photoproduct formed by *trans* → *cis* isomerization was converted into 94 % phostationary state. The reverse *cis* → *trans* conversion was activated by blue (436 nm) light, successfully converting the photoproduct back into original the 28 % *trans* phase, while fully reversing the transformation within two weeks at 293 K in the dark. Isomerization in the acetone solution of the free ligand L3 in *trans-* configuration was exposed to 365 nm light. A decrease of the band corresponding to the π → π* transition at 359 nm was monitored by UV-VIS spectroscopy. Additionally, the slight increase of the band at 445 nm attributed to the *n* → π* transition upon UV irradiation confirmed the formation of the *cis-* isomer at 293 K. Absorption spectra of the [Fe(*trans*-L3)$_3$](BF$_4$)$_2 \cdot 3$H$_2$O solution showed three bands at 355, 440, and 550 nm, the first two being assigned to intraligand π → π* and *n* → π* transitions and the band at 550 nm assigned to MLCT transition. Temperature dependent absorption spectra of the complex were analyzed during cooling (300—192 K), increased intensity of the MLCT band associated also with color change from yellow to brown clearly indicated the HS → LS conversion. Additionally, spectral changes of the complex solution were comparable with those observed for free ligand L3 upon UV and visible light irradiation (Fig. 9c). The light induced *trans* ↔ *cis* isomerization of ligand moieties in the complex was determined by room temperature NMR measurements. The fresh [Fe(*trans*-L3)$_3$](BF$_4$)$_2 \cdot 3$H$_2$O solution consisting of 1.5 equivalent excess of free *trans*-L3 was added to ensure the complex stability (ligand may dissociate upon photoexcitation) and $\chi_M T$ was partly reversible in the 2.05—2.20 cm$^3 \cdot$ mol$^{-1} \cdot$ K range, where it was either increased or decreased upon 20 min of the 365 nm or 436 nm irradiation, respectively (Fig. 9d). The zig-zag responses were not fully reversible but the complex showed reversible $\chi_M T$ switching upon different light (UV and VIS) excitation (Hasegawa et al., 2009). Based on Co(II) complex of azobenezenes-attached tris(bipyridine) ligands (Yamaguchi et al., 2005), it can be assumed that the three azobenzene moieties in the Fe(II) complex are photoisomerized independently and therefore probably only one of three moieties on average is converted to a *cis-* isomer in the photostacionary state (365 nm) (Hasegawa et al., 2009). This shows new potential LD-LISC active homoleptic Fe(II) compounds with $T_{1/2}$ and T_w temperatures close to 293 K. SCO properties can be modulated by the position of light-sensitive substituents, for example by introducing azophnenyl or ethylenebenzene substituents into the pyridyl ring of pyridylbenzimidazole ligands.

Tridentate N-donor heterocyclic ligand with photoactive phenylethenyl moiety (L4 = 2,6-di-(pyrazol-1*H*-yl)-4-styrylpyridine) and its substituted derivates in *para* position of styryl moiety, like cyano (L5 = 2,6-di(1*H*-pyrazolyl)-4-(4-cyanostyryl)-pyridine) and nitro (L6 = 2,6-di(1*H*-pyrazol-1-yl)-4-(4-nitrostyryl)-pyridine) groups, were selectively prepared in both isomeric forms and used for the preparation of homoleptic coordination compounds. Incorporation of the electron-withdrawing substituent into their structure led to the reduction of the energy π* orbitals of ligands creating stronger ligand field and rather stabilizing the LS state. Crystal structure of [Fe(*cis*-L4)$_2$](BF$_4$)$_2$ and [Fe(*cis*-L5)$_2$](BF$_4$)$_2$ were measured at 90 K and

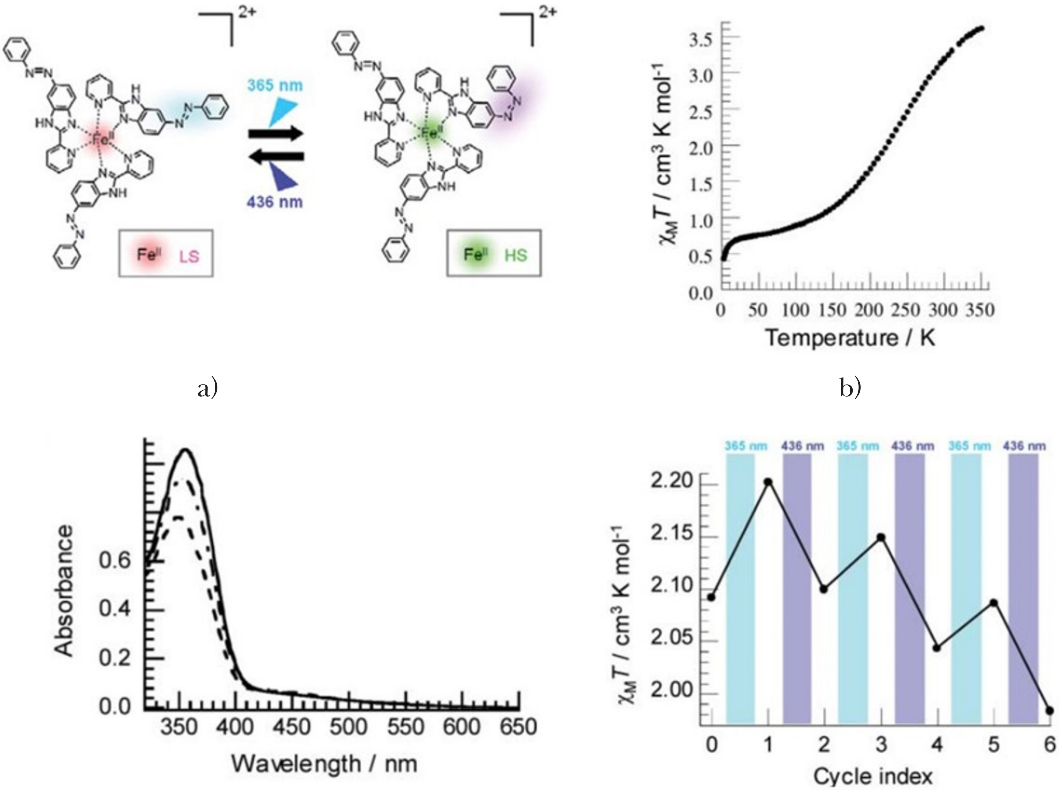

a) b)

c) d)

Fig. 9. a) Schematic visualization of reversible trans ↔ cis isomerization *in* [Fe(trans-L3)$_3$](BF$_4$)$_2 \cdot 3H_2O$ induced by UV (365 nm) and VIS (436 nm) light at 293 K. b) $\chi_M T$ vs. T plot of the bulk complex. c) UV-VIS absorption spectra of [Fe(trans-L3)$_3$](BF$_4$)$_2 \cdot 3H_2O$ (solid line) in acetone and its spectral changes upon irradiation by 365 nm (dotted line) and 436 nm (broken line) light at 295 K. d) $\chi_M T$ changes of the complex upon repeated irradiation by 365 nm and 436 nm light at 293 K (Hasegawa et al., 2009).

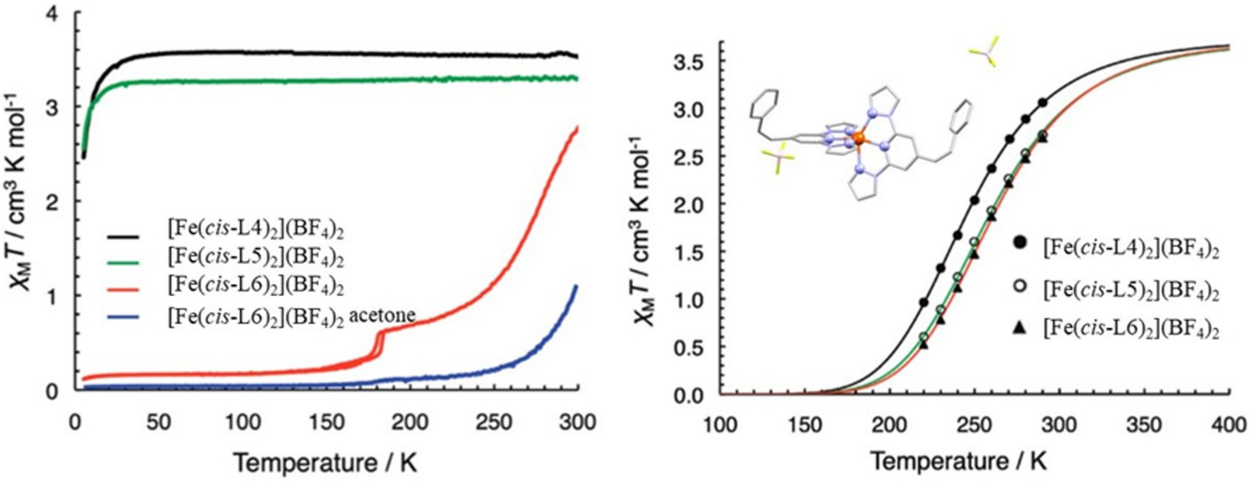

a) b)

Fig. 10. χ_MT vs. T plots of a) [Fe(*cis*-L4)$_2$](BF$_4$)$_2$ (black), [Fe(*cis*-L5)$_2$](BF$_4$)$_2$ (green), [Fe(*cis*-L6)$_2$](BF$_4$)$_2$ (red) and [Fe(*cis*-L6)$_2$](BF$_4$)$_2 \cdot C_3H_6O$ (blue) powders. b) $\chi_M T$ vs. T plots of their d$_6$-acetone solutions determined by the Evans's method (Takahashi et al., 2012).

113 K. Bond distances of Fe—N were ~2.170 Å on average with distortion parameter Σ of 172.4 ° and 183.1 °, respectively, these values are typical for Fe(II) species in the HS state. The HS state was probably stabilized by π-π interactions between the pyrazole rings of *cis*-L4 and *cis*-L5 ligands in the relevant complex. In [Fe(*cis*-L6)$_2$](BF$_4$)$_2$, these interactions were absent so the Fe—N bond lengths

and Σ were lower (~1.946 Å, 88.7 °) at 113 K and LS state with almost ideal octahedral geometry was detected. Structural information on [Fe(*trans*-L4)$_2$](BF$_4$)$_2$ was similar (~1.935 Å, 84.6 °) indicating the LS state of Fe(II) ions at low temperatures after photoisomerization. Solvated and desolvated compounds of [Fe(*cis*-L6)$_2$](BF$_4$)$_2$ showed LS state behavior up to 150 K (Fig. 10a, red and blue line). Thermal SCO occurred near the room temperature region at $T_{1/2}$ of ~270 K for [Fe(*cis*-L6)$_2$](BF$_4$)$_2$ and at above 300 K for [Fe(*cis*-L6)$_2$](BF$_4$)$_2 \cdot$ C$_3$H$_6$O. On the other hand, microcrystalline structure of [Fe(*cis*-L4)$_2$](BF$_4$)$_2$ and [Fe(*cis*-L5)$_2$](BF$_4$)$_2$ showed permanent HS state (~3.15 cm$^3 \cdot$ mol$^{-1} \cdot$ K) over the whole temperature region. Below 30 K, a small decrease of $\chi_M T$ caused by the zero-field splitting and/or intermolecular antiferromagnetic interaction of distorted octahedral environment of the HS state Fe(II) ions was observed (Fig. 10a, black and green lines). Solution study by ^{1}H-NMR analysis revealed gradual SCO at 245 K for [Fe(*cis*-L4)$_2$](BF$_4$)$_2$, 259 K for [Fe(*cis*-L5)$_2$](BF$_4$)$_2$, and 365 K for [Fe(*cis*-L6)$_2$](BF$_4$)$_2$ (Fig. 10b). The plot of $\chi_M T$ vs. T of the complexes with *trans-* ligands was not acquired because of their low solubility in acetone. LD-LISC behavior of the complexes in the solid state was monitored by variable-temperature magnetic susceptibility measurements. The complexes were irradiated by visible light ($\lambda > 420$ nm) at room temperature and *cis*→*trans* isomerization was reached after several days of light exposure. All compounds displayed similar trend of magnetic curve with very gradual and incomplete character. Complexes in permanent HS state showed a decrease of $\chi_M T$ after irradiation, which represents partial HS → LS conversion (~20 %) at ambient temperature (Figs. 11a and 11b). On the other hand, $\chi_M T$ of compounds [Fe(*cis*-L6)$_2$](BF$_4$)$_2$ and [Fe(*cis*-L6)$_2$](BF$_4$)$_2 \cdot$ C$_3$H$_6$O increased upon the irradiation with the HS → LS transition of ~42 % and 87 %, respectively, at 273 K (Figs. 11c and 11d). The *cis* → *trans* isomerization of acetonitrile solutions of all compounds with *cis-* configuration upon blue light (436 nm, 293 K) irradiation was analyzed by UV-VIS spectroscopy. A strong absorption band with the maximum around 320 nm corresponded to π → π* and n → π* transitions and a weak band of the MLCT transition at 450 nm was identified for all compounds (Fig. 11e). Upon the irradiation (436 nm, 293 K), all compounds showed irreversible *cis-* to *trans-* photoisomerization expressed by the MLCT band increasing intensity over time (Fig. 11f). Solid-state *cis* → *trans* isomerization investigation revealed color change from yellow to dark orange or red. The complexes were dispersed in

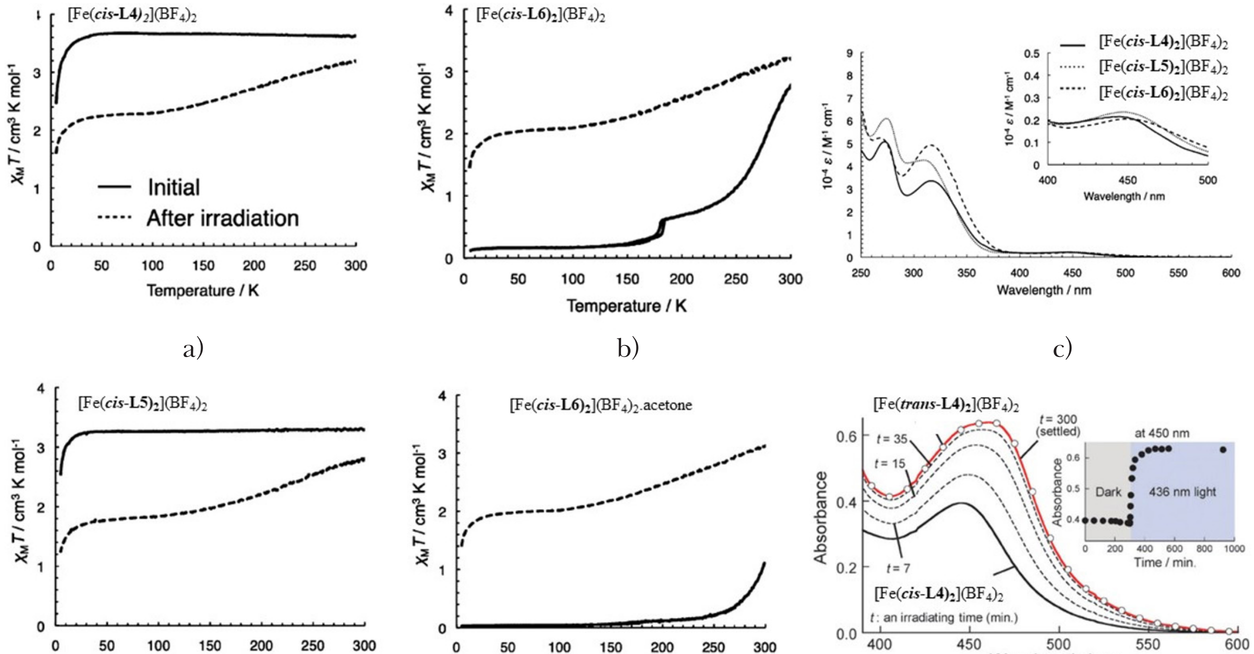

a) b) c)

d) e) f)

Fig. 11. χ_MT vs. T plots of a) [Fe(*cis*-L4)$_2$](BF$_4$)$_2$, b) [Fe(*cis*-L5)$_2$](BF$_4$)$_2$, c) [Fe(*cis*-L6)$_2$](BF$_4$)$_2$, d) [Fe(*cis*-L10)$_2$](BF$_4$)$_2 \cdot$ C$_3$H$_6$O measured before (solid line) and after (broken line) irradiation ($\lambda > 420$ nm). e) Absorption spectra of the complexes in acetone solutions (Takahashi et al., 2012). f) [Fe(*cis*-L4)$_2$](BF$_4$)$_2$ absorption change of the MLCT band upon 300 minutes of 436 nm irradiation (Hasegawa et. al., 2011).

KBr pellets, and their isomerization was analyzed by FT-IR spectroscopy upon visible light excitation ($\lambda > 420$ nm), the peak characteristic for C—H out-of-plane bending vibration at ~974 cm^{-1} showed expected shifting to 971 cm^{-1}. Both methods confirmed that the conversion ratio of the new *trans*-phase was no less than 88 % (Hasegawa et al., 2011; Takahashi et al., 2012).

Photoactive Fe(II) coordination polymers

SCO active Fe(II) ions with relatively high $T_{1/2}$ were also identified in coordination polymers of the 2D Hofmann-type framework composed of undulating $[Fe^{II}Pd(CN)_4]$ layers in the *a-c* plane separated from each other by axial ligands such as L7 = *trans*-3-azophenylpyridine or L8 = *trans*4-azophenylpyridine. In {Fe(*trans*-L7)$_2$[Pd(CN)$_4$]}, the adjacent L7 ligands along the *a*-axis interact *via* azo- and benzene groups forming weak N···C(H) contacts. The 2D layers of the coordination polymer are close-packed along the b-axis and the ligands interact *via* weak $\pi \cdots \pi$ interactions. Bonds lengths between the Fe(II) ion and the N-donor atoms of {Fe(*trans*-L7)$_2$[Pd(CN)$_4$]} changed by ~0.20 Å between 150–220 K, and the extension of the bonds upon heating was caused by the thermal SCO effect (Fig. 12a). Red crystals of {Fe(*trans*-L8)$_2$[Pd(CN)$_4$]} and polycrystalline mixture of {Fe(*trans*-L8)$_2$[Pd(CN)$_4$]} and {Fe(*trans*-L8)$_2$[Pd(CN)$_4$]}.1/2 *trans*-L8 phases were prepared. Both ligands were selectively coordinated to the Fe(II) ion and they interacted via weak N···C(H) contacts. Co-crystallized *trans*-L8 molecules interacted with the coordinated *trans*-L8 ligands *via* weak C(H)···π interactions (Fig. 12b). {Fe(*trans*-L8)$_2$[Pd(CN)$_4$]}.1/2 *trans*-L8 showed that the Fe—N bond length did not change (~2.1 Å) upon cooling to 100 K thus, permanent HS configuration of Fe(II) ions is expected. The unit-cell volume collected by variable temperature powder X-ray diffraction data in the range of 280–200–280 K showed that the volume of {Fe(*trans*-L8)$_2$[Pd(CN)$_4$]} was bigger (~30 Å^3) than that of the Fe(II) polymer with shorter *trans*-L7 ligands.

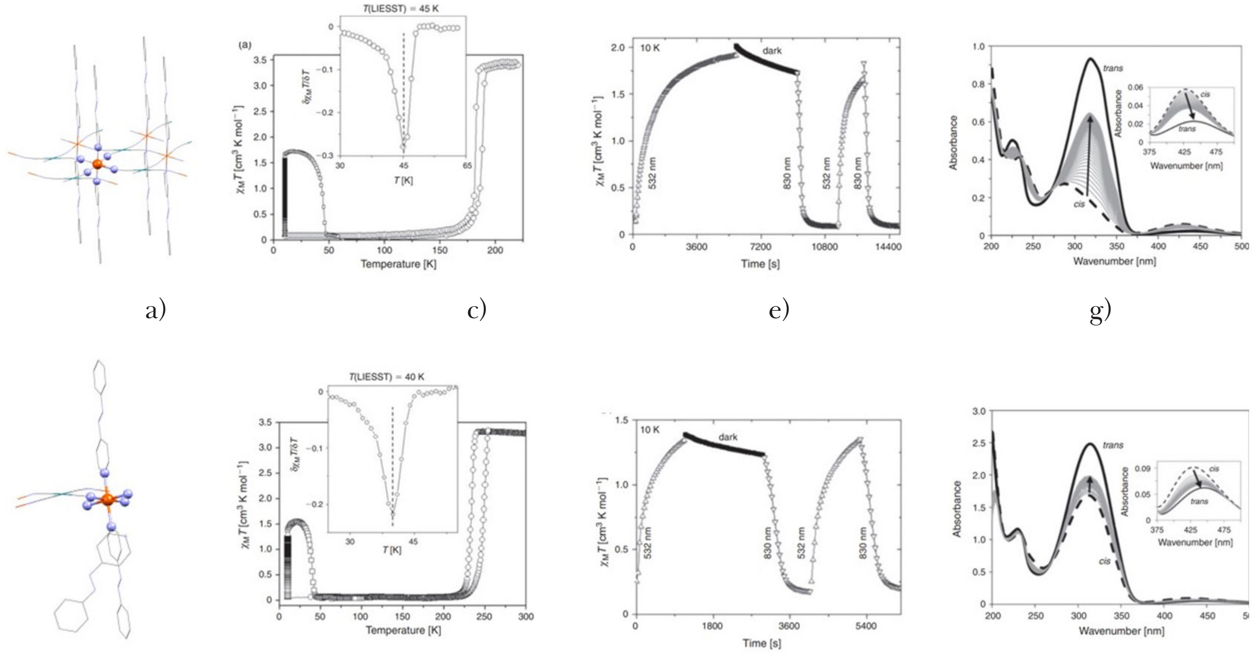

a) c) e) g)

b) d) f) h)

Fig. 12. Crystal structure of a) {[Fe(*trans*-L7)$_2$Pd(CN)$_4$]} and b) {[Fe(*trans*-L8)$_2$Pd(CN)$_4$]}.1/2 *trans*-L8, where Fe(II) atoms are orange, nitrogen – blue, carbons – grey, platinum – green. Thermal (open circles) and photo-induced (opened squares) experiments characterized by the χ_MT vs. T plots measured for the 2D Hofmann-type framework of c) {Fe(*trans*-L7)$_2$[Pd(CN)$_4$]} and d) {Fe(*trans*-L8)$_2$[Pd(CN)$_4$]}. Insert plots show χ_MT function derivative resulting in *T*(LIESST). Conversion into metastable HS state via 532 nm photoexcitation at 10 K measured (open triangles) for e) {Fe(*trans*-L7)$_2$[Pd(CN)$_4$]} and f) {Fe(*trans*-L8)$_2$[Pd(CN)$_4$]} accompanied by χ_MT saturation stabilized in the dark (closed markers) while the *reverse*-LIESST (open triangles) was induced by 830 nm light. UV-VIS absorbance spectra of free g) *trans*-L7 and h) *trans*-L8 molecules dissolved in ethanol/H_2O measured before (black dotted curve) and after one hour of 365 nm light exposure (black solid curve). Grey curves show the change of the spectra under ambient light over time. Insert plots show expanded view of the n–π* band (Ragon et al., 2014).

Variable temperature synchrotron powder X-ray diffraction data collected for the 240–140 K temperature range revealed single-phase behavior pronounced in an abrupt shift in the Bragg reflections associated with reversible HS → LS transition. Subsequently, Le Bail analysis of individual patterns revealed unit cell evolution mimicking the abrupt and hysteretic SCO behavior. Abrupt and narrow thermal hysteresis (~12 K) was determined by the $\chi_M T$ vs. T plots for {Fe(*trans*-L7)$_2$[Pd(CN)$_4$]} and the SCO curve of the cooling cycle abruptly increased at 178 K while that of the heating curve at 190 K (Fig. 12c). A sample with prevailing ratio of {Fe(*trans*-L8)$_2$[Pd(CN)$_4$]} isomer showed SCO with thermal hysteresis width of 15 K near room temperature ($T_{1/2}(\downarrow)$ and $T_{1/2}(\uparrow)$ at 235 K and 250 K, respectively) (Fig. 12d). Photomagnetic studies of both polymers were performed at 10 K by green 543 nm light excitation from ground LS to metastable HS state, $\chi_M T$ values of {[Fe(*trans*-L7)$_2$Pd(CN)$_4$]} and {[Fe(*trans*-L8)$_2$Pd(CN)$_4$]} were saturated at 1.74 $cm^3 \cdot mol^{-1} \cdot K$ and 1.52 $cm^3 \cdot mol^{-1} \cdot K$, respectively, which corresponds to ~50 % efficiency. The T(LIESST) of both mentioned polymers were determined at 40 K and 45 K for {Fe(*trans*-L7)$_2$[Pd(CN)$_4$]} and {Fe(*trans*-L8)$_2$[Pd(CN)$_4$]}, respectively (Figs. 12c and 12d). Stability of the photoinduced HS state after 532 nm irradiation was assessed by recording $\chi_M T$ values in the dark that slowly decreased over one hour. The *reverse*-LIESST process (transition from metastable HS to ground LS state) was induced by 830 nm irradiation, whereby the ground LS state was completely recovered in less than 30 min. The $\chi_M T$ values of cycling experiments indicated that the LS → HS transition (switch 'on') and its *reverse*-LIESST HS → LS (switch 'off') are fully reversible after multiple irradiating cycles (Figs. 12e and 12f). The *trans* → *cis* conversion of azophenyl moiety was analyzed for both polymers in solutions using UV-VIS spectroscopy, however, no isomerization was observed. Isomerization activity was successfully identified only for ethanol/H_2O solutions of free *trans*-L7 and *trans*-L8 molecules. Two characteristic signals were identified as the intensive absorption $\pi \rightarrow \pi^*$ band centered at 340 nm and the weaker $n \rightarrow \pi^*$ band at 425 nm. The *trans* → *cis* transformation of the ligand is expressed by a decrease of the $\pi \rightarrow \pi^*$ band intensity with the $n \rightarrow \pi^*$ band increase (Figs. 12g and 12h) after one hour of 365 nm irradiation. Reverse isomerization of the photoproduct in the absence of light took one hour until the original electronic spectra were identified. Unfortunately, the isomerization of both ligands in appropriate coordination polymers was not detected in the solutions or in the solid state (Ragon et al., 2014).

The 3D Hofmann-type SCO clathrate of {Fe(L9)$_2$[Pt(CN)$_4$]} · L9 · H_2O consists of hexacoordinated Fe(II) centers tetracoordinated with diamagnetic tetracyano-metalate Pt(II) complex units in the equatorial plane, the last two coordination positions in the axial direction are occupied by pillared N-donor ligands L9 = bis(4-pyridyl) acetylene ligands while the cavities are occupied by free L9 ligand and water molecules (Fig. 13a). Clathrate lost its water molecule at about 390 K according to thermogravimetric data but rehydration was reached after 1 hour of air exposition.

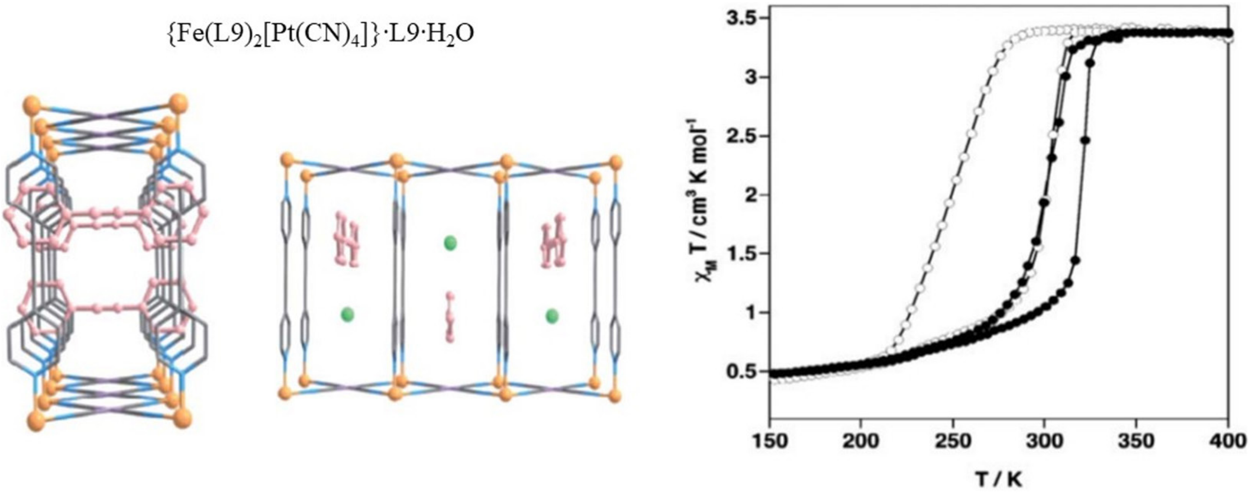

a) b)

Fig. 13. a) Fragmets of 3D Hofmann-type SCO clathrate {[Fe(L9)$_2$[Pt(CN)$_4$]]} · L9 · H_2O; Fe(II) atoms – yellow, nitrogen – blue, carbon – grey, platinum – purple, incorporated molecules of L9 – pink, water – green. b) $\chi_M T$ vs. T plot of {Fe(L9)$_2$[Pt(CN)$_4$]} · L9 · H_2O (closed circles) and dehydratated {Fe(L9)$_2$[Pt(CN)$_4$]} · L9 (opened circles) clathrate (Bartual-Murgui et al., 2011).

At 120 K, the void space took half of the total unit cell volume and bond distances between Fe(II) and N-donor atoms of the axial and equatorial direction were 1.996(6) Å and 1.935(5) Å, respectively. Heating up to 350 K caused the bond lengths increase (~0.20 Å), which is associated with the color of the crystals change from deep red to yellow. $\{Fe(L9)_2[Pt(CN)_4]\} \cdot L9 \cdot H_2O$ showed temperature-induced SCO with thermal hysteresis (21 K) and its $T_{1/2}(\downarrow)$ and $T_{1/2}(\uparrow)$ were situated at 301 K and 322 K, respectively. Dehydration of original clathrate *in situ* in a SQUID magnetometer caused an increase and shift of thermal hysteresis to lower temperatures ($T_{1/2}(\downarrow)$ = 251 K and $T_{1/2}(\uparrow)$ = 300 K) (Fig. 13b, Bartual-Murgui et al., 2011).

$\{[Fe(L9)[Pt(CN)_4]\} \cdot H_2O$ host has relatively large pore size (~300 Å^3), which is suitable for molecule incorporation of such compounds as azobenzene or stilbene. The concept of the **G**uest-**D**riven **L**ight-**I**nduced **S**pin **C**rossover (GD-LISC) effect as an analogy to the LD-LISC principle was introduced for SCO active porous metal-organic frameworks. Therefore, *trans*-azobenzene, *trans*-stilbene, and *cis*-stilbene molecules were incorporated into the framework and their quantity was estimated by the combination of elemental analysis and thermogravimetric measurements, which resulted in the molecular formulas $\{[Fe(L9)[Pt(CN)_4]\} \cdot H_2O \cdot$ *trans*-azobenzene, $\{[Fe(L9)[Pt(CN)_4]\} \cdot H_2O \cdot$ *trans*-stilbene, and $\{[Fe(L9)[Pt(CN)_4]\} \cdot 2.3H_2O \cdot 0.6$*cis*-stilbene. Upon SCO of $\{[Fe(L9)[Pt(CN)_4]\} \cdot H_2O \cdot$ *trans*-azobenzene, bond distances between the Fe(II) center and N-donor ligands expanded by about ~0.20 Å and, and lattice volume increased by 3 %. The transition was also accompanied by supramolecular changes, where the N—C—Pt angle in the 2D $\{Fe[Pt(CN)_4]\}$ sub-layers decrease upon heating from 177.453(3) ° at 100 K to 159.255(4) ° at 180 K. Also, *trans*-azobenzene formed a weak non-covalent bond and benzene rings were face-to-face oriented with pillared L9 ligands in distances exceeding 3.5 Å. The guest incorporation into the host identified by FT-IR and Raman spectroscopy shows characteristic peaks of the guest's molecules. In the transmittance spectrum of $\{[Fe(L9)[Pt(CN)_4]\} \cdot H_2O \cdot$ *trans*-azobenzene, bending in-plane and out-of-plane vibration signals of phenyl groups typical *trans*- configuration (1484 cm^{-1} and 1453 cm^{-1}, respectively) were observed. Intense peaks in the Raman spectrum of *trans*-azobenzene clathrate were assigned to C—N, N═N, N═N + C—N, N═N + C═C vibrations at 1145, 1438, 1473 and 1492 cm^{-1}, respectively. In transmittance spectra of both stilbene clathrates, vibrational peak of C—H bending mode of benzene ring (963 cm^{-1} for *trans*-stilbene and 922 cm^{-1} for *cis*-stilbene clathrates) was found. In the Raman spectra of both stilbene clathrates, a peak of C═C stretching vibration appeared at 1632 cm^{-1} for *trans*-stilbene and at 1630 cm^{-1} for *cis*-stilbene guest molecule. Magnetic investigation of $\{Fe(L9)[Pt(CN)_4]\} \cdot H_2O \cdot$ *trans*-azobenzene showed complete and abrupt SCO with hysteresis (Fig. 14a). Thermal hysteresis (11 K) of the mentioned clathrate occurred at lower temperatures ($T_{1/2}(\downarrow)$ at 137 K and $T_{1/2}(\uparrow)$ at 148 K) compared to the polymer with incorporated L9 molecule. $\{Fe(L9)[Pt(CN)_4]\} \cdot H_2O \cdot$ *trans*-stilbene showed gradual and incomplete SCO with approximately ~30 % of molecules in the permanent HS state (Fig. 14b). While $\{Fe(L9)[Pt(CN)_4]\} \cdot 2.3\ H_2O \cdot 0.6$*cis*-stilbene displayed two-step SCO behavior between 200—60 K. The first transition at $T_{1/2}(1)$ = 165 K was associated with an abrupt decrease of $\chi_M T$ down to ~1.52 cm$^3 \cdot$ K $\cdot$ mol^{-1}, which corresponds to 50 % conversion from HS to LS state. The second, more gradual, transition involved a 30 % conversion of Fe(II) centers. The permanent HS fraction (~25 %) of Fe(II) ions was determined by the higher $\chi_M T$

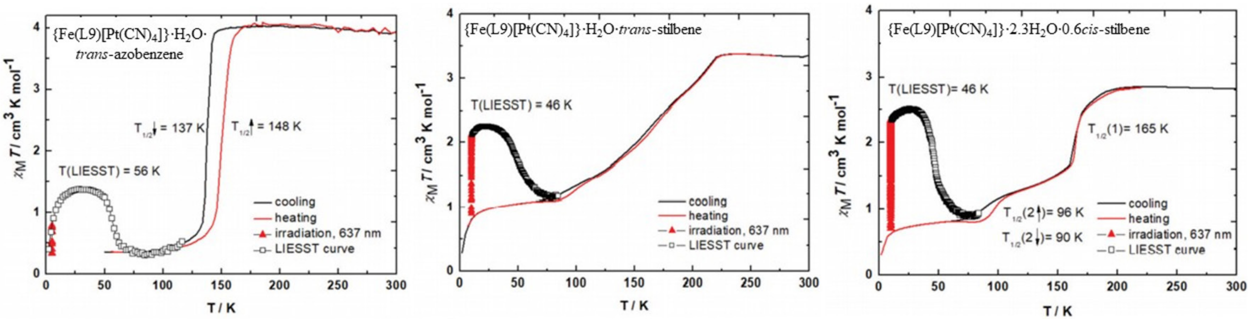

a) b) c)

Fig. 14. χ_MT vs. T plot of a) $\{Fe(L9)[Pt(CN)_4]\} \cdot H_2O \cdot$ trans-azobenzene, b) $\{Fe(L9)[Pt(CN)_4]\} \cdot H_2O \cdot$ trans-stilbene, and c) $\{Fe(L9)[Pt(CN)_4]\} \cdot 2.3H_2O \cdot 0.6$ cis-stilbene on cooling and heating (solid lines). Photoexcitation by red light (637 nm) at 5 K or at 10 K (red triangles) and subsequent heating in the dark (white squares) (Brachňaková et al., 2021).

($\sim$0.74 $cm^3 \cdot K \cdot mol^{-1}$) value in the low temperature region (Fig. 14c). Drastic downshift of $T_{1/2}$ in the presence of the guests compared to the $T_{1/2}$ of empty clathrate indicates that SCO properties were altered *via* steric hindrance due to the bulky guest molecules. The quantity of stilbenes in the polymer channels affected the conversion curve by increasing the $\chi_M T$ value, as presented by increased permanent HS phase of Fe(II) ions at low temperatures. The plot of $\chi_M T$ vs. T for clathrate with azobenzene guest showed similarity and the different number of incorporated guests had only an insignificant effect on SCO. This can be explained by the electron effect of the guest molecules being more significant than their quantity. Photoinduced SCO effect based on the LIESST principle was induced by red (637 nm) light at 5 K and 10 K for the *trans*-azobenzene and stilbenes clathrate, respectively. The $\chi_M T$ function measured for $\{Fe(L9)[Pt(CN)_4]\} \cdot H_2O \cdot$ *trans*-azobenzene was saturated at 0.86 $cm^3 \cdot K \cdot mol^{-1}$ (Fig. 14a, red triangles). Heating in the dark revealed a further increase of $\chi_M T$ value to 1.52 $cm^3 \cdot K \cdot mol^{-1}$ at 27 K, indicating that the LS to metastable HS state transition resulted in $\sim$30 % photo-induced conversion of the Fe(II) ions. Further heating led to a decrease of $\chi_M T$ and T(LIESST) took place at 57 K (Fig. 14a, white squares).

The value of $\chi_M T$ for clathrates with incorporated *trans-* or *cis-* stilbene molecules was saturated at 22 K and 27 K, respectively, which represents 65 % and 90 % of photoconversion with the same T(LIESST) = 46 K. Properties of the guest molecules such as their electron effects or supramolecular interactions with the host network affect the thermally induced SCO. Temperature-dependent Raman spectra were measured upon 532 nm excitation for all three clathrates at 113 K and 298 K, where different spin states of the compounds were expected. At 298 K, the ring breathing vibration of L9 ligands was identified at 1017 cm^{-1} in $\{Fe(L9)[Pt(CN)_4]\} \cdot$ *trans*-azobenzene (Fig. 15a), while the peak of both polymers with incorporated stilbene guest was localized at slight lower energy (1014 cm^{-1}) (Figs. 15b and 15c). At 113 K, the Fe(II) centers were partially converted to the LS state and a new peak appeared at 1027 cm^{-1} for $\{Fe(L9)[Pt(CN)_4]\} \cdot$ *trans*-azobenzene and at 1026 cm^{-1} for both *trans-* and *cis*-stilbene clathrates. Thus, the peaks at 1017 cm^{-1} and 1027 cm^{-1} allowed SCO identification and $T_{1/2}$ was estimated at 135 K, 173 K, and 162 K, respectively. The introduction of the relatively large guests into the host compound caused higher stabilization of the HS fraction and therefore $T_{1/2}$ shifted down compared to the host molecule. Photoisomerization of incorporated guests and subsequently its impact on the magnetic behavior of the host showed to be strongly hindered by the host framework. Effective photoconversion of the guest in the solid state was suppressed because both the host and the guest absorbed the same UV (260–360 nm) light and the penetration depth of the light, which was supposed to induce the guest's photoisomerization, was considerably reduced. Steric hindrance and specific interactions with the host probably constitute an insurmountable barrier for the photoconversion of the guests within the host framework (Brachňaková et al., 2021).

Successful GD-LISC has recently been observed in $\{[Fe(L10)(Ag(CN)_2)_2]\} \cdot$ *trans*-azobenzene with Fe(II) centers coordinated with equatorial $[Ag(NCS)_2]^-$ linkers creating a 2D rhombic grid along the *bc*-plane interconnected by two ligands of L10 = = 1,4-bis(4-pyridyl)naphthalene along the *a*-axis. A void space of empty clathrate is 1201.3 Å corresponding to 35.1 % of the unit cell. Edge-to-face π-π interactions were observed between the *trans*-azobenzene molecules and the pyridine moiety of L10. Fe—N bond lengths were extended ($\sim$0.19 Å) upon heating, which is associated with

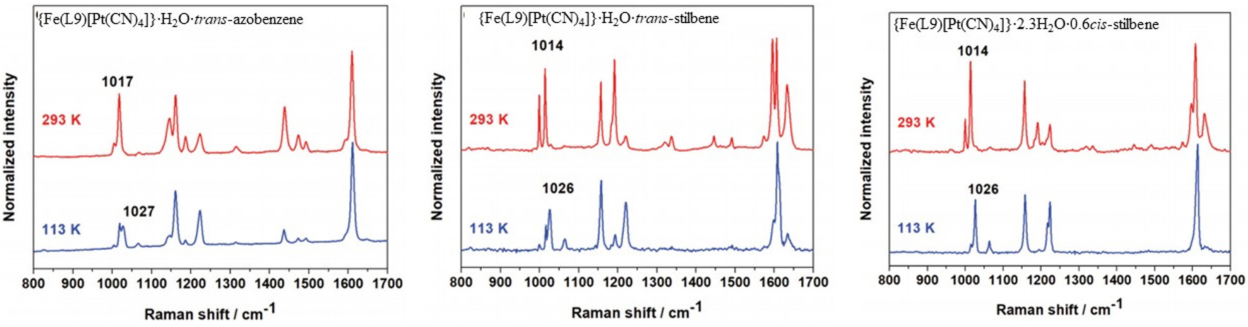

a) b) c)

Fig. 15. Raman spectra measured upon 532 nm excitation at 293 K and 113 K for a) $\{Fe(L9)[Pt(CN)_4]\} \cdot H_2O \cdot$ trans-azobenzene, b) $\{Fe(L9)[Pt(CN)_4]\} \cdot H_2O \cdot$ trans-stilbene, and c) $\{Fe(L9)[Pt(CN)_4]\} \cdot 2.3H_2O \cdot 0.6$ cis-stilbene (Brachňaková et al., 2021).

the LS (90 K) to HS (298 K) conversion. Distortion parameter Σ of the HS species was unusually low at ambident temperature (13.4 °) compared to that at 125 K (13.9 °), indicating the presence of elastic frustration which acts as the fundamental mechanism for multi-step SCO. Orange-yellow crystals showed thermal hysteresis of four-step SCO behavior in the 75—200 K region (Fig. 16a, black and red circles). Photomagnetic experiments based on LIESST investigation were performed at 10 K and the excitation was induced by several laser sources (355, 473, 532, and 671 nm). Although UV light did not induce the excitation from LS to metastable HS state (Fig. 16a, purple circles), visible light (473, 532, 671 nm) induced photoconversion in 56 %, 66 %, and 39 % yields while $\chi_M T$ rapidly decreased upon heating and reached the baseline at about 70 K. Two-step relaxation was observed after the 473 nm and 532 nm irradiation (Fig. 16a, blue and green circles) and two minima related to T(LIESST) occurred at 50/62 K and at 50/61 K. However, exposure to 671 nm light resulted in one-step relaxation (T(LIESST) = 56 K) (Fig. 16a, orange circles). *reverse*-LIESST can be observed upon 830 nm irradiation hence light-induced SCO at 5 K was cycled 'on' and 'off' via alternating irradiation at 532 and 830 nm. (Fig. 16b) The light-induced effect was based on the principle of different spin states of Fe(II) ions instead of the photoisomerization of the azobenzene guests. The *trans* → *cis* photoisomerization (365 nm, 298 K, 12 h) of the *trans*-azobenzene guests in microcrystalline $\{[Fe(L10)(Ag(CN)_2)_2]\} \cdot$ *trans*-azobenzene and its effect on the host's magnetic properties showed that $T_{1/2}$ and the character of four-step hysteresis remained the same after the irradiation, but $\chi_M T$ increased to 1.03 cm$^3 \cdot$ K $\cdot$ mol^{-1} in low the temperature region (Fig. 17a) green line). This indicates that the LS → HS transition accompanied by *trans* → *cis* conversion occurred (~22 %) and the new HS phase of the Fe(II) ions was stabilized by the photoconverted *cis*-azobenzene guest. Intermolecular interactions between the host and either *trans*- or *cis*-azobenzene guests before and after the UV irradiation were investigated through the Hirshfeld surfaces. Relatively weak host-guest interactions were expected in planar *trans*-azobenzene arranged along 1D channel. Stronger steric hindrance of non-planar *cis*-azobenzene in the LS framework generated by multiple host-guest and guest-guest interactions caused extension of the pore size (2.9 %) and destabilized the host LS Fe(II) ions, which partly favored their transition to HS state upon the *trans* → *cis* azobenzene isomerization. Reverse-process of *cis* → *trans* isomerization ($\lambda >$ 400 nm, 298 K, 24 h) showed full $\chi_M T$ recovery at low temperatures and indicated the HS → LS conversion (Fig. 17a, red and blue lines). Recovery to the original *trans*- LS state was estimated to be 62 % after 9 days in dark (Fig. 17a, grey line). The amount of new *cis*- HS or *trans*- LS species were identified by $\chi_M T$ changes upon either UV or visible light exposure. The same trend was observed at two different temperatures (20 K and $T_{1/2}$ = 154 K) but different starting values (~0.15 and 2.10 cm$^3 \cdot$ K $\cdot$ mol^{-1}, respectively) were determined. Increase or decrease of $\chi_M T$ with the irradiation time represents the LS → HS and HS → LS conver-

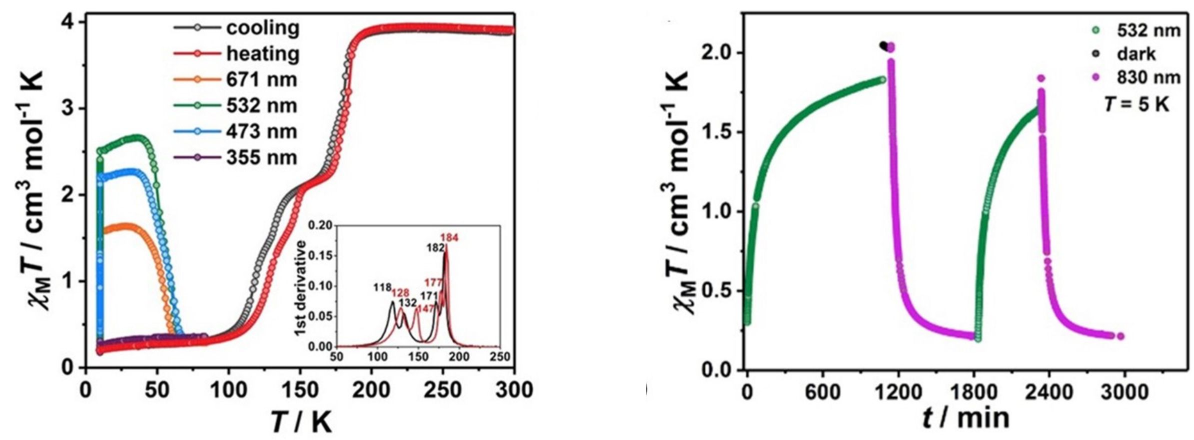

a)

b)

Fig. 16. a) χ_MT vs. T plots of $\{[Fe(L10)(Ag(CN)_2)_2]\} \cdot$ trans-azobenzene and its thermal SCO effect determined upon cooling (black) and heating (red circles). LIESST effect induced at 10 K by 355 nm (purple), 473 nm (blue), 532 (green), and 671 nm (orange circles) irradiation. b) Cycles of LIESST (green) and reverse-LIESST (pink circles) effects recorded as the time-dependence χ_MT plots, induced by 532 and 830 nm light, respectively, at 5 K (XIE et al., 2021).

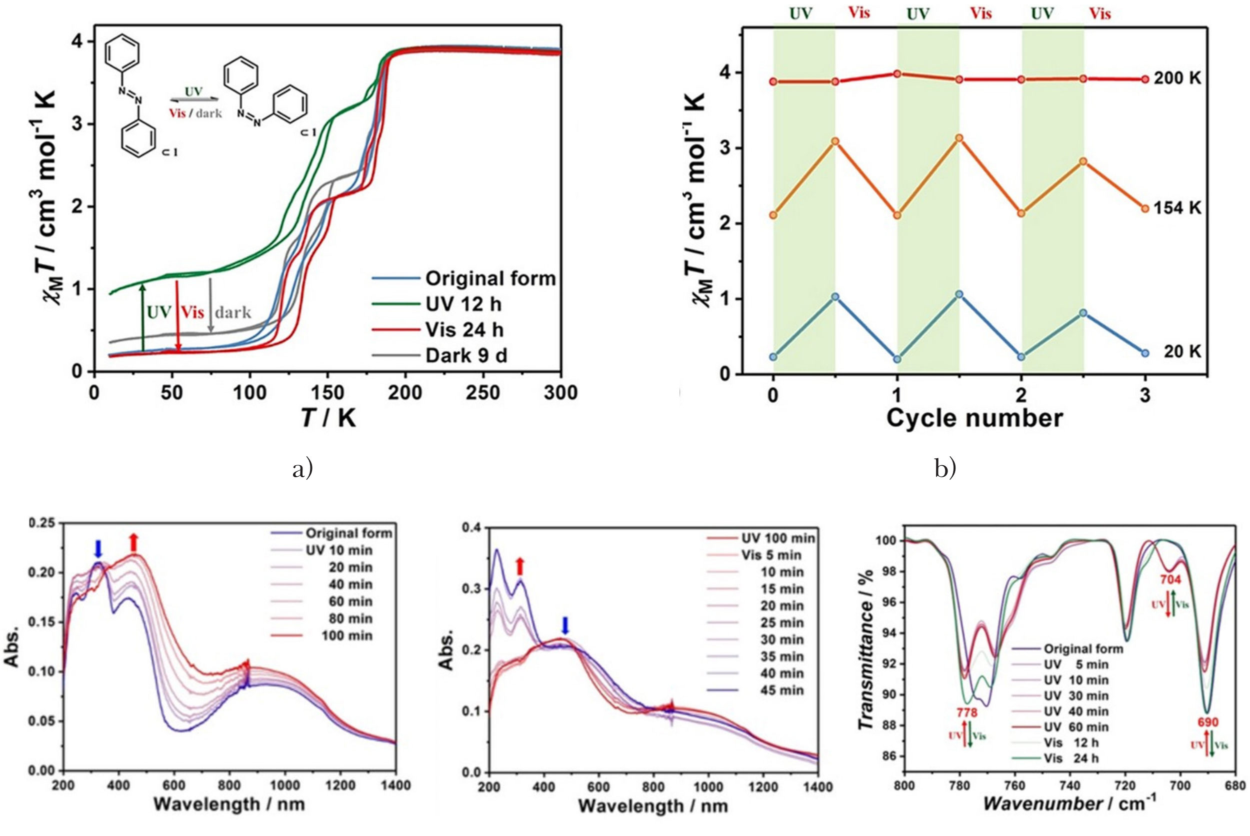

a) b)

c) d) e)

Fig. 17. a) χ_MT vs. T plots of $\{[Fe(L10)(Ag(CN)_2)_2]\}\cdot$trans-azobenzene before (blue) and after UV light (365 nm, 298 K, 12 h) (green), visible light ($\lambda > 400$ nm, 298 K, 24 h) irradiation (red); plot of photoproduct after UV irradiation in dark for 9 days (grey line). b) χ_MT change upon several cycles of irradiation (UV or VIS) measured at 20 K (blue), 154 K (orange), and 200 K (red line). c) Absorbance spectra of $\{[Fe(L10)(Ag(CN)_2)_2]\}\cdot$trans-azobenzene diluted in $BaSO_4$ tablet before (blue) and after UV (365 nm, 298 K, 100 min) light irradiation (red line) representing cis → trans isomerization of trans-azobenzene guest. d) Absorbance change of reverse trans → cis conversion induced by visible light ($\lambda > 400$ nm, 298 K, 45 min) (blue line) identified based on photoproduct spectrum after UV irradiation (red line). e) Transmittance spectra of diluted $\{[Fe(L10)(Ag(CN)_2)_2]\}\cdot$trans-azobenzene in KBr pellet before and after UV or VIS light irradiation at room temperature (XIE et al., 2021).

sions, respectively (Fig. 17b, blue and orange lines), while at 200 K, photoisomerization upon irradiation did not cause any magnetism changes because the SCO effect was complete and the Fe(II) ions were fully in the HS state (Fig. 17b, red line). These results confirmed the reversible GD-LISC effect at low temperatures based on *cis* ↔ *trans* isomerization of *trans*-azobenzene guests induced by different light irradiation. The *trans* → *cis* photoisomerization of diluted $\{[Fe(L10)(Ag(CN)_2)_2]\}\cdot$*trans*-azobenzene in a $BaSO_4$ tablet showed a decrease of absorbance $\pi \rightarrow \pi^*$ band (324 nm) and a significant increase of $n \rightarrow \pi^*$ band (435 nm) upon UV (365 nm) irradiation (Fig. 17c). On the contrary, reverse *cis* → *trans* isomerization was either induced by visible light ($\lambda > 400$ nm) or the dark and in both cases showed a decrease of the absorbance of $n \rightarrow \pi^*$ band and significant increase of the $\pi \rightarrow \pi^*$ band (Fig. 17d). Bidirectional isomerization of the guests was identified by using different light irradiation at 298 K in diluted polycrystalline form. Transmittance spectra of the KBr pellet $\{[Fe(L10)(Ag(CN)_2)_2]\}\cdot$*trans*-azobenzene showed a decrease and shift of the peak at 774 cm^{-1} to 778 cm^{-1}, while the peak at 690 cm^{-1} also decreased in intensity and a new peak appeared at 704 cm^{-1}, which was assigned to the γ(CH), δ(NNC) and τ(ring) vibrational modes of *cis*-azobenzene. Based on the 690 cm^{-1} peak decrease, 20 % conversion to the new *cis*- phase was calculated at 298 K (Fig. 17e, XIE et al., 2021).

Conclusion

This review is focused on mononuclear LD-LISC (ligand-driven light-induced spin change) active Fe(II) complexes with heterocyclic mono-, di-, and tridentate N-donor ligands with photoactive ethylenephenyl or azophenyl moiety. Different Fe—N bond length lengths and distortion parameters between the paramagnetic more distorted HS state and diamagnetic LS state with shorter bond lengths were obtained based on different ligand fields, which is affected by the ligand's electronic properties. Their magnetic characterization, like $T_{1/2}$ and $\chi_M T$ values, are affected by various ligand substituents. The *cis-* or *trans-* configuration of the photoactive moiety also influences the ligand field strength, and different spin states of the corresponding complexes is reached at some temperatures. Moreover, *cis* → *trans* isomerization of $[Fe(cis\text{-}L1)_4(NCSe)_2]$ occurs by two different mechanisms based on the temperatures of the 532 nm irradiation. Photoswitching at ambient temperature based on the LD-LISC principle was partially successful for some of the above-described thin doped films, solutions, and polycrystalline samples of the homoleptic and heteroleptic Fe(II) complexes. This review is also focused on 2D and 3D Fe(II) Hofmann coordination polymers, which showed thermal and photo-induced SCO effect. By incorporation of a photosensitive guest into the host clathrate, a new concept of GD-LISC (guest-driven light-induced spin crossover) effect is introduced based on the guest's reversible *trans* ↔ *cis* isomerization. Reversible isomerization of *trans*-azobenzene upon UV and VIS irradiation resulted in spherical hindrance, which affected the geometry of Fe(II) centers in the low temperature region ($T \leq 154$ K), and caused changes of $\chi_M T$. These findings call for further investigation, which should be extended for different host and guest systems (larger size of pores).

Acknowledgement

Slovak grant agencies APVV-18-0197, APVV-18-0016, APVV-19-0087, VEGA 1/0029/22, and STU grant for young researchers MAFOMA are acknowledged for providing financial support. This article was written thanks to the generous support under the Operational Program Integrated Infrastructure for the project: "Strategic research in the field of SMART monitoring, treatment and preventive protection against coronavirus (SARS-CoV-2)", Project no. 313011ASS8, co-financed by the European Regional Development Fund.

References

Ando H, Nakao Y, Satoa H, Sakaki S (2010) Dalton Trans. 39, 7, 1836—1845.

Bandara HMD, Burdette SC (2012) Chem. Soc. Rev. 41, 1809—1825.

Bartocci G, Bortolus P, Mazzucato U (1973) J. Phys. Chem. 77, 5, 605—610.

Bartocci G, Mazzucato U, Masetti, F, Galiazzo G (1980) J. Phys. Chem. 84, 8, 847—851.

Bartual-Murgui C, Ortega-Villar NA, Shepherd HJ, Muñoz MC, Salmon L, Molnár G, Bousseksou A, Real JA (2011) J. Mater. Chem. 21, 7217—7222.

Bertoni R, Cammarata M, Lorenc M, Matar SF, Létard J-F, Lemke HT, Collet E (2015) Am. Chem. Soc. 48, 3, 774—781.

Boillot M-L, Roux C, Audière J-P, Dausse A, Zarembowitch J (1996) Inorg. Chem. 35, 13, 3975—3980.

Boillot M-L, Zarembowitch J, Sour A (2004) Top. Curr. Top. Curr. Chem. 234, 261—276.

Boillot M-L, Pillet S, Tissot A, Rivière E, Claiser N, Lecomte C (2009) Inorg. Chem. 48, 4729—4736.

Boukheddaden K, Miyashita S, Nishino M (2007) Phys. Rev. B 75, 094112.

Bousseksou A, Molnár G, Salmon L, Nicolazzi W (2011) Chem. Soc. Rev. 40, 3313—3335.

Brachňaková B, Šalitroš I (2018) Chem. Pap. 72, 773—798.

Brachňaková B, Adamko Kožíšková J, Kožíšek J, Melníková E, Gál M, Herchel R, Dubaj T, Šalitroš I (2020) Dalton Trans. 49, 17786—17795.

Brachňaková B, Moncoľ J, Pavlik J, Šalitroš I, Bonhommeau S, Valverde-Muñoz FJ, Salmon L, Molnár G, Routaboula L, Bousseksou A (2021) Dalton Trans. 50, 8877—8888.

Castellano M, Ferrando-Soria J, Pardo E, Julve M, Lloret F, Mathonière C, Pasán J, Ruiz-Pérez C, Cañadillas-Delgado L, Ruiz-García R, Cano J (2011) Chem. Comm. 47, 11035—11037.

Capes L, Létard J-F, Kahn O (2000) Chem. Eur. J. 6, 12, 2246—2255.

Decurtins S, Gütlich P, Köhler CP, Spiering H (1984) J. Chem. Soc., Chem. Commun. 105, 1, 1—4.

Decurtins S, Gütlich P, Hasselbach KM, Hauser KM, Spiering H (1985) Inorg. Chem. 24, 2174—2178.

Gütlich P, Hauser A, Spiering H (1994) Angew. Chem. Int. Ed. Engl. 33, 2024—2054.

Gütlich P, Garcia Y, Goodwin HA (2000) Chem. Soc. Rev. 29, 6, 419—427.

Gütlich P, Goodwin HA (2004) Top. Curr. Chem. 233, 1—47.

Halcrow MA (2011) Chem. Soc. Rev. 40, 11, 4119—4142.

Hartley GS, Le Févre RJW (1939) J. Chem. Soc. 531—535.

Hasegawa Y, Kume, S, Nishihara H (2009) Dalton Trans. 2, 280—284.

Hasegawa Y, Kume S, Takahashi K, Nishihara H (2011) Chem. Comm. 47, 6846—6848.

Hauser A (1991) Coord. Chem. R. 111, 6, 275—290.

Hauser A, Alder P (1991) J. Chern. Phys. 95, 12, 8710—8717.

Hauser A (2004) Top. Curr. Chem. 233, 49—58.

König E (1991) Complex Chem. 76, 51—152.

Létard J-F (2005) Chem. Eur. J. 11, 4582—4589.

Merino E, Ribagorda M (2012) Beilstein J. Org. Chem. 2012, 8, 1071—1090.

Murray KS, Kepert CJ (2004) Top. Curr. Chem. 233, 195—228.

Ragon F, Yaksi K, Sciortino NF, Chastanet G, Létard J-F, D'Alessandro DM, Kepert CJ, Neville SM (2014) Aust. J. Chem. 67, 1563—1573.

Real JA, Gaspar AB, Muñoz MC (2005) Dalton Trans. 12, 2062—2079.

Rösner B, Milek M, Witt A, Gobaut B, Torelli P, Fink RH, Khusniyarov MM (2015) Angew. Chem. Int. Ed. 54, 12976–12980.

Roux C, Zarembowitch J, Gallois B, Granier T, Claude R (1994) Inorg. Chem. 33, 10, 2273–2279.

Sheu Ch-F, Chen K, Chen S-M, Wen Y-S, Lee G-H, Chen J-M, Lee, J-F, Cheng B-M, Sheu H-S, Yasuda N, Ozawa Y, Toriumi K, Wang Y (2009), Chem. Eur. J. 15, 2384–2393.

Šalitroš I, Madhu NT, Boča R, Pavlik J, Ruben M (2009) Monatsh. Chem. 140, 695–733.

Šalitroš I, Fuhr O, Eichhöfer A, Kruk R, Pavlik J, Dlháň L, Boča R, Ruben M (2012) Dalton Trans. 41, 5163–5171.

Šalitroš I, Pogány L, Ruben M, Boča R, Linert W (2014) Dalton Trans. 43, 16584.

Šalitroš I, Pavlik J (2018) Encyclopedia of Physical Organic Chemistry.

Šalitroš I, Fuhr O, Gál M, Valášek M, Ruben (2017) Chem. Eur. J. 23, 42, 10100–10109.

Takahashi K, Hasegawa Y, Sakamoto R, Nishikawa M, Kume S, Nishibori E, Nishihara H (2012) Inorg. Chem. 51, 5188–5198.

Tao J, Wei R-F, Huang R-B, Zheng L-S (2012) Chem. Soc. Rev. 41, 703–737.

Tissot A, Boillot M-L, Pillet S, Codjovi E, Boukheddaden K, Daku MLM (2010) J. Phys. J, 114, 49, 21715–21722.

Xie K-P, Ruan Z-Y, Lyu B-H, Chen X-X, Zhang X-W, Huang G-Z, Chen Y-C, Ni Z-P, Tong M-L (2021) Angew. Ch. International Edition 60, 52, 27144–27150.

Yamaguchi K, Kume S, Namiki K, Murata M, Tamai N, Nishihara H (2005) Inorg. Chem., 44, 9056–9067.

Zarembowitch J, Roux C, Boillot M-L, Claude R, Itie J-P, Polian A, Bolte M (1993) Mol. Cryst. Liq. Cryst. 234, 247–254.

sciendo

Stability of ferrate during long-term storage

Michaela Benköová[a], **Emília Mališová**[a], **Peter Peciar**[b],
Adam Guštafík[b], **Ján Híveš**[a]

[a]*Department of Inorganic Technology, Faculty of Chemical and Food Technology,*
Slovak University of Technology in Bratislava, Radlinského 9, 812 37 Bratislava, Slovak Republic
[b]*Institute of Process Engineering, Faculty of Mechanical Engineering,*
Slovak University of Technology in Bratislava, Námestie Slobody 17, 812 31 Bratislava, Slovak Republic
michaela.benkoova@stuba.sk

Abstract: Surface water and groundwater are polluted with pharmaceuticals, detergents, pesticides, and many other substances. Application of ferrates seems to be a perspective option for wastewater treatment as ferrates are not only powerful oxidizing agents but also an excellent disinfecting and coagulating agents decomposing many stable inorganic, organic, and biological compounds. Final products of their decomposition do not include carcinogenic or toxic products. In this paper, stability of electrochemically prepared potassium ferrate encapsulated in packaging materials printed on a 3D printer was monitored. In the experiment, electrochemically prepared potassium ferrate with different purity (21.4 %, 63.5 % and 67.3 %) was used. Stability of potassium ferrate was monitored for one month and that of other ferrates for three months. Different storage conditions of ferrate samples were also compared. Storage conditions had a significant influence on the ferrate stability.

Keywords: ferrate, stability, zeolit, encapsulation, 3D printing

Introduction

Currently, the issue of water contamination by various pollutants is very pressing. Surface and underground waters are polluted by pharmaceuticals, daily hygiene products, cleaning agents, pesticides, and other substances. Removal of these unwanted substances from water and, therefore, from the environment in general, is a current problem. Ferrates $(FeO_4)^2$ are compounds of iron in the high-oxidation state +VI. They are solid crystalline substances with characteristic dark purple color (Lee, 2004; Kubiňáková, 2015). Ferrates are very strong oxidizing agents. They have high redox potential, which is the reason for their high reactivity but also for their relatively low stability. Their oxidation reduction potential is 0.72 V for alkaline environment and 2.2 V for acidic environment (Eng, 2006; Jiang, 2002). There are two ways of ferrates preparation: chemical and electrochemical. Chemical methods are multistep syntheses using a wide range of different chemicals. These, however, generate a lot of waste. There are two types of chemical methods: dry chemical oxidation and wet chemical oxidation. The first method is the oldest method of iron oxides preparation and is very dangerous as an explosion may occur at higher temperatures. In the electrochemical method, the working temperature used ranges from 20 °C to 70 °C for aqueous solutions and from 70 °C to 170 °C for melts. Hydroxide concentration in the melts must be at least 70 wt. %. Synthesis is a two-step process where pure product is created, thus, the amount of waste produced during production is significantly decreased. In addition, the requirements for product cleaning decrease (Kubiňáková, 2015; Eng, 2006; Jiang, 2002; Jiang, 2017; Mura, 2017; Mácová, 2009; Thompson, 1951). Ferrates break down stable inorganic, organic, and biological substances without carcinogenic or toxic products. They are called a “green oxidant” and during the decomposition, only substances commonly found in the environment (iron oxides and hydroxides) are formed. These substances are also coagulating, disinfecting, and oxidizing agents in water (Mura, 2017; Mácová, 2009). Considering these properties, they can be used in various fields; e.g. in organic syntheses, corrosion engineering, or in galvanic alkaline cells. The most promising is the use of iron oxides in the field of the cleaning and repurification of waste and surface water. Murmann and Robinson (1974) used ferrates in their research to reduce the quantity of metal ions Pb(II), Cu(II), Zn(II), Fe(III), Hg(II), Cd(II) and Cr(III) in river water and in water from wells. They used sodium ferrate (Na_2FeO_4), which subsequently decomposed into ferric hydroxide $(Fe(OH)_3$. A series of experiments were carried out to investigate the factors influencing the degradation of bisphenol A (BPA) by iron oxides. Degradation was effective and fast (3 min) with an efficiency of up to 97.5 % (Han, 2015). Feng and Sharma (2018), dealt with the removal of antibiotics by iron sulfur or iron sulfate (hydrogen sulfate) systems. These systems provided almost immediate oxidation of the removed antibiotics trimetropin (TMP) and flumequin (FLU). The oxidation lasted for 15 s and a smaller dose of iron oxide was used than was necessary for the oxidation of iron oxide itself. Ni et al. (2020) addressed the removal of intracellular antibiotic resistance genes (ARGs) from the secondary effluent of wastewater treatment plants (WTPs) using iron oxides. The results showed that iron treatment can effectively remove 15 ARGs, which cover eight different types of resistance genes. Furthermore, viability and relative abundance of potential ARG hosts in wastewater decreased. However, a problem of their massive application is their very high redox potential which complicates their production and it is related to their relatively low stability during long-term storage. Encapsulation of ferrates can be used to solve this problem. The first solid potassium ferrate was encapsulated into molten paraffin and the stability of encapsulated Fe(VI) was monitored for 40 days (Yuan, 2008). Next, the encapsulation of K_2FeO_4 by the phase separation method in organic solvents with ethylcellulose and paraffin was studied. The stability of encapsulated Fe(VI) was monitored for 30 days (Wang, 2009). Encapsulation of Fe (VI) was detected in three different packaging materials. Three different materials (3D printed polyvinyl alcohol capsules, commercially available hydroxypropyl methylcellulose capsules, and gelatin capsules) were used. The stability of encapsulated Fe (VI) was monitored for 30 days (Czölderová, 2018). Chitosan has been studied as another material forming a shell layer for ferrate (VI). Chitosan-ferrite capsules remained stable for at least 20 days without significant loss of Fe (VI) content. It is questionable whether these results are relevant since the initial purity of iron oxide used was only 12 % (Chen, 2019). Considering all these materials used for encapsulation, three basic conclusions can be drawn. Encapsulation always has positive effect on stability. Encapsulation in these selected materials has negative effect on the oxidizing power of iron oxides during their subsequent use. Stability of encapsulated ferrates has so far been studied only within a relatively short time horizon (only for about a month). Yuan et al. (2008) dealt with the elimination of trichlorethylene from wastewater using paraffin-encapsulated iron oxides. The effects of three main factors: mixing time, ultrasound time, and water bath temperature, on the preparation of encapsulated iron oxide were studied. Primary research indicates that degradation of trichlorethylene (TCE) is more efficient in acidic environment. More than 90 % of TCE was degraded within the reaction time of 60 minutes in solutions with pH = 4 6 compared to only 60 % degradation of TCE after 150 minutes in solutions with pH = 10. Mikolic-Bujanovic et al. (2020) studied the synthesis of microcrystals and barium ferrate nanocrystals ($BaFeO_4$) employing precipitation from an electrochemically synthesized potassium ferrate solution using barium hydroxide. These crystals were then encapsulated with paraffin dissolved in cyclohexane and used to remove pesticide clomazone from water with the removal efficiency of almost 95 %. When nonencapsulated $BaFeO_4$ was used, the efficiency was lower by 20 %. Research of other materials suitable for ferrate encapsulation is important for water treatment. Zeolites are used as they appear to be excellent sorption and filtration material due to their porous structure. These substances have proven to be extremely effective in the treatment of wastewater for selective groups of contaminants. Zeolites as an adsorbent are particularly suitable for the removal of metal ions. Adsorption of other toxic contaminants has also been investigated. In addition, they are a natural and nontoxic material. There are two types of zeolites: natural and synthetic. The first type of zeolites is often contaminated with various mineral impurities (volcanic glass, quartz, mica, etc.). Synthetic zeolites are modified chemically. They have larger active surface, higher sorption capacity, and improved physicochemical properties. Zeolites are used as building materials as a component of Portland zinc in the production of cement as they are resistant to aggressive environments (e.g. sea water). Another area of use is plant and animal production in agriculture. Zeolites are added to pig, poultry, and cattle feed to increase weight gain. Another important use of zeolites is in the production of drugs and in the petrochemical industry. They are used in catalytic crackers to break down large hydrocarbon molecules into gasoline, diesel, kerosene, and waxes (Fajnor, 1989; Hudec, 2015).

In this study, stability of different encapsulated potassium ferrate powders was monitored. They were encapsulated in packaging materials printed on a 3D printer using different types of filaments (PVA, PLA, PVA+, and BVOH). The ferrates were in the form of a tablet and powder and they were stored for one month or for three months under different conditions (desiccator and laboratory).

Materials and Methods

Preparation of potassium ferrate

Potassium ferrate was prepared electrochemically in an electrolyzer (Híveš, 2018). In this paper, potassium ferrates with the purity of 21.4 wt. % to 67,3 wt. % were used.

Determination of ferrates purity

Purity of the ferrates was determined spectrophotometrically. A weighed amount of the ferrate sample was dissolved in a 20 wt. % sodium hydroxide solution and filtered through an injection microfilter to remove insoluble residues, such as degradation products of ferrates ($Fe(OH)_3$). Subsequent ferrous concentration was calculated using the Lambert-Beer law based on the absorbance measured using a UV-VIS spectrophotometer (Specord 250 Plus, Analytik Jena, Germany).

Preparation of tablets

In the beginning, the effect of the ferrate content on tablet compactness was monitored. Several tablets with zeolite:ferrate ratio of 95:5, 90:10, 70:30, 50:50, 30:70 and 10:90 were prepared. The actual amounts of these mixtures of ferrate and zeolite are summarized in Table 1.

Tab. 1. Additions of mixtures of ferrate and zeolite required to produce tablets.

ratio zeolite: Fe (VI)	quantity of zeolite [g]	quantity of ferrate [g]
95:5	9,50	0,51
90:10	9,01	1,01
70:30	7,00	3,00
50:50	5,00	5,01
30:70	1,51	3,51
10:90	0,50	4,50

To verify the compactness of the tablets, pressure tests were also performed indicating that the higher the amount of ferrate, the more compact the tablet. The tablet compactness was sufficient for convenient handling even with the smallest proportion of ferrates.

Three fractions of zeolites in the tablets production were applied. The third fraction, the thickest, was poorly compressible, and compact tablets could not be formed. The first and second finer fractions had powdery structure and resulted in compact tablets when mixed with ferrates. In the end, the second fraction was used in the production of tablets as it is not the softest one and, therefore, is technologically and economically more advantageous.

The production of tablets was carried out on a Kistler 2153A electromechanical press.

Preparation of capsules

Capsules were printed on a 3D printer (Creality ENDER 3-V2) from four materials: polylactic acid (PLA), which is biodegradable and has black color; butenediol vinyl alcohol copolymer (BVOH), which is soluble in water and has natural color; polyvinyl alcohol (PVA), and polyvinyl alcohol (PVA+), both soluble in water. The difference between PVA and PVA+ is that PVA+ is easier to compress. The capsules were pressed into the shape of a cube with the dimensions (1.2 × 1.2 × 1.0) mm and (0.7 × 0.7 × 1.2) mm. The wall thickness of larger cubes was 0.2 mm and that of smaller cubes was 0.1 mm.

Experimental part

The prepared tablets were inserted into the printed capsules. The second part of the ferrate was collected as a powder and placed in the capsule. It was the same amount as the amount needed to create one tablet. A part of the capsules prepared in this way was stored in a closed plastic zip sachet, without air access in a desiccator (humidity around 10 %), and the rest was stored freely in the air at temperature and light natural for laboratory environment (daylight, temperature in the laboratory of around (20 – 25) °C), and humidity in the laboratory of around (30 – 60) %. Successive measurements following the decrease in the stability of encapsulated ferrates were planned for a period of 12 weeks for the long-term experiment and 30 days for the short-term experiment. The measurements were done at the same time for both encapsulated groups to determine the influence of the environment and storage on the stability of iron oxides. In the long-term experiment of 12 weeks was performed analogously. Stability of the encapsulated ferrates was also monitored at different conditions: in a desiccator and in the laboratory.

Results and discussion

In the first figure, graphs of the ferrates purity dependence on time in different environments are shown. The ferrate purity decreases in the order: ferrate tablet, ferrate tablet encased in a capsule of BVOH material, free ferrate powder, and ferrate powder placed in a BVOH capsule. The measurements started at the purity of 67.3 %. In the first picture, potassium ferrate's purity change with time is depicted for the experiments in a desiccator (Fig. 1a) and in laboratory (Fig. 1b). Purity decrease was smooth and the value stabilized at 50 % for tablets and at 49 % for powders. For samples stored freely in the laboratory, ferrates purity was 45 % for tablets while for powders it was only 41 %.

In Figure 2, the dependence of potassium ferrate's purity on the time of experiment in a desiccator and in laboratory is depicted using biodegradable PLA filament. Purity of the ferrates used at the beginning was the same as that in the previous case. As in the previous case, only a slight decrease in the purity of free and encapsulated ferrates in tablet form can be observed. Purity of the ferrates stopped after 30 days and the values are very similar to those

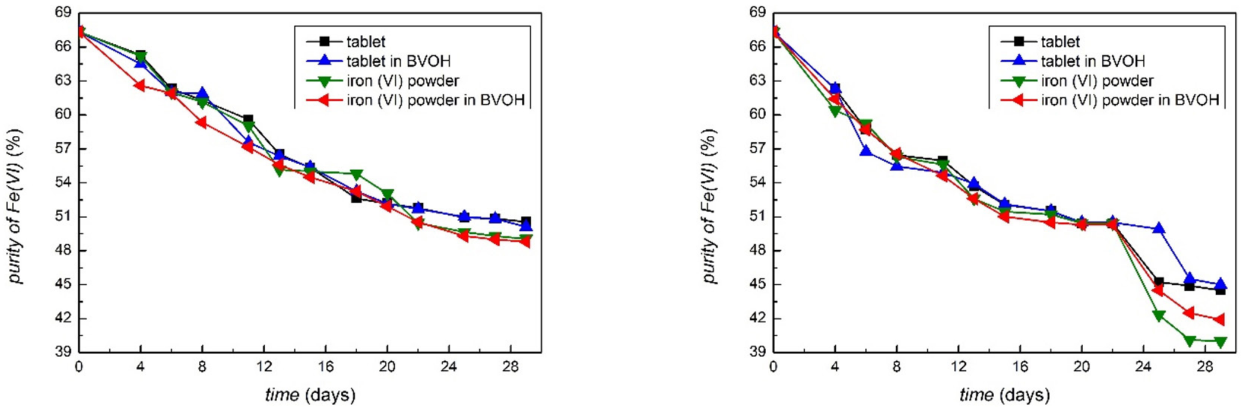

a)

b)

Fig. 1. Dependence of potassium ferrate's purity on the time of experiment a) in desiccator, b) in laboratory for ferrate tablet, powder and encapsulated tablet and powder in BVOH.

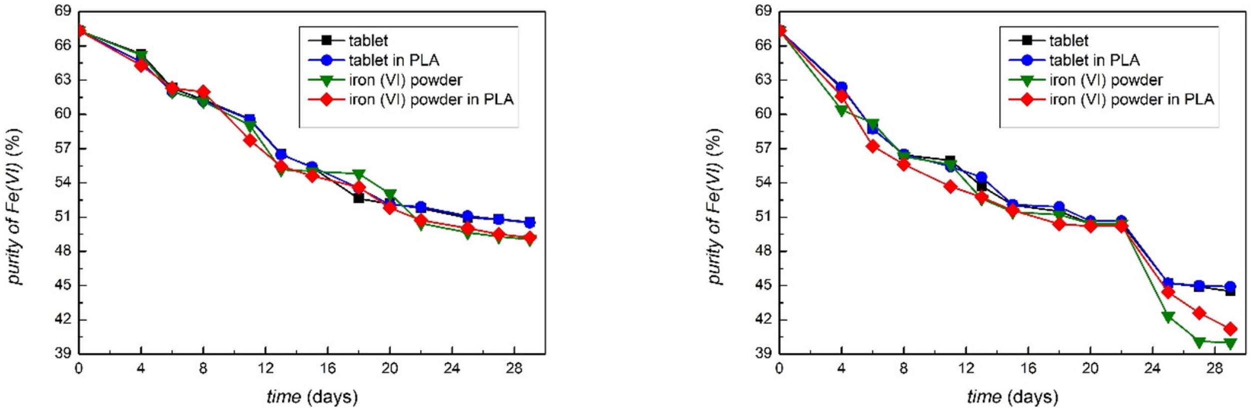

a)

b)

Fig. 2. Dependence of potassium ferrate's purity on the time of experiment a) in desiccator, b) in laboratory for ferrate tablet, powder and encapsulated tablet and powder in PLA.

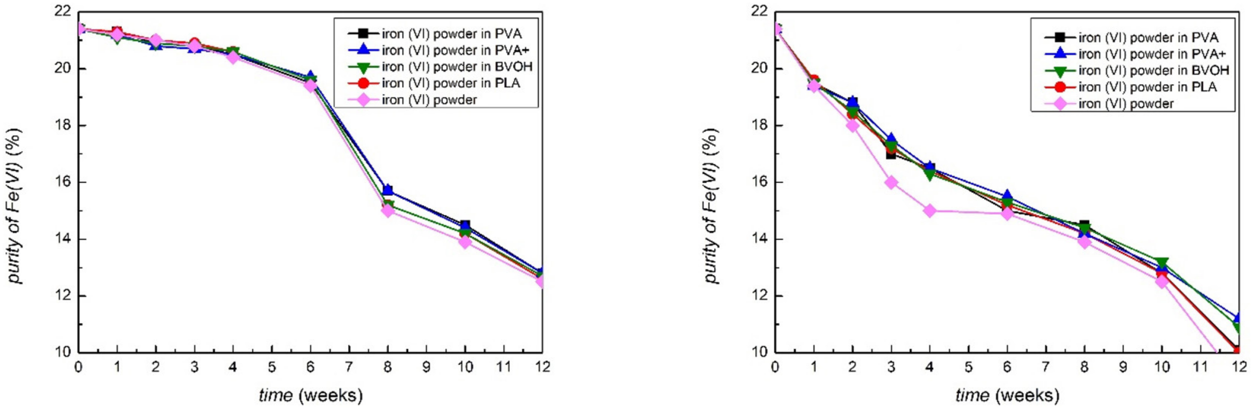

a)

b)

Fig. 3. Dependence of potassium ferrate's purity on the time of experiment a) in desiccator, b) in laboratory, comparison for nonencapsulated powder and powder in different encapsulation materials.

reached with the previous packaging material. Even in this case, from the point of view of stability, the environment in the desiccator, without the presence of air humidity and CO_2, appears to be better.

In Fig. 3, ferrate's purity for free ferrate powder and ferrate powder placed in a capsule decreases with time in different environments. The capsules were from different materials: PVA, PVA+, BVOH

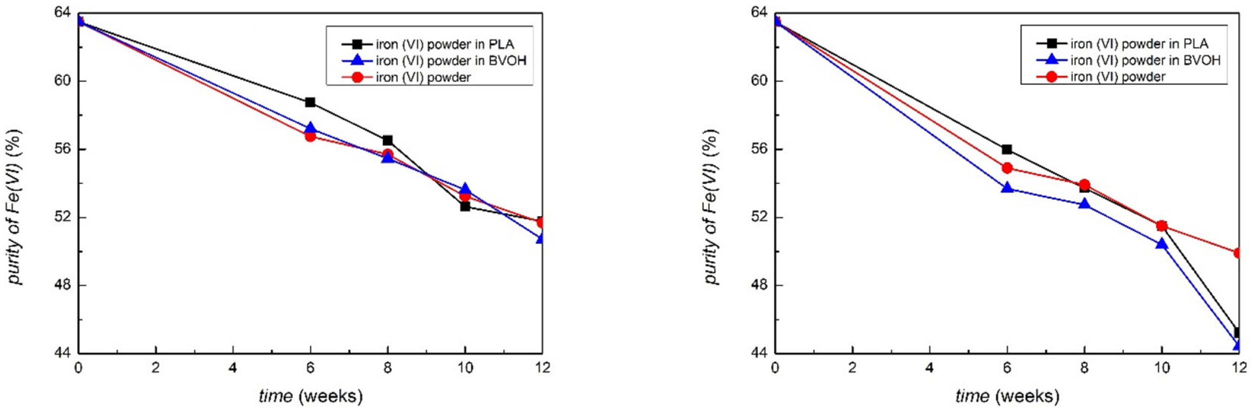

a) b)

Fig. 4. Dependence of potassium ferrate's purity on the time of experiment a) in desiccator, b) in laboratory, comparison for free ferrate powder and powder encapsulated in PLA and BVOHr.

and PLA. Measurements started at the purity of 21.4 % and the decrease in purity was smooth when the samples were placed in a desiccator (Fig. 3a), its value stabilizing at 12.8 % for material PVA and BVOH, at 12.6 % PVA+, and 12.7 for PLA, while it stabilized at 12.5 % for powder. Unlike measurements of samples stored freely in the laboratory (Fig. 3b), where the decrease in purity was significant: 10.1 % for PVA, 10 % for PVA+, 11.2 % for BVOH, 10.9 % for PLA, and only 9 % for the ferrate powder.

Fig. 4 shows the dependence of the ferrate's purity on time in different environments. Purity decrease for free ferrate powder and ferrate powder placed in a capsule from PLA and BVOH. The measurements started at the purity of 63.5 % and the decrease in purity was significant when for samples in a desiccator (Fig. 4a): 51.8 % for PLA, 51.7 % for BVOH, and only 50.7 % for free powder. The purity stabilized at 44.4 % for ferrate powder. In samples stored freely in the laboratory (Fig. 4b), the purity stabilized at 45.2 % for PLA, and at 49.9 % for BVOH.

Conclusion

Potassium ferrate was prepared electrochemically in high purity. Encapsulation was implemented using three different ways: various water-soluble or biodegradable capsules printed on a 3D printer; natural substances- zeolites, a combination of zeolites and 3D printed capsules. Ferrate (and ferrate mixture) was used in powder form and in tablet form. At the same time, the influence of different storage conditions on the ferrates degradation rate was monitored. Within 30 days of experiments, a 3D printed capsule made of BVOH and PLA had no significant effect on the degradation rate of almost 70 % pure ferrate. The decrease in purity was slight but continuous for both free and encapsulated ferrates. A positive effect on stability is evident for storage in an environment without access to air. Within 12 weeks, ferrates encapsulated in 3D printed capsules from PVA, PVA+, BVOH and PLA showed slight but continuous decrease in purity. The 12 weeks experiments with ferrate encapsulation in a 3D printed capsules from PLA and BVOH showed significant changes after only six weeks. Better results were obtained when the samples were stored in air-free environment.

Acknowledgements

This work was supported by the Ministry of Education, Science, Research and Sport of the Slovak Republic: VEGA 1/0436/23 and by the Slovak Research and Development Agency: APVV-17-0183. The authors would like to thank for financial contribution from the STU Grant scheme for Support of Young Researchers.

References

Czölderová M, Behúl M, Filip J, Zajíček P, Grabic R, Vojs-Staňová A, Gál M, Kerekeš K, Híveš J, Ryba J, Rybanská M, Brandeburová P, Mackuľak T (2018) Chem. Eng. J. 349, 269–275.

Eng YY, Sharma VK, Ray AK (2006) Chemosphere. 63, 1785–1790.

Fajnor V, Jesenák K (1989) Elektrón.

Feng M, Sharma VK (2018) Chem. Eng. J. 341, 137–145.

Han Q, Wang H, Dong W, Liu T, Yin Y, Fan H (2015) Chem. Eng. J. 262, 34–40.

Híveš J, Kerekeš K (2018) Patent 8530.

Hudec P (2015) WTS news 9–13.

Chen BY, Kuo HW, Sharma VK, Den W (2019) Scientific Reports 9, 18268.

Jiang JQ (2017) J. Hazard. Mater. 143, 617–623.

Jiang JQ, Lloyd B (2002) Water Research. 36, 397–1408.

Kubiňáková E, Gál M, Kerekeš K, Híveš J (2015) Chemické listy. 109, 714–717.

Lee Y, Cho M, Kim JY, Yoon J (2004) J. Ind. Eng. Chem. 10, 161–171.

Mácová Z, Bouzek K, Híveš J, Sharma VK, Terryn RJ, Baum JC (2009) Electrochim. Acta. 54, 2673–2683.

Mikolić-Bujanović L, Čekerevac M, Simičić M, Tomić M (2020) Journal of Materials Science. 55, 7295–7303.

Mura S, Malfatti L, Greppi G, Innocenzi P (2017) Rev. Environ. Sci. Bio/Technol. 16, 15–35.

Murmann RK, Robinson PR (1974) Water Research. 8, 543–547.

Ni BJ, Yan X, Dai X, Liu Z, Wei W, Wu SL, Xu Q, Sun J (2020) Water Research. 185, 1–11.

Thompson GW, Ockerman LT, Schreyer JM (1951) J. Am. Chem. Soc. 73, 1379.

Wang HL, Liu SQ, Zhang XY (2009) J. Hazard. Mater. 169, 448–453.

Yuan BL, Ye MR, Lan HC (2008) American Chemical Society, 378–388.

sciendo

Utilization of *Opuntia* as an alternative ingredient in value added bread and pasta products

Tatiana Holkovičová, Zlatica Kohajdová,
Michaela Lauková, Lucia Minarovičová

Department of Food Technology, Institute of Food Science and Nutrition,
Faculty of Chemical and Food Technology, Slovak University of Technology,
Radlinského 9, 812 37 Bratislava, Slovak Republic
tatiana.holkovicova@stuba.sk, zlatica.kohajdova@stuba.sk

Abstract: Natural sources and healthy cereal-based food have recently received a lot of attention by both professionals and the common population for improving overall well-being. In this case, *Opuntia* cactus and *Opuntia* derivates show high potential in the production of health-promoting cereal-based products.
This study comprehensively reviews nutritional composition, health benefits of *Opuntia* spp. and its utilisation in the production of bread and pasta products. Moreover, the effect of this ingredient on the rheological properties of wheat dough and physical parameters as well as sensory properties of incorporated products is also discussed.

Keywords: bread, dough rheology, nopal, *Opuntia*, pasta, sensory attributes

Introduction

Due to increasing awareness and interest in health and various beneficial diets, the demand for value-added food continues to rise. Cereals and bakery products have the main importance in human nutrition, they are widely available and represent the main food source for humans. Bakery products are considered suitable medium for nutrients, particularly dietary fibre. Consequently, the bakery industry is one of the fastest growing food industries in the world (Biljwan et al., 2019; Codină, 2022).

Incorporation of bakery products with plant materials offers opportunities to include beneficial components into the human diet. The positive effects of plant sources can be obtained from active components found in the entire plant, parts of the plant or plant materials, whether in the crude or processed state. Nowadays, there is increasing interest in *Opuntia* cactus, fruits, and cladodes, because of their high content of valuable bioactive compounds. Numerous studies have been focused on this topic (Das et al., 2012; Msaddak et al., 2017; Andreu et al., 2018; Rocchetti et al., 2018; Berrabah et al., 2019; Baniwal et al., 2021; Dubeux et al., 2021; Sciacca et al., 2021).

The genus *Opuntia* spp. includes more than 300 species of cacti. *Opuntia* is a tropical to subtropical plant belonging to the *Cactaceae* family, which originates in America. However, due to its high adaptability to different climatic conditions (drought, high temperatures, UV radiation), its production has expanded to Europe and Africa (Oniszczuk et al., 2020; Taşkin and Aksoylu, 2021). This genus appears to have its centre of genetic diversity in Mexico where it originates from and is still extensively produced. The other largest producers and suppliers of *Opuntia* spp. include Mediterranean countries, India, the USA, and South Africa (Taşkin and Aksoylu, 2021). Currently, Mexico and Italy are the main producer countries, accounting for approximately 70 % and 3.3 % of the global production on approximately 590 000 ha, respectively (Silva et al., 2021). Moreover, Mexico has the widest variation comprising at least 126 species with various degree of domestication (Wit and Fouché, 2021). It is confirmed that due to domestication, *Opuntia* spp. has improved in shape, colour, flavour, texture, and mucilage quality and quantity (Díaz et al., 2017; López-Palacios et al., 2019).

Morphologically, the plant consists of root, vegetable part (cladodes or stems), fruit (peel, pulp, seeds), and flower. The fruit is also known as “cactus pear” or “prickly pear” in different growing areas (Stintzing and Carle, 2005; Amani et al., 2019). While the cactus is primarily produced for its edible fruit, several parts of the cactus (mainly seeds, cladodes, and flowers) are utilised in the food and cosmetic industry (Osuna-Martínez et al., 2014; Abbas et al., 2022).

Opuntia species globally produced include *Opuntia ficus-indica, Opuntia robusta, Opuntia streptocantha, Opuntia amyclaea, Opuntia megacantha, Opuntia hyptiacantha, Opuntia rastera, Opuntia engelmannii, Opuntia phaecantha, Opuntia dillenii cactus* and *Opuntia lindheimeri* (Yahia and Sáenz, 2011). It was found that these species are a good source of natural bioactive compounds such as dietary fibre, polysaccharides, vitamins (A, B1, B2, and C), antioxidants (phenolic compounds), and minerals (mainly Mg, Ca, K, Mn, and Fe). Many of these compounds have beneficial hypoglycemic, anti-inflammatory, and antimicrobial effects. Due to the potential health benefits of *Opuntia*, current studies are focused on incorporating different parts of this plant into various foods, including baked goods (Das et al., 2021; Silva et al., 2021; Taşkın and Aksoylu, 2021; Abbas et al., 2022).

Currently, *Opuntia ficus-indica* is the most promoted and domesticated species worldwide for commercial production (Barba et al., 2017; Mazri, 2021). *Opuntia ficus-indica* is assumed to be a spineless species obtained from *Opuntia megacantha*, a native species from Mexico (Díaz et al., 2017; Mounir et al., 2020).

Chemical composition

The content of bioactive compounds, chemical composition, and the nutraceutical potential of *Opuntia* spp. depend on many factors, including production practices, region, climatic conditions, plant age, and maturation stage (Amaya-Cruz et al., 2019; Al Juhaimi et al., 2020; Pessoa et al., 2020; Taşkın and Aksoylu, 2021). Tab. 1 provides the chemical composition of different parts of the commonly grown species *Opuntia ficus-indica* (Cota-Sánchez, 2016; El-Beltagi et al., 2019; Mounir et al., 2020; Silva et al., 2021).

Cladodes

Opuntia cladodes represent the green stems of the plant (Ginestra et al., 2009; Magarelli et al., 2022). Proximate composition of cladodes from different *Opuntia* spp. has been evaluated by various authors, and the values are always variable (Astello-García et al., 2015; Díaz et al., 2017; Dubeux et al., 2021; Perucini-Avendaño et al., 2021; Hernández-Becerra et al., 2022). These variations can be attributed to different environmental conditions at the production site, as well as structural differences between individual species (Angulo-Bejarano et al., 2014). Tab. 2 shows the chemical composition of cladodes from selected wild and domesticated *Opuntia* species (Astello-García et al., 2015; Díaz et al., 2017).

According to Diaz et al. (2017), De Santiago et al. (2018), and Rocchetti et al. (2018) water is the primary component of *Opuntia ficus-indica* cladodes (80—95 %), followed by carbohydrates (3—7 %), fibre (1—3 %), and proteins (0.5—1 %) (Diaz et al., 2017).

Studies by Figueroa-Pérez et al. (2018) and Perucini-Avendaño et al. (2021) have revealed that certain wild *Opuntia* species have higher protein content compared to most domesticated species. For example, *Opuntia robusta* can reach protein values in the range from 17.40 % to 19 %. Higher protein content has also been reported in young cladodes. Significant differences in the composition between young and mature cladodes was also discovered in the content of amino acids. In young cladodes, various amino acids like alanine, isoleucine, and asparagine were found, whereas mature cladodes have shown only threonine content (Díaz et al., 2017; Figueroa-Pérez et al., 2018; Perucini-Avendaño et al., 2021).

Carbohydrates present in cactus cladodes can be divided into two types, structural carbohydrates, and storage carbohydrates. Structural polysaccharides are mainly cellulose (21.6 %), hemicellulose (8.19 %), and lignin (36 %). They are part of the cladodes cell wall and contribute to dietary fibre. The main constituents of storage carbohydrates are monosaccharides (glucose, galactose, arabinose, rhamnose, fructose), galacturonic, and glucuronic acid (López-Palacios et al., 2016; Perucini-Avendaño et al., 2021). Carbohydrates also include mucilaginous components that contain polymers, such as chains of (1-4)-linked β-D-galacturonic acid and R(1-2)-linked L-rhamnose residues (Ginestra et al., 2009; Perucini-Avendaño et al., 2021).

Tab. 1. Nutritional composition (g/100 g) of *Opuntia ficus-indica* different parts (Cota-Sánchez, 2016; El-Beltagi et al., 2019; Elshehy et al., 2020; Mounir et al., 2020; Silva et al., 2021).

	***Opuntia ficus-indica* part**			
Component	**Pulp**	**Seed**	**Peel**	**Cladode**
Water	84—94.40	18	90.30	87.01—94
Ash	0.24—4.03	10.37	0.29	1.08—2.97
Protein	0.08—1.60	3.67	0.14	0.30—1.39
Lipids	0.04—0.97	3.00—16.30	0.04—2.43	0.11—1.83
Total fibre	0.02—5.37	54.20^{DM}	0.65	2.70—4.14
Carbohydrates	92.50	–	–	5.63—8.52
Starch	4.55^{DM}	5.35^{DM}	7.12^{DM}	0.71^{DM}

DM — dry matter

Tab. 3 lists the mineral composition of *Opuntia* spp. cladodes (Jun et al., 2013; Astello-García et al., 2015; Díaz et al., 2017). Several studies have shown that, in general, K and Ca are present in higher concentration compared to other minerals (Jun et al., 2013; Astello-García et al., 2015; Díaz et al., 2017; Dubeux et al., 2021). Cladodes of some species (*Opuntia humifusa*) are characterised by even higher Ca content than cow milk (113–122 mg/100 g), some fruits, vegetables, and nuts. Examples include spinach (1151 mg/100 g), lettuce (703 mg/100 g), cabbage (511 mg/100 g), and broccoli (43 mg/100 g) (Ceballos et al., 2009; Astello-García et al., 2015; Kapadiya et al., 2016; Díaz et al., 2017; Lambrini et al., 2021).

Cactus cladodes contain significant amounts of organic acids such as malic acid, citric acid, and succinic acid (Figueroa-Pérez et al., 2018; Wit and Fouché, 2021). Andreu et al. (2018) identified malic acid as the prevailing organic acid in cladodes (71.8 g/L).

Cladodes are characterised by low fat content (Elshehy et al., 2020). Rocchetti et al. (2018) and El-Safy (2013) documented that the amount of fat in *Opuntia ficus-indica* cladodes varies from 0.11 to 0.87 %. The most abundant fatty acids in cladodes are linoleic acid (C18:2) (25.84–53.77 %), palmitic acid (C16:0) (15.02–26.54 %), and oleic acid (C18:1c9) (8.52–36.30 %). Previously, it was found that the content of linoleic acid in cladodes is similar to that in argan oil (29–41 %), but lower than that determined in soybean (53.3 %) and barley (51.2 %) (Abidi et al., 2009; El-Mostafa et al., 2014; Andreu-Coll et al., 2019; Gharby et al., 2021; Wit and Fouché, 2021).

Total phenolic content of *Opuntia* spp. varies and correlates with the domestication gradient of individual species (Díaz et al., 2017). The wild species *Opuntia streptacantha* show the highest concentration of phenolic compounds (Astello-García et al., 2015). The most frequently occurring phenolic compounds in *Opuntia* spp. (domesticated as well as wild species) include quercetin (90.5 µg/g), kaempferol (12.9–45.6 µg/g), and isorhamnetin (58.9–326.9 µg/g) (Díaz et al., 2017).

Fruits

Opuntia fruit consists of a juicy pulp (28–58 % of the fruit mass) with seeds (2–10 %), encompassed by a thick peel (37–67 %) (Mona and Nesreen, 2011; Barba et al., 2017). *Opuntia* fruits contain a large amount of water, approximately 84–93 % of the fresh mass. Monosaccharides, as well as dietary

Tab. 2. Chemical composition of wild and domesticated species of *Opuntia* spp. cladodes (Astello-García et al., 2015; Díaz et al., 2017).

Species	**Composition (g/100 g)**				**Phenolic acids (mmol GA/g)**	**Flavonoids (mmol quercetin/g)**
	Proteins	**Fat**	**Crude Fibre**	**Ash**		
Opuntia streptacantha	11.20	0.73	7.30	12.60	56.80	18
Opuntia hyptiacantha	11	0.80	6.50	15.10	33.40	17.10
Opuntia megacantha	10.70	0.69	6.50	13.60	44.70	16.80
Opuntia albicarpa	11.60	0.75	6.50	13.20	40.80	17.20
Opuntia ficus-indica	11.20	0.69	5.90	14.40	40.10	19.40
Opuntia humifusa	4.70	1.25	50.30	2	–	–

GA – gallic acid

Tab. 3. Mineral composition of wild and domesticated species of *Opuntia* spp. cladodes (Jun et al., 2013; Astello-García et al., 2015; Díaz et al., 2017).

Species	**Minerals (mg/100 g of sample)**					
	K	**Ca**	**Na**	**P**	**Fe**	**Mn**
Opuntia streptacantha	2213	667	70	0.09	2.90	16.50
Opuntia hyptiacantha	2690	740	87	0.09	3.90	9.80
Opuntia megacantha	1960	683	137	0.08	5.10	13.30
Opuntia albicarpa	1956	647	77	0.09	0.70	24.10
Opuntia ficus-indica	2403	627	63	0.09	8.60	13.80
Opuntia humifusa	1269	1968	–	1110	–	1411

fibre (about 50 % of dry matter in total) are the main components of dry matter. Proteins accounting for about 8.30 % of dry matter and lipid content are negligible (0.09–0.7 %) (Feugang et al., 2006; De Wit et al., 2010).

In general, the fruit pulp shows lower protein and dietary fibre content than seeds and peel. The highest amounts of dietary fibre, protein and lipids were found in seeds (54.2 %, 11.8 % and 6.77 %, respectively) (Silva et al., 2021).

Minerals, sugars, and organic acids

Opuntia fruit pulp is considered a good source of minerals, especially Ca (12.8–59 mg/100 g), K (90–220 mg/100 g), and Mg (16.1–98.4 mg/100 g). Seeds are rich in minerals (Mg, P, K, Zn, Cu) and sulphur amino acids (Feugang et al., 2006; Özcan et al., 2011; Jana, 2012). Relatively high total sugar content (12–17 %) and low acidity render sweet but sometimes bland taste to the fruit. Sugar composition in the fruit pulp is very simple, consisting of glucose and fructose in virtually equal amounts, while the organic acid pattern is dominated by citric acid ranging from 1.60 to 3.20 g/L in peel and pulp (Feugang et al., 2006; De Wit et al., 2010; García et al., 2020).

Vitamins, carotenes, and amino acids

Vitamins are nutritionally important constituents of the *Opuntia* fruit. Beta-carotene and fat-soluble vitamin E – tocopherols were found in the lipid fraction of both cactus fruit pulp and seeds. Vitamin E homologues isoforms gamma-tocopherol (3.3 g/100 g) and delta-tocopherol (0.05 g/100 g) are the main components of the pulp and seed oils, respectively, representing approximately 80 % of the total vitamin E content (Jana, 2012; Berrabah et al., 2019; Oniszczuk et al., 2020). Eventually, only trace amounts of ascorbic acid, vitamin B6, vitamin B1, niacin, riboflavin, and pantothenic acid have been found in fruit pulp (Feugang et al., 2006; Medina et al., 2007; Berrabah et al., 2019; Oniszczuk et al., 2020). Several authors found that *Opuntia* contains a substantial number of amino acids, especially two predominant amino acids: proline (1265.2 mg/L) and taurine (434.3 mg/L), followed by serine (174.5 mg/L) (Feugang et al., 2006; Slimen et al., 2016; Berrabah et al., 2019; Oniszczuk et al., 2020).

Lipids

Fruit pulp contains lower amounts of oil (0.1–1.0 %), representing approximately 8.70 g of total lipid content per 1 kg of pulp dry weight compared to 98.8 g of total lipid content per 1 kg of seeds (Feugang et al., 2006). The major representative of fatty acids is linoleic acid with a content range from 20.19–53.85 %. Other abundant compounds are oleic and palmitic acids (Andreu-Coll et al., 2019).

The peel fraction contains 36.8 g of lipids per 1 kg (Feugang et al., 2006). In this case, the major fatty acids are linoleic acid ranging from 39.58–52.02 %, followed by oleic (6.83–30.99 %) and palmitic (21.53–32.06 %) acids. The next most common compounds are linoleic acid (18.70–21.88 %) and stearic acid (1.74–3.76 %) (Feugang et al., 2006; Andreu-Coll et al., 2019).

Phenolic compounds

High antioxidant activity of *Opuntia* fruit pulp and peel is attributed to its content of polyphenols and betalains. Betalains present in the epidermis give the *Opuntia* fruit a colour ranging from yellow to purple (betaxanthins: orange and yellow and betacyanins: blue and red). These pigments are derivates of betalamic acid (Khatabi et al., 2016; Ciriminna et al., 2019; Oniszczuk et al., 2020). Oniszczuk et al. (2020) reported high free radical scavenging potential of DPPḤ (99.7 %) and total phenolic content of 14.9 mg GAE/g dry weight in *Opuntia* fruits. Fruit is considered a good source of flavonols, of which quercetine (58.7 %) was detected as predominant, followed by isorhamnetin (31.7 %), luteolin (11.5 %), and kaempferol (11 %) (Barba et al., 2017). Furthermore, *Opuntia* fruits are also a rich source of free phenolic acids (57.96 µg/g of dry matter), especially benzoic and cinnamic acid derivatives (Ramírez-Moreno et al., 2017; Oniszczuk et al., 2020; Taşkın and Aksoylu, 2021).

Health benefits

Despite the enormous amount of synthetic substances used today, there is a growing trend to use natural compounds to prevent and manage chronic diseases. In addition, their promising effects are supported by scientific studies and evidence as possible therapeutics under certain conditions (Hashem et al., 2020; Abd-Elhakim and Al-Sagheer, 2021).

Opuntia spp. has been used for centuries in traditional medicine due to their beneficial health properties in chronic diseases, particularly obesity, diabetes, cardiovascular diseases, and cancer (Aragona et al., 2018; Abd-Elhakim and Al-Sagheer, 2021). Recent scientific studies, both *in vitro* and *in vivo,* have demonstrated the pharmacological potential of *Opuntia* spp., indicating the need for further research (El-Mostafa et al., 2014; Madrigal-Santillán et al., 2022). Several authors described different parts of *Opuntia ficus-indica* (cladodes, fruit pulp, peel, and seeds) and their extracts have been characterised by various favourable biological activities (Abd-Elhakim and Al-Sagheer, 2021); in particular, its cholesterol-lowering, anti-ulcer, anti-inflammatory, cardioprotective, antidiabetic, neuroprotective, hepatoprotective, and wound healing effect (Milán-Noris et al., 2016; Aruwa et al., 2018; Abbas et al., 2022).

The antihyperglycemic effect of *Opuntia* spp. is related to its high fibre content (Díaz et al., 2017; Gouws et al., 2019b; Rbia and Smiti, 2019; Kashif et al., 2022). Deldicque et al. (2013) and Aragona et al. (2018) reported that oral intake of *Opuntia ficus-indica* (cladodes, flower extracts) contributes to insulin release in serum, so the extract can reduce blood glucose. Aragona et al. (2018) and Gouws et al. (2019b) documented that *Opuntia* fibre can slow the rate of intestinal absorption of glucose.

Recently, *Opuntia* spp. has been confirmed to play an important role in the prevention of cardiovascular diseases (Osuna-Martínez et al., 2014; Daniloski et al., 2022; Madrigal-Santillán et al., 2022). Antiatherogenic properties of cacti can be attributed to its high content of substances with antioxidant potential. *Opuntia* species contain mostly flavonoids, with significant amounts of quercetin followed by isorhamnetin, luteolin, and kaempferol, which can decrease lipid peroxidation and help prevent or slow down the development of atherosclerosis (Osuna-Martínez et al., 2014; Díaz et al., 2017). Although antioxidants are able to block lipid peroxidation, their lipid lowering properties are not completely clarified (Abd-Elhakim and Al-Sagheer, 2021).

According to the World Health Organization, cancer is classified as the second main cause of death. The fruit of *Opuntia* spp. is indicated as a promising natural source of functional substances for the development of novel chemotherapeutic agents. The anticancer activity of fruits is mostly connected to bioactive polysaccharides composed of rhamnose, arabinose, and glucose, which induce cell apoptosis or cell cycle arrest in different types of cancer cells (Abdulazeem et al., 2018; El-Beltagi et al., 2019; Dalila et al., 2021).

Abdulazeem et al. (2018) showed the cytotoxic effects of different parts of *Opuntia* on cancerous cell lines. *In vitro* tests have show that the *Opuntia* fruit extract inhibits the proliferation of ovarian, cervical, and bladder cancer cell lines (Abdulazeem et al., 2018; Dalila et al., 2021; Madrigal-Santillán et al., 2022). Based on the previously described reports, it can be summarised that the *Opuntia* plant represents a safe and promising available alternative drug, which could lead to new research in cancer therapy (Abou-Elella and Ali, 2014; Dalila et al., 2021; Madrigal-Santillán et al., 2022).

On the other hand, a few cases reporting allergic contact dermatitis with *Opuntia* fruit have also been published (Yoon et al., 2004; García-Menaya et al., 2009). The small glochids (hair-like or short prickles) from this crop cause dermatological problems by physical penetration into the skin (Otang et al., 2014). Patients developed an erythematous plaque with exudation followed by itching. The skin lesions improved after application of topical and systemic corticosteroids (Yoon et al., 2004; García-Menaya et al., 2009; Otang et al., 2014).

Opuntia as a potential ingredient of cereal based products

Several parts of *Opuntia* spp., such as seeds, stems, pear pulp, peel, and mucilage are potential ingredients in breadmaking or in other cereal products. These raw materials are usually applied in powdered form (Gül, 2021).

During processing, plant material collected from plantations is washed with distilled water and disinfected in order to eliminate microorganisms (Contreras-Padilla et al., 2016; Di Bella et al., 2022).

After than, fruits are cleaned with a brush to remove prickles and dirty particles. Peels are manually removed by a knife and cut into slices, seeds are separated from the pulp by sieving and processed individually (El-Shahat et al., 2019; Abou-Zaid et al., 2022).

Vegetative parts, i.e., cladodes are cleaned and cut longitudinally or into cubes (Moreno-Álvarez et al., 2009; Msaddak et al., 2017).

In the next step, individual parts of pre-treated *Opuncia* plant (cladodes, fruit peel, and seed) are processed by drying using various drying methods: sun drying (Nharingo and Moyo, 2016; Rebah and Siddeeg, 2017; Reda and Atsbha, 2019; Albergamo et al., 2022), convection drying (45—60°C) (Touil et al., 2014; Cruz-Rubio et al., 2020; Di Bella et al., 2022) or freeze-drying (–18°C) (Gouws et al., 2019a; Romero et al., 2021) until the required moisture content is reached (4—8 %) (Cruz-Rubio et al., 2020).

Seeds obtained from the fruit pulp can be roasted after drying. This procedure improves sensory acceptance of seed products (Ali et al., 2020; Gül, 2021).

Special by-product derived from *Opuntia* spp. is cactus mucilage. It is a slimy polysaccharide substance that appears right after cutting or crushing the cladode cuticle (Hussain et al., 2022a). Mucilage is a promising hydrocolloid because of its ability to retain large amounts of water and create gels (Rodríguez-González et al., 2014; Sepúlveda et al., 2007). Preparation of mucilage extract includes

Fig. 1. Flow chart of processing different parts of *Opuntia ficus-indica* into cladodes, seeds and mucilage powders (Contreras-Padilla et al., 2016; Dick et al., 2019; Reda and Atsbha, 2019; Ali et al., 2020; Dick et al., 2020; Nabil et al., 2020; Chaloulos et al., 2021; Sciacca et al., 2021).

several steps; first, cladodes are crushed to obtain pulp that is homogenised, heated, precipitated, and filtered to get the mucilage extract. The prepared product can be processed by drying to obtain mucilage powder (Dick et al., 2019; Dick et al., 2020).

Dried material from various parts of *Opuntia* plant is usually ground and sieved to obtain the powder (Ali et al., 2020; Gül, 2021). Powder particle sizes vary from 80 to 500 µm (Moreno-Álvarez et al., 2009; Chahdoura et al., 2018; Rayan et al., 2018; Anchondo-Trejo et al., 2020; Arias-Rico et al., 2020; Parafati et al., 2020).

Previously it was stated that the drying method significantly affects the composition of final powders. The most preferred method of drying in commercial production of *Opuntia* powder is convention drying. This is the most economical method, especially if it is done using a solar drier, which is optimally suited to the dry and hot regions where *Opuntia* spp. is produced. However, a big disadvantage of this method is thermal degradation of bioactive compounds and the subsequent change in the quality profile of the plant material (Ali et al., 2020; Barba et al., 2020; Cruz-Rubio et al., 2020). According to Ali et al. (2020), temperature used during drying should not reach 60 °C. The mucilage quality is the most affected by temperature as mucilage proteins and polysaccharides undergo partial denaturation at high temperatures (León-Martínez et al., 2011; Barba et al., 2020; Cruz-Rubio et al., 2020).

Opuntia ficus-indica commonly known as nopal cactus, is the most widespread and commercially important cactus used in powder form; also, most published studies focus on this species (Dick et al., 2019; Reda and Atsbha, 2019; Dick et al., 2020; Gül, 2021). A detailed diagram of the individual parts of nopal cactus processing into powdered form is shown in Fig. 1. (Contreras-Padilla et al., 2016; Dick et al., 2019; Reda and Atsbha, 2019; Ali et al., 2020; Dick et al., 2020; Nabil et al., 2020; Chaloulos et al., 2021; Sciacca et al., 2021).

Incorporation of *Opuntia* into cereal-based food products

Recently, attempts to incorporate *Opuntia* spp. into various cereal-based foods, predominantly bread, pasta, cakes, and gluten-free products have been made to improve their nutritional quality. Most published studies focus on the production of bakery products by partially substituting wheat flour with *Opuntia* powders (Guevara-Arauza et al., 2015; Anwar and Sallam, 2016; Mata et al., 2016; Jotangiya and Samani, 2017; Rayan et al., 2018; Liguori et al., 2020; Gül, 2021). The significant number of potentially active nutrients (dietary fibre, proteins, phenolic compounds) and their multifunctional (hydration, textural, stabilising and hydrocolloid) properties make edible parts of *Opuntia* spp. great candidates for the production of health-promoting cereal-based foods with reduced energy and carbohydrate levels (Jana, 2012; Msaddak et al., 2017; Ali et al., 2020).

Bread

Bread, commonly consumed food worldwide, is usually prepared by mixing simple ingredients such as wheat flour, water, salt, and yeast. It is characterised by low antioxidant potential and therefore enrichment with bioactive compounds could increase its nutritional quality (Dziki et al., 2014; Msaddak et al., 2017). The addition of *Opuntia* spp. derivatives could produce bread containing higher proportions of protein, fibre, and phenolic compounds, as well as increase oxidative stability of bread (Ali et al., 2020; Gül, 2021).

Several studies have reported that many parts of *Opuntia* spp. such as cactus peel fruits, cladodes, seeds and fresh mucilage have great potential to be used in breadmaking (Anwar and Sallam, 2016; Ali et al., 2020; Gül, 2021; Sciacca et al., 2021). However, cladodes are the most common parts of the cactus that are used in the production of bread (Moreno-Álvarez et al., 2009; De Wit et al., 2015; Msaddak et al., 2017; Gül, 2021; Sciacca et al., 2021).

Rheological parameters of dough

Rheological behaviour of dough is very important because it has significant effect on baking characteristics, mechanical properties of the dough and quality of final products (Mirsaeedghazi et al., 2008; Culetu et al., 2021).

Farinograph water absorption (WA) represents the amount of water required to produce a dough of optimum consistency depending on the content of wheat gluten in the flour (Linlaud et al., 2009; Hussin et al., 2022). It is well known that the addition of non-protein components modifies WA of flour (Wang et al., 2016; Hussin et al., 2022).

Moreno-Álvarez et al. (2009) and Sciacca et al. (2021) have concluded that incorporation of cladode powder to wheat or durum wheat flour at different levels (5–20 %) significantly increased WA. This can be explained by higher water holding capacity of cladode powder attributed to the presence of a large amount of dietary fibre (Msaddak et al., 2015; Taşkın and Aksoylu, 2021). Similar results have also been reported for flour mixtures based on plant materials with high fibre content, such as pumpkin, carrot, hemp (Moreno-Álvarez et al., 2006; Turksoy and Özkaya, 2011; Shahzad, 2012).

In the fibre structure, hydroxyl groups which absorb a significant quantity of water by hydrogen bonding are present (Moreno-Álvarez et al., 2009; Gül, 2021).

During dough mixing, water hydrates flour components and dough is developed (Lauková et al., 2016). Dough development time (DDT) is the time required for the dough to reach its optimal consistency during mixing (Hussain et al., 2022a). Several researchers have documented that the increase in the level (3—15 %) of cladode powder in dough resulted in prolongation of DDT (Sciacca et al., 2021; Hussain et al., 2022a, 2022b). Elhassaneen et al. (2022) suggested that this effect can be caused by the formation of a gluten-fibre complex inhibiting the protein hydration and gluten structure development.

The addition of *Opuntia* cladodes to wheat dough also influences dough stability (DS) (indication of dough strength) and elasticity (ability to bounce back once dough is stretched) (Nassar et al., 2008; Ayadi et al., 2009; Patel and Chakrabarti-Bell, 2013; Sciacca et al., 2021). De Wit et al. (2015) and Moreno-Álvarez et al. (2009) documented that inclusion of 5—20 % of cladode powder into wheat dough decreased DS. This effect is attributed to the higher dietary fibre content; wheat–cladode mixtures produce weak flour (Moreno-Álvarez et al., 2009; Gül, 2021).

The effect of *Opuntia* addition on rheological properties of dough can also be analysed by the alveographic test (Msaddak et al., 2017; Mironeasa and Mironeasa, 2019; Sciacca et al., 2021). Glutenin and gliadin, two components that make up gluten, give the dough toughness and extensibility (Sciacca et al., 2021). The alveographic parameter P (tenacity) indicates the maximum overpressure required to blow a dough bubble (Codină et al., 2019). This parameter is connected with the gluten quantity and quality and also its ability to absorb water (Msaddak et al., 2017). According to Ayadi et al. (2009) and Sciacca et al. (2021), P parameter increases with the increasing addition of cladodes powder (10—20 %), which is probably due to poor gluten hydration. The L index (dough extensibility) indicates the ability of gluten to hold gas (Msaddak et al., 2017). Several studies have concluded that the L value decreases with partial substitution (from 5 % to 20 %) of wheat flour or durum wheat semolina with cladode powder (Ayadi et al., 2009; Msaddak et al., 2017; Mironeasa and Mironeasa, 2019; Bouazizi et al., 2020). Thus, the action of the cladode powder on both these parameters (P and L) leads to the P/L configuration ratio (dough balance between tenacity and extensibility) increase with the increasing amount of cladode powder (Ayadi et al., 2009; Bouazizi et al., 2020). Similar results were described by Borchani et al. (2011) and Bchir et al. (2014) in alveographic parameters of dough incorporated with different levels of apple, pear, and date flesh fibre concentrate. These findings can be attributed to the high water-holding capacity of cladode powder (Msaddak et al., 2017). The deformation energy (W), the index of dough strength, increased with the increasing addition of cladode powder (5—20 %) (Ayadi et al., 2009; Msaddak et al., 2017; Bouazizi et al., 2020), probably due to the high fibre content in cladodes. The fibre structure contains a large number of hydroxyl groups, which enable more interactions with water through hydrogen bonding (Ayadi et al., 2009; Sciacca et al., 2021).

Physical parameters of enriched bread

Several studies have shown that incorporation of *Opuntia* to bread significantly affects its physical characteristics such as volume, specific volume, hardness, and colour (De Wit et al., 2015; Ali et al., 2020; Gül, 2021; Sciacca et al., 2021; Hussain et al., 2022a).

The volume of bread is a result of the gas-holding capacity of the dough, which is created during fermentation (Hussain et al., 2022a). It was determined that the incorporation of 4—10 % of *Opuntia* seed powder reduces the volume and specific volume of bread (Ali et al., 2020). A similar trend was also observed when up to 17 % of cladode powder were added to wheat bread (De Wit et al., 2015). This effect is attributed to the interactions between insoluble fibre and gluten, which leads to a decrease in the gas-holding capacity (Gómez et al., 2003; Msaddak et al., 2017).

Bread hardness describes the resistance of bread to pressure (Budžaki et al., 2014). The replacement of wheat flour with cladode powder can cause an increase in bread hardness with the increasing concentration of the substitute (2—17 %) (Ayadi et al., 2009; De Wit et al., 2015; Sciacca et al., 2021). The fibre in *Opuntia* powder can interfere with gluten network which leads to weaker gluten structure and more crumbly and brittle bread texture, which contributes to increased bread hardness (De Wit et al., 2015; Gül, 2021).

Golden brown crust and creamy white bread crumb are the most important appealing factors to indicate the quality of a bakery product to consumers (Kurek and Wyrwisz, 2015). The incorporation of *Opuntia* cladode powder into the bread affects the colour parameters L*, a*, and b* of bread, whereas L* represents the lightness of bread, a* represents the red-green spectrum, and b* represents the yellow-blue spectrum (Brühl

Tab. 4. The impact of *Opuntia* addition on the sensory characteristics of bread (Álvarez et al., 2009; De Wit et al., 2015; Msaddak et al., 2017; Reda and Atsbha; 2019; Ali et al., 2020; Liguori et al., 2020).

Part of Cactus	*Opuntia* spp.	Substitution levels/%	Effect on final product	References
Roasted seed powder (RPPS)	*Opuntia ficus-indica*	0/2/4/6/8/10	Sensory properties were not sufficiently affected at substitution levels up to 6 %. Higher substitution levels: ↓ colour scores because of darker colour of RPPS powder due to the presence of natural pigments (carotenoids, flavonoids, and chlorophyll) ↓ texture score due to high amount of dietary fibres.	De Wit et al. (2019) Ali et al. (2020)
Seed powder	*Opuntia ficus-indica*	0/5/10/15/20/25	Substitution of *Opuntia* seeds up to 15 % showed no negative effect on sensory acceptability. ↑ aroma scores for all samples probably caused by the presence of volatile organic matter (hexanal and 2-methylpropanal) from *Opuntia* seeds.	Reda and Atsbha (2019) Nounah et al. (2020)
Stem powder (cladodes)	*Opuntia boldinghii Britton et Rose*	0/5/10/15/20	Wheat flour substitution up to the 10 % level without negative effect on sensory acceptability. Higher substitution levels: ↓ colour score due to the presence of chlorophyl pigments ↓ odour score caused by herbaceous flavour of terpenes present in cladode powder ↓ texture scores caused by cladode polysaccharides interaction with wheat flour proteins.	Moreno-Álvarez et al. (2009) Feng et al. (2011) Abd El-Moaty et al. (2020) Dick et al. (2020)
Cladode mucilage extract	*Opuntia ficus-indica*	Formula water replaced by mucilage	↑ scores in colour of the crust and odour intensity in contrast with control wheat sample probably due to interactions between antioxidant compounds and mucilage carbohydrates.	Liguori et al. (2020) Czajkowska-González et al. (2021)
Cladode powder	*Opuntia ficus-indica and Opuntia robusta*	0/2/4/6/8/10/17	Substitution of up to 8 % showed no negative effect on overall acceptability. Higher substitution levels: ↓ odour score due to the presence of betalain pigments, which in high concentration have typical earthy flavour.	De Wit et al. (2015) Awolu and Oladeji (2021)
Cladodes powder	*Opuntia ficus-indica*	0/2,5/5/7,5/10	Substitution of wheat flour up to the 5 % level without negative effect on sensory acceptability. Higher substitution levels: ↓ colour score as the powder is a rich source of chlorophyll ↓ textural hardness score induced by high fibre content, which weakens the gluten structure.	Msaddak et al. (2017)

and Unbehend, 2021). It has been observed that bread fortified with cladodes powder is darker than wheat bread. Bread with cladode powder is characterised with lower L* values of the crust and crumb than wheat bread. Additionally, the a* and b* values for both the crust and crumb of the enriched bread also decreased as the substitution level increased, indicating a shift from the initial yellowish colour to a greenish one (Gül, 2021; Sciacca et al., 2021). This can be attributed to the high concentration of chlorophyll and other pigments present in the cladodes powder (Msaddak et al., 2017). According to Gül (2021), these changes can also be linked with the presence of different dietary fibre fractions of *Opuntia ficus-indica*, which have different effects on the crust colour of bread. Darker crust and green colour of crumb is caused by nopal insoluble fibre fractions. With the addition of soluble fibre, no significant changes in either crust or crumb colour were observed (Guevara-Arauza et al., 2015). However, according to Liguori et al. (2020), the addition of *Opuntia ficus-indica* mucilage does not cause any changes in L* and a* values.

Sensory evaluation

Sensory evaluation is an important part of bread quality assessment, which leads to the development of new cereal based products (Elia, 2011). The impact of *Opuntia* addition on the sensory characteristics of bread is presented in Tab. 4. (Moreno-Álvarez et al., 2009; De Wit et al., 2015; Msaddak et al., 2017; Reda and Atsbha; 2019; Liguori et al., 2020; Ali et al., 2020). Incorporation of cladodes powder into bread was reported to influence consumer preferences. Thus, higher concentration of the incorporated cladodes powder decreased the trend in average scores for sensory attributes.

No significant differences were found with the incorporation of up to 3 % of cladode powder into wheat bread. Several studies concluded that bread fortified with 5 % and 10 % *Opuntia* cladode powder is best accepted in sensory evaluation (Moreno-Álvarez et al., 2009; Msaddak et al., 2017; Liguori et al., 2020; Gül, 2021). According to studies of Lassoued et al. (2008) and Msaddak et al. (2017), it can be assumed that the formulation with 5—15 % of cladode powder shows the highest values of colour, taste, and aroma in comparison with higher additions of cladode powder, whereas the formulation with 5 % cladode powder was most accepted in terms of texture. Higher addition levels (above 20 %) were unacceptable because of textural hardness of the final bread (Lassoued et al., 2008; Msaddak et al., 2017; Gül, 2021). The observed changes in bread texture can be caused by either dilution of gluten proteins or interactions between polysaccharides from the cladodes and wheat flour proteins. The presence of fibrous materials in the cladode flour may also have contributed to this change in texture properties by affecting the mixing properties of gluten (Ayadi et al. 2009; De Wit, 2015).

Pasta

Current strategy of the food industry is to incorporate fibre into conventional food formulations to improve their functional properties (Micale et al., 2017). Pasta is a globally consumed food and many studies are focused on innovation of wheat pasta using different sources of dietary fibre (Krishnan et al., 2012; Padalino et al., 2017; Madenci et al., 2018; Makhlouf et al., 2019; Oniszczuk et al., 2020).

In order to develop new functional pasta, several studies have focused on incorporation of *Opuntia ficus-indica* powder into wheat pasta (Micale et al., 2017, 2018; Attanzio et al., 2019; Oniszczuk et al., 2020; Palmieri et al., 2021). Cladodes and fruits are two parts of *Opuntia ficus-indica* used to enrich pasta (Micale et al., 2017, 2018; Attanzio et al., 2019; Oniszczuk et al., 2020; Palmieri et al., 2021). The addition of *Opuntia* powder to pasta can increase not only the fibre content but also the phenol level in the final products (Micale et al., 2017).

One of the most important factors in pasta quality assessment is optimal cooking time (time needed for the central core of a pasta strand to disappear after pasta is immersed in cooking water) (De Pilli et al., 2013; De la Peña et al., 2014; Attanzio et al., 2019). Previous studies concluded that the substitution of durum wheat flour with cladode powder at various levels (3—30 %) does not significantly affect the cooking time of pasta compared to wheat pasta (Biernacka et al., 2018; Attanzio et al., 2019; Vimercati et al., 2020). On the other hand, the swelling ability of pasta (indicator of water absorption during cooking) with a 10 % addition of cladode powder (1.73 g water/g dry pasta) has shown statistically significant differences compared to durum wheat pasta (2.11 g water/g dry pasta), which can be due to the ability of *Opuntia* cladode mucilage to encapsulate starch, slowing down its rate of swelling and increasing pasta firmness (Gutiérrez et al., 2018; Attanzio et al., 2019; Tashim et al., 2022).

Considering content and quality, protein evaluation is a fundamental cooking loss parameter (amount of solid substance that dissolves in water during cooking) and an indicator of pasta structural integrity during cooking (De la Peña et al., 2014; Desai et al., 2018). Enrichment of pasta with 10 % and 20 % of cladode powder did not significantly change the cooking loss parameter in comparison with wheat pasta, which indicates that starch-protein matrix integrity is preserved during cooking. On the contrary, fortification of pasta with up to 30 % of *Opuntia* cladode powder showed a 15 % increase of the cooking loss (Attanzio et al., 2019), probably caused by disruption of the protein-starch matrix and unequal distribution of water in the pasta matrix due to competitive hydration of the fibre preventing starch swelling due to limited water availability (Tudorica et al., 2002; Foschia et al., 2017; Attanzio et al., 2019). Thus, more solid substances leak into cooking water (Simonato et al., 2019).

It was stated that pasta incorporated with up to 30 % of cladode powder showed good sensory acceptance. Higher addition of the powder in pasta resulted in slightly bitter aftertaste of the product (Micale et al., 2017, 2018; Attanzio et al., 2019; Park et al., 2021). Furthermore, Sepúlveda et al. (2013) and Dick et al. (2020) reported that the taste and aroma of cereal-based foods prepared with cladode powder can be negatively affected by such addition due to its herbaceous flavour. Sensory characteristics are mostly affected by powders derived from the cladodes with epidermis (peel), where the most chlorophyll is found.

Moreover, it was documented that an addition of *Opuntia* cladodes powder affects the colour of pasta products, as increased addition level of cladode powder leads to greener colour (Micale et al., 2017; Attanzio et al., 2019). Several authors deduced that this is caused by the presence of green pigments, particularly chlorophyll, in cladodes (El Mannoubi et al., 2009; Ramírez-Moreno et al., 2013; Biernacka et al., 2018; Attanzio et al., 2019).

Aiello et al. (2018) and Attanzio et al. (2019) indicated that pasta incorporated with *Opuntia* cladode powder at the 30 % level can participate in lowering blood cholesterol levels because it significantly reduces the bioavailability of sterols. These results were also confirmed by i*n vitro* tests of Chong et al. (2014). In addition, pasta enriched with cladode powder can also be considered as beneficial for the prevention of age-related metabolic disorders, and hyperglycaemia, as well as for weight loss (Attanzio et al., 2019; Giglio et al., 2020; Sissons, 2022). Reduction of weight is probably linked with beneficial effect of soluble fibre (mainly pectin) on the reduction of appetite (Aiello et al., 2018; Attanzio et al., 2019).

Conclusion

Available literary research points out the importance of *Opuntia* and *Opuntia* derived products in human diet and nutrition as this plant is a rich source of bioactive substances such as dietary fibre, polysaccharides, vitamins, antioxidants (phenolic compounds), and minerals. This study presents nutritional composition and health benefits of the *Opuntia* plant and shows the possibility of its application as a potential ingredient for the production of selected cereal-based products like bread and pasta. Other important areas discussed include the effects of *Opuntia* on the rheological properties of dough, physical parameters of bread and pasta, and the sensory characteristics of these products. Given the increasing interest of consumers for value-added foods, incorporating cactus plants and cactus derived products into cereal-based food formulations is indeed a noteworthy innovation.

Acknowledgement

This publication was supported by grant VEGA No. 1/0583/20; by the Operational Program Integrated Infrastructure within the project: Demand driven research for the sustainable and innovative food, Drive4SIFood 313011V336, cofinanced by the European Regional Development Fund and by the Young Research Support Program/ Excellent Team of STU, Slovak Republic, grant No. 1893.

References

Abbas EY, Ezzat MI, El Hefnawy HM, Abdel-Sattar E (2022) J. Food Biochem. 46: e14310.

Abd El-Moaty HI, Sorour WA, Youssef AK, Gouda HM (2020) South Afric. J. of Botany 131: 320–327.

Abd-Elhakim YM, Al-Sagheer AA (2021) In: Ramadan MF, Ayoub TEM, Rohn S (Ed) Opuntia spp.: Chemistry, Bioactivity and Industrial Applications, Vol. 1 (pp. 421–456). Springer, Cham., Switzerland.

Abdulazeem L, Al-Alaq FT, Alrubaei HA, Al-Mawlah YH, Alwan WK (2018) J. Pharm. Sci. Res. 10(7): 1753–1754.

Abidi S, Salem HB, Vasta V, Priolo A (2009) Small Ruminant Research 87(1–3): 9–16.

Abou-Elella FM, Ali RFM (2014) Biochem Anal Biochem, 3(158): 2161–1009.

Abou-Zaid FO, Ahmed F, Zedan AEHI (2022) Alex. Sci. Exchange J. 43(2): 239–248.

Aiello A, Di Bona D, Candore G, Carru C, Zinellu A, Di Miceli G, Accardi G (2018) Rejuvenation Research, 21(3): 249–256.

Al Juhaimi F, Ghafoor K, Uslu N, Ahmed IAM, Babiker EE, Özcan MM, Fadimu GJ (2020) Food Chem. 303: 125387.

Albergamo A, Potortí AG, Di Bella G, Amor NB, Lo Vecchio G, Nava V, Lo Turco V (2022) Foods 11(2): 155.

Ali RF, El-Anany AM, Mousa HM, Hamad EM (2020) Food and Function 11(3): 2117–2125.

Amani E, Marwa L, Hichem, BS, Amel SH, Ghada B (2019) Scientia Horticulturae 248: 163–175.

Amaya-Cruz DM, Pérez-Ramírez IF, Delgado-García J, Mondragón-Jacobo C, Dector-Espinoza A, Reynoso-Camacho R (2019) Food Chem. 278: 568–578.

Anchondo-Trejo C, Loya-Carrasco JA, Galicia-García T, Estrada-Moreno I, Mendoza-Duarte M, Castellanos-Gallo L, Soto-Figueroa C (2020) Molecules 26(1): 54.

Andreu L, Nuncio-Jáuregui N, Carbonell-Barrachina ÁA, Legua P, Hernández F (2018) J. Sci. Food Agri. 98(4): 1566–1573.

Andreu-Coll L, Cano-Lamadrid M, Sendra E, Carbonell-Barrachina A, Legua P, Hernández F (2019) J. Food Comp. Anal. 84: 103294.

Angulo-Bejarano PI, Martínez-Cruz O, Paredes-López O (2014) Current Nut. Food Sci. 10(3): 196–217.

Anwar MM, Sallam EM (2016) Arab J. Nuc. Sci. Appli. 49(2): 151–163.

Aragona M, Lauriano ER, Pergolizzi S, Faggio CJNPR (2018) Nat. Prod, Res. 32(17): 2037–2049.

Arias-Rico J, Cruz-Cansino NDS, Cámara-Hurtado M, López-Froilán R, Pérez-Rodríguez ML, Sánchez-Mata M DC, Ramírez-Moreno E (2020) Foods 9(4): 403.

Aruwa CE, Amoo SO, Kudanga T (2018) Food Res. Inter. 112: 328–344.

Astello-García MG, Cervantes I, Nair V, del Socorro Santos-Díaz M, Reyes-Agüero A, Guéraud F, de la Rosa APB (2015) J. Food Comp. Anal. 43: 119–130.

Attanzio A, Diana P, Barraja P, Carbone A, Spanò V, Parrino B, Montalbano A (2019) J. Sci. Food Agri. 99(9): 4242–4247.

Awolu O, Oladeji O (2021) Eurasian J. of Food Sci. Tech. 5(1): 25–40.

Ayadi MA, Abdelmaksoud W, Ennouri M, Attia H (2009) J. Indust. Crop. Prod. 30: 40–47.

Baniwal P, Mehra R, Kumar N, Sharma S, Kumar S (2021) The Pharma Innovation 10(2): 343–349.

Barba FJ, Putnik P, Kovačević DB, Poojary MM, Roohinejad S, Lorenzo JM, Koubaa M (2017) Trends Food Sci. Tech. 67: 260–270.

Bchir B, Rabetafika HN, Paquot M, Blecker C (2014) Food and Bioprocess Tech., 7: 1114–1127.

Berrabah H, Taïbi K, Ait Abderrahim L, Boussaid M (2019) J. Food Meas. Charact. 13(2): 1166–1174.

Biernacka B, Dziki D, Rozylo R, Mis A, Romankiewicz D, Krzysiak Z (2018) International Agrophysics 32(2).

Biljwan, M, Naik B, Sharma D, Singh A, Kumar V (2019) The Pharma Innovation J. 8(5): 654–658.

Borchani C, Masmoudi M, Besbes S, Attia H, Deroanne C, Blecker C (2011) J. Text. Stud. 42(4): 300–308.

Bouazizi S, Montevecchi G, Antonelli A, Hamdi M (2020) LWT – Food Sci. Tech. 124: 109155.

Brühl L, Unbehend G (2021) Eu. J. of Lipid Sci. Tech. 123(7): 2000329.

Budžaki S, Komlenic DK, Čačic JL, Čačic F, Jukic M (2014) Croatian J. Food Sci. Tech. 6(2): 72–78.

Ceballos LS, Morales ER, de la Torre Adarve G, Castro JD, Martínez LP, Sampelayo MRS (2009) J. Food Comp. Anal. 22(4): 322–329.

Chahdoura H, Chaouch MA, Chouchéne W, Chahed A, Achour S, Adouni K, Achour L (2018) LWT – Food Sci. Tech. 90: 15–21.

Chaloulos P, Bazanis AE, Georgiadou M, Protonotariou S, Mandala I (2021) LWT – Food Sci. Tech. 151: 112171.

Chong PW, Lau KZ, Gruenwald J, Uebelhack R (2014) Evidence-Based Complement. Alter. Med. 2014: 943713.

Ciriminna R, Chavarría-Hernández N, Rodríguez-Hernández AI, Pagliaro M (2019) Biofuels, Bioproducts and Biorefining 13(6): 1417–1427.

Codină GG, Dabija A, Stroe SG, Ropciuc S (2019) J. Food Process. Preserv. 43(6): e13857.

Codină, GG (2022) Applied Sciences 12(3): 1–4.

Contreras-Padilla M, Rodríguez-García ME, Gutiérrez-Cortez E, del Carmen Valderrama-Bravo M, Rojas-Molina JI, Rivera-Muñoz EM (2016) European Polymer J. 78: 226–234.

Cota-Sánchez JH (2016) In: Simmonds MSJ, Preedy VR (Ed) Nutritional Composition of Fruit Cultivars Vol.1 (pp 691–712). Academic Press, London.

Cruz-Rubio JM, Mueller M, Loeppert R, Viernstein H, Praznik W (2020) Scientia Pharmaceutica, 88(4): 43.

Culetu A, Duta DE, Papageorgiou M, Varzakas T (2021) Foods, 10(12): 3121.

Czajkowska-González YA, Alvarez-Parrilla E, del Rocío Martínez-Ruiz N, Vázquez-Flores AA, Gaytán-Martínez M, de la Rosa LA (2021) Food Prod. Process. Nutri. 3(1): 1–12.

Dalila M, Soltane R, Chrouda A, Dhahri A, Pashameah RA, Almulla N (2021) In: Ramadan MF, Ayoub TEM, Rohn S (Ed) Opuntia spp.: Chemistry, Bioactivity and Industrial Applications, Vol. 1 (pp. 491–497). Springer, Cham., Switzerland.

Daniloski D, D'cunha NM, Speer H, McKune AJ, Alexopoulos N, Panagiotakos DB, Naumovski N (2022) Food Biosience 47: 101665.

Das A, Raychaudhuri U, Chakraborty R (2012) J. Food Sci. Tech. 49(6): 665–672.

Das G, Lim KJ, Tantengco OAG, Carag HM, Goncalves S, Romano A, Patra JK (2021) Phytotherapy Research 35(3): 1248–1283.

De la Peña E, Wiesenborn DP, Manthey FA (2014) Cereal Chemistry 91(5): 489–495.

De Pilli T, Derossi A, Severini C (2013) Int. J. Food Sci. Tech. 48(11): 2348–2355.

De Santiago E, Domínguez-Fernández M, Cid C, De Peña MP (2018) Food Chem. 240: 1055–1062.

De Wit M, Bothma C, Hugo A, Sithole T, Absalom C, Van den Berg C (2015) J. Prof. Assoc. Cactus Develop. 17: 89–106.

De Wit M, Du Toit A, Osthoff G, Hugo A (2019) J. of Food Measurement and Charact. 13: 2347–2356.

De Wit M, Nel P, Osthoff G, Labuschagne MT (2010) Plant Foods for Human Nutrition 65(2): 136–145.

Deldicque L, Van Proeyen K, Ramaekers M, Pischel I, Sievers H, Hespel P (2013) J. Int. Soc. Sport. Nutr. 10(1): 45.

Desai A, Brennan MA, Brennan CS (2018) LWT – Food Sci. Tech. 89: 52–57.

Di Bella G, Vecchio GL, Albergamo A, Nava V, Bartolomeo G, Macrì A, Potortì AG (2022) J. Food Comp. Anal. 106: 104307.

Díaz MDSS, de la Rosa APB, Héliès-Toussaint C, Guéraud F, Nègre-Salvayre A (2017) Oxidative Medicine and Cellular Longevity 2017: 1–17.

Dick M, Dal Magro L, Rodrigues RC, de Oliveira Rios A, Flôres SH (2019) Int. J. Biolog. Macromol. 123:

900–909.

Dick M, Limberger C, Thys RCS, de Oliveira Rios A, Flôres SH (2020) Food Chem. 314: 126178.

Dubeux Jr JCB, dos Santos MVF, da Cunha MV, dos Santos DC, de Almeida Souza RT, de Mello ACL, de Souza TC (2021) Animal Feed Sci. Tech. 275: 114890.

Dziki D, Różyło R, Gawlik-Dziki U, Świeca M (2014) Trends Food Sci. Tech. 40(1): 48–61.

El Mannoubi I, Barrek S, Skanji T, Casabianca H, Zarrouk H (2009) Chem. Nat. Comp. 45(5): 616–620.

El-Beltagi HS, Mohamed HI, Elmelegy AA, Eldesoky SE, Safwat G (2019) Fresenius Envir. Bull. 28(2): 1545–1562.

Elhassaneen Y, Abd El-Rahman A, El-Samouny SH (2022) J. of Home Economics-Menofia Uni. 32(1): 19–42.

Elia M (2011) Journal of Sensory Studies 26(4): 269–277.

El-Mostafa K, El Kharrassi Y, Badreddine A, Andreoletti P, Vamecq J, El Kebbaj MHS, Cherkaoui-Malki M (2014) Molecules 19(9): 14879–14901.

El-Safy S (2013) World Applied Sci. J. 27: 512–523.

El-Shahat MS, Rabie MA, Ragab M, Siliha H (2019) J. Food Sci. Tech. 56(8): 3635–3645.

Elshehy HR, El Sayed SS, Abdel-Mawla EM, Agamy NF (2020) J. Fd. Sci. Technol, 17: 17–25.

Feng T, Zhuang H, Ye R, Jin Z, Xu X, Xie Z (2011) Sensors and Actuators B: Chemical 160(1): 964–973.

Feugang JM, Konarski P, Zou D, Stintzing FC, Zou C (2006) Frontiers in Bioscience-Landmark 11(3): 2574–2589.

Figueroa-Pérez MG, Pérez-Ramírez IF, Paredes-López O, Mondragón-Jacobo C, Reynoso-Camacho R (2018) Int. J. Food Prop. 21(1): 1728–1742.

Foschia M, Beraldo P, Peressini D (2017) J. Sci. Food Agri. 2: 572.

García FH, Coll LA, Cano-Lamadrid M, Lluch DL, Barrachina ÁAC, Murcia PL (2020) In: El-Shafie, H. (Ed) Invasive Species-Introduction Pathways, Economic Impact, and Possible Management Options, (pp. 127–142). IntechOpen, London.

García-Menaya JM, Cordobés-Durán C, Bobadilla P, Ledesma A, Pérez-Rangel I (2009) Allergy, 64(11): 1689–1690.

Gharby S, Guillaume D, Nounah I, Harhar H, Hajib A, Matthäus B, Charrouf Z (2021) Grasas y Aceites, 72(1): 397.

Giglio RV, Carruba G, Cicero AF, Banach M, Patti AM, Nikolic D, Rizzo M (2020) Metabolites 10(11): 428.

Ginestra G, Parker ML, Bennett RN, Robertson J, Mandalari G, Narbad A, Waldron KW (2009) J. Agri. Food Chem. 57(21): 10323–10330.

Gómez M, Ronda F, Blanco CA, Caballero PA, Apesteguía A (2003) Europ. Food Res. Tech. 216(1): 51–56.

Gouws CA, D'Cunha NM, Georgousopoulou EN, Mellor DD, Naumovski N (2019a) J. Food Process. Preserv. 43(3): 1–11.

Gouws CA, Georgousopoulou EN, Mellor DD, McKune A, Naumovski N (2019b) Medicina 55(5): 138.

Guevara-Arauza JC, Bárcenas DG, Ortega-Rivas E, Martínez JDP, Hernández JR, de Jesús Ornelas-Paz J (2015) J. Food Sci. Tech. 52(5): 2990–2997.

Gül H (2021) In: Ramadan MF, Ayoub TEM, Rohn S (Ed) Opuntia spp.: Chemistry, Bioactivity and Industrial Applications, Vol. 1 (pp. 753–776). Springer, Cham., Switzerland.

Gutiérrez MC, Utrilla-Coello RG, Soto-Castro D (2018) J. Food Process. Preserv. 42(2): 1–8.

Hashem MA, Shoeeb SB, Abd-Elhakim YM, Mohamed WA (2020) Journal of Functional Foods 66: 103831.

Hernández-Becerra E, de los Angeles Aguilera-Barreiro M, Contreras-Padilla M, Pérez-Torrero E, Rodriguez-Garcia ME (2022) Journal of Functional Foods 95: 105183.

Hussain S, Alamri MS, Mohamed AA, Ibraheem MA, Qasem AAA, Shamlan G, Ababtain IA (2022a) Foods 11(9): 1208.

Hussain S, Alamri MS, Mohamed AA, Ibraheem MA, Qasem AAA, Shamlan G, Ababtain IA (2022b). Molecules 27(21): 7217.

Hussin MF, El-Gazaly FM, Aly AS, Abd El-Sabor RG, Sayed KM (2022) J. Res. Field. Spec. Educ. 38(8): 363–408.

Jana S (2012) J. Engineer. Res. Stud. 3(2): 60–66.

Jotangiya DJ, Samani VS (2017) Food Sci. Res. J. 8(1): 25–28.

Jun HI, Cha MN, Yang EI, Choi DG, Kim YS (2013) Horticulture, Environment and Biotechnology 54(3): 288–295.

Kapadiya DB, Prajapati DB, Jain AK, Mehta BM, Darji VB, Aparnathi KD (2016) Veterinary World 9(7): 710.

Kashif RR, D'cunha NM, Mellor DD, Alexopoulos NI, Sergi D, Naumovski N (2022) Medicina, 58(2): 1–15.

Khatabi O, Hanine H, Elothmani D, Hasib A (2016) Arab. J. Chem. 9: 278–281.

Krishnan JG, Menon R, Padmaja G, Sajeev MS, Moorthy SN (2012) Europ. Food Res. Tech. 234(3): 467–476.

Kurek M, Wyrwisz J (2015) J. Food Process. Tech. 6(5): 447–450.

Lambrini K, Aikaterini F, Konstantinos K, Christos I, Ioanna PV, Areti T (2021) J. Pharm. Pharmacol. 9: 8–13.

Lassoued N, Delarue J, Launay B, Michon C (2008) J. Cereal Sci. 48(1): 133–143.

Lauková M, Kohajdová Z, Karovičová J (2016) Potravinárstvo 10(1): 506–511.

León-Martínez FM, Rodriguez-Ramirez J, Medina-Torres LL, Lagunas LM, Bernad-Bernad MJ (2011) Carbohydrate Polymers 84(1): 439–445.

Liguori G, Gentile C, Gaglio R, Perrone A, Guarcello R, Francesca N, Settanni L (2020) J. Biosci. and Bioengineer. 129(2): 184–191.

Linlaud NE, Puppo MC, Ferrero C (2009) Cereal Chem. 86(4): 376–382.

López-Palacios C, Peña-Valdivia CB, Rodríguez-Hernández AI, Reyes-Agüero JA (2016) Plant Foods for Human Nutrition 71(4): 388–395.

López-Palacios C, Reyes-Agüero JA, Peña-Valdivia CB, Aguirre-Rivera JR (2019) Gen. Res. Crop Evol. 66(2): 349–362.

Madenci AB, Bilgiçli N, Türker S (2018) Quality Assurance and Safety of Crops and Foods 10(3): 315–324.

Madrigal-Santillán E, Portillo-Reyes J, Madrigal-Bujaidar E, Sánchez-Gutiérrez M, Mercado-Gonzalez PE, Izquierdo-Vega JA, Morales-González JA (2022) Horticulturae 8(2): 1–28.

Magarelli RA, Trupo M, Ambrico A, Larocca V, Martino M, Palazzo S, Bevivino A (2022) Fermentation 8(5):

225.

Makhlouf S, Jones S, Ye SH, Sancho-Madriz M, Burns-Whitmore B, Li YO (2019) Food Quality and Safety 3(2): 117–127.

Martínez MM, Gómez M (2017) J. Food Engineer. 197: 78–86.

Mata A, Ferreira JP, Semedo C, Serra T, Duarte CMM, Bronze MR (2016) Food Chem. 210: 558–565.

Mazri, MA (2021) In: Ramadan MF, Ayoub TEM, Rohn S (Ed) Opuntia spp.: Chemistry, Bioactivity and Industrial Applications, Vol. 1 (pp. 83–107). Springer, Cham., Switzerland.

Medina ED, Rodríguez ER, Romero CD (2007) Food Chem. 103(1): 38–45.

Micale R, Giallanza A, Enea M, La Scalia G (2018) J. Food Engineer. 237: 171–176.

Micale R, Giallanza A, Russo G, La Scalia G (2017) Sustainability 9(6): 885.

Milán-Noris, AK, Chavez-Santoscoy RA, Olmos-Nakamura A, Gutiérrez-Uribe JA, Serna-Saldívar SO (2016) Current Bioactive Compounds 12(1): 10–16.

Mironeasa S, Mironeasa C (2019) J. Food Process Eng. 42(6), e13207.

Mirsaeedghazi H, Emam-Djomeh Z, Mousavi SMA (2008) Int. J. Agri. and Bio. 10(1): 112–119.

Mona MM, Nesreen M (2011) Egypt. J. Appl. Sci. 26 (3): 63–85.

Moreno-Álvarez MJ, García-Pantaleón D, Belén-Camacho DR, Medina-Martínez, Muñoz-Ojeda N, Herrera I, Espinoza C (2006) Boletín Nakari 17(1): 9–12.

Moreno-Álvarez MJ, Hernández R, Belén-Camacho DR, Medina-Martínez CA, Ojeda-Escalona CE, García-Pantaleón DM (2009) J. Prof. Assoc. for Cactus Develop. 11: 78–87.

Mounir B, Asmaa M, Abdeljalil Z, Abdellah A (2020) Journal of Plant Physiology 251: 153196.

Msaddak L, Abdelhedi O, Kridene A, Rateb M, Belbahri L, Ammar E, Zouari N (2017) Lipids in Health and Disease 16(1): 1–8.

Msaddak L, Siala R, Fakhfakh N, Ayadi MA, Nasri M, Zouari N (2015) Int. J. Food Sci. Nut. 66(8): 851–857.

Nabil B, Ouaabou R, Ouhammou M, Essaadouni L, Mahrouz M (2020) Journal of Food Quality 2020: 1–12.

Nassar AG, Abdel-Hamied AA, El-Naggar EA (2008) World J. Agri. Sci. 4(2018): 612–616.

Nharingo T, Moyo M (2016) J. Environ. Man. 166: 55–72.

Nounah I, Chbani M, Matthäus B, Charrouf Z, Hajib A, Willenberg I (2020) Foods 9(9): 1280.

Oniszczuk A, Wójtowicz A, Oniszczuk T, Matwijczuk A, Dib A, Markut-Miotła E (2020) Molecules 25(4): 916.

Osuna-Martínez U, Reyes-Esparza J, Rodríguez-Fragoso L (2014) Nat. Prod. Chem. Res. 2: 153.

Otang WM, Grierson DS, Afolayan AJ (2014) J. of ethnopharmacology, 157: 274–284.

Özcan MM, Al Juhaimi FY (2011) Int. J. Food Sci. and Nut. 62(5): 533–536.

Padalino L, Conte A, Lecce L, Likyova D, Sicari V, Pellicanò TM, Del Nobile MA (2017) Czech J. Food Sci. 35(1): 48–56.

Palmieri N, Suardi A, Stefanoni W, Pari L (2021) Foods 10(4): 803.

Parafati L, Restuccia C, Palmeri R, Fallico B, Arena E (2020) Foods 9(9): 1189.

Park SH, Jeong BG, Song W, Jung J, Chun J (2021) Food Bioscience 41: 100921.

Patel MJ, Chakrabarti-Bell S (2013) J. Food Enginer. 115(3): 371–383.

Perucini-Avendaño M, Nicolás-García M, Jiménez-Martínez C, Perea-Flores MDJ, Gómez-Patiño MB, Arrieta-Báez D, Dávila-Ortiz G (2021) Food Sci. Nutri 9(7): 4007–4017.

Pessoa DV, de Andrade AP, Magalhães ALR, Teodoro AL, dos Santos DC, de Araújo GGL, Cardoso DB (2020) J. Arid Environ. 18: 1–8.

Ramírez-Moreno E, Cariño-Cortés R, Cruz-Cansino NDS, Delgado-Olivares L, Ariza-Ortega JA, Montañez-Izquierdo VY, Filardo-Kerstupp T (2017) Journal of Food Quality 2017: 3075907.

Ramírez-Moreno E, Córdoba-Díaz D, de Cortes Sánchez-Mata M, Díez-Marqués C, Goñi I (2013) LWT – Food Sci. Tech. 51(1): 296–302.

Rayan AM, Morsy NE, Youssef KM (2018) J. Food Sci. Tech. 55(2): 523–531.

Rbia O, Smiti SA (2019) MOJ Food Process. Technol. 7(2): 39–42.

Rebah FB, Siddeeg SM (2017) J. Mat. Environ. Sci. 8(5): 1770–1782.

Reda TH, Atsbha MK (2019) Int. J. Food Sci. 2019: 1–7.

Rocchetti G, Pellizzoni M, Montesano D, Lucini L (2018) Foods 7(2): 1–12.

Rodríguez-González S, Martínez-Flores HE, Chávez-Moreno CK, Macías-Rodríguez LI, Zavala-Mendoza E, Garnica-Romo MG, Chacón-García L (2014) J. of Food Process Eng. 37(3): 285–292.

Romero MC, Fogar RA, Fernández CL, Doval MM, Romero AM, Judis MA (2021) J. Food Sci. Tech. 58(5): 1918–1926.

Sciacca F, Palumbo M, Pagliaro A, Di Stefano V, Scandurra S, Virzì N, Melilli MG (2021) CyTA-Journal of Food 19(1): 96–104.

Sepúlveda E, Gorena T, Chiffelle I, Sáenz C, Catalán E (2013) VII Internat. Congress on Cactus Pear and Cochineal 995: 269–272.

Sepúlveda ESCAE, Sáenz C, Aliaga E, Aceituno C (2007) J. of Arid Enviro. 68(4): 534–545.

Shahzad A (2012) J. Comp. Material. 46(8): 973–986.

Silva MA, Albuquerque TG, Pereira P, Ramalho R, Vicente F, Oliveira MBP, Costa HS (2021) Molecules 26(4): 951.

Simonato B, Trevisan S, Tolve R, Favati F, Pasini G (2019) LWT – Food Sci. Tech. 114: 108368.

Sissons M (2022) Foods 11(1): 123.

Slimen IB, Najar T, Abderrabba M (2016) J. of Food and Nutri. Sci. 4(6): 162–169.

Stintzing FC, Carle R (2005) Mol. Nut. Food Res. 49(2): 175–194.

Tashim NAZ, Lim SA, Basri AM (2022) J. Sci. Food Agri. 102(15): 7331–7342.

Taşkın B, Aksoylu Özbek Z (2021) In: Ramadan MF, Ayoub TEM, Rohn S (Ed) Opuntia spp.: Chemistry, Bioactivity and Industrial Applications, Vol. 1 (pp. 923–952). Springer, Cham., Switzerland.

Touil A, Chemkhi S, Zagrouba F (2014) J. Food Process. 2014: 1–9.

Tudorica CM, Kuri V, Brennan S (2002) J. Agri. and Food Chem. 50(2): 347–356.

Turksoy,ň S, Özkaya B (2011) Food Sci. Tech. Research 17(6): 545–553.

Vimercati WC, Macedo LL, Araujo CDS, Maradini Filho AM, Saraiva SH, Teixeira LJQ (2020) J. Food Process. Preserv. 44(9): 1–12.

Wang JJ, Liu G, Huang YB, Zeng QH, Song GS, Hou Y, Hu SQ (2016) Food Chem. 213: 682–690.

Wit MD, Fouché H (2021) In: Ramadan MF, Ayoub TEM, Rohn S (Ed) Opuntia spp.: Chemistry, Bioactivity and Industrial Applications, Vol. 1 (pp. 259–285). Springer, Cham., Switzerland.

Yahia EM, Sáenz C (2011) In: Yahia EM (Ed) Postharvest biology and technology of tropical and subtropical fruits, Vol. 2 (pp. 290–331). Woodhead Publishing, London.

Yoon HJ, Won CH, Moon SE (2004) Contact Dermatitis, 51(5–6): 311–312.

sciendo

Colour masterbatches and their use in polylactic acid fibres dyeing

Agáta Hudecová[1], Marcela Hricová[1], Mária Petková[1],
Roderik Plavec[1], Zita Tomčíková[2], Anna Ujhelyiová[1]

[1]Department of Plastics, Rubber and Fibres, Faculty of Chemical and Food Technology,
Slovak University of Technology in Bratislava, Radlinského 9, 812 37 Bratislava, Slovakia
[2]Research Institute for Man-Made Fibres a.s., Štúrova 2, 05921 Svit, Slovakia
agata.hudecova@stuba.sk

Abstract: This article is focused on the preparation of colour masterbatches from renewable sources based on polylactic acid, which were modified with inorganic pigments. Titanium dioxide, carbon black, and iron oxides were used as inorganic pigments. Due to the composition of the prepared colour PLA masterbatches, the influence of the inorganic pigment on the rheological and thermal properties was monitored. Rheological properties were determined using a capillary viscosimeter and a rotary rheoviscosimeter with a geometry plate/plate. The colour PLA masterbatches prepared in this way were subsequently used to dye polylactic acid fibres in the mass. The prepared fibres were drawn to the maximum drawn ratio λ_{max}. In case of fibres, the influence of composition and drawn ratio on thermal and mechanical properties was monitored.

Keywords: biodegradable polymers, inorganic pigment, mechanical properties, polylactic acid, rheological properties, thermal properties

Introduction

Polymeric materials obtained from petroleum sources are an integral part of life. They are mainly used in the food industry, agriculture, construction, medicine or in the automotive industry. The problem is that these materials are not biodegradable, they accumulate in landfills and pollute the environment. A good alternative are biodegradable polymers, which can decompose in nature and thus do not pollute the environment. Polylactic acid belongs to the best-known biodegradable polymers (Vroman and Tighzert, 2009).

Polylactic acid (PLA) is a linear aliphatic polyester derived from lactic acid which exists in two enantiomeric forms: D- and L-. Therefore, it is possible to produce polylactic acid from pure isomers of L- and D-lactic acid, when homopolymers of poly-L-lactic acid and poly-D-lactic acid are formed, or from a racemic mixture of L- and D-monomers, when a copolymer of poly- D, L-lactic acid is formed. PLA can be synthesised from lactic acid monomers by polycondensation, azeotropic dehydration condensation, ring-opening polymerisation reactions and enzymatic polymerisation. Ring-opening polymerisation reactions are the most widely used in industry due to the undemanding reaction conditions and the resulting polymers with high molecular weights. Polylactic acid can also be obtained by fragmentation from natural sources such as sugar beet, wheat, or corn (Casalini et al., 2019). Polylactic acid is characterised by high tenacity at break and high Young's modulus. However, it is a brittle material with low impact strength, low elongation at break, low thermal stability and poor barrier properties (Farah et al., 2016). PLA is a thermoplastic behaving as a solid substance at normal temperatures but changing at elevated temperatures into highly viscous liquids, which can be shaped and re-cooled to fix their shape. Thus, PLA can be processed by standard technologies such as extrusion, spinning, mixing, pressing, or injection molding, to produce fibres, foils, boards, cables, or 3D materials (Rasal et al., 2010).

Fibres made from polylactic acid belong to the most innovative textile materials and are increasingly in demand. PLA fibres are produced from renewable resources. Compared to fibres made from commercial polymers, PLA fibres are characterised by properties such as biodegradability, ease of processing, ease of composting and recycling, breathability, dyeability and stability against UV radiation (Yang et al., 2021). PLA fibres can be prepared by melt spinning, wet spinning, or electrospinning. One of the most used methods of PLA fibres preparation is melt spinning due to its simplicity and environmental friendliness (Gupta et al., 2007). Melt spinning is a process where solid polymer phase is formed from a polymer melt in the form of a fibre with primary structure. In the spinning process, the melt from the extruder is dosed and forced through holes of the spinning nozzle with a circular cross-section at a defined temperature and viscosity creating fine fibrils. The resulting fibrils solidify due to air cooling behind the nozzle. By pulling and winding these fibrils, endless fibres are prepared. However, endless fibres do not have the required mechanical and physical properties necessary for further processing. Therefore, these fibres have to be drawn, which refers to axial deformation of a fibre in solid state under dynamic conditions. During drawing, macromolecules of the polymer chain are oriented in the direction of the applied deformation force. Orientation changes the physical and mechanical properties as well as the optical properties of the fibre. In addition to the change in properties, there is also a change in the geometry of the fibres, the length of the fibres increases and their diameter decreases. By drawing the fibres, tenacity at break and Young's modulus increase, while elongation at break decreases (Marcinčin, 1989; Rawal et al., 2014).

An important process of final treatment of polymer materials as well as fibres is their dyeing. Dyeing is a finishing process resulting in polymer materials of the required colour and thereby improved consumer properties. The colouring must be resistant to various influences of mechanical, chemical, or physical nature, to which the material is exposed during further technological processing or practical use, such as fastness to light, sweat, washing, water, abrasion, etc. PLA fibres can most often be dyed in two ways: by exhaust dyeing process from bath or in the mass. Exhaust dyeing process from bath consists of two phases, where the first phase consists of the fibre and the second of the dye bath. During the exhaust dyeing process from bath, diffusion, adsorption, and fixation of the dye from the dye bath onto the fibre occurs. However, from an ecological point of view, this method of dyeing is unacceptable because the discharge of waste substances from the dyeing process into rivers and streams causes pollution of water resources. In contrast to the exhaust dyeing process from bath, dyeing in the mass is a better option because the dye is incorporated into the polymer melt during fibre production, not polluting water sources and with better dyeability of the fibre. When dyeing in the mass, dyes are used in the form of powders, pastes or in granulated form, so-called colour masterbatches (Balakrishnan, 2020; Grishanov, 2011; Prchal, 1993; Trotman, 1970), which is the most widespread method of dyeing fibres in the mass. Advantages of this dyeing method include dust-free environment, good dosage, trouble-free increase in pigment content, and optimal use of colour strength. Colour masterbatches are processed to impart colour, texture, and various other properties to the polymer materials to which they are applied. Colour masterbatches are composed of three basic components: the carrier, the dispersing agent, and the pigment. In addition to these components, other additives can be included, such as various antistatic agents, antibacterial agents, nucleating agents, stabilizers, wetting agents, and others. The carrier is a polymer compatible with the dispersant and the pigment (Parra-Campos et al., 2020; Benetti et al., 2014). Dispersing agents are substances necessary for the dispersion and homogenisation of pigments in the preparation of colour concentrates. Without these substances, pigments in the polymer mass form unwetted agglomerates, which render the workability of colour concentrates unsatisfactory (Hricová et al., 2004). In general, pigments are fine coloured powders, the resulting colour of which is determined by the spectrum of reflected wavelengths of light. Pigments are insoluble in the polymer matrix, and are dispersed as fine particles (Koenig et al., 2020; Markarian, 2009). Pigments are inorganic and organic; inorganic pigments have high thermal stability and good light stability compared to organic pigments (Tolinski, 2009). Since coloured fibres were prepared from polylactic acid, which is a biodegradable polymer, it is necessary to use also biodegradable colour masterbatches (Chen, 2018). Therefore, in the production of colour masterbatches, polylactic acid was used as a carrier in combination with inorganic pigments, specifically titanium dioxide, carbon black, and iron oxides, which are biodegradable and can be obtained from renewable sources. In the preparation of colour masterbatches, mixing and homogenisation play an important role in achieving the best possible dispersion. Mixing is represented by two basic processes – distributive and dispersive mixing. During distributive mixing, homogeneous distribution of the pigment is achieved inside the polymer matrix. The process of distributive mixing depends on the magnitude of the shear deformations and the intensity of mass transport in the mixing device. During dispersion mixing, agglomerates break down into primary particles. Considering dispersive mixing, the size of the shear deformation is not important, the determining factor is the size of the shear stress, which ensures the disintegration of agglomerates into primary particles. In order for the agglomerates to break down into primary particles, cohesive forces between the agglomerate particles must weaken (Balakrishnan et al., 2022; Benetti et al., 2014; Niaounakis, 2015).

Rheological properties of polymers and colour PLA masterbatches are important from the point of view of their processing. Most polymer processing technologies are based on their processing in the melt, when the polymer flows (Alexy, 2016). Further processing of the prepared PLA masterbatches used for PLA fibres dyeing in the mass, requires the knowledge of rheological and thermal properties of the prepared colour PLA masterbatches. Properties of the prepared PLA masterbatches subsequently affect the processability of PLA during fibre preparation. PLA fibres are an oriented system unlike colour PLA masterbatches, which are a non-oriented system. Therefore, with PLA fibres, in addition to the influence of the composition, also the influence of the drawn ratio on thermal and mechanical properties was monitored.

Materials and Methods

Materials used

Polymer

Polylactic acid INGEO I6100D (**PLA6100**) is a thermoplastic fibre-grade resin (in pellet form) derived primarily from annually renewable resources, *MFI* = 24g/10 min at 210 °C, glass temperature T_g = 55—60 °C, melting temperature T_m = 165—180 °C (produced by NatureWorks LLC).

Inorganic pigments

1. titanium dioxide Pretiox AV01SF (**Ti**) is ultrafine milled anatase TiO_2 without surface treatment, primary particle size (TEM) of 21 nm, T_m = 1850 °C (produced by Precheza a.s.);
2. carbon black Printex Alpha (**PXA**) is a fine black powder with high specific area, average primary particle size of 20 nm, T_m > 3000 °C (produced by Orion Engineered Carbons GmbH);
3. iron oxide Fepren TP 303 (**Fe**) is a fine dry-milled pigment with very high tinting-strength, particle size <50 nm (BET), T_m = 1565 °C (produced by Precheza a.s.).

Silicone oil V350 was used as dispersing agent (produced by Azelis Slovakia, s.r.o.).

Colour masterbatches preparation

A laboratory line with twin-screw extruder WP ZDSK (screw diameter of 28 mm), in vacuum zone and in the temperature range of 180—210 °C, was used for the preparation of PLA colour masterbatches. Final concentration of inorganic pigments in the prepared masterbatches was 1 and 3 wt %.

Fibres preparation

Before spinning, pure PLA granulate and pigmented PLA masterbatches were dried in a laboratory oven for 3 hours at 60 °C. Pure PLA fibres and pigmented PLA fibres with the final concentration of pigments of 0.1 and 0.5 wt % were prepared using a laboratory spinning plant at 190 °C with the take-up speed of 150 $m \cdot min^{-1}$.

After spinning, the prepared PLA fibres and pigmented PLA fibres were drawn using a laboratory drawing machine at the maximal drawn ratio λ_{max} at drawing temperatures T_{dr} = 95 °C and T_{dr} = 105 °C. Composition of fibres and obtained drawn ratios are presented in Table 1.

Methods used

Rheological properties

Rotary rheoviscosimeter Physica MCR 101 (Anton Paar) was used to measure rheological behaviour of pure PLA and pigmented PLA masterbatches. Parallel plate geometry was used applying the diameter of 25 mm and the gap set to 1 mm. All rheological measurements were performed in air atmosphere at 190 °C and at 1 % strain from 0.1 to 100 $rad \cdot s^{-1}$.

Moreover, rheological properties of PLA and pigmented PLA masterbatches were measured using a capillary viscosimeter GÖTTFERT RG20 at 190 °C. The conditions of measurement: capillary with the circular diameter with L/D = 30/1 and a piston with the diameter of 15 mm was used in the range of shear speeds from 90 to 4500 s^{-1} with preheating for 5 minutes.

Thermal properties

Thermal properties were measured by DSC 1/750 with ceramic sensor FRS5 using software SW STARe by Metler Toledo. Conditions used in the measurement were: 1st heating: 20—190 °C, isothermally held for 3 minutes, cooling: 190—20 °C,

Tab. 1. Composition of PLA fibres with 0.1 and 0.5 wt % pigments with drawing temperatures T_{dr}, maximal drawn ratios λ_{max} and fineness of fibres T_t.

Composition of fibres	T_{dr} **[°C]**	λ_{max}	T_t **[tex]**
PLA6100	105	3.5	23.2
PLA6100+0.1 %Ti	105	3.6	20.1
PLA6100+0.1 %PXA		3.3	18.9
PLA6100+0.1 %Fe		3.4	18.1
PLA6100+0.5 %Ti	95	2.5	41.5
PLA6100+0.5 %PXA		2.5	49.8
PLA6100+0.5 %Fe		2.5	42.5

isothermally held for 3 minutes, 2nd heating: 20–190 °C. The rate of heating or cooling was 10 °C/min. The measurements were done in inert nitrogen atmosphere. From the measured thermograms, glass temperature (T_g), cold crystallisation temperature (T_{cc}), melting temperature (T_m), enthalpy of relaxation (ΔH_{er}), enthalpy of melting (ΔH_m) and enthalpy of cold crystallisation (ΔH_{cc}) obtained during the 1st heating and the crystallisation temperature (T_c) and enthalpy of crystallisation (ΔH_c) obtained during cooling were evaluated. During the 2nd heating, glass temperature (T_g), cold crystallisation temperature (T_{cc}), melting temperature (T_m), enthalpy of relaxation (ΔH_{er}), enthalpy of melting (ΔH_m), and enthalpy of cold crystallisation (ΔH_{cc}) were evaluated.

Mechanical properties

Mechanical properties (tenacity and elongation at break as well as Young's modulus) of PLA and pigmented PLA fibres were evaluated by Instron 3343 equipment and the mechanical characteristics were determined from 15 measurements according to ISO 2062:1993. The initial length of fibres was 125 mm and the time of deformation was about 20 sec.

Results and discussion

Rheological properties of colour masterbatches

Rheological properties of polymer materials and colour masterbatches are important for their processing. The influence of type (Ti, PXA, Fe) and concentration (1 and 3 wt %) of inorganic pigments on the rheological properties of colour masterbatches was monitored. Rheological properties were determined using a capillary viscosimeter and a rotary rheoviscosimeter with a geometry plate/plate. Dependences of viscosity on shear rate were constructed from the measured values and are

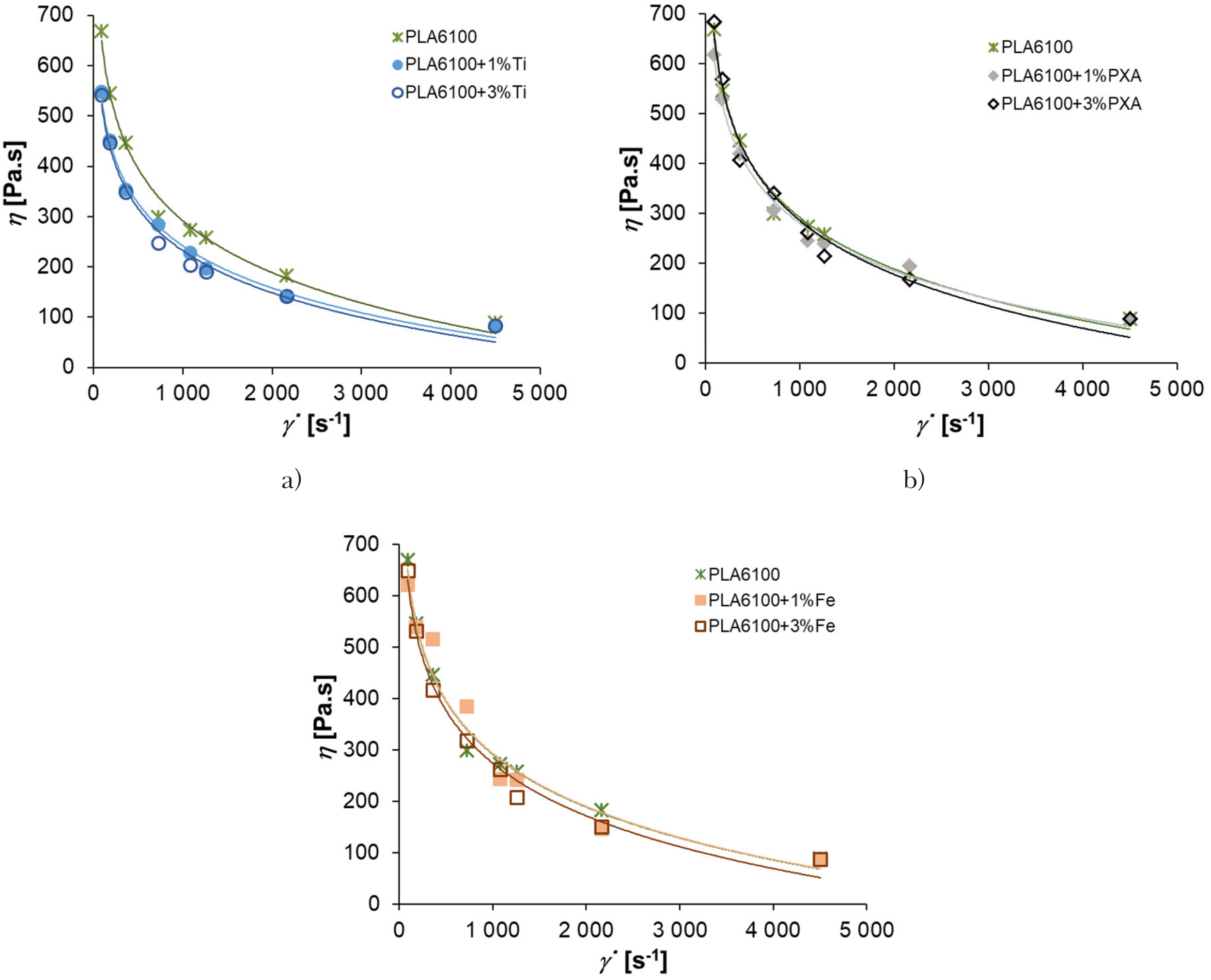

a)

b)

c)

Fig. 1. Dependence of viscosity η on shear rate $\gamma^{\cdot}$ obtained on the capillary viscosimeter for colour PLA masterbatches with 1 and 3 wt % of inorganic pigments: Ti (a), PXA (b), Fe (c).

shown in Figures 1 and 2 for the capillary viscosimeter (Figure 1) and for the rotary rheoviscosimeter with a geometry plate/plate (Figure 2) for colour masterbatches modified with 1 and 3 wt % of inorganic pigments, which show viscosity decrease with the increasing shear rate. Viscosity is defined as the ratio of shear stress to shear rate, implying that the higher the shear rate applied to the material, the faster the material flow and thus lower viscosity. As it can be seen, viscosity is not constant as in the case of Newtonian substances but varies with the shear rate. This is typical for pseudoplastic materials with non-Newtonian behaviour. Based on this, the prepared colour masterbatches modified with inorganic pigments can be considered as pseudoplastic substances.

Figure 1 shows the dependences of viscosity on the shear rate of the prepared colour PLA masterbatches modified with 1 and 3 wt % of inorganic pigments (Ti, PXA, Fe) measured on the capillary viscosimeter. Colour PLA masterbatches are pseudoplastic substances with non-Newtonian behaviour and therefore, the Rabinowitsch correction was used when measuring rheological properties, which takes into account the Newtonian nature of the flow on the capillary wall. In Figure 1a, a decrease in viscosity due to the addition of inorganic pigment Ti was observed comparing pure PLA6100 with PLA6100 masterbatches with 1 and 3 wt % of Ti. A comparison of PLA6100 masterbatch with 1 wt % of inorganic pigment Ti and with 3 wt % of Ti shows that the higher the content of inorganic pigments (3 wt %), the greater the drop in viscosity. In Figures 1b and 1c, small changes in the dependences of viscosity on shear rate when comparing pure PLA6100 with PLA6100 masterbatches with 1 and 3 wt % of inorganic pigments PXA and Fe can be seen.

Figure 2 shows the dependences of viscosity on the shear rate of the prepared colour PLA master-

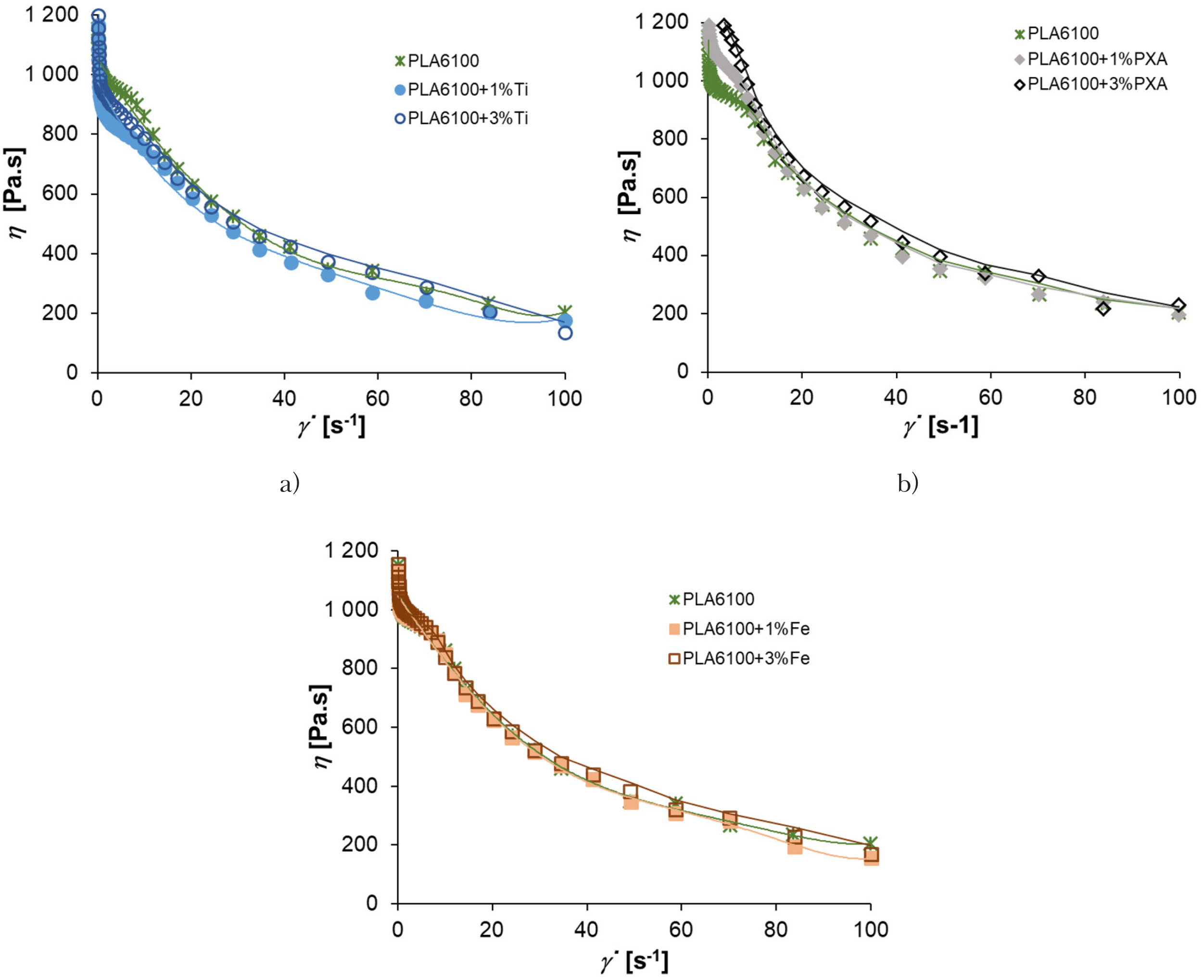

a)

b)

c)

Fig. 2. Dependence of viscosity η on shear rate $\gamma^{\cdot}$ obtained on the plate/plate rotary rheoviscosimeter for colour PLA masterbatches with 1 and 3 wt % of inorganic pigments: Ti (a), PXA (b), Fe (c).

batches with 1 and 3 wt % of inorganic pigments (Ti, PXA, Fe) measured on the rotary rheoviscosimeter with a geometry plate/plate. A comparison of PLA6100 masterbatches with 1 wt % of Ti (Figure 2a), PXA (Figure 2b), and Fe (Figure 2c) with those with 3 wt % of Ti (Figure 2a), PXA (Figure 2b) and Fe (Figure 2c), revealed an increase in the viscosity due to the addition of a higher content of inorganic pigments (3 wt %). In Figure 2a, a decrease in viscosity, which is more visible at low shear rates, is observed comparing pure PLA6100 with PLA6100 masterbatches with 1 and 3 wt % of Ti. Figure 2b shows an increase in viscosity due to the addition of PXA comparing pure PLA6100 with PLA6100 masterbatch with 3 wt % of PXA. The observed increase in viscosity caused by adding PXA compared to other pigments (Ti, Fe) can be evaluated considering different chemical structure, chemical properties, size of pigment particles, shape of pigment particles, and intermolecular interactions between pigment particles. It can be assumed that, as the content of inorganic PXA pigment increases, the dispersibility of PXA particles in the polymer matrix deteriorates and they remain aggregated which results in an increase in viscosity. By adding 1 or 3 wt % of Fe to pure PLA6100, minimal differences in the dependences of viscosity on the shear rate were observed.

Thermal properties of colour PLA masterbatches and PLA fibres

Thermal properties of prepared colour PLA masterbatches and PLA fibres were determined by DSC analysis by monitoring endothermic and exothermic processes. From the measured thermograms, basic thermal parameters such as glass temperature (T_g), cold crystallisation temperature (T_{cc}), melting temperature (T_m), crystallisation temperature (T_c), enthalpy of relaxation (ΔH_{er}), enthalpy of melting (ΔH_m), enthalpy of crystallisation (ΔH_c), and enthalpy of cold crystallisation (ΔH_{cc}) of the prepared colour PLA masterbatches and PLA fibres obtained during the 1st (Tables 2 and 4) and 2nd (Tables 3 and 5) heating were evaluated. During the 1st heating, thermal history of colour PLA masterbatches and PLA fibres, related to their preparation and storage, was cancelled. The following cooling allowed the formation of a new structure. The second heating is important for the characterisation of the examined colour PLA masterbatches and PLA fibres. During the 2nd heating, thermal properties of the colour PLA masterbatches and PLA fibres were monitored. To determine the properties of colour PLA masterbatches and PLA fibres, results from the 1st heating were compared. To determine the influence of the addition of 1 and 3 wt % pigment content in PLA masterbatches and 0.1 and 0.5 wt % pigment content in PLA fibres, results from the 2nd heating were compared.

When evaluating thermal properties of colour PLA masterbatches (Tables 2 and 3), PLA6100 masterbatches with 1 or 3 wt % of inorganic pigments showed lower glass temperature T_g than pure PLA during the 1st heating. The decrease in T_g of PLA colour masterbatches is due to the addition of inorganic pigments that act as nucleating agents, promote crystallisation, and increase the crystallinity thus decreasing T_g. The increased content of inorganic pigments (3 wt %) does not affect the glass temperature. During the 1st heating, PLA masterbatches showed higher value of the enthalpy of relaxation than pure PLA, which can be explained by weak interactions formed between the polymer carrier (PLA) and inorganic pigments during the preparation of colour masterbatches. Increased enthalpy of relaxation and decreases T_g. During the 1st heating, cold crystallisation was measured for all PLA masterbatches with 1 and 3 wt % of inorganic

Tab. 2. Glass temperature (T_g), cold crystallisation temperature (T_{cc}), melting temperature (T_m), enthalpy of relaxation (ΔH_{er}), enthalpy of cold crystallisation (ΔH_{cc}), and enthalpy of melting (ΔH_m) of prepared colour masterbatches obtained during the 1st heating, and crystallisation temperature (T_c) and enthalpy of crystallisation (ΔH_c) of prepared colour masterbatches obtained during cooling

Composition of masterbatches	1st heating								Cooling	
	T_g [°C]	ΔH_{er} [J/g]	T_{cc1} [°C]	ΔH_{cc1} [J/g]	T_{cc2} [°C]	ΔH_{cc2} [J/g]	T_m [°C]	ΔH_m [J/g]	T_c [°C]	ΔH_c [J/g]
PLA6100	68.4	0.6	–	–	163.1	1.7	176.7	37.6	103.8	0.5
PLA6100+1 %Ti	63.5	4.7	94.8	24.4	161.2	3.5	176.5	17.4	103.4	20.1
PLA6100+3 %Ti	64.4	4.9	94.8	22.6	161.1	3.1	176.4	19.0	93.6	9.6
PLA6100+1 %PXA	65.8	6.1	98.2	24.1	161.6	3.2	176.8	18.6	88.4	3.3
PLA6100+3 %PXA	65.8	5.7	101.9	26.5	162.5	2.8	177.4	14.4	100.4	1.3
PLA6100+1 %Fe	64.1	5.2	95.4	24.6	160.9	3.5	176.9	16.4	91.1	8.5
PLA6100+3 %Fe	63.0	3.5	95.9	23.0	161.2	3.2	177.3	17.0	92.4	5.1

pigments. The presence of pigments contributes significantly to cold crystallisation because no cold crystallisation was observed in pure PLA6100. Endothermic peak with a maximum at 176.7 °C, corresponding to the melting temperature, was detected during the 1st heating (Table 2). Comparing the melting temperature obtained during the 1st heating of pure PLA6100 with those of PLA6100 masterbatches with 1 and 3 wt % of inorganic pigments (Ti, PXA, Fe), minimal differences in melting temperatures were detected. During the 1st heating, a decrease in the enthalpy of melting of PLA masterbatches due to an addition of inorganic pigments was observed. Exothermic peak with a maximum at 103.8 °C, corresponding to the crystallisation temperature, was detected during the cooling of pure PLA (Table 2). Crystallisation of colour PLA masterbatch occurred at significantly lower temperatures. A comparison of pure PLA6100 with PLA6100 masterbatches with 1 and 3 wt % of inorganic pigments showed an increase in the enthalpy of crystallisation during cooling caused by the addition of inorganic pigments.

During 2nd heating, glass temperature T_g of pure PLA and PLA masterbatches was maintained and an increase in the enthalpy of melting of PLA masterbatches due to the addition of inorganic pigments was observed. This difference can be explained by a change in the formation of different crystalline modifications of PLA. During the 2nd heating, pure PLA6100 showed cold crystallisation with a maximum exothermic peak at 128.1 °C (Table 3), while for colour PLA masterbatches, cold crystallisation occurs at lower temperatures (94—104 °C) and shows another peak of cold crystallisation at 159—161 °C, where pure PLA does not crystallize.

Comparing melting temperature T_m of the 1st heating with that of the 2nd heating, a slight decrease in the melting temperature during the 2nd heating for both pure PLA6100 and for PLA6100 masterbatches can be seen.

The addition of pigments showed no effect on T_g and the differences in T_g are minimal (Tables 4 and 5). Crystallisation temperature of pure PLA fibres and of PLA fibres with 0.1 and 0.5 wt % of inorganic pigments revealed minimal differences.

Tab. 3. Glass temperature (T_g), cold crystallisation temperature (T_{cc}), melting temperature (T_m), enthalpy of relaxation (ΔH_{er}), enthalpy of cold crystallisation (ΔH_{cc}), and enthalpy of melting (ΔH_m) of prepared colour masterbatches obtained during the 2nd heating.

Composition of masterbatches	2nd heating							
	T_g [°C]	ΔH_{er} [J/g]	T_{cc1} [°C]	ΔH_{cc1} [J/g]	T_{cc2} [°C]	ΔH_{cc2} [J/g]	T_m [°C]	ΔH_m [J/g]
PLA6100	62.1	1.5	128.1	15.0			173.9	6.5
PLA6100+1 %Ti	62.1	0.5	94.0	7.9	159.7	2.1	174.5	34.7
PLA6100+3 %Ti	61.9	0.8	94.2	11.8	159.3	3.4	173.8	29.5
PLA6100+1 %PXA	62.1	1.3	94.7	21.5	158.9	3.7	174.1	21.7
PLA6100+3 %PXA	62.2	1.4	103.5	26.3	161.3	3.3	174.3	14.7
PLA6100+1 %Fe	62.0	0.9	93.9	16.8	159.2	3.2	174.2	27.7
PLA6100+3 %Fe	61.9	1.3	94.5	18.5	159.4	3.7	174.0	22.3

Tab. 4. Glass temperature (T_g), crystallisation temperature (T_c), enthalpy of crystallisation (ΔH_c) melting temperature (T_m), and enthalpy of melting (ΔH_m) of prepared colour masterbatches obtained during the 1st heating, and crystallisation temperature (T_c) and enthalpy of crystallisation (ΔH_c) of prepared colour masterbatches obtained during cooling.

Composition of fibres	1st heating					Cooling	
	T_g [°C]	T_c [°C]	ΔH_c [J/g]	T_m [°C]	ΔH_m [J/g]	T_c [°C]	ΔH_c [J/g]
PLA6100	56.3	74.7	2.3	174.4	41.9	98.9	27.8
PLA6100+0.1 %Ti	55.8	74.6	2.8	173.7	47.5	98.5	30.5
PLA6100+0.5 %Ti	58.9	75.7	16.6	172.4	32.5	99.6	33.4
PLA6100+0.1 %PXA	57.3	77.1	2.4	174.5	46.7	96.6	32.5
PLA6100+0.5 %PXA	59.1	76.2	15.8	173.4	32.0	95.4	31.4
PLA6100+0.1 %Fe	56.8	74.1	2.2	173.4	48.9	98.2	31.1
PLA6100+0.5 %Fe	58.9	76.0	10.6	172.2	37.2	95.7	30.3

During the 1st heating, PLA fibres with 0.1 wt % pigment content showed the enthalpy of crystallisation decrease with an increase in the drawn ratio due to the change in the crystalline modification and orientation of PLA. Cold crystallisation was measured for all PLA fibres with 0.1 and 0.5 wt % of all three inorganic pigments. Endothermic peak with maximum at 174.4 °C, corresponding to the melting temperature, was detected during the 1st heating. The addition of a higher pigment content (0.5 wt %) resulted in a decrease in the enthalpy of melting. PLA fibres with the 0.1 wt % pigment content were drawn at a higher temperature with higher values of maximum drawn ratios. Considering an oriented system, the enthalpy of melting increases with the increasing temperature, which is probably due to higher orientation leading to higher crystallisation ability. In regard to pigment addition, 0.1 wt % of pigment behaves as a nucleating agent that promotes the crystallisation process and increases the crystallinity.

Exothermic peak with a maximum at 98.9 °C, corresponding to the crystallisation temperature, was detected during the cooling (Table 4). Comparison of pure PLA fibres with pigmented PLA fibres, an increase in the enthalpy of crystallisation during cooling due to inorganic pigments addition was observed.

During the 2nd heating (Table 5), changes in the glass temperature of pure PLA fibres and those with 0.1 and 0.5 wt % pigment content were not observed. Since PLA is a semi-crystalline polymer, crystallisation during the 2nd heating results in a decrease in the content of the amorphous phase and an increase in the content of the crystalline phase, thereby eliminating the manifestation of T_g which is related to the amorphous phase.

Comparing the melting temperature obtained during the 1st and 2nd heating of pure PLA fibres and of PLA fibres with 0.1 and 0.5 wt % of inorganic pigments, minimal differences in the melting temperature were observed. The enthalpy of melting obtained during the 1st and 2nd heating of pure PLA fibres and of PLA fibres with 0.1 and 0.5 wt % of inorganic pigments decreased during the 2nd heating.

Mechanical properties of PLA fibres

The effect of the addition of 0.1 and 0.5 wt % of inorganic pigments (Ti, PXA, Fe) on mechanical properties such as tenacity at break σ, elongation at break ε, and Young's modulus E for PLA fibres drawn to maximum drawn ratio λ_{max} was monitored and the dependencies of tenacity at break, elongation at break, and Young's modulus on fibres composition were constructed(Figures 3a–c). Fineness of individual PLA fibres and pigmented PLA fibres was measured and the dependence of fineness of fibres T_t on their composition was constructed (Figure 3d).

The maximum drawn ratio of PLA fibres was significantly affected by the concentration of pigments; 0.1 wt % of pigments had minimal or positive effect on the values of λ_{max} at the drawing temperature of 105 °C. The higher pigment content (0.5 wt %) caused worsening of the drawing process and PLA fibres with 0.5 wt % of pigment content could not be drawn at the drawing temperature of 105 °C; instead, drawing temperature of 95 °C was used. At the drawing temperature of 95 °C, the maximum drawn ratio for all pigmented PLA fibres dropped to $\lambda_{max} = 2.5$ (see Table 1).

The tenacity at break of fibres is defined as the force required to break the fibre relative to the fineness of the fibres. From the dependencies in Figure 3a, an increase in the tenacity at break of fibres due to the addition of 0.1 wt % of pigment content to pure PLA fibres can be seen. This is probably caused by the pigment acting as a nucleating agent

Tab. 5. Cold crystallisation temperature (T_{cc}), melting temperature (T_m), enthalpy of cold crystallisation (ΔH_{cc}) and enthalpy of melting (ΔH_m) of prepared colour masterbatches obtained during the 2nd heating.

Composition of fibres	2nd heating					
	T_{cc1} [°C]	ΔH_{cc1} [J/g]	T_{cc2} [°C]	ΔH_{cc2} [J/g]	T_m [°C]	ΔH_m [J/g]
PLA6100	119.5	1.6	157.9	1.5	173.7	34.7
PLA6100+0.1 %Ti	106.9	3.9	156.9	2.1	172.9	38.5
PLA6100+0.5 %Ti	111.2	5.1	157.3	0.1	173.1	36.5
PLA6100+0.1 %PXA	118.9	5.6	158.3	1.7	173.1	35.7
PLA6100+0.5 %PXA	105.3	5.4	157.3	2.3	172.6	34.7
PLA6100+0.1 %Fe	116.8	2.3	156.8	2.6	172.8	40.9
PLA6100+0.5 %Fe	118.3	2.5	156.9	1.8	172.8	38.2

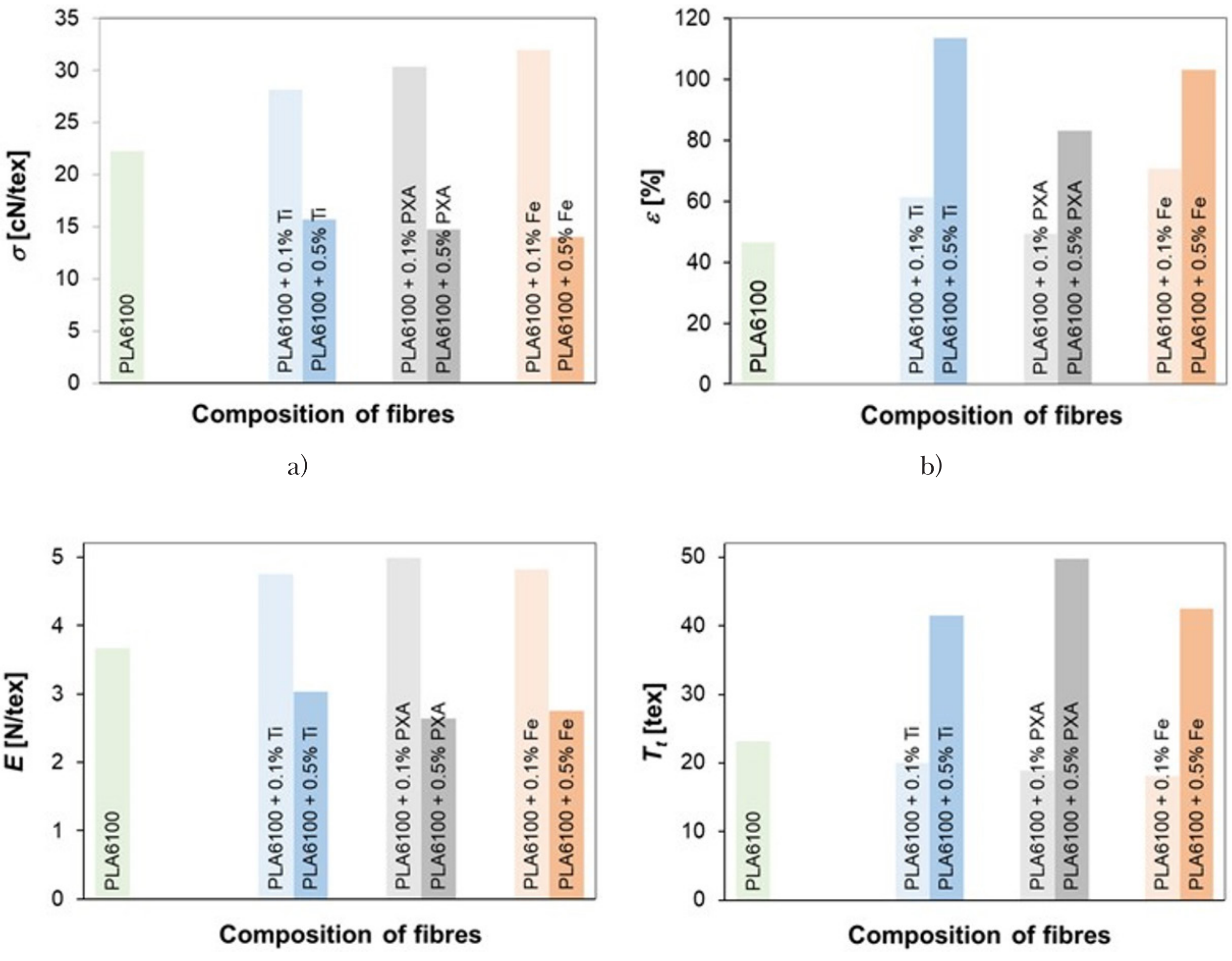

c) d)

Figure 3. Dependence of tenacity at break σ (a), elongation at break ε (b), Young's modulus E (c), and fineness of fibres T_t (d) on PLA fibres composition

at 0.1 wt %, thus increasing the crystallinity and improving mechanical properties of the fibres. At the higher pigment content of 0.5 wt %, a decrease in the tenacity at break of PLA fibres can be observed. Higher pigment content can lead to higher agglomeration of pigment particles, worsening thus the mechanical properties of the fibres. From the point of view of drawing temperature, an increase in the tenacity at break of fibres was observed in PLA fibres with 0.1 wt % pigment content drawn at 105 °C compared to those with 0.5 wt % pigment content drawn at 95 °C due to the increased drawing temperature. At higher drawing temperatures, fibres with higher orientation were prepared. Higher orientation of the chains causes tighter arrangement of macromolecules, thereby increasing the number and strength of intermolecular interactions, which is reflected in higher tenacity at break of fibres. A comparison of the dependence of tenacity at break on fibres composition (Figure 3a) with that of the dependence of elongation at break (Figure 3b), elongation at break of fibres has been confirmed to decrease with the increasing tenacity at break of fibres.

The elongation at break of fibres is given by the greatest elongation that the material achieves when it breaks. From the dependence of elongation at break on fibres composition (Figure 3b), an increase in the elongation at break of fibres with 0.1 and 0.5 wt % pigment content was observed compared to pure PLA fibres. The highest effect of the addition of pigments was observed in PLA fibres with 0.5 wt % pigment content. The higher the pigment content, the higher the elongation at break of fibres.

Young's modulus was another monitored quantity, it is a measure of resistance to deformation and depends on crystallinity and orientation. From the dependence of Young's modulus on fibres composition (Figure 3c), it can be seen that all PLA fibres containing 0.1 wt % of pigments have higher modulus than pure PLA fibres, while a decrease in Young's modulus in PLA fibres with 0.5 wt % pigment content was observed. All PLA fibres containing 0.5 wt % of pigments were drawn at the maximum drawn ratio $\lambda_{max} = 2.5$ at 95 °C. It follows that oriented systems with lower drawn ratio have lower Young's modulus.

From the dependence of fineness on fibres composition (Figure 3d), PLA fibres containing 0.1 wt % of pigments have shown lower fineness than pure PLA fibres, while an increase in fineness of PLA fibres with 0.5 wt % pigment content was detected.

Conclusion

This work was focused on the preparation of colour PLA masterbatches and PLA fibres. The influence of inorganic pigments on the rheological and thermal properties of the prepared colour PLA masterbatches and that of colour PLA masterbatches composition and PLA fibres drawn ratio on thermal and mechanical properties of PLA fibres were determined. Properties of the prepared PLA masterbatches subsequently affect the processability of PLA during fibre preparation. Based on the obtained data, the results can be formulated into the following conclusions:

1. Rheological properties of colour PLA masterbatches were determined using a capillary viscosimeter and a rotary rheoviscosimeter with geometry plate/plate. By adding 1 or 3 wt % of inorganic pigments PXA and Fe to pure PLA6100, small changes in the dependences of viscosity on shear rate were obtained on the capillary viscosimeter. A more significant drop in viscosity was detected after the addition of Ti to pure PLA compared to other pigments (PXA, Fe). An increase in the viscosity (dependences of viscosity on shear rate obtained on the rotary rheoviscosimeter with a geometry plate/plate) due to the addition of a higher pigment content (3 wt %) was observed compared to colour PLA masterbatches with 1 wt % pigment content. The largest increase in viscosity was observed when 3 wt % of PXA were added to pure PLA.
2. Thermal properties of prepared colour PLA masterbatches and PLA fibres were determined by DSC analysis. By adding 1 or 3 wt % pigment content to pure PLA6100, a drop in T_g of colour PLA masterbatches during the 1st heating was observed. The increased content of inorganic pigments (3 wt %) does not affect the glass temperature. During the 1st heating, cold crystallisation was measured for colour PLA masterbatches with all three pigments. During the 2nd heating, pure PLA6100 showed cold crystallisation with a maximum exothermic peak at 128.1 °C. And with colour PLA masterbatches, cold crystallisation occurs at lower temperatures (94–104 °C) and shows another peak of cold crystallisation at temperatures of 159–161 °C, where pure PLA does not crystallize. Considering the thermal properties of PLA fibres, the addition of pigment has no effect on T_g and the differences of T_g are minimal. During the 1st heating, cold crystallisation was measured for all pigmented PLA fibres with 0.1 and 0.5 wt % pigment content. An increase in the enthalpy of crystallisation during cooling due to the addition of inorganic pigments occurred. During the 1st heating, the addition of a lower pigment content (0.1 wt %) resulted in an increase in the enthalpy of melting, which increases with the increasing drawing temperature. A comparison of the enthalpy of melting obtained during the 1st and the 2nd heating of pure PLA fibres and of PLA fibres with 0.1 and 0.5 wt % of inorganic pigments, revealed a decrease in the enthalpies of melting during the 2nd heating.
3. A comparison of PLA fibres with 0.1 wt % pigment content drawn at 105 °C with PLA fibres with 0.5 wt % pigment content drawn at 95 °C showed an increase in the tenacity at break of fibres due to increased drawing temperature. A decrease in the tenacity at break of PLA fibres with higher (0.5 wt %) pigment content was observed. Higher pigment content can lead to a higher agglomeration of pigment particles, thus worsening the mechanical properties of the fibres. The highest effect on elongation at break was observed in PLA fibres with 0.5 wt % pigment content. The higher the pigment content, the higher the elongation at break of fibres. By comparing PLA fibres with 0.1 wt % pigment content and those with 0.5 wt % pigment content, a decrease in Young's modulus was detected for PLA fibres with 0.5 wt % pigment content. All PLA fibres containing 0.5 wt % of pigments were drawn at the maximum drawn ratio $\lambda_{max} = 2.5$ at 95 °C. It follows that oriented systems with lower drawn ratio have lower Young's modulus. By adding 0.5 wt % of pigment to pure PLA fibres, an increase in PLA fibres fineness can be seen.

Acknowledgement

This work was supported by the Slovak Research and Development Agency under the contract No. APVV-21-0172 and contract No. APVV-20-0193.

References

Alexy P (2016) Procesy spracovania polymérov, STU Bratislava, 6–46.

Balakrishnan NK et al. (2020) Polymers 12(10): 2321.

Balakrishnan NK et al. (2022) Polymers 14(22): 5021.

Benetti F et al. (2014) IPSP 2014 2: 23.

Casalini T et al. (2019) Front. Bioeng. Biotechnol. 7: 259.

Chen Ch et al. (2018) Polymer Testing 70: 526–532.

Farah S et al. (2016) Advan. Drug Delivery Reviews 107: 367.

Grishanov S (2011) Handbook of Textile and Industrial Dyeing 1: 28–63.

Gupta B et al. (2007) Progress in Polymer Sci. 32(4): 455–482.

Hricová M et al. (2004) Vlákna a textile (Fibres and Textiles), 11(4): 99–105.

Koenig K et al. (2020) Materials (Basel) 13(5): 1055.

Marcinčin A (1989) Procesy prípravy syntetických vlákien, STU Bratislava, 10–255.

Markarian J (2009) Plastics, Additives and Compounding 11(4): 12–15.

Niaounakis M (2015) Biopolymers: Processing and Products 5: 215–262.

Parra-Campos A et al. (2020) DYNA 87(212): 31–37.

Prchal V et al. (1993) Chemická technológia textilu, SVŠT Bratislava.

Rasal R et al. (2010) Progress in Polymer Science 35(3): 338–356.

Rawal A et al. (2014) Advances in Filament Yarn Spinning of Textile and Polymers, Woodhead publishing, 4: 75–99.

Tolinski M (2009) Additives for Polyolefins 9: 137–156.

Trotman ER (1970) Dyeing and Chemical technology of Textile fibres, Griffin London.

Vroman I, Tighzert L (2009) Materials 2(2): 307–344.

Yang Y et al. (2021) Textile Research J. 91(13–14): 1641–1669.

sciendo

Extraction of bioactive coumarins from lime peel as sample pretreatment before chromatographic analysis

Lucia Krasňanská, Katarína Hroboňová, Andrea Špačková

Slovak University of Technology in Bratislava, Faculty of Chemical and Food Technology,
Institute of Analytical Chemistry, Radlinského 9, SK-812 37 Bratislava, Slovak Republic
luci.krasn@gmail.com, katarina.hrobonova@stuba.sk

Abstract: Analysis of lime peel was applied to assess their suitability for various intended purposes, e.g., application in perfumery, cosmetics, and cleaning products, or as a source of bioactive or other value-added compounds. Targeted analysis allows wider usability of the waste part of these natural materials. In the present study, a novel, efficient, lab-simple, time-saving analytical method for coumarins determination in lime peel, including sample pretreatment by extraction and quantification by HPLC with fluorescence detection (FLD), is introduced. Optimal conditions of ultrasound assisted extraction included water as extraction solvent, temperature of 40 °C, and extraction time of 10 min. A magnetic molecularly imprinted polymer was employed as solid phase extraction adsorbent for primary extract cleaning, isolation, and enrichment of coumarins before chromatographic analysis. Recovery of herniarin and umbelliferone was more than 86 % ((RSD ≤ 4.8 %). Linear range of 50—1000 ng/mL with correlation coefficient above 0.998 was obtained for the proposed HPLC-FLD method. The limit of quantification was 8.2 and 44 ng/mL for herniarin and umbelliferone, respectively. These results show that the proposed sample pretreatment procedure is suitable for analytical purposes and is perspective also for the analysis of other citrus samples, as well as for future scale-up preparative isolation of bioactive coumarins from citrus peel.

Keywords: lime peel, coumarins, ultrasound assisted extraction, selective molecularly imprinted extraction, high performance liquid chromatography

Introduction

Natural materials are sources of many bioactive compounds useful in the treatment of a wide spectrum of diseases. They can be components of food, food supplements and cosmetics, as well as cleaning products (fragrance ingredients).

Coumarins, secondary plant metabolites, have an important function in the biochemistry and physiology of plants (Önder, 2020). From a chemical point of view, coumarins are organic heterocyclic compounds and their chemical structure is formed by 1,2-benzopyrone, which consists of a benzene ring connected to a pyrone ring (Annunziata et al., 2020). Citrus fruits are considered very important for the medical, pharmaceutical, perfumery and cosmetic industries due to their nutritional, medicinal, and fragrance properties (Raghavan and Gurunathan, 2021). Natural lemon peel powder was also applied as a heterogeneous catalyst for the synthesis of coumarin based heterocyclic compounds (Ganesh et al., 2020). Citrus peels can be also used in "zero waste" management at home, to cleaning various surfaces or as air freshener; however, grated fine "crumbs" from the peels (mainly lemon and lime) are also used to flavour dishes. Approximately 40—50 % of the total mass of citrus fruit is peel, which is generally considered as waste. This part of fruits is also a source of bioactive compounds, including coumarins, but some may also have undesirable effects (e.g., coumarin is regulated for the use in food and cosmetics products (Regulation (EC) No. 1334/2008; Regulation (EC) No. 1223/2009); herniarin is prohibited to be used in fragrance compounds (Safety Assessment of Citrus Peel-Derived Ingredients as Used in Cosmetics, 2015)). Citrus waste parts are also used as a source of other high value-added compounds with beneficial properties (e.g., pectin, ascorbic acid, phenolic acids). Several studies reported bioactive simple coumarins, such as umbelliferone and herniarin (Fig. 1), in citrus (Ramírez-Pelayo et al., 2019; Jungen et al., 2021). Higher amounts of these compounds have been determined in peels compared with the edible parts of the fruit (Singh et al., 2020). Antituberculotic, antiinflammatory, antidiabetic, antibacterial, antifungal, and antioxidant properties have been indicated for umbelliferone (Hussain et al., 2019; Mazimba, 2017), while herniarin has demonstrated antiinflammatory, antioxidant, anti-proliferative, and antinociceptive effects (Bose and Pattanayak, 2019). Despite their beneficial effects, they can cause skin, eye or respiratory irritation (at high concentrations), which needs further pharmacological research (Denisow-Pietrzyk et al., 2019; Lin et al., 2023).

umbelliferone herniarin

Fig. 1. Chemical structure of simple coumarins investigated in this study.

Thus, the utilisation of waste parts of citrus requires a simple, reproducible, and time-consuming analytical method for targeted analysis and quality evaluation. Sample pretreatment is an important step for subsequent analytes determination, e.g. chromatographic methods. Several extraction techniques, traditional and advanced, have been used for citrus sample pretreatment. Traditional methods, including Soxhlet extraction with methanol (Abosharaf et al., 2020), maceration with ethanol or ethylacetate (Munawaroh, 2017), as well as distillation (Li et al., 2021), were applied for the extraction of bioactive compounds including coumarins. Advanced extraction techniques, such as ultrasound assisted extraction (UAE) with water, methanol/water (80/20, v/v) or methanol (Ramírez-Pelayo et al., 2019; Zhao et al., 2020; Jungen et al., 2021; Aznar et al. 2022), microwave assisted extraction (MAE) with water or ethanol (Ciriminna et al., 2017), supercritical fluid extraction (SFE) with CO_2 or CO_2/ethanol, were also used for the isolation of coumarins from different citrus fruits. Solid phase extraction is a frequently used technique for primary extract purification and analyte preconcentration (Aznar et al. 2022; Li et al., 2019; Fan et al., 2015). In response to the requirement of rapid, efficient, and selective extraction, molecularly imprinted polymers (MIPs) have received attention as extraction materials. MIP based extraction is an innovative separation technique with many advantages, which include high selectivity, chemical and mechanical resistance, as well as material reusability. MIP production process is controlled (components of reaction mixture, type of polymerisation procedure, conditions) so as to obtain many complementary cavities with the memory of size, shape, and functional groups of template molecules. The cavities, generated after template removal from the polymeric matrix, have specific recognition and selectivity for the target molecule and sometimes also for its analogues. MIP selectivity is very advantageous in determining compounds in a complex sample, such as natural materials (Chen et al., 2016; Jablonský et al., 2020). In citrus analysis, a hybrid organic-inorganic monolithic MIP allowed the determination of flavone hesperetin (Wang et al., 2018) and of benzimidazole residues (Liang et al., 2019).

This article is devoted to the analysis of lime peel for the purpose of qualitative and quantitative evaluation of selected coumarins. Sample pretreatment procedures for the extraction of coumarins from lime have been developed. Solvent extraction and solid phase extraction with a selective molecularly imprinted adsorbent were incorporated in the analytical method for the determination of selected coumarins: umbelliferone and herniarin.

Material and Methods

Materials and Chemicals

Methanol (HPLC grade) and acetic acid (for analysis grade) were purchased from Centralchem (Slovakia). Umbelliferone (7-hydroxycoumarin) and herniarin (7-methoxycoumarin) (both 98 %) were purchased from Sigma Aldrich (USA). Lime samples (10 pieces of acid-fruit type, country of origin Mexico) were purchased from a local supermarket. Citrus peels were removed manually, cut into small pieces, and stored in a freezer before analysis.

Solvent extraction

Stirring-assisted solvent extraction: Finely chopped lime peel (1 g) was mixed with extraction solvent (3 mL), deionised water or methanol. The mixture was stirred for 30 min at the constant temperature of 23 or 40 °C. The extract was centrifuged for 1 min at 3000 rpm. The supernatant was collected and stored at –18 °C until HPLC-FLD analysis.

Ultrasound-assisted solvent extraction: An extraction solvent (3 mL) was added to finely chopped lime peel (1 g). The extraction solvent, deionised water or methanol, was added and the mixture was placed in an ultrasonic bath (45 KHz) with constant temperature (23 or 40 °C) for a certain time (10, 20 or 30 min). The extract was centrifuged (1 min, 3000 rpm) and supernatant was stored at –18 °C until HPLC-FLD analysis.

The tested extraction conditions are summarised in Table 1. Extractions were performed in triplicate.

Solid Phase Extraction

Solid Phase Extraction (SPE) was performed with lab-made Fe_3O_4@MIP-umbelliferone (Machyňáková and Hroboňová, 2017). For batch extraction, an aliquot of UAE sample extract (1.5 mL), or coumarins standard solution, or primary aqueous UAE sample extract (obtained at optimal conditions) were mixed with Fe_3O_4@MIP adsorbent (0.1 g, preconditioned with 1.5 mL of methanol/acetic acid (9/1 v/v) and water) and stirred for 30 min (180 rpm) at 23 °C. The sorbent was separated using an external magnet, washed with water (1 mL, 5 min, 180 rpm), and dried at 90 °C. Fe_3O_4@MIP was mixed with methanol/acetic acid (1.5 mL, 9/1 v/v) and stirred for 30 min (180 rpm). The sorbent was separated

Tab. 1. Experimental conditions for the extraction of coumarins from lime peel.

Experiment number	Extraction method	Temperature (°C)	Time (min)	Solvent
1	UAE	23	30	deionised water
2	UAE	40	10	deionised water
3	UAE	40	20	deionised water
4	UAE	40	30	deionised water
5	UAE	40	10	methanol
6	UAE	40	20	methanol
7	UAE	40	30	methanol
8	stirring	23	30	deionised water
9	stirring	40	30	deionised water
10	stirring	23	30	methanol
11	stirring	40	30	methanol

using an external magnet and stored at −18 °C until the HPLC-FLD analysis.

HPLC analysis

Liquid chromatograph (series 1200, Agilent Technologies, Germany) consisting of a binary pump, automatic injector, column oven, and fluorescence detector (FLD) was used. Separations were performed in reverse phase mode using a Kinetex C18 column (100 mm × 4.6 mm I.D., 5 µm particle size, Phenomenex, USA). Mobile phase consisted of 1 % aqueous solution of acetic acid (A) and 1 % solution of acetic acid in methanol (B). The gradient elution process was as follows: 0—12 min linear gradient for B component from 30 to 45 %, then to 100 % of B over 0.5 min, and held at 100 % of B for 2 min. Flow rate of mobile phase was 1.0 mL/min, injection volume was 20 µL, and column temperature was maintained at 23 °C. Fluorescence spectra were taken in the wavelength range of 250—550 nm, and chromatograms were recorded at excitation wavelength of 320 nm and emission wavelength of 450 nm. The HPLC-FLD method (Hroboňová and Špačková, 2020) was modified and verified using the system suitability test (umbelliferone: t_R = 6.49 ±0.03 min, k = 3.33 ±0.01, H = 0.013 mm; herniarin: t_R = 12.17 ±0.03 min, k = 7.11 ±0.02, H = 0.004 mm; R_s(umbelliferone/herniarin) = 16.6; analyses were realised in triplicate at the concentration level of 0.5 µg/mL), and validated which resulted in the limit of detection (LOD = 3.0/12.5 ng/mL), limit of quantification (LOQ = 8.2/44.0 ng/mL) for umbelliferone and herniarin, respectively, and linearity (R^2 = 0.9998/0.9981 in the concentration range of 50—1000 ng/mL for umbelliferone and herniarin, respectively.

Statistical analysis

Microsoft Excel 2018 (Microsoft Office, USA) and OriginPro 2018 (OriginLab Corporation, USA) was used for data processing (linear regression to determine calibration curve coefficients and parameters for LOD, LOQ, and RSD % calculation) and visualisation.

Results and discussion

The first step in the separation of desired natural coumarins from citrus peel is solvent extraction. Solid phase extraction with an adsorbent selective for coumarins, molecularly imprinted polymeric adsorbent, was performed for primary extract purification or analytes preconcentration. These sample pretreatment procedures were optimised to obtain extract suitable for the HPLC-FLD analysis.

Optimisation of the solvent extraction procedure

Solvent extraction is the most common sample pretreatment technique for solid matrices to separate/isolate compounds; solvent selection is crucial for obtaining high extraction efficiency. Solubility of analytes, selectivity, and safety should also be considered in solvent selection. Organic solvents are mostly used in extraction of coumarins from different matrices; however, extraction methods operating at higher temperatures, pressures, or with energy field assistance offer some advantages such as lower organic solvent consumption and shorter extraction time (Rodríguez-García and Raghavan, 2022).

In this work, optimisation of solvent extraction parameters (type of solvent, extraction technique, temperature, time) was performed by one-variable-at-a-time method for a sample of lime peel in which coumarins were detected. Solvents, methanol and deionised water, and conventional stirring assisted and advanced ultrasound assisted extraction procedures were used for the extraction. The yield of the targeted coumarins obtained under different extraction conditions (Table 1) is presented in Fig. 2. Higher temperature (40 °C) increases the solubility

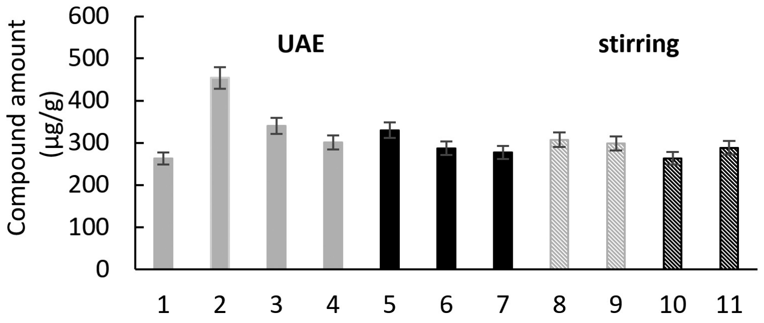

herniarin

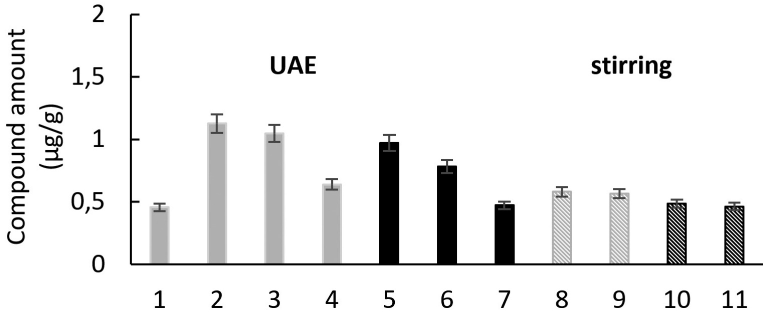

umbelliferone

Fig. 2. Amount of coumarins extracted from lime peel at different extraction conditions.
Legend: ■ — deionised water, ■ — methanol; n = 3.

of the compounds and diffusion of solvent into the sample matrix resulting in higher or comparable extraction efficiency for both extraction solvents and type of extraction procedures compared to laboratory temperature (23 °C) extractions (extraction time of 30 min, experimental conditions 1 and 4, 8 and 9, 10 and 11 listed in Table 1). However, such high temperatures may cause the decomposition of thermolabile components and extraction of undesirable impurities (e.g., umbelliferone is chemically and thermally unstable, which may result in many compounds formed during its reflux extraction by methanol, ethanol, buffers, and buffered or non-buffered alcohol/water mixtures (Dawidowicz et al., 2018)).

Extraction efficiency depends also on the extraction time and mostly increases with the increased extraction time in a certain time interval. However, increasing time does not significantly affect the extraction efficiency after the equilibrium of the solute is reached inside and outside the sample matrix (Zhang et al., 2018). In addition, long exposure times at high temperatures can lead to lower yield, e.g., due to the decomposition of compounds (Che Sulaiman et al., 2017). The conventional, stirring-assisted, extraction is inexpensive compared to advanced (e.g., UAE) techniques, but has varied efficiency and can be time consuming. In this study, the extraction time for conventional extraction of coumarins was set to 30 min for both investigated solvents. This extraction time was chosen due to sufficient penetration of solvent in matrix. Results in Fig. 2 show no significant difference between the amount of extracted compounds obtained by either technique at the same extraction time (30 min, solvent/sample ratio: 3 mL/1 g, 40 °C). UAE is efficient also within a short extraction time due to the employment of ultrasonic waves; however, this method is costly (Carreira-Casais et al., 2021). Using the UAE procedure in the tested time interval of 10–30 min and at the temperature of 40 °C (based on the previous experiment; this temperature is well maintained, as the solution heats up during UAE.), higher yields of coumarins were achieved in 10 min. A comparison of the results of coumarins extraction from lime peel using both techniques showed that UAE is more effective. In addition, the highest yields of coumarins were obtained in a shorter extraction time (10 min) using the UAE procedure compared to the stirring-assisted extraction realised at longer time (30 min), which can be translated into economic benefits. Thus, UAE can be proposed as a more suitable sample pretreatment technique for the extraction of coumarins from citrus peel. Optimal conditions for the extraction of coumarin derivatives, umbelliferone and herniarin, were set as: UAE with deionised water as the extraction solvent at 40 °C and extraction time of 10 min. These conditions are suitable for obtaining the primary extract from lime peel and could eventually be applicable also for other citrus fruits (e.g., lemon, orange,

Tab. 2. Summary of selected extraction and purification techniques for coumarins from citrus fruits.

Sample	Coumarins^a	Technique	Solvent system	Conditions	Ref.
	Traditional extraction techniques				
lemon rind	umbelliferone (kvalitative analysis)	Soxhlet extraction	petrolether reextraction with acetone	solvent/sample ratio: 5 mL/1 g time: 12 h (reextraction)	Jose et al., 2014
lemon peel	herniarin (0.01 mg/L of extract)	Maceration	ethanol	time: 30 days	Arigo et al., 2021
lime peel	coumarins^b		ethylacetate	solvent/sample ratio: 11 mL/1 g (dry peel), 5 mL/1 g (fresh peel) time: 24 h (3×)	Munawaroh, 2017
lemon peel	herniarin (1.3 mg/L of oil)	Distillation	water	ratio solvent/sample: 2 mL/1 g	Li et al., 2021
	Advanced extraction techniques				
peel and waste parts of lemon, orange, grapefruit	coumarins^b	MAE	distilled water	solvent/sample ratio: 0.8 mL/1 g time: 60—80 min	Ciriminna et al., 2017
lemon, lime peel	herniarin (185 mg/kg of lime flavedo; 3.6 mg/kg of lemon flavedo)	UAE	deionized water	solvent/sample ratio: 8 mL/1 g time: 30 s	Jungen et al., 2021
citrus peel (sweet orange, tangerine, lime)	coumarins^b		methanol	solvent/sample ratio: 3 mL (3×) /1 g time: 30 min	Ramírez-Pelayo et al., 2019
citrus peel	scoparone (0.1—0.5 %) and other coumarins^b	SFE	CO_2	temperature: 40 °C pressure: 10 MPa, CO_2 flow = 1.76 kg/h	Jerkovic et al., 2015
Citrus aurantium amara peel	coumarins^b		CO_2 + ethanol	pressure: 17 MPa CO_2 flow = 2.7 kg/h extraction time = 120 min; static time = 50 min	Trabelsi et al., 2016

MAE — microwave assisted extraction, UAE — ultrasound assisted extraction, SFE — supercritical fluid extraction.
^{a}samples also contain other coumarins/furanocoumarins but only results for the target analytes are shown.
^{b}other derivatives of coumarin/furanocoumarins.

pomelo, grapefruit). HPLC-FLD chromatogram of the lime peel extract is shown in Fig. 3B. Table 2 provides an overview of the traditional and advanced extraction techniques used extraction of bioactive substances, including coumarin derivatives, from citrus fruits. Traditional techniques usually require long extraction time (several hours) and the use of organic solvents (ethylacetate, petrolether, ethanol). Advanced techniques involved in coumarins extraction, such as UAE, SFE, MAE, are mostly "greener" and they allow for efficient extraction in shorter extraction time (several minutes). The proposed UAE procedure is an example of efficient and fast extraction suitable as a sample preparation method for targeted HPLC-FLD analysis.

Selective MIP based solid phase extraction

Solvent extraction is considered a good technique for organic compound extraction from different complex matrices; however, complex extract is mostly unsuitable for HPLC analysis in terms of possible interferences and/or concentration of analytes below LOD. Thus, the combination of UAE and subsequent SPE is useful for primary extract cleaning or analytes preconcentration with a high preconcentration factor. In addition, the use of a selective adsorbent enables the targeted extraction and isolation of analytes.

In the present work, aqueous extract of citrus peel (prepared by proposed optimal UAE conditions), was treated by batch SPE using a group selective magnetic molecularly imprinted polymeric adsorbent (Fe_3O_4@MIP imprinted with the umbelliferone molecule) produced by surface imprinting technology (Machyňáková and Hroboňová, 2017). The core-shell structure of the adsorbent (MIP coated on the surface of magnetic particles, Fe_3O_4) contain specific recognition sites for template molecules on

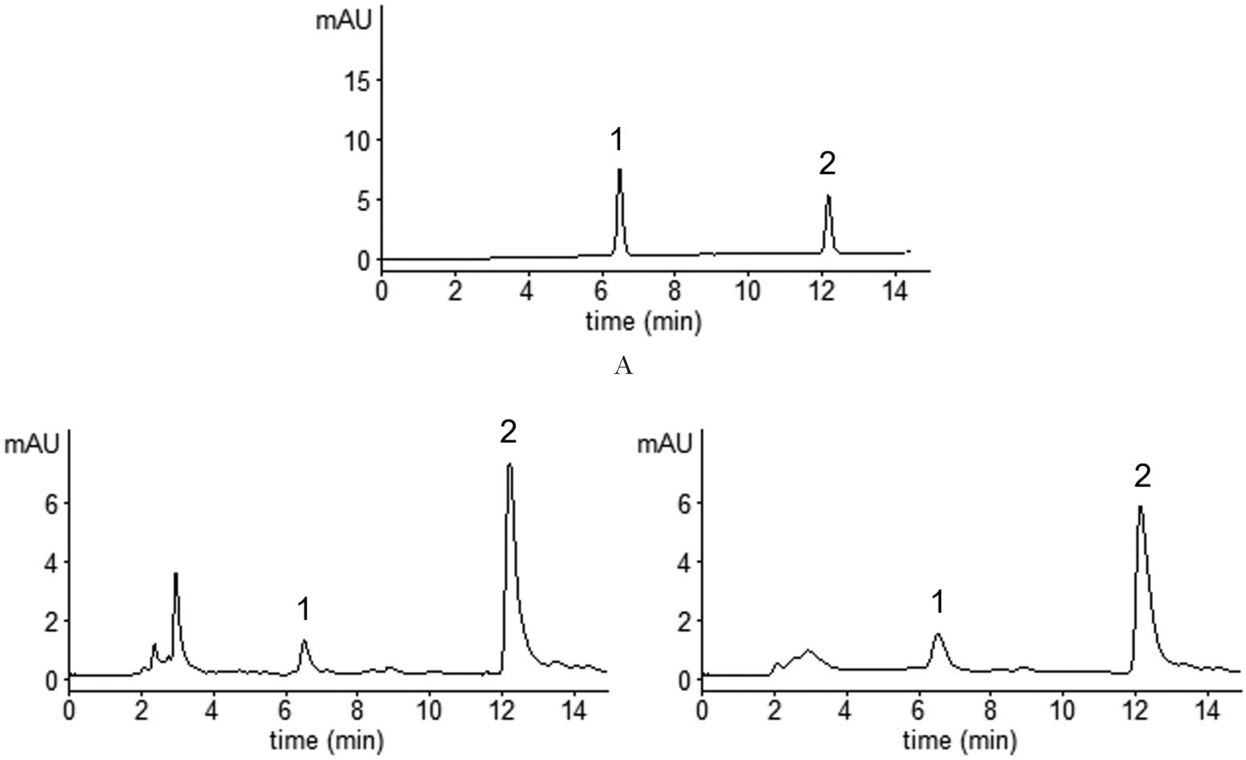

A

B

C

Fig. 3. HPLC-FLD chromatograms of standard solution of umbelliferone and herniarin (A), UAE aqueous lime peel extracts (B) and extract obtained by combined UAE and Fe_3O_4@MIP batch solid phase extraction sample pretreatment procedure (C). Legend: 1 — umbelliferone, 2 — herniarin.

the surface of carrier particles so that the adsorbent can easily rebind and remove the templates. The advantage of Fe_3O_4@MIP extraction is lower solvent consumption and the possibility of similar performance in the separation of solid and liquid phases with external magnetic field, as well as undemanding method development. The Fe_3O_4@MIP-SPE procedure used in this study includes standard steps: adsorbent conditioning, analyte sorption from sample solution, adsorbent washing with water, analyte elution with methanol/acetic acid mixture (9/1, v/v) (extraction conditions were optimised in a previous work, Machyňáková and Hroboňová, 2017). SPE was verified by a recovery study with reference solution of coumarins at the concentration level of 1 µg/mL providing satisfactory recovery values of 93.2 % and 86.9 % (RSD ≤ 4.8 %, n = 3) for umbelliferone and herniarin, respectively.

Using the proposed extraction procedure (UAE combined with Fe_3O_4@MIP) and HPLC-FLD quantification method, lime peel was analysed. Umbelliferone and herniarin were detected in the lime peel sample (comparing the elution characteristics with standards (Fig. 3A) and their fluorescence spectra) and quantified by the calibration curve method, providing values of 1.1 µg/g and 454 µg/g, respectively (RSD ≤ 5 %, n = 3). A chromatogram of the lime peel extract treated by batch extraction on Fe_3O_4@MIP is shown in Fig. 3C. Chromatograms before and after MIP extraction indicated that the extract was purified and batch extraction on the Fe_3O_4@MIP adsorbent can be successfully applied to selective separation of coumarins from lime peel. The peels of citrus fruits (e.g., orange, lemon, grapefruit, pomelo, or different lime species, e.g., Persian lime, Mexican lime) are different both in terms of structural diversity and composition, and thus the combination of the proposed procedures (UAE and Fe_3O_4@MIP-SPE) for sample pretreatment does not always have to be applied. UAE is suitable as the first step in obtaining primary extract. Fe_3O_4@MIP-SPE is convenient to use as an additional purification as well as preconcentration step before the HPLC-FLD analysis. This work shows the possibility of applying both single-step and combined sample preparation procedures for chromatographic analysis.

Research on different citrus peel (sweet orange, lemon, grapefruit, bergamot, pomelo, and clementine) has shown that orange and clementine contain lower amounts of coumarins in comparison with bergamot peel, while much higher amount was determined in flavedo. In lemon, graperfruit, and bergamot peel, trace concentrations of umbelliferon were determined by the UHPLC-MS method (Lončar et al., 2019; Dugrand et al., 2013; Jungen et al., 2021). The content of coumarins docum, ented in previous works are comparable to the results of this work and they vary in a wide interval depending on the citrus type, e.g. from 0.8 µg/g (orange) to 140 µg/g (grapefruit) (Lončar et al., 2019). Dosoky et al. (2022) observed differences in the coumarins and furanocoumarins content in citrus oils of different crop varieties and origins within the same species. In a sample of lime oil (*Citrus aurantifolia* (Christm., Swingle, Brazil)), herniarin was not detected by the UHPLC-MS/MS method. On the contrary, in samples of lime essential oils (Mexican lime, Key lime, Persian lime), herniarin was determined in the wide concentration interval of 7.4—3880 ppm.

Conclusion

Analysis of citrus peel was applied to assess their suitability for the intended purpose, i.e., application in perfumery, cosmetic and cleaning products, or as a source of bioactive or other value-added compounds. Efficient, lab-simple, and time-saving analytical methods able to reach the requirement of high-throughput screening and ecology can contribute to wider applicability of waste natural materials. This study demonstrates that UAE and selective MIP extraction are an effective tool for sample pretreatment and isolation of coumarins from lime peel for subsequent quantification by the HPLC-FLD method. The proposed extraction conditions for selected type of lime (UAE extraction with water at 40 °C, extraction time of 10 min; Fe_3O_4@MIP extract purification and analytes preconcentration) could become routine sample preparation methods for analytical purposes and they are a perspective tool for other citrus samples analyses, as well as for future scale-up extractions of bioactive coumarins from citrus peel.

Acknowledgments

The presented work was financially supported by a grant from the Science Grant Agency of the Ministry of Education of the Slovak Republic and the Slovak Academy of Sciences (grant no. VEGA 1/0412/20). This article was written thanks to the generous support under the Operational Program Integrated Infrastructure for the project: "Support of research activities of Excellence laboratories STU in Bratislava", Project no. 313021BXZ1, co-financed by the European Regional Development Fund."

References

Abosharaf HA, Diab T, Atlam FM, Mohamed TM (2020) Biotechnol. Rep. 28: e00531.

Annunziata F, Pinna C, Dallavalle S, Tamborini L, Pinto A (2020) Int. J. Mol. Sci. 21(4618): 1—81.

Arigo A, Rigano F, Russo M, Trovato E, Dugo P, Mondello L (2021) Foods 10: 1533.

Aznar R, Rodríguez-Pérez C, Rai DK (2022) Appl. Sci. 12(3): 1712.

Bose P, Pattanayak SP (2019) Pharmacogn. Mag. 15(66): 510—519.

Carreira-Casais A, Otero P, Garcia-Perez P, Garcia-Oliveira P, Pereira AG, Carpena M, Soria-Lopez A, Simal-Gandara J, Prieto MA (2021) Int. J. Environ. Res. Public Health. 18(17): 9153.

Ciriminna R, Fidalgo A, Delisi R, Carnoroglio D, Grillo G, Cravotto G, Tamburino A, Ilharco LM, Pagliaro M (2017) ACS Sustain. Chem. Eng. 5: 5578—5587.

Dawidowicz AL, Bernacik K, Typek R (2018) Monatsh. Chem. 149: 1327—1340.

Denisow-Pietrzyk M, Pietrzyk Ł, Denisow B (2019) Environ. Sci. Pollut. Res. Int. 26(7): 6290—6300.

Dosoky NS, Satyal P, Setzer WN (2022) Molecules. 27(19): 6277.

Dugrand A, Olry A, Duval T, Hehn A, Froelicher Y, Bourgaud FJ (2013) Agric. Food Chem. 61 (45), 10677—10684.

Fan H, Wu Q, Simon JE, Lou S-N, Ho CH-T (2015) J. Food Drug Anal. 23(1): 30—39.

Regulation (EC) No. 1334/2008 of the European Parliament and of the Council of 16 December 2008 on flavourings and certain food ingredients with flavouring properties for use in and on foods and amending Council Regulation (EEC) No 1601/91, Regulations (EC) No 2232/96 and (EC) No 110/2008 and Directive 2000/13/EC.

Ganesh JD, Taufique MAP, Sunil TU, Rajendra PP, Yogesh MV (2020) Curr. Organocatalysis 7(2): 140—148.

Hroboňová K, Špačková A (2020) Acta Chim. Slov. 13(1): 56—62.

Hussain MI, Syed QA, Khattak MNK, Hafez B, Reigosa MJ, El-Keblawy A (2019) Biologia 74: 863—888.

Che Sulaiman IS, Basri M, Fard Masoumi HR, Chee WJ, Ashari SE, Ismail M (2017) Chem. Cent. J. 11: 54.

Chen L, Wang X, Lu W, Wu X, Lia J (2016) Chem. Soc. Rev. 45: 2137—2211.

Jablonský M, Majová V, Šíma J, Hroboňová K, Lomenová A (2020) Crystals 10: 217.

Jerkovic I, Družic J, Marijanovic Z, Gugic M, Jokic S, Roje M (2015) Nat. Prod. Commun. 10(7): 1315—1318.

Jose M, Sunilkumar T, Antony VT (2014) Int. J. Bioassays. 3(12): 3594—3597.

Jungen M, Lotz P, Patz CD, Steingass ChB, Schweiggert R (2021) Food Chem. 359: 129804.

Li G, Xiang S, Pan Y, Long X, Cheng Y, Han L, Zhao X (2021) Front. Nutr. 8: 689094.

Li G-J, Wu H-J, Wang Y, Hung W-L, Rouseff RL (2019) Food Chem. 271: 29—38.

Liang G, Guo X, Tan X, Mai S, Chen Z, Zhai H (2019) Microchem. J. 146: 1285—1294.

Lin Z, Cheng X, Zheng H (2023) Inflam-mopharmacol (2023) https://doi.org/10.1007/s10787-023-01256-3.

Lončar M, Jakovljevic M, Šubaric D, Pavlic M, Buzjak-Služek V, Cindric I, Molnar M (2020) Foods 9: 645.

Machyňáková A, Hroboňová K (2017) Anal. Methods 9: 2168–2176.

Mazimba O (2017) Bull. Fac. Pharm. Cairo Univ. 55(2): 223–232.

Munawaroh R (2017) Pharmacon 18: 34–38.

Önder A (2020) Stud. Nat. Prod. Chem. 64: 85–109.

Raghavan S, Gurunathan J (2021) J. Herb. Med. 28: 100438.

Ramírez-Pelayo C, Martínez-Quinones J, Gil J, Durango D (2019) Heliyon. 5(6): e01937.

Regulation (EC) No. 1223/2009 of the European Parliament and of the Council of 30 November 2009 on cosmetic products.

Rodríguez-García SL, Raghavan V (2022) Crit. Rev. Food Sci. Nutr. 62: 6446–6466.

Safety assessment of citrus peel-derived ingredients as used in cosmetics (2015) Cosmetic Ingredient Review 1620 L Street NW, Suite 1200, Washington, DC

Singh B, Singh JP, Kaur A, Singh N (2020) Food Res. Int. 132: 109114.

Trabelsi D, Aydi A, Wust Zibetti A, Della Porta G, Scognamiglio M, Cricchio V, Langa E, Abderrabba M, Mainar AM (2016) J. Supercrit. Fluids 117: 33–39.

Wang DD, Gao D, Xu W-J, Li F, Yin M-N, Fu Q-F, Xia Z-N (2018) Talanta 184, 307–315.

Zhang QW, Lin LG, Ye WC (2018) Chin. Med. 13: 20.

Zhao XJ, Guo PM, Pang WH, Zhang YH, Zhao QY, Jiao BN, Kilmartin PA (2020) Food Chem. 325: 126835.

sciendo

Two novel potent perfluorophenylhydrazone derivatives, 1-((4-bromothiophen-2-yl)methylene)-2-(perfluorophenyl) hydrazine, and 1-((4-bromo-5-methylthiophen-2-yl)methylene)-2-(perfluorophenyl)hydrazine as multi-target compounds to combat Alzheimer disease and their crystal, molecular, and electronic properties

Július Sivý[1], **Dušan Bortňák**[2],
Daniel Végh[2], **Erik Rakovský**[3]

[1]Faculty of Mechanical Engineering, STU, Námestie slobody 17, Bratislava 1, SVK-812 31, Slovak Republic
[2]Institute of Organic Chemistry, Catalysis and Petrochemistry, Faculty of Chemical and Food Technology, STU,
Radlinského 9, Bratislava 1, SVK-812 37, Slovak Republic
[3]Department of Inorganic Chemistry, Faculty of Natural Sciences, Comenius University,
Ilkovičova 6, Bratislava 4, SVK-842 15, Slovak Republic
julius.sivy@stuba.sk

Abstract: Two potent novel perfluorophenylhydrazone derivatives are presented as multi-target compounds to combat Alzheimer disease $C_{11}H_4BrF_5N_2S$, 1-((4-bromothiophen-2-yl)methylene)-2-(perfluorophenyl) hydrazine, (**I**) and $C_{12}H_6BrF_5N_2S$, 1-((4-bromo-5-methylthiophen-2-yl)methylene)-2-(perfluorophenyl) hydrazine, (**II**), which can potentially be improved by further design. Their multi-target structures and features have been combined as potential AD therapeutics. Crystals (**I**), and (**II**), are molecules with two rings and a hydrazone part as a centre of the molecule. The compounds have been synthesised and characterised by elemental spectroscopic (^{1}H-NMR) analysis. Crystal structures of the solid phase were determined by single crystal X-ray diffraction method. Both compounds crystallise in the monoclinic space group with $Z = 4$ and $Z = 2$ molecules per unit-cell. Compound (**I**) crystallises as a racemate in the centrosymmetric space group and compound (**II**) crystallises as a non-racemate in the non-centrosymmetric space group. Their "absolute configuration and conformation for bond values" were derived from the anomalous dispersion (rmad) for (**II**). Crystal structures revealed diverse non-covalent interactions such as intra- and inter-hydrogen bonding, π-ring$\cdots\pi$-ring, C—H$\cdots\pi$-ring. The expected stereochemistry of hydrazones atoms C7, N2 and N1 were confirmed for (**I**) and (**II**). Both molecules show "boat conformation" like a 6-membered ring. Results of single crystal studies were reproduced with the help of Hirshfeld surface study and Gaussian software.

Keywords: *Ab initio* DFT/B3LYP/6-311G/Auto calculation, hydrazine, Hirshfeld surface, hydrogen interactions, single-crystal X-ray study

Introduction

Microbial resistance to antibiotics is an urgent and well-known problem worldwide. Several hydrazones synthesised under benign reaction conditions have proved to be potent growth inhibitors of drug-resistant strains of *Staphylococcus aureus* and *Acinetobacter baumannii* with minimum inhibitory concentration values. These molecules are non-toxic to human cells at appropriate concentrations. Although hydrazones possess greater intrinsic hydrolytic stability than the corresponding imines, these molecules can be converted into the starting materials by reacting with water under physiological condition. Antimicrobial activity of hydrazones is probably caused by the hydrolysed products, aldehydes, and hydrazines. For example, the aldehyde derivative did not show any activity, but the hydrazine showed weak growth inhibition. Thus, it can be concluded that the antimicrobial activity of the compounds is due to their hydrazone functional groups, not due to their possible hydrolysed products. Fluorine substitution has been extensively studied in drug discovery to enhance biological activity and increase chemical and metabolic stability of the resultant molecules. Hydrazone derivatives have been designed and synthesised not only for antimicrobial studies. They are of general wide interest not only in medicinal chemistry (Verma et al., 2014; Kuman and Chauhan, 2014; Giliberti et al., 2010; Bari et al., 2019; Tonelli et al., 2008; Saha et al., 2019) but also in material chemistry (Su and Aprahamian, 2014; Burdette, 2012; Feringa and Browne, 2011; Xu et al., 2018; Lukeš et al. 2016; Sandoval-Torrientes et al., 2017; Beverina et al., 2011; Tarabová and Milata, 2012), and they exhibit nematicidal and insecticidal activity (Eloh et al., 2015). Hydrazones exhibit a broad spectrum of biological activities and have been described in the treatment of tuberculosis, malaria, and cancer. They have also been identified as strong radical scavengers and their multitarget properties have been combined as potential Alzheimer's disease (AD) therapeutics. Hydrazones were found to be very good inhibitors of amyloid beta fibril and oligomer formation and they showed highly effective radical scavenging properties (Baier et al., 2021). N-pentafluorophenyl substituted hydrazones can also be used as analytical reagents. Two principles are most often used in the analysis:

1. Interaction of an ion (anion, cation) with a secondary amino group leading to a colour change after the addition of the analyte.
2. Formation of a stable molecular ion or a fragment well detectable in mass spectrometry (usually pentafluorophenyl).

Ions such as the fluoride anion (Ghosh et al., 2018; Chowdhury et al., 2015) (Scheme 1, 2, 3) can be well determined. Fluorine is the thirteenth most abundant element on Earth and occurs mainly in form of the minerals fluorite, fluorapatite, and cryolite. Only twelve organic compounds of fluorine have been identified in nature, all of which show considerable toxicity. Despite the low occurrence of fluoroorganic compounds in nature, which are without exception highly toxic, chemical research and industry currently produce thousands of new fluorine-containing organic compounds. The year 1941 is considered the beginning of synthetic fluoroorganic chemistry. According to data from the Internet, global demand for fluorine-containing chemicals in 2015 reached 3.35 million tons per year. Due to the wide range of issues in different research works, crystal, molecular and electronic properties of N-pentafluorophenyl hydrazones will be discussed. These compounds show diverse crystal-molecular interactions including interactions such as $\pi\cdots\pi$, C—H$\cdots\pi$, etc. Here, the crystal-base structural properties were investigated by the single crystal X-ray diffraction method, Gaussian method, and the Hirshfeld surface analysis. Synthesis, molecular, crystal, and electronic structure of title compounds (**I**) and (**II**) are reported. The interest of our research group is to develop novel hydrazone derivative routes for their synthesis in simple and efficient ways. Molecules of the title compounds crystallise in the space group $P2_1/n$ and Pn. Accordingly, compound (**I**) is a racemate and consists of one molecule in the independent part of the unit-cell with relative configuration of carbon atoms, while compound (**II**) is a non-racemate and consists of one molecule in the independent part of the unit-cell. Hydrazone part of the molecule and its left and right side possess "a boat conformation" like a 6-membered ring. The first right-side ring, hexafluorophenyl, is planar and adopts a plane conformation, while atom N1 is displaced from this plane with the out-of-plane displacement of 0.011 (3) for (**I**) and 0.034 (7) Å for (**II**); out-of-plane displacement for atoms F1, F2, F3, F4, F5 is 0.078 (3), –0.039 (3), –0.013 (3), 0.018 (3), –0.028 (3) for (**I**), and 0.075 (7), –0.032 (8), 0.009 (7), –0.009 (7), –0.047 (6) Å, (**II**). The second left-side ring, thiophene, is also planar, the out-of-plane displacement for atom Br1 is –0.013 (3) for (**I**) and –0.008 (7), (**II**) and for atom C12 it is 0.066 (10) Å, (**II**).

Dihedral angle between the planes is 32.00 (5)° for (**I**) and 31.77 (11)° for (**II**). Compounds (**I**) and (**II**) were investigated by *ab initio* DFT/B3LYP/6-311G calculations, and properties of the conformation of products (**I**) and (**II**) were checked by X-ray structure determination. Title compound (**I**) (Scheme 1) as a hydrazone derivative crystallises in the centrosymmetric space group, while title compound (**II**) (Scheme 2) as a hydrazone derivative crystallises in the non-centrosymmetric space group (monoclinic crystal system). Simple Hirshfeld surface analysis was used to visualize the map for the different intermolecular interactions (energies) in the crystal structure and the Gaussian natural bond order analysis was performed (Frisch et al., 2016).

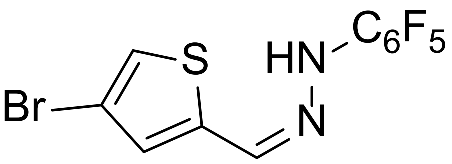

Scheme 1. Molecular scheme of title compound (**I**).

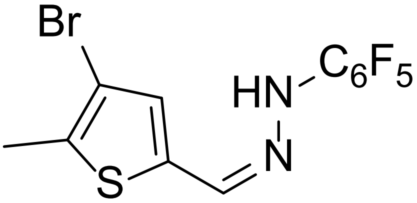

Scheme 2. Molecular scheme of title compound (**II**).

Material and Methods

Chemicals

Synthesis and crystallisation

Compounds (**I**) and (**II**) were prepared according to a standard protocol (Scheme 3) described in literature. All NMR spectra were obtained using an INOVA NMR 300 MHz spectrometer (operating frequencies 300 MHz (^{1}H), 75 MHz (^{13}C), and 282 MHz (^{19}F)) equipped with an inverse triple resonance probe and a standard tuneable X/H probe with the possibility to tune the high frequency channel to the resonance frequency of ^{19}F. Tetramethylsilane was used to calculate the ^{1}H and ^{13}C chemical shift scales and for correct reference using the (residual) solvent signals (2.50 and 39.52 ppm for DMSO, and 7.26 and 77.00 ppm for chloroform). CFCl$_3$ was used to calculate the ^{19}F chemical shift scale; in order to correctly reference the ^{19}F chemical shift scale, an automatic referencing mechanism exploiting the ^{2}H signal of the deuterated solvent was used.

General procedure for hydrazone synthesis

To a solution of the corresponding aldehyde in 20 ml of ethanol, ethanolic solution (10 ml) of pentafluorophenylhydrazine was added. Then, a catalytic amount of concentrated hydrochloric acid was added (approximately 3—5 drops) and the reaction mixture was refluxed for 8 hours (under TLC + UV control). The solvent was evaporated under reduced pressure and the residue was crystallised from ethanol to obtain pentafluorophenylhydrazone (**I**) — (**II**).

1-((4-Bromothiophen-2-yl)methylene)-2-(perfluorophenyl) hydrazine, (I), (Scheme 3)

4-Bromothiophene-2-carbaldehyde (1.000 g, 5.23 mmol, 1 eq.) and pentafluorophenylhydrazine (1.037 g, 5.23 mmol, 1 eq.) were left to react in ethanol following the general procedure for hydrazones synthesis. Hydrazone (**I**) was obtained as a brown crystalline matter in a 51 % yield (0.991 g), m.p. 138—140 °C. ^{1}H NMR (300 MHz): δH = 7.07 (d, J = 1.3 Hz , ^{1}H), 7.20 (d , J = 1.1 Hz, ^{1}H), 7.88 (s, ^{1}H). ^{13}C NMR (75 MHz): δC = 109.88, 119.75, 124.26, 129.87 135.78, 136.05, 138.15, 139.67. ^{19}F NMR (282 MHz): δF = –165.80 (tt, J = 3.8 Hz, J = 21.6, ^{1}F), –163.30 (dt, J = 4.8 Hz, J = 21.4, ^{2}F), –155.64 (d, J = 21.6, ^{2}F).

1-((4-Bromo-5-methylthiophen-2-yl)methylene)-2-(perfluorophenyl)hydrazine, (II) (Scheme 3)

4-Bromo-5-methylthiophene-2-carbaldehyde (1.000 g, 4.88 mmol, 1 eq.) and pentafluorophenylhydrazine (0.966 g, 4.88 mmol, 1 eq.) were left to react in ethanol following the general procedure for hydrazones synthesis. Hydrazone (**II**) was obtained as a brown crystalline matter in a 60 % yield (1.127 g), m.p. 153—155 °C. ^{1}H NMR (300 MHz) δ 10.37 (s, ^{1}H), 8.17 (s, ^{1}H), 7.23 (s, ^{1}H), 2.34 (s, ^{3}H). ^{13}C NMR (75 MHz) δ 137.7 (dm J = 245 Hz), 137.3 (dm J = 246 Hz) 137.2, 136.0, 135.0, 133,9 (dm J = 247 Hz) 129.9, 120.8 (m) 108.7, 14.6. ^{19}F NMR (282 MHz): δF= –169.73 (m, ^{1}F), –164.33 (m, ^{2}F), –155.75 (m, ^{2}F) (Bortňák et al., 2020).

Crystallography and Hirshfeld surface analysis

Manuals: “The CIF file, refinement details and validation of the structure, IUCr, 2011” and “User guide to crystal structure refinement with SHELXL, IUCr, 2008” defined the refinement rules for all H atoms, e.g. positioning with non-idealised geometry using a constrained riding model with C—H distances in the range of 0.70—0.99 Å (AFIX cards were not used) and non-idealised geometry N—H distance in the range of 0.82—0.87 Å (AFIX cards were omitted) (Sheldrick, 2015). The U_{iso}(H) values were set to 1.2U_{eq} (*C*-aromatic, N) and 1.5U_{eq} (*C*-methyl), respectively.

Crystal data and conditions of data collection and refinement are reported in Table 1. Data collection for (**I**):

A single crystal was measured on an Eulerian four-circle diffractometer Stoe STADIVARI with a Dectris Pilatus 300 K detector (computing data collection: X-Area Pilatus3_SV 1.31.150.0 (STOE, 2018), computing cell refinement: X-Area Recipe 1.33.0.0 (STOE, 2015), computing data reduction: X-Area Integrate 1.73.1.0 (STOE, 2018), X-Area X-Red32 1.65.0.0 (STOE, 2018), computing publication material: STOE & Cie GmbH, X-Area, software package for collecting single-crystal or multi-domain crystal data on STOE area-detector diffractometers, for image processing, for correction and scaling of reflection intensities and for outlier rejection, version 1.84, (Darmstadt (2018)). Data collection for (**II**): Rigaku Oxford Diffraction, (2022), CrysAlisPro Software system, version 171.42.49 (computing data collection, computing cell refinement and computing data reduction: CrysAlisPro, Agilent Technologies, Version 1.171.37.31), programs used to solve structure

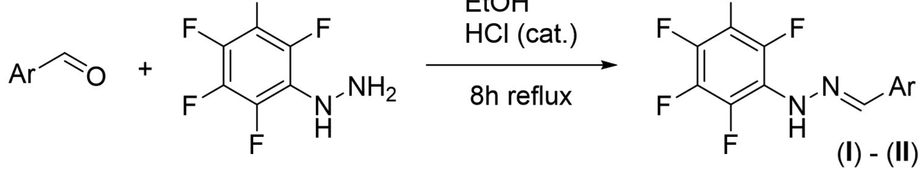

Scheme 3. Ar = 4-bromothiophene-2-yl (**I**), 4-bromo-5-methylthiophene-2-yl (**II**).

(Sheldrick, 2008; Burla et al., 2015), to refine structure (Sheldrick, 2015; Hübschle, 2011), molecular graphics (Brandenburg, 1999), to prepare material for publication (Frisch et al., 2016; Jayatilaka et al., 2005; Spackman et al., 2008; Spackman and Jayatilaka, 2009; Spackman et al., 2021; Sheldrick, 2015; Turner et al., 2017; Dolomanov et al., 2009; Spek, 2003; Hübschle, 2011).

Results and Discussion

The start 'configuration' of the molecules in absolute formulation is known from the synthesis and 'stereochemistry' of atoms in the molecules was confirmed. Molecular geometry and atom numbering scheme of (**I**) and (**II**) are shown in Figs. 1, and 3, respectively. Molecular crystal packing view of (**I**) and (**II**) are shown in Figs. 2 and 4, and experimental characteristics of compounds (**I**) and (**II**) are listed in Table 1, selected geometric parameters are listed in Tables 3 and 5.

Central hydrazone part of the molecule is planar for both title compounds. Atom N1 possesses more negative net charge than N2 (Figs. 5, 6, NBO analysis). Molecular structures are moreover stabilised by one intramolecular N1—H1···F5 hydrogen bond and one intramolecular C12—H12C···Br1 hydrogen interaction only for (**II**) with an H-atom as the donor, Figs. 1, 3, Tabs. 4, 5. The N1—N2 [1. 380 (6)—1. 384 (2) Å] distances are slightly shorter compared to the hydrazine Nsp^2—Nsp^2 (about 1.40 Å) single bond (Allen et al., 1987) and about 1.46 Å single bond (Collin and Lipscomb, 1951) which indicates that there is a significant delocalisation of π-electron density over the hydrazone portion of the molecule. Conformation

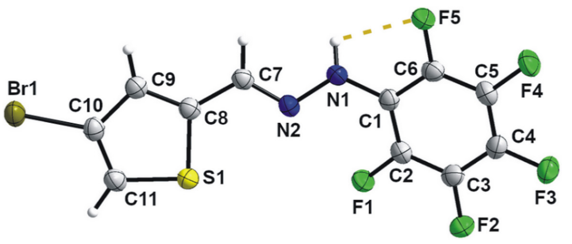

Fig. 1. Molecular structure of title compound (**I**) with atomic numbering scheme. Displacement ellipsoids are drawn at the 50 % probability level.

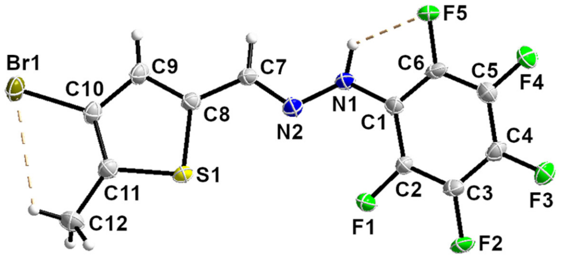

Fig. 3. Molecular structure of title compound (**II**) with atomic numbering scheme. Displacement ellipsoids are drawn at the 50 % probability level.

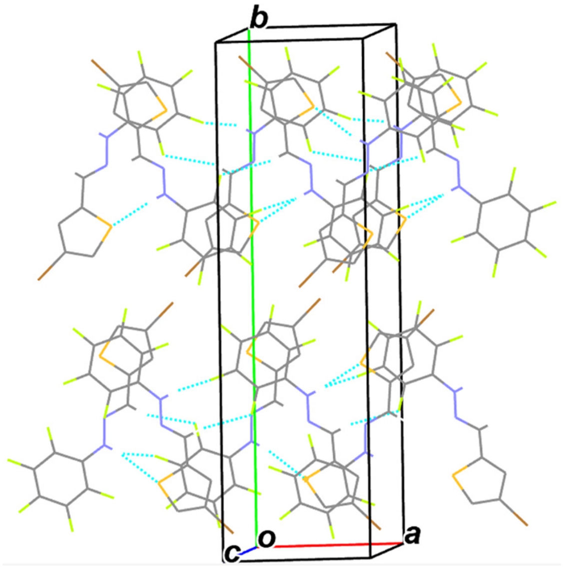

Fig. 2. Part of the crystal structure of title compound (**I**) showing formation of intermolecular hydrogen interactions. Chains of molecular structure of the title compound extend along the *a* axis. H atoms not involved in the motif have been omitted.

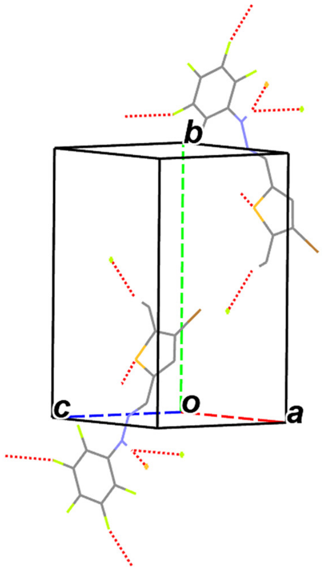

Fig. 4. Part of the crystal structure of title compound (**II**) showing the formation of intermolecular hydrogen interactions. Chains of molecular structure of the title compound extend along the *b* and *c* axes. H atoms not involved in the motif have been omitted.

Tab. 1. Experimental characteristics of compounds (**I**)[a] and (**II**)[b].

Empirical formula	$C_{11}H_4BrF_5N_2S$	$C_{12}H_6BrF_5N_2S$
Formula weight	371.13	385.16
Temperature (K)	298(2)	298(2)
Wavelength (Å)	1.54178	0.71073
Crystal system	Monoclinic	Monoclinic
Space group	$P2_1/n$ (centro)	Pn (non-centro)
Unit-cell dimensions (Å, °)	a = 7.11250(10) b = 25.0194(5) c = 7.1935(2) β = 109.457(2)	a = 7.1916(3) b = 13.5415(5) c = 7.2384(4) β = 109.951(6)
Volume (Å^3)	1206.98(5)	662.61(6)
Z	4	2
Density (calculated) (Mg/m^3)	2.042	1.930
Absorption coefficient (mm^{-1})	6.826	3.311
F(000)	720	376
Crystal size (mm)	0.594 × 0.220 × 0.091	0.591 × 0.306 × 0.065
Theta range for data collection (°)	3.533 to 71.747	1.504 to 32.774
Index ranges	$-8 \leq h \leq 8$, $-30 \leq k \leq 29$, $-8 \leq l \leq 8$	$-10 \leq h \leq 10$, $-20 \leq k \leq 20$, $-10 \leq l \leq 10$
Reflections collected	32397	11109
Independent reflections	2331 [$R_{(int)}$ = 0.0402]	4379 [$R_{(int)}$ = 0.0508]
Completeness to theta (°, %)	67.679, 100.0	25.242, 100.0
Refinement method	Full-matrix least-squares on F^2	Full-matrix least-squares on F^2
Data/restraints/parameters	2331/0/184	4379/2/194
Goodness-of-fit on F^2	1.036	1.032
Final R indices [$I > 2\sigma(I)$]	R_1 = 0.0296, wR_2 = 0.0866	R_1 = 0.0447, wR_2 = 0.1013
R indices (all data)	R_1 = 0.0298, wR_2 = 0.0869	R_1 = 0.0531, wR_2 = 0.1097
Absolute structure parameter	–	0.007(11) (Flack)
Chemical absolute configuration	–	rmad
Extinction coefficient	–	–
Largest diff. peak and hole (e·Å^3)	0.523 and –0.832	1.063 and –1.137

[a] CCDC_2027085,

[b] CCDC_2027086. Crystallographic data for the structures reported in this paper will be available from the Cambridge Crystallographic Data Centre.

Tab. 2. H-bond geometry and Y—X···π-centroid (Cg(1)) stacking interactions (Å, °) for (**I**).

D—H···A	D—H	H···A	D···A Y—X···Cg(1)	D—H···A
N1—H1···F5	0.87(3)	2.39(2)	2.739(2)	105(2)
C7—H7···F1^{i}	0.99(3)	2.63(3)	3.404(2)	135(2)
N1—H1···F2^{i}	0.87(3)	2.55(3)	3.087(2)	121(2)
N1—H1···S1^{ii}	0.87(3)	2.74(3)	3.538(2)	152(2)
C5—F4···Cg(1)^{iii}			3.766(2)	

Symmetry codes:

^{i}1 + x, + y, + z;

^{ii}1/2 + x, 1/2 – y, 1/2 + z;

^{iii}–1/2 + x, 1/2 – y, –1/2 + z; Cg(1): C8, C9, C10, C11, S1.

Tab. 3. Selected geometric parameters for (**I**): bond lengths (Å), bond and torsion angles (°).

C1—N1	1.393(3)	C7—N2—N1	115.73(17)
C7—N2	1.277(3)	N1—C1—C6—F5	0.8(3)
C8—S1	1.732(2)	N1—C1—C6—C5	-179.68(19)
C9—S1	1.717(2)	N2—C7—C8—C11	174.6(2)
C10—Br1	1.886(2)	N2—C7—C8—S1	-7.3(3)
N1—N2	1.383(2)	S1—C9—C10—C11	-0.2(2)
C7—C8	1.452(3)	S1—C9—C10—Br1	179.47(11)
C2—C1—N1	120.40(18)	Br1—C10—C11—C8	-179.73(15)
N1—C1—C6	123.03(19)	C2—C1—N1—N2	-138.44(19)
N2—C7—C8	119.23(18)	C6—C1—N1—N2	43.9(3)
N2—C7—H7	120.4	C8—C7—N2—N1	176.83(17)
C11—C8—S1	111.53(16)	C1—N1—N2—C7	162.23(18)
C7—C8—S1	120.84(15)	C10—C9—S1—C8	0.33(17)
C10—C9—S1	110.80(16)	C11—C8—S1—C9	-0.34(17)
C9—C10—Br1	123.26(16)	C7—C8—S1—C9	-178.76(17)
C11—C10—Br1	122.38(15)	N1—C1—C2—F1	2.1(3)
N2—N1—C1	117.00(17)	N1—C1—C2—C3	-178.16(18)
C9—S1—C8	91.86(10)		

Tab. 4. H-bond geometry and Y—X···π-centroid (Cg(1)) stacking interactions (Å, °) for (**II**).

D—H···A	D—H	H···A	D···A Y—X···Cg(1)	D—H···A
C12—H12C···Br1	0.99(8)	3.08(8)	3.359(7)	98(5)
N1—H1···F5	0.82(7)	2.28(6)	2.748(5)	117(6)
C12—H12C···Br1$^{\mathrm{i}}$	0.99(8)	3.06(7)	3.892(6)	143(6)
C12—H12B···F4$^{\mathrm{ii}}$	0.95(8)	2.39(8)	3.138(7)	135(6)
N1—H1···F2$^{\mathrm{iii}}$	0.82(7)	2.55(7)	3.084(6)	124(5)
N1—H1···S1$^{\mathrm{iv}}$	0.82(7)	2.91(7)	3.620(5)	146(6)
C2—F1···Cg(1)$^{\mathrm{v}}$			3.924(4)	
C5—F4···Cg(1)$^{\mathrm{vi}}$			3.756(4)	

Symmetry codes:
$^{\mathrm{i}}$x + 1/2, -y + 1, z + 1/2;
$^{\mathrm{ii}}$x, y + 1, z;
$^{\mathrm{iii}}$x, y, z - 1;
Cg(1): C8, C9, C10, C11, S1.
$^{\mathrm{iv}}$x - 1/2, -y, z - 1/2;
$^{\mathrm{v}}$-1/2 + x, -y, 1/2 + z;
$^{\mathrm{vi}}$1/2 + x, -y, 1/2 + z;

of the N1—H1 group of the hydrazone part is advantageous for intramolecular H bond to the hexafluorophenyl part of the molecule(s). Unit-cell density for the parent compound (**I**) is 2.042 g/cm^3 (V = 1206.98, F(000) = 720.0, μ = 6.83 mm^{-1}, cell weight = 1484.53, ρ = 2.042). The introduction of a methyl-substituent to H atom of the thiophene ring for (**II**) changed this to value of 1.930 g/cm^3 (V = 662.61, F(000) = 376.0, μ = 3.31 mm^{-1}, cell weight = 770.32, ρ = 1.930).

Different values of the unit-cell densities indicate the role of the crystallisation process of the substituent on this parameter. The methyl-substituted compound has the lowest value of unit-cell density.

The observed bond lengths and Wiberg bond indices of the compounds showed a clear distinction between single and double bonds in the central spacer unit and the rest of the molecules (Wiberg, 1968). Atoms C7—C8 [1.452 (3) Å, I_{w} = 1.110 and 1.447, I_{w} = 1.118] and N2═C7 [1.277 (3) Å, I_{w} = 1.737 and 1.280, I_{w} = 1.729] interatomic distances confirm their character as single and double bonds, (Br1—C10: I_{w} = 1.033 and I_{w} = 1.027). Atom S1 represents the strong stability effect for this molecule side part (charge 0.433 and 0.425, Figs. 5, 6).

Torsion angle of C2, C1, N1, N2 atoms suggests that H1 atom participates in intra- and intermolecular

Tab. 5. Selected geometric parameters for (**II**): bond lengths (Å), bond and torsion angles (°).

C1—N1	1.390(6)	C7—N2—N1	116.7(4)
C7—N2	1.280(6)	C8—S1—C11	92.8(2)
C7—C8	1.447(7)	N1—C1—C2—C3	179.7(5)
C8—S1	1.725(5)	N1—C1—C6—C5	-177.8(5)
C10—Br1	1.883(5)	N2—C7—C8—C9	173.9(5)
N1—N2	1.380(6)	N2—C7—C8—S1	-8.1(6)
C2—C1—N1	123.4(4)	C12—C11—C10—Br1	3.1(8)
C6—C1—N1	119.8(4)	S1—C11—C10—Br1	-179.7(3)
N2—C7—C8	119.7(4)	Br1—C10—C9—C8	179.8(3)
C9—C8—S1	111.3(4)	C2—C1—N1—N2	44.4(5)
C7—C8—S1	121.5(4)	C6—C1—N1—N2	-138.0(7)
C10—C11—S1	109.1(4)	C8—C7—N2—N1	177.1(4)
C9—C10—Br1	122.9(4)	C1—N1—N2—C7	162.1(4)
C11—C10—Br1	122.1(4)	N2—N1—C1	117.7(4)

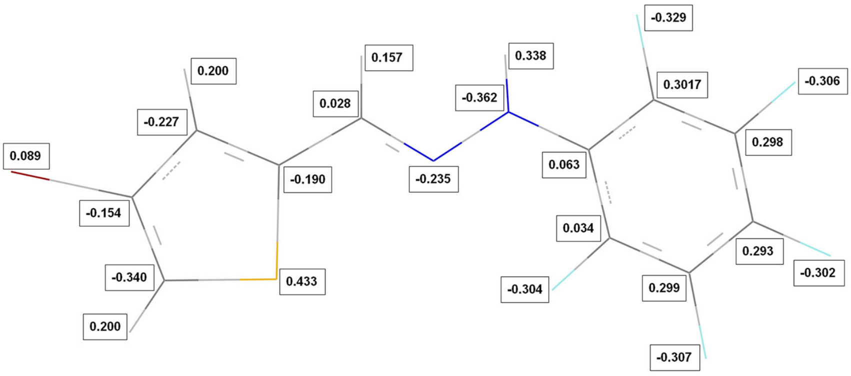

Fig. 5. Molecular structure of title compound (**I**) shoving net atomic charges.

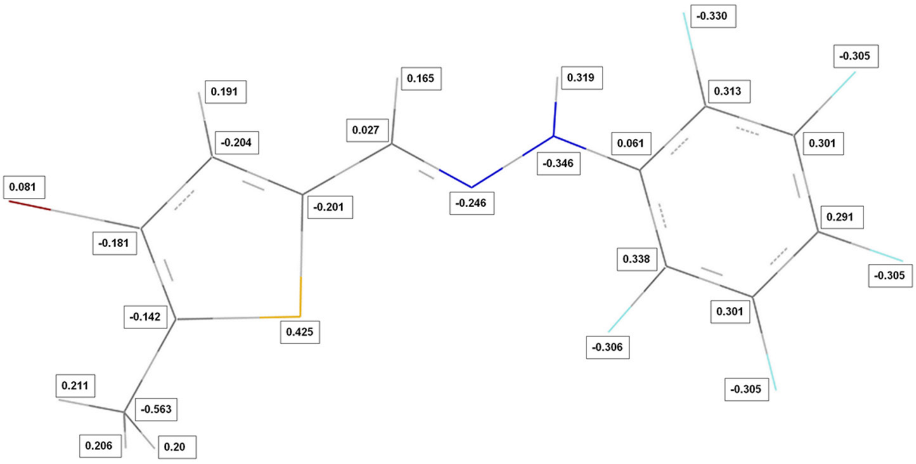

Fig. 6. Molecular structure of title compound (**II**) shoving net atomic charges.

hydrogen bonds. Fig. 7 shows the best least-squares fit (RMS Error = 5.714 × 10^{-3} Å, atoms C1, N1, N2, C7, C8,) between the close molecules (**I**) and (**II**) (Hypercube, 2007). In Fig. (7) it is shown how molecules fit together to form the molecular structure of (**I**) and (**II**).

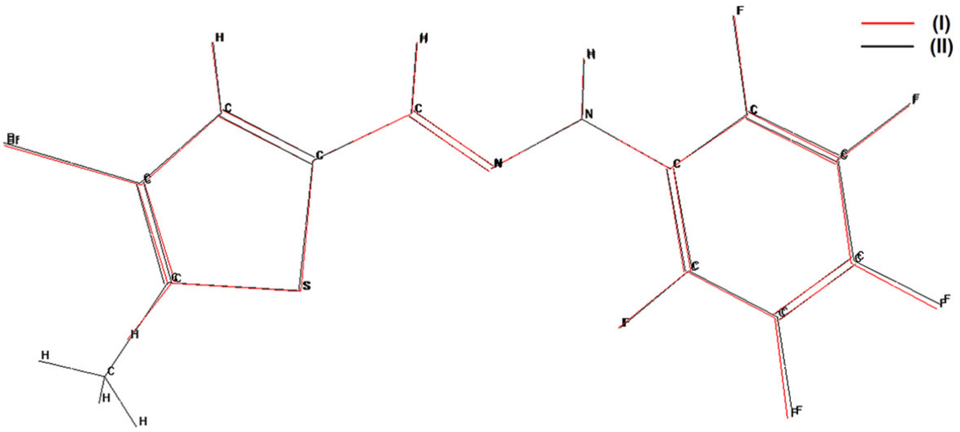

Fig. 7. Molecular structure fit of compounds (**I**) and (**II**).

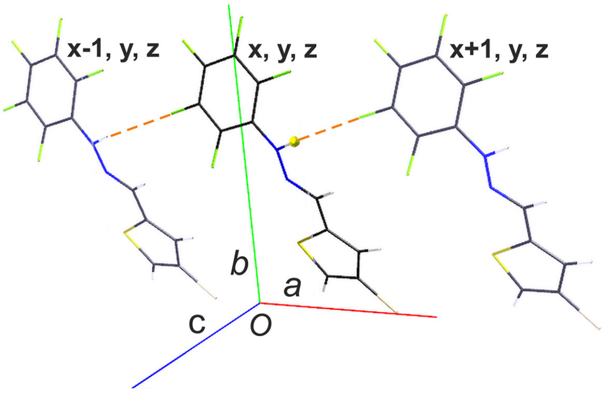

Fig. 8. Molecular packing view of the crystal structure of (**I**) showing the formation of the **C**(6) graph-set motif.

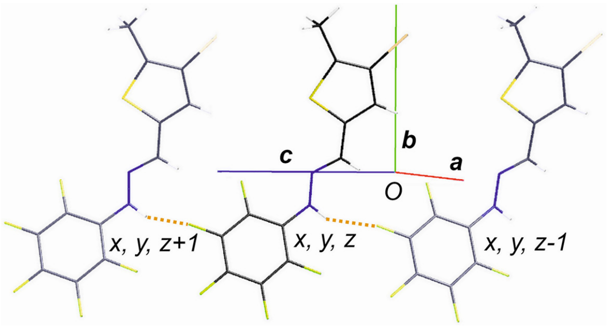

Fig. 9. Molecular packing view of the crystal structure of (**II**) showing the formation of the **C**(6) graph-set motif.

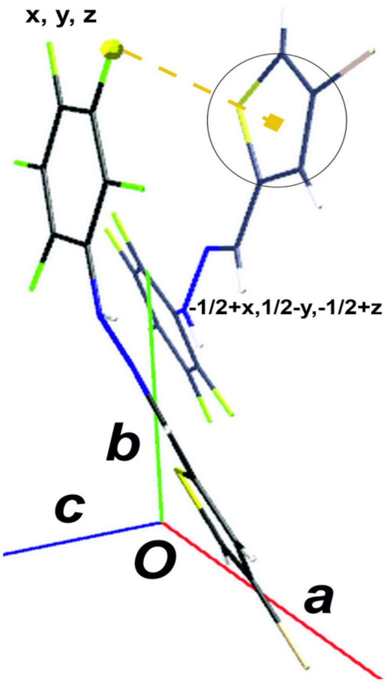

Fig. 10. Molecular packing view of the crystal structure of (**I**) showing the formation of the Y—X· · ·Cg(1) bond motif.

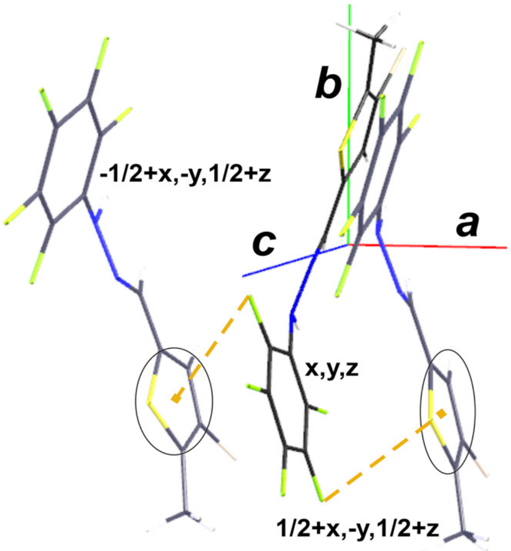

Fig. 11. Molecular packing view of the crystal structure of (**II**) showing the formation of the Y—X· · ·Cg(1) bond motifs.

Graph-set motif of the molecules was proved to be a **C**(6) graph-set motif (Bernstein et al., 1995), (Figs. 8 and 9). Cremer-Pople puckering parameters of the parts of molecules were not confirmed for either crystal structure. Molecular packing view of the crystal structures shows the formation of the Y—X···Cg(1) bond motifs (Figs. 10 and 11).

Results of these calculations are in good agreement with the experimental values of bond lengths found by X-ray structure analysis. NBO analysis of theoretical calculations in vacuum (without an addition of polarisation functions) at the *ab initio* DFT/B3LYP level using the 6-311G basis set model (single point geometry, NBO net charges) is shown for selected atoms in Figs. 5 and 6. Hirshfeld surface analysis is a powerful tool for gaining additional view into the intermolecular interactions of molecular crystals. The size, shape and type of Hirshfeld surface allows for qualitative and quantitative investigation and visualisation of intermolecular close contacts in molecular crystals. The structure with its Hirshfeld's approach considers each molecule enclosed surface (Hirshfeld surface) so that in any point, half or more electron density comes from the atoms of the molecule. The Hirshfeld surface map over d_{norm} analyses the electron density, shape-index, and the curvedness of a surface. Hirshfeld surface (Figs. 12 and 13) shows simple workable places for biological activity including the shortest distances of worthy molecule-hydrogen bonds to suitable receptor site-locality and thus for the molecular "dimension", biological activities will be as few as adequate (d_{norm} range of (–0.187, 1.017) and d_{norm} range of (–0.193, 1.116), atoms within the radius of 3.80 Å). Hirshfeld surface analysis was carried out in order to study the nature of the surface molecu-

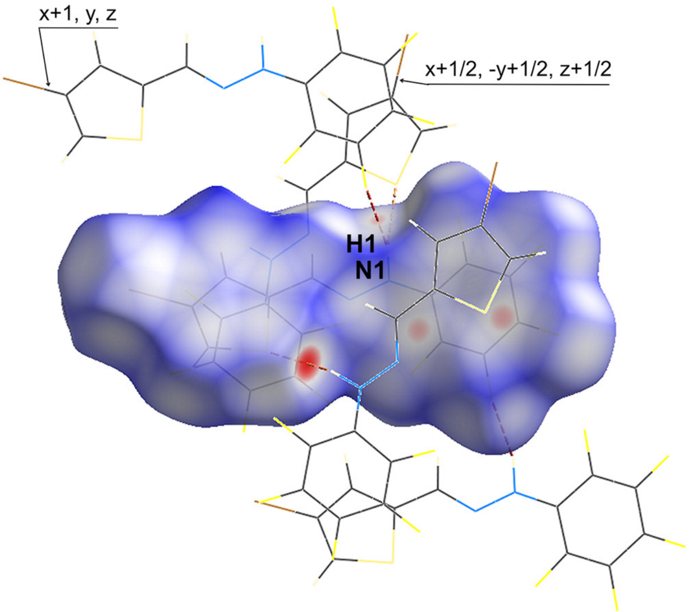

Fig. 12. Simple Hirshfeld surface for title compound (**I**).

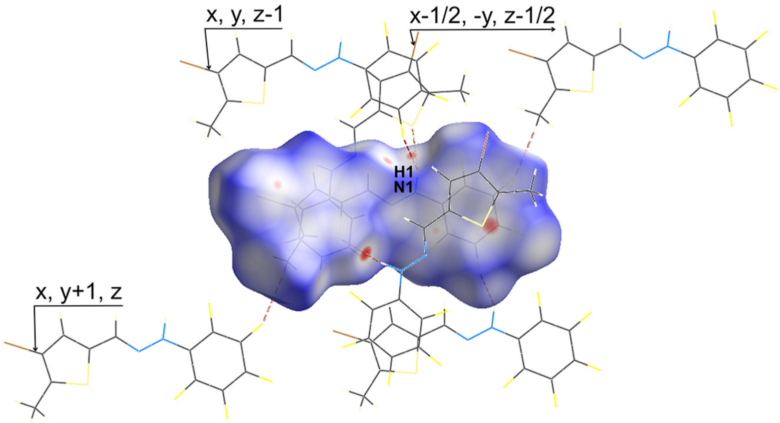

Fig. 13. Simple Hirshfeld surface for title compound (**II**).

Tab. 6. Interaction energies (kJ/mol, kcal/mol) for (**I**).

R	E_ele	E_pol	E_dis	E_rep	E_tot	complexation energy (raw)/ (corrected)
C7—H7· · ·F1, N1—H1· · ·F2, 1 + x, + y, + z						
7.11	–6.91	–1.79	–23.38	11.70	–21.76	–10.82/–6.00
N1—H1· · ·S1, 1/2 + x, 1/2 – y, 1/2 + z						
4.23	–17.23	–3.81	–58.08	52.65	–39.09	–15.82/–11.15
C5—F4· · ·Cg(1), –1/2 + x, 1/2 – y, –1/2 + z						
4.23	–17.23	–3.81	–58.08	52.65	–39.09	–15.82/–11.15

Tab. 7. Interaction energies (kJ/mol, kcal/mol) for (**II**).

R	E_ele	E_pol	E_dis	E_rep	E_tot	complexation energy (raw)/ (corrected)
C12—H12C· · ·Br1, x + 1/2, –y + 1, z + 1/2						
13.08	–1.13	–0.37	–7.50	0.00	–8.00	–3.61/–1.72
C12—H12B· · ·F4, + x, + y + 1, + z						
13.54	–0.56	–0.26	–6.26	0.00	–6.23	–2.91/–1.61
N1—H1· · ·F2, + x, + y, + z – 1						
7.24	–7.07	–1.68	–25.61	13.95	–22.40	–11.66/–6.30
N1—H1· · ·S1, x – 1/2, –y, z – 1/2						
4.29	–17.31	–3.31	–60.91	49.97	–42.92	–17.01/–12.10
C2—F1· · ·Cg(1), –1/2 + x, –y, 1/2 + z						
6.02	–10.82	–1.12	–45.72	32.09	–32.26	–13.93/–6.50
C5—F4· · ·Cg(1), 1/2 + x, –y, 1/2 + z						
4.29	–17.31	–3.31	–60.91	49.97	–42.92	–17.01/–12.10

lar bond contacts of the title compounds. Hirshfeld surfaces were generated using CrystalExplorer 17.5 to analyse the nature of the intermolecular contacts and their quantitative contributions to the crystal packing in (**I**) and (**II**). Electrostatic potentials, obtained using TONTO, integrated in CrystalExplorer using the DFT/B3LYP/6-31G basis set model were involved to map the Hirshfeld surfaces over the electrostatic potentials.

To define CrystalExplorer model energies, total energy of interaction between molecules in the crystal structure is commonly expressed in terms of four key components: electrostatic, polarisation, dispersion, and exchange-repulsion and the preferred energy model B3LYP/6-31G(d, p) was employed. The model B3LYP/6-31G(d,p) 6d 10f NoSymm Counterpoise=2 EmpiricalDispersion=GD2 was applied by Gaussian.

The CrystalExplorer and Gaussian unit cell crystal packing model energies for (**I**) and (**II**) are listed in Tables 6 and 7, respectively. It is noteworthy that binding abilities with N1—H1· · ·S1 hydrogen bond geometry and corrected complexation energy results are more effective in (**I**) compared to (**II**) considering the same participation of N1—H1· · ·S1 with respect to the appropriate crystal structure.

Conclusions

1-((4-Bromothiophen-2-yl)methylene)-2-(perfluorophenyl)hydrazine and 1-((4-bromo-5-methylthiophen-2-yl) methylene)-2-(perfluorophenyl)hydrazine were synthesised and NMR spectra, X-ray investigation, and Gaussian analyses were performed. Two hydrazone derivatives and its "chemical, molecular-structural, NBO charges, Hirshfeld surface and fitting interaction properties" were confirmed experimentally as well as theoretically. Atoms of sulfur, nitrogen and their hydrogen atoms play a considerable role in the bond system of the molecule and participate in the "configuration diversity" of the spatial forms of the molecules in the crystal structure. "Conformation diversity" has not been shown in the fitting scheme (Fig. 7).

Acknowledgement

This contribution was written thanks to the generous support under the Operational Program Integrated Infrastructure for the project: "Strategic research in the field of SMART monitoring, treatment and preventive protection against coronavirus (SARS-CoV-2)", Project no. 313011ASS8, co-financed by the European Regional Development and the Fund Science and Technology Assistance Agency under contract No. APVV-17-0513 and APVV-20-0213.

References

Allen FH, Kennard O, Watson DG, Brammer L, Orpen AG, Taylor R (1987) J. of the Chemical Society, Perkin Transactions 2: 12 S19.

Baier A, Kokel A, Horton W, Gizińska E, Pandey G, Szyszka R, Török B, Török M (2021) ChemMedChem Agric.FoodChem. 16: 1927–1932.

Bari A, Grenier D, Azelmat J, Syed SA, Al-Obaid AM, Hosten EC (2019) Chem. Biol. Drug Des. 94 4: 1750–1759.

Bernstein J, Davis RE, Shimoni L, Chang NL (1995) Angew. Chem. Int Ed. Engl. 34: 1555–1573.

Beverina L, Drees M, Facchetti A, Salamone M, Ruffo R, Pagani GA (2011) Eur. J. Org. Chem. 28: 5555–5563.

Bortňák D, Pecher D, Végh D, Breza M, Mikuš P, Milata V (2020) J. of Mass Spectrometry 55(10): e4540.

Brandenburg K (1999) Crystal Impact GbR Bonn Germany.

Burdette SC (2012) Nat. Chem. 4 (9): 695–699.

Burla MC, Caliandro R, Carrozzini B, Cascarano GL, Cuocci C, Giacovazzo C, Mallamo M, Mazzone A, Polidori G (2015) J. Appl. Cryst. 48: 306–309.

Collin RL, Lipscomb WN (1951) Acta Cryst. 4: 10–14.

Dolomanov OV, Bourhis LJ, Gildea RJ, Howard JAK, Puschmann H (2009) J Appl. Cryst. 42: 339–341.

Eloh K, Demurtas M, Deplano A, Mfopa AN, Murgia A, Maxia A, Onnis V, Caboni P (2015) J. Agric. Food Chem. 63(45): 9970–9976.

Feringa BL, Browne WR (2011) Molecular Switches Vol. I, II 595–627; Feringa BL, Browne WR Eds.; Wiley-VCH Verlag GmbH & Co. KGaA Weinheim.

Frisch MJ, Trucks GW, Schlegel HB, Scuseria GE, Robb MA, Cheeseman JR, Scalmani G, Barone V, Petersson GA, Nakatsuji H, Li X, Caricato M, Marenich AV, Bloino J, Janesko BG, Gomperts R, Mennucci B, Hratchian HP, Ortiz JV, Izmaylov AF, Sonnenberg JL, Williams-Young D, Ding F, Lipparini F, Egidi F, Goings J, Peng B, Petrone A, Henderson T, Ranasinghe D, Zakrzewski VG, Gao J, Rega N, Zheng G, Liang W, Hada M, Ehara M, Toyota K, Fukuda R, Hasegawa J, Ishida M, Nakajima T, Honda Y, Kitao O, Nakai H, Vreven T, Throssell K, Montgomery JA Jr, Peralta JE, Ogliaro F, Bearpark MJ, Heyd JJ, Brothers EN, Kudin KN, Staroverov VN, Keith TA, Kobayashi R, Normand J, Raghavachari K, Rendell AP, Burant JC, Iyengar SS, Tomasi J, Cossi M, Millam JM, Klene M, Adamo C, Cammi R, Ochterski JW, Martin RL, Morokuma K, Farkas O, Foresman JB, Fox DJ (2016) Gaussian 16 Revision D.01 Gaussian Inc. Wallingford CT.

Giliberti G, Ibba C, Marongiu E, Loddo R, Tonelli M, Boido V, Laurini E, Posocco P, Fermeglia M, Pricl S (2010) Bioorganic Med. Chem. 18(16): 6055–6066.

Ghosh P, Hazra A, Ghosh M, Chandra Murmu N, Banerjee P (2018) J. Mol. Struct. 1157: 444–449.

Hübschle ChB, Sheldrick GM, Dittrich B (2011) J App. Cryst. 44: 1281–1284.

Hypercube Inc. (2007) Hyperchem 7.0 Gainesville FL 32601 USA.

Chowdhury AR, Ghosh P, Roy BG, Mukhopadhyay SK, Murmu NC, Banerjee P (2015) Aqueous Solvent. Sensors Actuators B. Chem. 220: 347–355.

Jayatilaka D, Grimwood DJ, Lee A, Lemay A, Russel AJ, Taylor C, Wolff SK, Cassam-Chenai P, Whitton A (2005) TONTO.

Kuman L, Chauhan LJ (2014) Chem. Pharm. Res. 6(12): 916.

Lukeš V, Michalík M, Poliak P, Cagardová D, Végh D, Bortňák D, Fronc M, Kožíšek J (2016) Terminal Unit. Synth. Met. 219: 83–92.

Oxford Diffraction (2012) CrysAlis CCD and CrysAlis RED Oxford Diffraction Ltd, Yarnton, Oxfordshire, England.

Saha SJ, Siddiqui AA, Pramanik S, Saha D, De R, Mazumder S, Debsharma S, Nag S, Banerjee C, Bandyopadhyay U (2019) ACS Infect. Dis., 5(1): 63–73.

Sandoval-Torrientes R, Pascual J, García-Benito I, Collavini S, Kosta I, Tena-Zaera R, Martín N, Delgado JL (2017) ChemSusChem 10(9): 2023–2029.

Sheldrick GM (2008) SHELXS Acta Cryst. A64: 112–122.

Sheldrick GM (2015) SHELXL Acta Cryst. C71: 2053–2096.

Spackman MA, Jayatilaka D (2009) CrystEngComm 1: 19–32 Chemistry M313 School of Biomedical Biomolecular and Chemical Sciences University of Western Australia.

Spackman MA, McKinnon JJ, Jayatilaka D (2008) CrystEngComm. 10: 377–388.

Spackman PR, Turner MJ, McKinnon JJ, Wolff SK, Grimwood DJ, Jayatilaka D, Spackman MA (2021) Crystal Explorer 21.5 University of Western Australia Perth Australia.

Spek AL (2003) J Appl. Cryst. 36: 7–13.

STOE & Cie GmbH (2018) X-AREA Stoe & Cie GmbH, Darmstadt, Germany.

Su X, Aprahamian I (2014) Chemical Society Reviews March 21: 1963–1981.

Tarabová D, Milata V (2012) Acta Chimica Slovaca 5 2: 232–235.

Tonelli M, Boido V, Canu C, Sparatore A, Sparatore, F, Paneni MS, Fermeglia M, Pricl S, La Colla P, Casula L, Ibba C, Collu D, Loddo R (2008) Bioorganic Med. Chem. 16 (18): 8447–8465.

Turner MJ, McKinnon JJ, Wolff SK, Grimwood DJ, Spackman PR, Jayatilaka D, Spackman MA (2017) CrystalExplorer 17.5 University of Western Australia.

Verma G, Marella A, Shaquiquzzaman M, Akhtar M, Ali MR, Alam MM (2014) J. of Pharmacy and Bioallied Sciences 69–80.

Wiberg KB (1968) Tetrahedron 24: 3 1083–1096.

Xu W, Shao Z, Han Y, Wang W, Song Y, Hou H (2018) Elsevier Ltd. 152: 171–179.

sciendo

Extraction of biologically active compounds from *Aronia melanocarpa*: Comparison of techniques and multiple response optimization

Katarína Medveďová[1], Lenka Nahliková[1], Petra Strižincová[2], Tibor Dubaj[3], František Kreps[1]

[1]Department of Food Science and Technology, Faculty of Chemical and Food Technology, Slovak University of Technology in Bratislava, Radlinského 9, 812 37 Bratislava, Slovakia
[2]Department of Wood, Pulp, and Paper, Faculty of Chemical and Food Technology, Slovak University of Technology in Bratislava, Radlinského 9, 812 37 Bratislava, Slovakia
[3]Department of Physical Chemistry, Faculty of Chemical and Food Technology, Slovak University of Technology in Bratislava, Radlinského 9, 812 37 Bratislava, Slovakia
kmedvedova33@gmail.com

Abstract: The presented paper deals with the selection of most efficient extraction method for obtaining biologically active compounds (mainly antioxidants) from the black chokeberry (*Aronia melanocarpa*) fruits. Two conventional methods (maceration and Soxhlet extraction) as well as a more recent accelerated solvent extraction (ASE) were employed. The extracts were evaluated by means of their overall yield, antioxidant activity (TEAC assay), total phenolic content (TPC), ascorbic acid (AA), and malic acid (MA) content. Both Soxhlet extraction and ASE led to the highest overall yields (42 %) of the extract; however, in terms of TEAC and TPC, the extracts obtained by ASE were usually superior. The highest TEAC value (227.7 mg TE/g) as well as the highest TPC (67.9 mg GAE/g) were obtained by ASE using 40 % (v/v) ethanol at 140 °C after 30 min. The ASE method was further analyzed using a 2^3-factorial design where the effect of temperature (40—140 °C), extraction time (5—30 min), and solvent composition (40—96 % ethanol) was investigated. While temperature and solvent composition significantly affected the extract properties, the effect of extraction time was small or even insignificant. The regression model obtained from ANOVA was further used for multiresponse optimization of ASE conditions using the global desirability function as a criterion for overall extract quality.

Keywords: Accelerated solvent extraction, antioxidant activity, desirability function, factorial design

Introduction

Genus *Aronia* consists of three distinct species, namely *Aronia melanocarpa* (black chokeberry), *Aronia arbutifolia* (red chokeberry), and their potential hybrid *Aronia prunifolia* (purple chokeberry) (Jurendić and Ščetar, 2021). Owing to their astringency, black chokeberry fruits are rarely consumed in their raw form; however, there is a substantial market for juices, purées, jams, syrups, and various food supplements derived from black chokeberry fruits (Jia et al., 2022; Çelik et al., 2022). In fact, the astringent nature of these fruits is mainly caused by exceptionally high amounts of polyphenols (Sidor et al., 2019), which are considered beneficial for human health (Cory et al., 2018). Polyphenols are secondary metabolites found abundantly in certain parts of plants, especially in fruits, seeds, and leaves (Szwajkowska-Michałek et al., 2020; Dufour et al., 2018; Gao et al., 2019; Wu and Zhou, 2021; Swallah et al., 2020; Bae et al., 2022). In general, polyphenols can be divided into three classes: phenolic acids, flavonoids, and nonflavonoids (Rudrapal et al., 2022). Oszmiański and Wojdylo (2005) identified procyanidins, oligomeric and polymeric catechins/epicatechins as the major classes of polyphenolic compounds present in chokeberries. Even though chokeberries are usually associated with high amount of polyphenols, like chlorogenic acid, neochlorogenic acid, and anthocyanins, they are also moderately rich in other beneficial plant-derived compounds, such as ascorbic acid, β-carotene, and dietary fiber (about 55 g/kg, (Chiorean et al., 2022)).

Notwithstanding the benefits of consuming native food (Aguilera and Toledo, 2022), there is a growing demand for various food supplements in which beneficial compounds are present in significantly higher concentrations or have better organoleptic properties. Extraction is frequently employed in the manufacturing of such supplements. However, conventional extraction techniques such as maceration and solvent extraction at room temperature are rather time consuming and require large amounts of solvents whose removal (or recovery) is an energy-demanding process. Moreover, these techniques may not yield extracts of the desired quality and/or quantity. Recently, more efficient and "green" methods of extraction have been employed at industrial scale (Chemat et al., 2012). Among said methods, accelerated solvent extraction (ASE) is especially valued for relatively simple implementation and ease of full automation (Repajić et al., 2020). In ASE, extraction is carried out using a liquid solvent which can be heated above its normal boiling point as the process takes place in a closed system at elevated pressure. The elevated temperature employed in ASE improves both the kinetics and the equilibrium of extraction by increasing the diffusion rate and solubility of analytes while decreasing the solvent viscosity and surface tension (Alhallaf et al., 2022; Khanyile et al., 2022; Efthymiopoulos et al., 2019). Moreover, high pressure improves penetration of the solvent into porous matrices (Efthymiopoulos et al., 2019) thus improving the overall contact surface area. Apart from the operation at high pressures, the closed system also makes ASE suitable for extraction of oxygen-sensitive compounds (Liang et al., 2022).

This work deals with qualitative and quantitative comparison of extracts from *Aronia melanocarpa* fruits obtained by various extraction techniques. The results of ASE were compared with those of conventional methods, maceration and Soxhlet extraction. Since the performance of ASE depends on various parameters (solvent used, extraction time, temperature, pressure), a 2^k factorial design was employed and the effects of solvent, extraction time and temperature on five chosen extract properties were assessed. Finally, the extraction parameters were optimized with respect to various extract properties using the response surface methodology with the global desirability function.

Material and Methods

Plant material and chemicals

Chemicals used in the study were of analytical grade and were purchased from local and international vendors and used without further purification. Food grade ethanol (96 % v/v, Centralchem, Slovakia) and its mixtures with deionized water in various proportions (80, 60, 40 % v/v) was used as extraction solvent.

Fresh *Aronia melanocarpa* fruits originating from Ekofarma Aronia in Central Slovakia were ground by blender ETA 1-012 (ETA a.s., Slovakia) and dried in a thin layer at 60 °C for 24 hours. Dry biomass was further pulverized and extracted by means of maceration, Soxhlet extraction, or ASE. Between the various stages of handling, the plant material was stored in a freezer at –20 °C.

Extraction procedures

ASE was carried out using accelerated solvent extractor Dionex ASE 350 (Thermo Scientific, MO, USA) with 5 g of pulverized biomass. The 2^k factorial design was performed using 96 % and 40 % (v/v) ethanol for 5 min and 30 min at 40 °C and 140 °C. Center point conditions were: 17,5 min, 90 °C, and 68 % (v/v) ethanol. In all ASE runs, the pressure was maintained at 10.3 MPa.

Maceration was done at 22 °C for 2 hours using ethanol—water mixtures (40 %, 60 %, 80 %, and 96 %, v/v) and the biomass to solvent ratio of 1:10 (w/w) with 5 g of pulverized biomass. During maceration, the mixture was stirred in a laboratory stirrer.

Soxhlet extraction was carried out for 2 hours using Soxtherm apparatus (Gerhardt, Bonn, Germany) with an extraction thimble filled with 5 g of pulverized biomass. The biomass to solvent ratio was the same as in case of maceration; extraction temperature (78—83 °C) was determined by the boiling point of the solvent (ethanol 40—96 % v/v).

Finally, the extracts were dried in a rotary evaporator Heidolph Hei-VAP Precision, (Heidolph instruments, Germany) under reduced pressure at 40 °C until a gum-like semisolid matter was obtained. Dried extracts were used for all subsequent analyses.

Antioxidant activity

Trolox equivalent antioxidant capacity (TEAC) assay was carried out using a stock solution of DPPH (350 $\mu mol \cdot L^{-1}$ in ethanol) and extract samples dissolved in ethanol (0.1 $g \cdot L^{-1}$); the Trolox calibration curve was measured in the concentration range of 5—75 $\mu mol \cdot L^{-1}$. The spectroscopic assay was performed using a microplate reader BioTeK EPOCH 2 (Germany) where an extract sample of 200 µL was mixed with 75 µL of DPPH solution. Absorbance was measured every 10 min over a 1-hour interval at $\lambda = 517$ nm.

Total phenolic content

Total phenolic content (TPC) was determined in extract samples dissolved in water (10 $g \cdot L^{-1}$) and homogenized in an ultrasound bath; gallic acid in the mass concentration range of 0.001—0.9 $g \cdot L^{-1}$ was used for the calibration curve construction. The assay was carried out using a 100 µL sample of extract mixed with 500 µL of Folin-Ciocalteu reagent. After 3 min, the mixture was alkalized with 1.5 mL of sodium carbonate (20 % solution), filled up with water to 10 mL and left in dark for 2 hours. Subsequently, absorbance of the mixture was measured at the wavelength of 765 nm using a microplate reader BioTeK EPOCH 2 (Germany).

HPLC analysis of organic acids

HPLC analysis was conducted using 1260 Infinity II LC System (Agilent Technologies, USA) with a diode array detector (190—950 nm). The extracts were diluted in water ($1\ \mathrm{g \cdot L^{-1}}$); solutions of ascorbic acid, malic acid, and fumaric acid were prepared in $0.001—1\ \mathrm{g \cdot L^{-1}}$ mass concentration range for calibration. Mobile phase was $0.020\ \mathrm{mol \cdot L^{-1}}$ solution of potassium dihydrogen phosphate buffered with phosphoric acid to pH = 2.4; HALO AQ-C18 column was used as the stationary phase. Analysis conditions were as follows: flow rate of $0.6\ \mathrm{mL \cdot min^{-1}}$, sample volume of 20 µL, pump pressure of 307 bar.

Statistical analyses

All quantitative analyses were performed in duplicates; the mean values with standard deviation are presented if not stated otherwise. ANOVA was performed using Minitab 17 (Minitab Inc., PA, USA); optimization of the response surface was done using Design-Expert 13 (Stat-Ease, MN, USA). Data plots were created in OriginPro 8.1 (OriginLab, MA, USA).

Results and discussion

Maceration and Soxhlet extraction

Maceration and Soxhlet extraction are considered “classical” methods for extraction of valuable components from biomass. Maceration is especially suitable for thermally sensitive compounds; however, despite the process being usually performed for several days, it may provide low yields. Table 1 lists the overall yields from both maceration and Soxhlet extraction.

In case of maceration, the highest overall yields were obtained using 40 % and 60 % ethanol; higher ethanol fractions led to only slightly lower yields. Almost identical trend with respect to solvent composition ($r = 0.96$, $P < 0.05$) was observed for the Soxhlet method, however, it led to yields approximately twofold higher (up to 42.2 %), most probably due to extraction at the boiling point. It is generally recognized that elevated temperatures contribute to extraction efficiency more prominently than prolonged extraction time (Hidalgo and Almajano, 2017).

Regarding the antioxidant activity, both conventional methods led to comparable results except for maceration with 96 % ethanol, which gave inferior product in almost all analyzed properties. Except for this solvent, the TEAC values fell into a narrow range from 158 to 185 mg TE per gram of dry extract. A direct comparison of these results with published ones is difficult not only because of differences in the extraction conditions but also due to the changes in antioxidants content during the ripening of chokeberry fruits (Ünal et al., 2023). Since phenols are probably responsible for a major part of antioxidant activity of chokeberry extracts, it is not surprising that TEAC and TPC values are highly correlated for both methods ($r = 0.96—0.97$, $P < 0.05$). Similarly, the AA and MA content did not vary much with the extraction method employed or with extraction conditions. The AA content in extracts was remarkably low (mostly bellow 6 mg/g); however, the *Aronia melanocarpa* fruits are reported as a rather poor source of dietary AA with only 0.13 mg AA per gram of fresh fruit (Benvenuti et al., 2004). It is interesting to note that while maceration led to significantly lower yields, all qualitative parameters of the extracts were similar if not better compared to Soxhlet extraction. However, with respect to the starting weight of the fruit biomass, the Soxhlet method led to approximately twofold increase in the total amount of extractives.

Results summarized in Table 1 show that a binary solvent system containing aqueous mixtures of or-

Tab. 1. Yield and other extract parameters obtained by conventional methods (extraction time 120 min).

	Temperature (°C)	Solvent (EtOH %, v/v)	Yield[a] (%)	TEAC[b] (mg TE/g)	TPC[c] (mg GAE/g)	AA (mg/g)	MA (mg/g)
Maceration	22	96	14.9	86.3 ±0.5	38.2 ±0.9	5.66 ±0.05	32.5 ±0.2
	22	80	16.3	178.3 ±0.1	56.6 ±0.4	5.91 ±0.07	40.2 ±1.1
	22	60	18.0	184.5 ±0.3	57.8 ±0.8	5.97 ±0.02	40.8 ±0.2
	22	40	17.9	157.8 ±0.9	47.6 ±0.4	6.09 ±0.04	32.2 ±0.4
Soxhlet extraction	78	96	22.7	137.1 ±2.0	46.4 ±1.4	5.33 ±0.03	30.1 ±0.2
	79	80	36.9	167.8 ±3.8	60.9 ±2.7	5.47 ±0.02	32.2 ±0.2
	81	60	42.2	166.7 ±0.6	60.1 ±1.4	5.51 ±0.01	33.1 ±0.1
	83	40	42.0	158.7 ±0.2	59.6 ±0.4	5.58 ±0.01	28.8 ±0.2

[a] overall yield of dried extract with respect to the starting biomass (determined from extract mass)

[b] trolox equivalent antioxidant capacity in mg of Trolox equivalents per gram of dry extract

[c] total phenolic content in mg of gallic acid equivalents (GAE) per g of dry extract

ganic solvents is more effective than a single-component solvent system (ethanol) in the extraction of phenolic compounds. While ethanol is responsible for disrupting the bond between the solutes and the plant matrix, water plays an important role in matrix swelling thus improving the mass transport of extractives between the phases.

Comparison of ASE with conventional methods

Due to the influence of multiple factors (solvent, time, temperature) and monitoring of several parameters of the resulting extracts, the comparison of ASE with conventional extraction methods is not straightforward and unambiguous. Thus, the performance of ASE was investigated using a 2^3-factorial design in a wide range of conditions; the investigated factors and their levels are listed in Table 2. For the sake of simple graphical comparison with conventional methods, the results of ASE performed at 140 °C for 30 min (for TPC and TEAC) and at 40 °C for 30 min (for AA and MA) were chosen. Figure 1 compares all three methods with respect to TEAC, TPC, AA and MA content. In all cases, the ASE method provided better extract quality while the overall yield (see Table 3), after 30 min at 140 °C using 96 % and 40 % ethanol, ranged between 23 % and 42 %, respectively. As it is further discussed in section *ANOVA of ASE performance*, extract of similar yield and quality can be obtained even after 5 min of ASE which corresponds to a significant improvement compared to conventional methods.

Tab. 2. Values and labelling of factors employed in 2^3-factorial design of ASE.

Label	Factor	Coded levels	
		–1	+1
A	Temperature (°C)	40	140
B	Time (min)	5	30
C	Solvent composition (% EtOH, v/v)	40	96

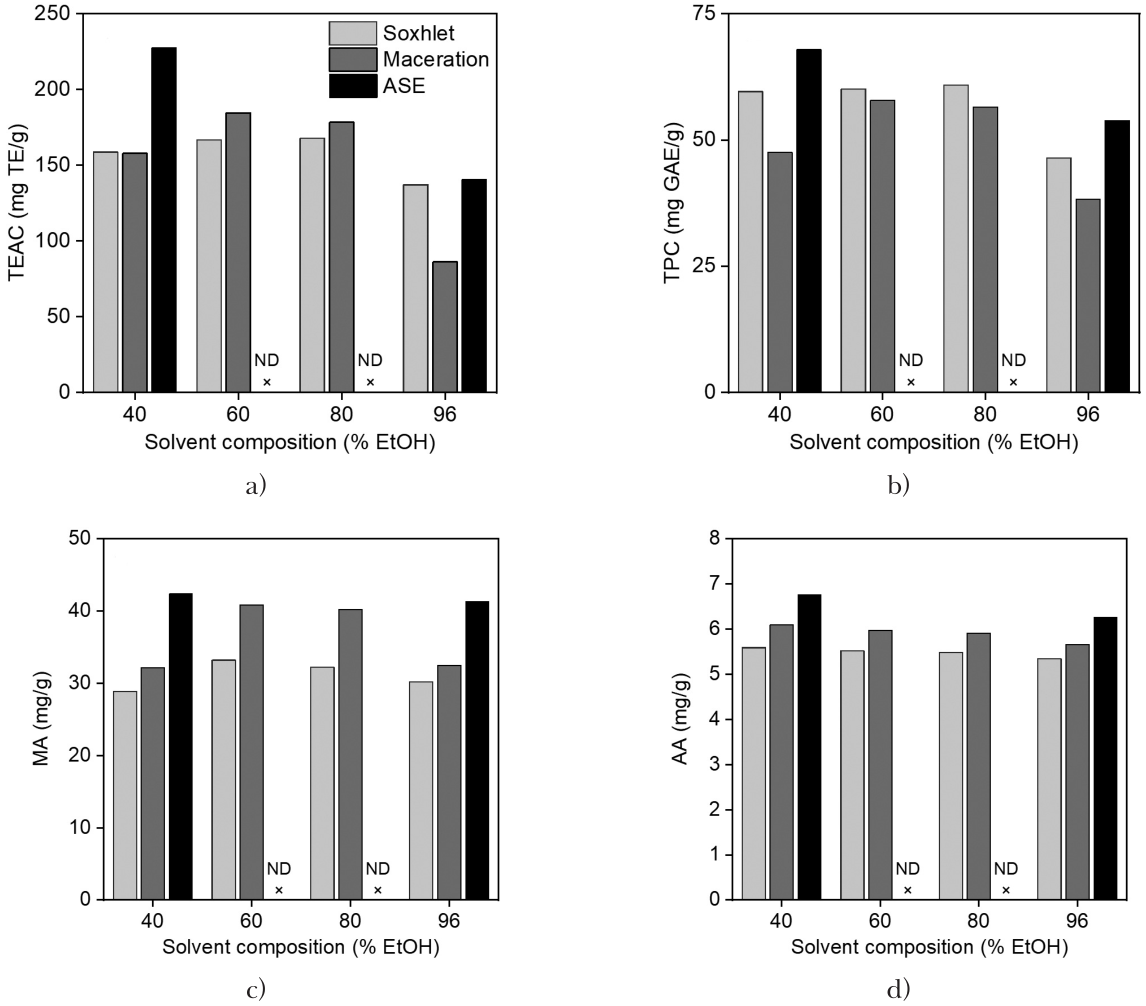

a) b) c) d)

Fig. 1. Antioxidant activity (a), total phenolic content (b), malic acid content (c), and ascorbic acid content (d) of extracts obtained using various extraction methods and solvent composition (ND — value not determined).

Tab. 3. Yield and other extract parameters obtained by ASE.

Run #	Coded levels			Yield	TEAC	TPC	AA	MA
	A	B	C	(%)	(mg TE/g)	(mg GAE/g)	(mg/g)	(mg/g)
1	−1	−1	−1	25.8	125.9 ±0.3	51.7 ±1.6	6.52 ±0.01	42.4 ±0.3
2	+1	−1	−1	37.1	219.7 ±1.4	66.7 ±1.1	6.12 ±0.01	36.4 ±0.1
3	−1	+1	−1	26.9	149.6 ±2.0	53.7 ±0.9	6.76 ±0.03	40.4 ±0.2
4	+1	+1	−1	41.9	227.7 ±1.2	67.9 ±0.5	5.93 ±0.01	31.7 ±0.3
5	−1	−1	+1	17.3	83.5 ±0.9	31.8 ±0.7	6.19 ±0.09	36.5 ±0.2
6	+1	−1	+1	22.1	128.7 ±0.3	48.8 ±0.4	5.28 ±0.01	30.6 ±0.4
7	−1	+1	+1	18.1	91.7 ±0.8	38.8 ±1.5	6.26 ±0.08	41.4 ±0.3
8	+1	+1	+1	23.7	140.7 ±7.0	53.8 ±1.1	5.09 ±0.10	7.0 ±0.2

ANOVA of ASE performance

Additional ASE experiments in a 2^3-factorial design arrangement were conducted to assess the effect of solvent composition, extraction time, and temperature on the overall yield of the extract, amount of malic acid (MA), ascorbic acid (AA), and phenolic compounds (TPC) in the extract from *Aronia melanocarpa L.*, and its antioxidant activity (TEAC). Marginal levels employed for each factor are given in Table 2; extraction pressure was kept at 10.3 MPa in all runs. The analysis was performed with respect to main effects and all possible pairwise interactions; regression model for each response was:

$$y_i = \sum_i \beta_i x_i + \sum_{i<j} \beta_{ij} x_i x_j \qquad (1)$$

In addition to 2^3 corner points a center point with five repetitions was included to assess repeatability of the results and to check for curvature of the response surface. High *P* values corresponding to the quadratic curvature for all responses (see Table 4) suggest that first-order model with pairwise interaction terms is adequate.

As it can be seen from Table 4, all three factors affect the overall yield of the extract with statistical significance ($P \leq 0.001$). Among the factors, the positive main effect of temperature and negative main effect of ethanol content in the solvent dominate over a surprisingly small effect of extraction time. As a matter of fact, in all responses (overall yield, TEAC, TPC, AA, and MA) the extraction time is the weakest factor and even fails to attain significance in case of AA and MA content. Similarly, the interaction terms involving time (*AB* and *BC*) are mostly insignificant or borderline significant, which indicates that relatively rapid extraction equilibrium is achieved during ASE regardless of the temperature and solvent used. In terms of overall yield, TEAC, and TPC, the best results were obtained using 40 % ethanol at 140 °C. On the other hand, AA and MA content was maximized at 40 °C (with only a negligible effect of time). This can be explained by increased solubility of phenolic compounds, as well as structure breakdown following their release from macromolecules due to higher temperature. Chokeberry is a rich source of polyphenols with antioxidant properties which also explains the increase of TEAC with higher temperature. In case of organic acids, thermal degradation could be the reason of their decrease

Tab. 4. Regression coefficients and *P* values from ANOVA of 2^3-factorial design.

	Yield (%)		TEAC (mg TE/g)		TPC (mg GAE/g)		AA (mg/g)		MA (mg/g)	
	Coeff.	***P***	**Coeff.**	***P***	**Coeff.**	***P***	**Coeff.**	***P***	**Coeff.**	***P***
Constant	26.62	< 0.0005	145.6	< 0.0005	51.66	< 0.0005	6.01	< 0.0005	33.27	< 0.0005
A	4.60	< 0.0005	33.26	< 0.0005	7.63	< 0.0005	−0.41	< 0.0005	−6.87	0.002
B	1.02	0.001	6.49	0.001	1.92	< 0.0005	−0.009	0.40	−3.17	0.052
C	−6.30	< 0.0005	−34.78	< 0.0005	−8.35	< 0.0005	−0.31	< 0.0005	−4.42	0.015
AB	0.57	0.012	−1.50	0.2	−0.34	0.009	−0.084	< 0.0005	−3.89	0.025
AC	−1.99	< 0.0005	−9.72	< 0.001	0.36	0.007	−0.11	< 0.0005	−3.19	0.051
BC	−0.43	0.036	−1.42	0.2	1.09	< 0.0005	−0.021	0.09	−1.49	0.30
Curvature	–	0.95	–	0.62	–	1.00	–	0.60	–	1.00
R^2	0.9954		0.9947		0.9993		0.9957		0.8193	

after exposition to high temperature, especially for AA, which is known to have very poor thermal stability (Dönmez and Kadakal, 2023; Tomsone et al., 2020). Such co-occurrence of high yield, TEAC, and TPC on one side and high AA and MA content on the other can also be seen from pairwise correlations among these variables: yield, TEAC, and TPC all exhibit strong positive correlation among themselves ($P < 0.001$); the same applies to the AA and MA content ($r = 0.849$, $P < 0.001$). Thus, high yield is a good predictor of both high TEAC and high TPC values (and *vice versa*).

In general, the AA content exhibited the smallest variability among the evaluated properties of the extracts. Based on the thermolabile nature of AA, a detrimental effect of extraction at 140 °C on its content is not surprising; however, the effect is quite small (6.5 *vs.* 6.1 mg/g of AA after 5 min at 40 °C and 140 °C, respectively). Moreover, contrary to expectation, the effect of elevated temperature is essentially independent from extraction time (6.1 *vs.* 5.9 mg/g of AA after 5 and 30 min using 40 % ethanol, respectively).

Optimization of ASE performance with desirability function

Finding optimum conditions for the extraction of a complex matrix such as *Aronia melanocarpa* fruits is a typical problem of multiple responses: certain set of conditions may lead to optimization of TEAC or TPC while the content of AA and MA is maximized at a different set of conditions. Thus, a trade-off between different desired properties of the extract is usually sought by maximizing appropriately defined global desirability function. In this case, all responses (yield, TEAC, TPC, AA, and MA) can be considered desirable and the corresponding partial desirability functions d_i can be written as

$$d_i = \frac{y_i - y_i^{\min}}{y_i^{\max} - y_i^{\min}}, \tag{2}$$

where y_i is the particular value of the i-th response and $y^{\min}$ and $y^{\max}$ are the extreme values found during factorial design. Global desirability function is usually expressed as a weighed product of partial desirability functions:

$$D = \left(\prod_i d_i^{w_i}\right)^{1/\Sigma w_i}, \tag{3}$$

where w_i is the weighing coefficient associated with the importance of the i-th response variable. It should be noted that, in this case, the choice of weights is rather arbitrary as there is no quantitative measure of "beneficial" effect of extract properties and the weights ultimately may determine the optimum solution. In this study, the overall yield ($w = 4$) was prioritized over both TEAC and TPC ($w = 2$) as both parameters are expressed per gram of extract and such weighing maximizes the absolute amount of desired extractives with respect to the starting biomass. Concentration of ascorbic acid, which is more abundant in other dietary sources, was optimized with $w = 1$; concentration of malic acid was omitted from global desirability as its beneficial properties are not conclusive. Apart from the extract properties, the global desirability function also included partial desirability functions for extraction time and temperature:

$$d_i = \frac{x_i^{\max} - x_i}{x_i^{\max} - x_i^{\min}}, \tag{4}$$

so that short extraction times and low extraction temperatures are favored. Optimization (maximization of D function) was done using Design-Expert 13 (Stat-Ease, Minneapolis, MN, USA) software; results (in uncoded values) are summarized in Table 5. Since the overall yield was given the highest weight in the global desirability, the location of optimum is quite close to the highest yield (see Table 3); however, inclusion of time and temperature into the optimization procedure led to a much more economic set of conditions (119 °C and 6 min).

Tab. 5. Factors maximizing the global desirability function and the corresponding responses.

Factor/response	Value	d_i
Temperature (°C)	119.1	0.210
Time (min)	6.3	0.948
Solvent composition (% EtOH, v/v)	40	–
Yield (%)	35.2	0.727
TEAC (mg TE/g)	199.0	0.801
TPC (mg GAE/g)	63.7	0.883
AA (mg/g)	6.2	0.655
MA (mg/g)	39.1	–

Conclusions

Compared to maceration and Soxhlet extraction, the ASE method has proven to be more efficient for extracting the valuable compounds from *Aronia melanocarpa* fruits. The results of ANOVA show that temperature, extraction time, and ethanol content significantly affect the overall yield, antioxidant activity and total phenolic content of extracts. While elevated extraction temperatures have positive effect on all the aforementioned extract parameters, the content of ascorbic acid and malic acid show an opposite trend. Despite meeting the significance criteria, the effect of time is surprisingly small, and 5 min of ASE can provide extracts of similar quantity and quality as do conventional methods after 120 min. Solvent composition (ethanol percentage) was shown as the most important factor affecting the extract yield and properties regardless of the extraction method; the best results were obtained using water–ethanol mixtures containing 40–60 % (v/v) of ethanol. In addition to the results of factorial design, a different set of optimum conditions for ASE was obtained by optimizing the global desirability function with a goal to maximize extract yield and quality while considering the process economy. Tailoring plant extracts using the desirability function can be valuable especially when various properties of the extract lead to contradictory sets of optimum conditions.

Acknowledgements

This research was supported by the Slovak Scientific Grant Agency VEGA based on contracts no. 1/0141/23 and 1/0498/22.

References

Aguilera JM, Toledo T (2022) Critical Reviews in Food Science and Nutrition 62: 1–15.

Alhallaf W, Bishop K, Perkins LB (2022) Food Analytical Methods 15: 2777–2790.

Bae JY, Seo YH, Oh SW (2022) Food Science and Biotechnology 31: 985–997.

Benvenuti S, Pellati F, Melegari M, Bertelli D (2004) Journal of Food Science 69: 164–169.

Çelik H, Karabulut B, Uray Y (2022) International Journal of Innovative Approaches in Agricultural Research 6: 246–254.

Chemat F, Vian MA, Cravotto G (2012) International Journal of Molecular Sciences 13: 8615–8627.

Chiorean AM, Buta E, Mitre V (2022) Bulletin of University of Agricultural Sciences and Veterinary Medicine Cluj-Napoca. Horticulture 79: 1–13.

Cory H, Passarelli S, Szeto J, Tamez M, Mattei J (2018) Frontiers in Nutrition 5: 1–9.

Dönmez A, Kadakal Ç (2023) Chemical Industry & Chemical Engineering Quarterly 30: 59–72.

Dufour C, Loonis M, Delosière M, Buffière C, Hafnaoui N, Santé-Lhoutellier V, Rémond D (2018) Food Chemistry 240: 314–322.

Efthymiopoulos I, Hellier P, Ladommatos N, Eveleigh A, Mills-Lamptey B (2019) Detritus 5: 75–83.

Gao HX, He Z, Sun Q, He Q, Zeng WC (2019) Carbohydrate Polymers 215: 1–7.

Hidalgo GI, Almajano M (2017) Antioxidants 6: 1–27.

Jia G, Jiang M, Sun A, Gan Z (2022) Molecules 27: 1–8.

Jurendić T, Ščetar M (2021) Antioxidants 10: 1–16.

Khanyile AT, Andrew JE, Paul V, Sithole BB (2022) Sustainable Chemistry and Pharmacy 26: 100608.

Liang Z, Zhang P, Fang Z (2022) Critical Reviews in Food Science and Nutrition 62: 1284–1307.

Oszmiański J, Wojdylo A (2005) European Food Research and Technology 221: 809–813.

Repajić M, Cegledi E, Kruk V, Pedisić S, Çınar F, Bursać Kovačević D, Žutić I, Dragović-Uzelac V (2020) Processes 8: 1–19.

Rudrapal M, Khairnar SJ, Khan J, Dukhyil AB, Ansari MA, Alomary MN, Alshabrmi FM, Palai S, Deb PK, Devi R (2022) Frontiers in Pharmacology 13: 1–15.

Sidor A, Drożdżyńska A, Gramza-Michałowska A (2019) Trends in Food Science and Technology 89: 45–60.

Swallah MS, Sun H, Affoh R, Fu H, Yu H (2020) International Journal of Food Science 2020: 1–8.

Szwajkowska-Michałek L, Przybylska-Balcerek A, Rogoziński T, Stuper-Szablewska K (2020) Applied Sciences 10: 1–24.

Tomsone L, Galoburda R, Kruma Z, Cinkmanis I (2020) European Food Research and Technology, 246: 1647–1660.

Ünal N, Saridaş MA, Ağçam E, Akyildiz A, Paydaş Kargi S (2023) Notulae Botanicae Horti Agrobotanici Cluj-Napoca, 51: 1–17.

Wu Q, Zhou J (2021) Advances in Food and Nutrition Research, 98: 35–99.

sciendo

Development and validation of HPLC-FLD method for aflatoxin M_1 determination in milk and dairy products

Lukáš Kolarič, Peter Šimko

Slovak University of Technology in Bratislava, Faculty of Chemical and Food Technology,
Institute of Food Science and Nutrition, Radlinského 9, 812 37 Bratislava, Slovak Republic
lukas.kolaric@stuba.sk

Abstract: Milk and dairy products are the most consumed foods in human diet and their safety is in the attention centre of control authorities. Aflatoxin M_1 (AFM_1) is a dangerous toxin that can occur in milk and dairy products as a metabolite formed from aflatoxin B_1 contained in contaminated animal feed. Therefore, the aim of this study was to develop and validate a reliable method for the determination of AFM_1 content in milk and dairy products based on HPLC with fluorescence detection employing immunoaffinity columns (IAC) pre-treatment. Optimal chromatographic separation of AFM_1 was achieved using a water/acetonitrile mixture (80/20, v/v) as a mobile phase, column with C_{18} stationary phase maintained at 25 °C, and fluorescence detection at excitation wavelengths of 360 nm and emission of 440 nm. Efficacy of AFM_1 extraction from the samples was found to be influenced by the elution agent composition. The best results were obtained using 1.25 mL of acetonitrile/methanol (3/2, v/v) and 1.25 mL of water. Validation parameters of the proposed method met the criteria set by the European legislation with the limits of detection and quantification at 0.002 and 0.007 µg/kg, respectively. Also, suitability of the method was confirmed by its application for AFM_1 determination in certified reference material. Finally, the method was applied for AFM_1 determination in 25 milk and dairy products collected in Slovakia; the AFM_1 content was below the limit of quantification. It was concluded that the method is suitable for AFM_1 content monitoring in milk and dairy products.

Keywords: aflatoxin M_1, HPLC, immunoaffinity chromatography, milk, dairy products, validation, optimisation, food safety

Introduction

Aflatoxins are low molecular weight secondary metabolites mainly generated by fungal species of *Aspergillus flavus*, *Aspergillus parasiticus*, or *Aspergillus nominus*. These fungi produce more than 20 toxic metabolites, however, in terms of food safety, the most relevant are aflatoxin B_1 and B_2 (AFB_1, AFB_2), aflatoxin G_1 and G_2 (AFG_1, AFG_2), and aflatoxin M_1 (AFM_1) (Buzás et al., 2023). Aflatoxins were discovered in England in 1960, when a severe outbreak of turkey *'X'*disease resulted in the death of more than 100,000 turkeys (Bellio et al., 2016; Pickova et al., 2021). Aflatoxins are chemical substances without any smell or taste, they are fluorescent in ultraviolet light and withstand temperatures above 320 °C without decomposing (Maggira et al., 2021).

According to the US Food and Drug Administration (FDA), AFB_1 is one of the most dangerous unavoidable food contaminants with serious adverse effects such as acute illness and death, liver cancer, nutritional interference, or immunologic suppression. AFM_1 is metabolised in liver from AFB_1 after the consumption of contaminated food/feed and then excreted into milk of lactating animals (Murphy et al., 2006; Šimko and Kolarič, 2022). Aflatoxins have been classified into group 1 (human carcinogens) by the International Agency for Research on Cancer (IARC) (Silva et al., 2023). Therefore, some countries have limited the maximum acceptable limits for AFM_1 in milk: 0.5 µg/kg in the USA and 0.05 µg/kg in the EU for adult food and 0.025 µg/kg for infant food (Šimko and Kolarič, 2022).

According to Pickova et al. (2021) approximately 4.5 billion people have been chronically exposed to aflatoxins through contaminated food. The latest risk assessment of aflatoxins in food published by the European Food and Safety Authority (EFSA) panel (EFSA CONTAM Panel, 2020) revealed that grains and grain-based products make the largest contribution to AFB_1 exposure, while liquid milk and fermented milk products are the main contributors to the mean exposure of AFM_1. In milk, AFM_1 binds strongly to casein, and higher levels of AFM_1 can be expected in dairy products high in protein, such as cheese. Furthermore, traditional milk manufacturing processes, such as pasteurisation or sterilisation, do not destroy its molecule (Silva et al., 2023). The contamination with aflatoxins occurs mainly after harvesting and during inappropriate management of transport and storage, e.g., at high humidity (>65 %) and temperature (Azam et al., 2021). In the past, aflatoxin outbreaks were mainly the problem of tropical and subtropical areas. Until 2004, aflatoxin contamination in the EU was confined only in imported foods. However, in the last 15 years, several hot and dry seasons have led to severe infections with *Aspergillus flavus* in maize in several countries in Europe, including Italy, Romania, Serbia, and Spain. Regarding the recent climate change problems, in the +2 °C scenario, increased probability in aflatoxin risk in many areas throughout Europe is expected (Moretti et al., 2019).

Thus, a wide range of analytical methods have been developed for aflatoxins analysis, with the most applied methods being liquid chromatography (LC) combined with fluorescence detection (FLD) or mass spectrometry (MS); for the determination of AFM_1 content, the most common methods include enzyme-linked immunosorbent assays (ELISA) or LC with FLD or MS detection (EFSA CONTAM Panel, 2020). In general, chromatographic methods are mainly used to confirm the results obtained from rapid screening tests or for precise quantitative determination of aflatoxins content. Immunochemical methods are used for rapid screening of aflatoxins in various sample matrices (Bellio et al., 2016). High-performance liquid chromatography (HPLC) with FLD detection using eventual post-column derivatisation is a reference method and currently the most often applied method for qualitative and quantitative determination of AFM_1 content in milk (Maggira et al., 2021). The methodology of AFM_1 analysis in milk has been improved by the application of immunoaffinity column technology (IAC), which provides a combination of extraction and clean-up stages of the analysis. Previously, liquid-liquid extraction or solid phase extraction (SPE) followed by a silica gel column, or another purification step were used (Dragacci et al., 2001). Wang et al. (2012) presented a simple and inexpensive method using SPE for the determination of AFM_1 in liquid milk and milk powder and achieved recoveries between 85.4 and 96.9 %. Moreover, a comparison of SPE and IAC showed that both clean-up methods provided consistent results.

Therefore, considering recent observations, the objective of this study was to validate a rapid and reliable method for quantitative determination of AFM_1 content in milk and dairy products purchased in the Slovak market using HPLC-FLD detection with IAC sample clean-up extraction. During the study, optimal IAC and HPLC conditions were developed and tested employing the analysis of a certified reference material. Finally, obtained results were compared with the rapid screening method MilkSafe^{TM} AflaM$_1$ applied in the screening of AFM_1 in raw milk in a Slovak dairy company (RAJO s.r.o.).

Material and Methods

Samples and Chemicals

For the determination of AFM_1 content, 25 milk samples were tested: 11 samples of raw milk were obtained from RAJO s.r.o. (Bratislava, Slovakia), and were collected from five different farms in Slovakia (Bukovec, Búč, Sevita, Prašník, and Uherec) during April 2023. Moreover, other four samples of raw milk were purchased from local markets during the summer of 2022. Then, ten samples of milk and dairy products from local markets were examined (UHT homogenised milk with the fat content of 0.5 %, 1.5 %, and 3.5 %; milk drink “Actimel”; Greek yogurt; milk drink “Brejky”; mini creamers; milk dessert “Pribiňáček”; cooking cream with the fat content of 10 %; curd cheese with the fat content of 0.5 %). Certified reference material (ERM-BD284, whole milk powder) was obtained from the European Commission Joint Research Centre (Belgium). AFM_1 analytical standard solution in acetonitrile (0.5 µg/mL) with the purity of ≥ 99,9 % was obtained from Sigma-Aldrich (USA). Acetonitrile and methanol were of HPLC grade and were purchased from Fisher Chemical (UK) and Lab-Scan Analytical Sciences (Poland).

Optimisation of HPLC conditions

First, HPLC conditions were tested using AFM_1 solution in water/acetonitrile mixture (80/20, v/v) with the concentration of 0.5 µg/kg. The HPLC system (Agilent Technologies 1260 Infinity system, Santa Clara, CA, USA) was equipped with a vacuum degasser, quarterly pump, autosampler, and FLD detector. A Zorbax Eclipse Plus C_{18} column (2.1 × 150 mm, 5 µm particle size, Agilent, Santa Clara, CA, USA) with the guard column Zorbax SB-C_{18} (4.6 × 12.5 mm, 5 µm particle size, Agilent, Santa Clara, CA, USA) were used as the stationary phase. As the mobile phase, three liquids (acetonitrile, methanol, water) were tested in various compositions: 1. water/acetonitrile/methanol (67/25/8, v/v/v); 2. water/acetonitrile/methanol (80/15/5, v/v/v); 3. water/acetonitrile (50/50, v/v); 4. water/acetonitrile (70/30, v/v); 5. water/acetonitrile (80/20, v/v); 6. acetonitrile/methanol (50/50, v/v); 7. water/methanol (80/20, v/v). The separation was carried out in the temperature range of 5—40 °C. Optimisation of FLD detection was made using various excitation wavelengths (260—360 nm) and emission wavelengths (400—460 nm). Injection volume was 50 µL. Flow rate of the mobile phase was set to 0.5 mL/min. The results were recorded using the OpenLab CDS software, ChemStation Edition for LC, and LC/MS systems (product version A.01.08.108).

Optimisation of IAC purification

Extraction of AFM_1 from milk matrix was performed using an IAC column (Vicam, AFM_1) according to the modified procedure of Mendonça and Venâncio (2005) with the variables being the type of elution solvent and volume as follows: A. 1.25 mL of water/acetonitrile 7/3 (v/v) + 1.25 mL of deionised water; B. 3 mL of methanol/acetonitrile 7/3 (v/v); C. 2 mL of acetonitrile/methanol 3/2 + 0.5 mL of deionised water; D. 2 mL of acetonitrile/methanol 3/2 + 2 mL of deionised water; E. 1.25 mL of water/methanol 17/3 (v/v) + 1.25 mL of deionised water; F. 1.25 mL of acetonitrile/methanol 3/2 + 1.25 mL of deionised water. Optimisation measurements were carried out in skim milk matrix enriched with AFM_1 standard to reach the final concentration of 0.1 µg/kg. Then, 50 mL of the tested sample were transferred to the column with a syringe and passed at the slow steady flow rate of 2—3 mL/min in vacuum manifold. The column was then washed twice with 10 mL of deionised water. Elution of the analyte was performed with different solvents and volumes (A—F) and collected in glass cuvettes each, which were vortexed and injected into HPLC.

In-house method validation

The optimised method was validated according to previously published methodology (Kolarič and Šimko, 2020) and the Eurachem guide for The fitness for purpose of analytical methods (Magnusson and Örnemark, 2014) using a certified reference material (ERM-BD284, whole milk powder). The milk reference sample was prepared according to the procedure reported by the manufacturer: 10 g of the sample were weighed in a beaker, 50 mL of pre-warmed water were added at 50 °C, and the mixture was mixed until a homogeneous mixture was obtained. The solution was cooled to 20 °C and quantitatively transferred to a 100 mL volumetric flask. The reference value of AFM_1 was reported at 0.44 µg/kg.

Linearity was recorded using the correlation coefficient (R^2) of the calibration curve calculated by FLD signal plotting against a known amount of AFM_1 standards at 0.003, 0.005, 0.008, 0.01, 0.015, 0.02, 0.03, 0.05, 0.075, and 0.1 ng. The limit of detection (LOD) and the limit of quantification (LOQ) were calculated as 3 and 10 times the standard deviation of the blanks divided by the slope of the calibration curve, respectively. Accuracy of the method was studied as a recovery test in two approaches: 1. standard addition at three concentrations (0.10, 0.30, and 0.60 µg/kg), and 2. comparison of measured concentration with the reference one. Accuracy of the HPLC-FLD method was also compared to that of the screening method used in Rajo s.r.o. For that purpose, raw milk was spiked with four different AFM_1 standard concentrations to obtain AFM_1 concentration equal to 0.03, 0.05, 0.08 or 0.10 µg/kg and analysed by HPLC-FLD detection and MilkSafe^{TM} AflaM_1 (Chr. Hansen Holding, Denmark). Precision of the detection was determined by comparing repeatability and intermediate precision. Repeatability was recorded by analysing four replicates of the samples on the same day, and intermediate precision was then evaluated on three different days. Precision was calculated from standard deviation (SD) and relative standard deviation (RSD). The Horwitz ratio (HorRat) was also calculated as the ratio of the observed RSD to the corresponding predicted relative standard deviation calculated from the Horwitz equation, $PRSD_R$ (%) = $2C^{-0.15}$, where C is the concentration expressed as mass fraction (Horwitz and Albert, 2006).

Determination of AFM_1 content in milk and dairy products

The analysis of AFM_1 content in 25 milk and dairy products was performed applying the developed method of HPLC-FLD and IAC extraction described earlier in this study. All high fat samples were first defatted by centrifugation (Hettich Zentrifugen, Tuttlingen, Germany) at 1800 g for 15 min and the upper layer was removed before the extraction.

Statistical analysis

Statistical evaluation was performed using Microsoft Excel 365 (version 2012). All results are expressed as mean ± standard deviation or as a percentage and were repeated at least twice. Data were subjected to a one-way analysis of variance (ANOVA) with the Tukey comparison test, the values were considered significantly different at $p < 0.05$.

Results and discussion

Optimisation of HPLC conditions

In general, HPLC is the most used method for AFM_1 content determination in milk. The main parameters influencing the effectivity and efficiency of liquid chromatography are: mobile phase composition, stationary phase type, or column particle size (Albuquerque et al., 2016). Regarding the characteristics of the AFM_1 molecule, the mobile phase is mostly polar, while the stationary phase is silica, alumina, or polysiloxanes with the most common hydrophobic octadecyl (C_{18}) group (Pisoschi et al., 2023). A comparison of different AFM_1 detection methods, showed that ELISA, HPLC-FLD and simultaneous use of ELISA and HPLC-FLD were used in 55 (76.4 %), 10 (13.9 %), 3 (4.2 %) and 4 (5.5 %) studies, respectively (Massahi et al., 2023).

In this work, three types of liquids were tested as mobile phase components (acetonitrile, methanol, and water). Manetta et al. (2005) used a mobile phase composed of four various liquids: acetic acid/acetonitrile/2-propanol/water (2/10/10/78, v/v/v/v). However, most current methods use the mixtures of methanol, water, and acetonitrile (Vaz et al., 2020). The obtained results relating mobile phase composition can be seen in Fig. 1. The first two mobile phases were the mixtures of all solvents tested. It was found that the resolution of AFM_1 cannot be properly achieved. Chavarría et al. (2015) used ternary mobile phase of water/methanol/acetonitrile (65/25/10, v/v/v) and achieved satisfactory elution of AFM_1 in milk, cheese, and sour cream samples, similarly to Bellio et al. (2016), who used water/methanol/acetonitrile (65/20/15, v/v/v). However, according to Dragacci et al. (2001), most participants in the collaborative trial used the recommended mobile phase (water/acetonitrile 75/25 (v/v)) and only two participants selected a ternary mobile phase. In this study, better resolution of AFM_1 was observed using a binary mobile phase composed of water and acetonitrile. In the equimolar mixture of water and acetonitrile, the elution time of AFM_1 was too short (1.9 min). The best results were obtained with the water to acetonitrile ratio of 70/30 and 80/20 (v/v), respectively. The peaks were sufficiently shaped with appropriate elution time (4.6 min). Finally, it was noticed that the mobile phase composed of water and methanol (80/20, v/v) or acetonitrile and methanol (50/50, v/v) was not suitable for the elution of AFM_1 from IAC extracts. The same suitable composition of the mobile phase (water/acetonitrile 80/20 (v/v)) was used by Jakšić et al. (2021) in the optimisation of HPLC method for AFM_1 detection in cheese. The ratio 75/25 (v/v) of these solvents was applied in the study by Masrouri et al. (2021). According to Shuib et al. (2017), the most common mobile phase used in the determination of AFM_1 by chemical derivatisation is water/methanol/acetonitrile (70/20/10, v/v/v). In their study, acetonitrile was substituted by methanol in different ratios (water/methanol 70/30, 65/35, 60/40, v/v). Among these methanolic mixtures, 65/35 (v/v) produced sharper peaks and improved resolution. Additionally, the retention time for AFM_1 was increased to 9 min compared to 6 min with a mixture of water/methanol/acetonitrile (70/20/10, v/v/v). Chiavaro et al. (2001) reported that the water/methanol mixture (58/42, v/v) resulted in higher response than the acetonitrile/water mixture. However, in both studies, the AFM_1 molecule was derivatised prior to FLD detection. According to Shephard (2009), binary systems of water and methanol resulted in broad HPLC peaks and long chromatographic run times, which was also confirmed in this work. Based on the elution strength, water/acetonitrile mobile phase seems to provide the highest elution strength. The elution strength of water/methanol mixture was lower thus the elution time of AFM_1 was higher. On the contrary, acetonitrile/methanol mixture resulted in higher elution strength than water/acetonitrile, thus the retention of AFM_1 on the stationary phase was weakened and elution time was too low. Similarly, to the ternary mobile phase of water/methanol/acetonitrile, as methanol has lower polarity than acetonitrile, the elution strength of such mixtures was weakened and AFM_1 resolution was not appropriate (Ramis-Ramos et al., 2017).

The second part of the optimisation process of HPLC-FLD detection of AFM_1 was dedicated to monitoring the influence of column temperature and FLD wavelength on the retention time and the area of AFM_1 peak. The results are summarised in Table 1. Temperature of the column statistically affected the area and the elution time of AFM_1. The results for the optimal temperature of 25 °C and other temperatures were statistically different at $p < 0.05$. This is in accordance with the theory of molecular spectroscopy, when intensification of vibration and relaxation processes in the molecules at elevated temperatures compete with fluorescence, thus causing decreased fluorescence output, while at lowered temperatures, the fluorescence output is affected negatively by the lack of energy needed for excitation. In other studies, the results are variable, Jakšić et al. (2021) maintained the column temperature at 30 °C, Bellio et al. (2016) at 35 °C, and Shuib et al. (2017) at 40 °C. However, no study was found to apply temperatures below 20 °C. Aflatoxins are colourless to pale yellow crystals and they fluoresce in ultraviolet light: blue for AFB_1 and AFB_2, green for AFG_1 and AFG_2, and blue violet for AFM_1 (EFSA CONTAM Panel, 2020). The presence of a chromophore in the molecule supports the detection of AFM_1 through fluorescence (Iqbal et al., 2015). Therefore, FLD is the most widely used detection technique for AFM_1 determination, as it provides detection limits at the level of ng/kg, which is recommended according to the Commission Regulation (EC) No. 401/2006 laying down the sampling and analysis methods for official control of mycotoxin levels in foodstuffs. Optimal excitation and emission wavelengths of 360 and 450 nm, respectively, are used in most methods (Pisoschi et al., 2023), which was also confirmed in this study, where the highest signal of the AFM_1 peak was observed

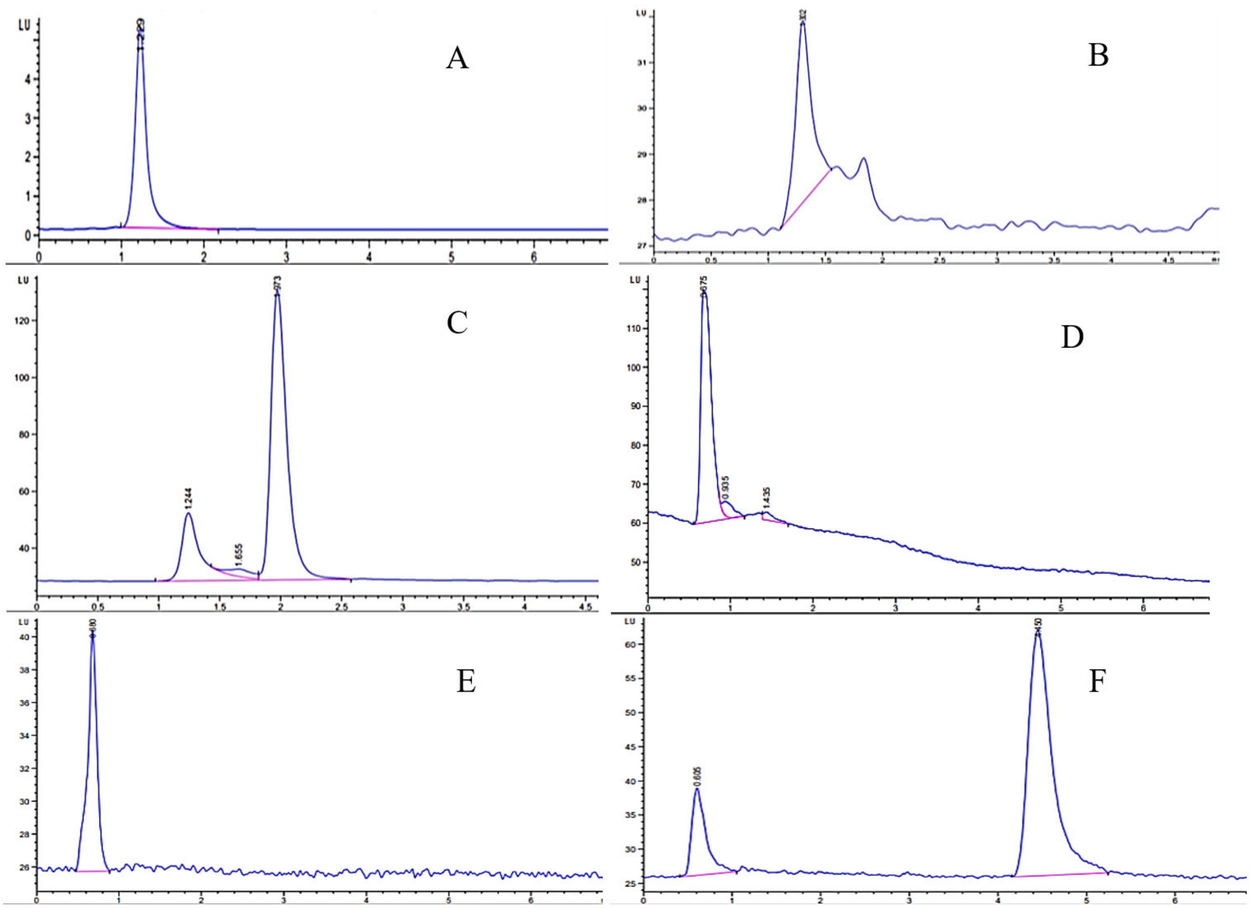

Fig. 1. Selected chromatograms of HPLC-FLD analysis of AFM_1 standard solution (0.5 µg/kg) using various compositions of mobile phase: A — water/acetonitrile/methanol (67/25/8, v/v/v); B — water/acetonitrile/methanol (80/15/5, v/v/v); C — water/acetonitrile (50/50, v/v); D — acetonitrile/methanol (50/50, v/v); E — water/methanol (80/20, v/v); F — water/acetonitrile (80/20, v/v).

at the excitation and emission wavelengths of 360 and 440 nm, respectively. Statistically significant differences were observed at $p < 0.05$ in comparison to the values obtained at other wavelengths.

Therefore, it can be concluded that optimal HPLC-FLD conditions for the analytical standard AFM_1 are: 1. mobile phase — water/acetonitrile (80/20, v/v), 2. — stationary phase — column with C_{18}, 3. — column temperature –25 °C, 4. FLD setting — excitation at 360 nm and emission at 440 nm.

Optimisation of IAC purification

Methods for mycotoxins extraction from milk include techniques such as liquid-liquid extraction (LLE), SPE, or LLE followed by a SPE cleaning step (Aguilera-Luiz et al., 2011). Commonly used purification procedures for the extraction of AFM_1 from milk matrix are IAC or multifunctional one-step cleaning columns, which are very efficient and easy to use providing high selectivity. However, they are only for disposable use due to denaturation of antibodies during the elution step and their costs are high (Vaz et al., 2020). The principle of IAC is the immobilisation of analyte in an antibody (polyclonal or monoclonal) on a gel packed into a small plastic column. The column is initially conditioned with a buffer solution, mostly phosphate buffered saline, and the crude sample extract is applied slowly to the column. After the extract is loaded, the gel is washed and finally the analyte is eluted from the IAC column by breaking the antibody-antigen bond. Liquid matrices are frequently defatted and/or filtrated before passing directly through the IAC because as extraction and purification in an IAC proceed simultaneously. In case of solid matrices (e.g., cheese), solvent extraction is required, which is usually carried out in a blender or by shaking. Elution solvents need to be aqueous to be compatible with the IAC, so methanol/water and acetonitrile/water combinations are mostly applied (Şenyuva and Gilbert, 2010).

In this work, it was found that the type of elution solvent significantly affects the recovery of AFM_1 from the milk matrix (Table 2). The combination of acetonitrile and methanol without the addition of water (solvent B) was not suitable for proper

Tab. 1. Influence of column temperature and FLD wavelengths on retention time and area of AFM_1 peak.

Column temperature [°C]	Average area [LU][a]	Elution time [min][a]
5	325.4 ±7.2*	6.3 ±0.0*
15	333.9 ±12.0*	5.4 ±0.1*
25	426.7 ±17.3	4.6 ±0.0*
40	358.0 ±14.8*	3.8 ±0.1*
Excitation wavelength [nm][b]		
260	285.0 ±16.5*	–
300	66.2 ±5.0*	–
320	237.5 ±1.2*	–
360	806.8 ±13.4	–
Emission wavelength [nm][c]		
400	12.2 ±1.8*	–
420	305.8 ±98.9*	–
440	816.3 ±0.7	–
460	700.8 ±18.2*	–

[a] Values are expressed as mean ± standard deviation, n = 3.

[b] Values are determined at emission wavelength of 440 nm.

[c] Values are determined at excitation wavelength of 360 nm.

*Values are significantly different at $p < 0.05$.

elution of AFM_1 as the peak was not separated and interference from other substances occurred. According to the Commission Regulation (EC) No. 401/2006, the recovery of AFM_1 in concentrations above 0.05 μg/kg should reach values between 70 and 110 %. This value was obtained only with one elution solvent, 1.25 mL of acetonitrile/methanol (3/2, v/v) and 1.25 mL of water (solvent F). Moreover, it was noticed that the volume of solvents also played an important role. In case of solvents C and D, the same composition as in F was used, however, different volumes caused a decrease in the recovery to 35.2 % and 60.2 %, respectively.

Khalil et al. (2013) tested various amounts of acetonitrile and methanol and suggested that all solvents showed recovery above 70 %, but the best recoveries were obtained from the mixture of acetonitrile/methanol (3/2, v/v). The AOAC official method 2000.08 of AFM_1 content determination in liquid milk uses elution with acetonitrile alone (4 mL) with the recovery of not less than 80 % (Dragacci et al., 2001). Jakšić et al. (2021) tested two types of IAC columns for the treatment of cheese matrix (AlfaStar^{TM} M1R, Protealmmun IAC AFM_1), and the recovery of both types reached satisfactory efficiency using acetonitrile as the elution agent. Some studies also showed the application of other methods. For example, Aguilera-Luiz et al. (2011) evaluated the efficiency of SPE or QuEChERS methods, finding that the latter procedure was not suitable for AFM_1 extraction at very low levels, while SPE allowed the extraction without increasing the amount of impurities in the extract. The analytes were eluted with 5 mL of pure methanol. Wang et al. (2012) studied clean-up efficiency of OASIS HLB and IAC cartridges for AFM_1 elution from liquid milk and milk powder. Optimal results of the elution were observed with 5 mL of methanol and 5 mL of acetonitrile. Using OASIS HLB, the recovery reached 92.6 %. Compared to IAC, impurity peaks were obtained using OASIS HLB, however, the cleaning effect was sufficient for qualitative and quantitative determination of AFM_1.

In-house method validation

After optimisation of the HPLC and IAC conditions, the method was validated for linearity, accuracy, and precision using certified reference material in milk powder form provided by the European Commission Joint Research Centre. The results are summarised in Table 3. Validation criteria for AFM_1 content determination milk are set in the Commission Regulation (EC) No. 401/2006.

Linearity of the method was calculated from the calibration curve, the results were linear in all concentration ranges of 0.003 to 0.1 ng of AFM_1 in the calibration solution, R^2 was 0.99. From the calibration curve parameters (slope and intercept), LOD

Tab. 2. Influence of elution agent composition on AFM_1 recovery.

Agent	The percentage of AFM_1 recovery [%][a]
A	51.4 ±8.8[*]
B	–
C	35.2 ±2.1[*]
D	60.2 ±1.6[*]
E	11.4 ±5.6[*]
F	90.5 ±3.6

[a] Values are expressed as mean ± standard deviation, n = 2.

[*] Values are significant different at $p < 0.05$. Composition of agent: A – 1.25 mL of water/acetonitrile (7/3, v/v) + 1.25 mL of water; B – 3 mL of methanol/acetonitrile (7/3, v/v); C – 2 mL of methanol/acetonitrile (3/2, v/v) + 0.5 mL of water; D – 2 mL of methanol/acetonitrile (3/2, v/v) + 2 mL of water; E – 1.25 mL of water/methanol (17/3, v/v) + 1.25 mL of water; F – 1.25 mL of methanol/acetonitrile (3/2, v/v) + + 1.25 mL of water.

and LOQ values were calculated. Regarding the analysis of AFM_1 content in milk samples in the EU, it is important to reach LOQ of at least 0.05 µg/kg as it is the maximal acceptable level of AFM_1 in milk according to the Commission Regulation (EC) No. 1881/2006. In this work, both the LOD and the LOQ values were significantly below this limit, 0.002 and 0.007 µg/kg, respectively. These results are also similar to other studies, which used the HPLC-FLD method for AFM_1 content determination in milk. According to EFSA CONTAM Panel (2020), the reported LOQs for AFM_1 are typically between 0.0007 and 0.014 µg/kg. Similar conditions for the analysis of AFM_1 in raw milk were used by Patyal et al. (2020) and their method exhibited LOD and LOQ at 0.004 and 0.01 µg/kg, respectively. In addition, Bellio et al. (2016) showed the same LOD (0.002 µg/kg) in milk purchased in Northern Italy. Chen et al. (2005) reached lower LOD for AFM_1 in whole milk (0.0006 µg/kg) using liquid chromatography coupled with tandem mass spectrometry. Comparison of ELISA, HPLC-FLD and HPLC-MS/MS methods showed that all methods are suitable for the determination of AFM_1 in milk samples with almost the same LOQ ranging from 0.004 to 0.008 µg/kg (Kos et al., 2016).

Another important parameter that describes the suitability of the method for the given purpose is its accuracy, which was monitored in two steps as AFM_1 recovery. First, AFM_1 concentration obtained by the

Tab. 3. Validation parameters of proposed HPLC-FLD method for AFM_1 determination in milk.

Method linearity				
Slope	16925			
Intercept	0.3132			
Correlation coefficient (R^2)	0.99			
LOD [µg/kg]	0.002			
LOQ [µg/kg]	0.007			
Method recovery[a]				
Certified reference material	Reference value [µg/kg]	Determined value [µg/kg]	Recovery [%]	
ERM-BD 284	0.44 ±0.06	0.38 ±0.01	87.3 ±0.6	
Spiked milk sample [µg/kg]	Determined value [µg/kg]	Recovery [%]		
0	> LOQ	–		
0.10	0.10 ±0.01	103.7 ±9.0		
0.30	0.24 ±0.01	86.2 ±4.1		
0.60	0.55 ±0.01	91.7 ±1.4		
Method precision[b]				
Reference material	Repeatability	RSD [%]	Intermediate precision [RSD%]	Horrat
ERM-BD 284	Day 1	3.1	4.2	0.12
	Day 2	4.7		0.18
	Day 3	3.8		0.15

[a] Values are expressed as mean ± standard deviation, n = 3.

[b] Values are expressed as mean ± standard deviation, n = 4.

LOD – limit of detection; LOQ – limit of quantification.

analysis of certified reference material was compared with the manufacturer's data, it was shown to be 87.3 %. Subsequently, accuracy was evaluated in milk spiked with three various amounts of AFM_1 standard solution. In this case, the recoveries ranged from 86.2 to 103.7 %. It is notable that all values are acceptable according to the Commission Regulation (EC) No. 401/2006. Maggira et al. (2021) published that the HPLC-FLD method for the determination of AFM_1 content in raw milk exhibited recoveries between 90—109 %. Moreover, they found that HPLC showed slightly better accuracy for the target compound than ELISA. The mean recovery of the HPLC method for AFM_1 determination in spiked milk and cheese samples was found to be 90 % for milk and 76 % for cheese (Manetta et al., 2005). In Shuib et al. (2017), recovery values for milk and milk products ranged from 85.2 to 107.0 %. The proposed method was also compared with the screening method for AFM_1 content determination in raw milk used by the Slovak dairy company Rajo s.r.o. This company applied the MilkSafe™ instrument (Chr. Hansen Holding, Denmark), which is suitable for rapid determination of antibiotics and aflatoxins presence in milk. Four different spiking concentrations of AFM_1 were tested as requested by the provider (CLIMAX, s.r.o., Slovakia); the results are shown in Fig. 2. Both methods showed excellent recovery value ranging from 82.9 to 103.6 % for HPLC and 92.3 to 103.6 % for MilkSafe™.

Finally, precision of the proposed method was examined as the RSD of values obtained in one day (repeatability) and on three different days (intermediate precision). In addition, the HorRat parameter was calculated. The results are shown in Table 3. The repeatability RSD ranged from 3.1 to 4.7 %, while the intermediate precision RSD was 4.2 %. HorRat ranged from 0.12 to 0.18. According to official requirements, reproducibility of a method is approved when HorRat is below or equal to 2 (Horwitz and Albert, 2006; Ribeiro and Brandäo, 2017). Very low HorRat values (0.31—0.42) were also confirmed by Dragacci et al. (2001) in a collaborative study for the determination of AFM_1 in liquid milk. Relatively the same values of repeatability were reported by Maggira et al. (2021) (RSD < 3.6 %) in the determination of AFM_1 in raw milk using the HPLC-FLD method. In contrast, higher values were reported by Kos et al. (2016), ranging from 9.5 to 11.3 %. Manetta et al. (2005) published a HPLC method with postcolumn derivatisation and FLD detection for AFM_1 determination in milk and cheese and found the RSD precision ranging from 1.7 to 2.6 % for milk and 3.5 to 6.5 % for cheese.

Determination of AFM_1 content in milk and dairy products

Milk and dairy products are predominant subject of AFM_1 contamination. According to the worldwide systematic review and meta-analysis (Mollayusefian et al., 2021), total AFM_1 content in raw and pasteurised milk was found to be 0.06 µg/kg and 0.09 µg/kg, respectively. Additionally, the highest content was found in raw buffalo milk and pasteurised cow milk, indicating that the pasteurisation process cannot reduce the concentration of aflatoxin to an acceptable level (Mollayusefian et al., 2021). According to recent risk assessment of aflatoxins in food (EFSA CONTAM Panel, 2020), the highest estimated mean lower bound (LB) and upper bound (UB) exposure to AFM_1 in infants was up to 0.001 ng/kg and 0.002 µg/kg bw per day, respectively. The main contributors to overall AFM_1 mean exposure are liquid milk and fermented milk products throughout all age groups. In Hricíková et al. (2023), positive findings for AFM_1 in milk in Slovakia were presented (32 samples were tested

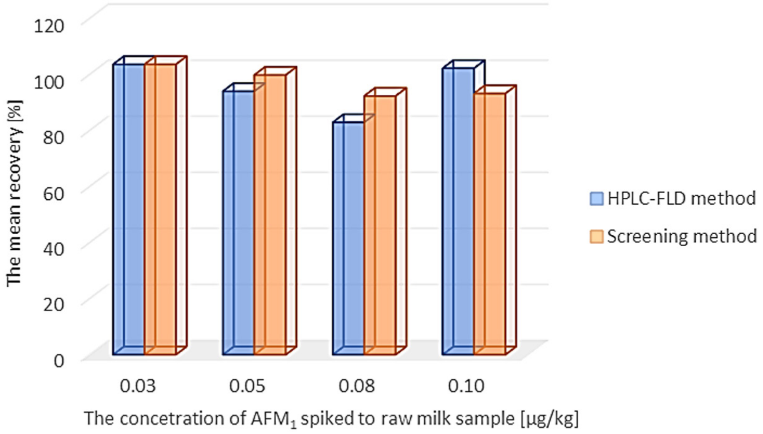

Fig. 2. Comparison of AFM_1 recovery using our proposed HPLC-FLD method and MilkSafe™ AFM_1 screening method applied in RAJO s.r.o.

Tab. 4. Determination of AFM_1 content in milk samples collected in Slovakia.

Sample	AFM_1 content [µg/kg]	Sample	AFM_1 content [µg/kg]
Raw milk (1)	>LOQ	UHT pasteurized skimmed milk (fat content 0.5 %)	>LOQ
Raw milk (2)	>LOQ	UHT pasteurized milk (fat content 1.5 %)	>LOQ
Raw milk (3)	>LOQ	UHT pasteurized milk (fat content 3.5 %)	>LOQ
Raw milk (4)	>LOQ	Curd cheese (fat content 0.5 %)	>LOQ
Raw milk (5)	>LOQ	Greek yogurt	>LOQ
Raw milk (6)	>LOQ	Mini creamers	>LOQ
Raw milk (7)	>LOQ	Cooking cream (fat content 33 %)	>LOQ
Raw milk (8)	>LOQ	Milk dessert "Pribináček"	>LOQ
Raw milk (9)	>LOQ	Milk drink "Brejky"	>LOQ
Raw milk (10)	>LOQ	Milk drink "Actimel"	>LOQ
Raw milk (11)	>LOQ		
Raw milk (12)	>LOQ		
Raw milk (13)	>LOQ		
Raw milk (14)	>LOQ		
Raw milk (15)	>LOQ		

n = 2; LOQ = 0.007 µg/kg.

positive and 8 negative). In this study, 15 raw milk samples collected in Slovakia were tested for AFM_1 concentration. The AFM_1 content was found to be below LOQ in all cases (Table 4). Furthermore, other ten dairy products were purchased randomly in Slovak markets and the AFM_1 content was also found below the LOQ. In a one-year survey (September 2021 to November 2022) on AFM_1 detection in raw and drinking milk in Hungary (Buzás et al., 2023), 11.9 % of raw milk samples and 0.5 % of drinking milk samples contained AFM_1 above the EU limit (0.05 µg/kg). Furthermore, the highest mean AFM_1 level was measured during fall and lower in spring and summer. According to Bellio et al. (2016), only 0.5 % of total milk samples collected in northern Italy during a three-year period (2012–2014) were found to be non-compliant with the EU regulation. Analysis of 109 samples collected from the Greek market (52 samples of infant/toddler milk and formulas, 32 pasteurised milk, and 25 samples of feta cheese) revealed that AFM_1 was present in 60 % of infant/toddler formulas, 69 % of pasteurised milk samples, and 28 % of cheese samples; however, no sample exceeded the maximum tolerable limit (Malissiova et al., 2022). AFM_1 levels in Europe are increasing due to climate changes; however, generally they are still lower than in other regions, such as African or South Asian countries. The lower content of AFM_1 in European milk and dairy products could also be attributed to modern processing technology, especially strict regulations, hygiene, adoption of food safety systems, continuous monitoring of aflatoxins, and advanced analytical techniques (Mollayusefian et al., 2021).

Conclusion

In this study, the HPLC-FLD method was developed, optimised, and validated for the determination of AFM_1 content in milk. First, HPLC conditions were tested for the analytical standard AFM_1 solution, and the best AFM_1 chromatographic separation was obtained at the following conditions: 1. mobile phase composed of water/acetonitrile mixture (80/20, v/v); 2. column with stationary phase C_{18}; 3. column temperature of 25 °C; and 4. FLD wavelengths at excitation at 360 nm and emission at 440 nm. IAC extraction of AFM_1 from the spiked milk sample was optimised for the elution agent. The best recovery was obtained using 1.25 mL of methanol/acetonitrile (3/2, v/v) + 1.25 mL of water. The method was validated according to the Commission Regulation (EC) No. 401/2006 regulations, and it was observed that all parameters meet the criteria set by the Regulation including LOD and LOQ which were 0.002 and 0.007 µg/kg, respectively. Precision of the proposed method was confirmed with the data declared by the reference material provider, and significant similarity was found with the method used in daily screening of AFM_1 concentration at the dairy factory. Finally, AFM_1 was determined in 25 milk and dairy products collected in Slovakia; however, the concentration in all samples was below LOQ.

Acknowledgement

The authors would like to thank RAJO s.r.o. (Slovakia) and CLIMAX s.r.o. (Slovakia) for providing samples of raw milk and for the possibility to compare our proposed HPLC method with their screening MilkSafe^{TM} *AflaM*$_1$ *method.*

This work was supported by the Slovak Research and Development Agency under Contract APVV-22-0102.

References

Aguilera-Luiz MM, Plaza-Bolaños P, Romero-González R, Vidal JLM, Frenich AG (2011) Anal. Bioanal. Chem. 399: 2863–2875.

Albuquerque TG, Oliveira MBPP, Sanches-Silva A, Costa HS (2016) Food Chem. 193: 18–25.

Azam MS, Ahmed S, Islam MN, Maitra P, Islam MM, Yu D (2021) Toxins 13: 323.

Bellio A, Bianchi DM, Gramaglia M, Loria A, Nucera D, Gallina S, Gili M, Decastelli L (2016) Toxins 8: 57.

Buzás H, Szabó-Sárvári LC, Szabó K, Nagy-Kovács K, Bukovics S, Süle J, Szafner G, Hucker A, Kocsis R, Kovács AJ (2023) J. Food Compos. Anal. 121: 105368.

Commission Regulation (EC) No 401/2006 of 23 February 2006 laying down the methods of sampling and analysis for the official control of the levels of mycotoxins in foodstuffs. Available on https://eur-lex.europa.eu/legal-content/EN/ALL/?uri=celex%3A32006R0401.

Commission Regulation (EC) No 1881/2006 of 19 December 2006 setting maximum levels for certain contaminants in foodstuffs. Available on https://eur-lex.europa.eu/legal-content/EN/ALL/?uri=celex%3A32006R1881.

Dragacci S, Grosso F, Gilbert J (2001) J. AOAC Int. 84: 437–443.

EFSA CONTAM Panel (EFSA Panel on Contaminants in the Food Chain), Schrenk D, Bignami M, Bodin L, Chipman JK, del Mazo J, Grasl-Kraupp B, Hogstrand C, Hoogenboom LR, Leblanc JC, Nebbia CS, Nielsen E, Ntzani E, Petersen A, Sand S, Schwerdtle T, Vleminckx C, Marko D, Oswald IP, Piersma A, Routledge M, Schlatter J, Baert K, Gergelova P and Wallace H (2020) EFSA Journal 18(3): 6040.

Horwitz W, Albert R (2006) J. AOAC Int. 89: 1095–1109.

Hriciková S, Kožárová I, McGoldrick D, McCaul O (2023) Folia Vet. 67: 35–44.

Chavarría G, Granados-Chinchilla F, Alfaro-Cascante M, Molina A (2015) Food Addit. Contam.: B Surveill. 8: 128–135.

Chen CY, Li WJ, Peng KY (2005) J. Agric. Food Chem. 53: 8474–8480.

Chiavaro E, Dall'Asta C, Galaverna G, Biancardi A, Gambarelli E, Dossena A, Marchelli R (2001) J. Chromatogr. A 937: 31–40.

Iqbal SZ, Jinap S, Pirouz AA, Faizal ARA (2015) Trends Food Sci. Technol. 46: 110–119.

Jakšić S, Baloš MŽ, Popov N, Torović L, Krstović S (2021) Int. J. Dairy Technol. 74: 681–688.

Khalil MMH, Gomaa AM, Sebaei AS (2013) J. Anal. Methods Chem. 2013: 817091.

Kolarič L, Šimko P (2020) Foods 9: 1378.

Kos J, Hajnal EJ, Jajić I, Krstović S, Mastilović J, Šarić B, Jovanov P (2016) Acta Chim. Slov. 63: 747–756.

Maggira M, Ioannidou M, Sakaridis I, Samouris G (2021) Vet. Sci. 8: 46.

Magnusson B, Örnemark U (2014) Eurachem Guide: The Fitness for Purpose of Analytical Methods – A Laboratory Guide to Method Validation and Related Topics (2nd ed.). ISBN 978-91-87461-59-0.

Malissiova E, Soultani G, Tsokana K, Alexandraki M, Manouras A (2022) Clin. Nutr. ESPEN 47: 189–193.

Manetta AC, Di Giuseppe L, Giammarco M, Fusaro I, Simonella A, Gramenzi A, Formigoni A (2005) J. Chromatogr. A 1083: 219–222.

Masrouri M, Mogaddam MRA, Farajzadeh MA, Nemati M, Lotfipour F (2021) J. Sep. Sci. 44: 1501–1509.

Massahi T, Kiani A, Sharafi K, Matin BK, Omer AK, Ebrahimzadeh G, Jaafari J, Fattahi N (2023) Food Control 150: 109733.

Mendonça C, Venâncio A (2005) J. Sci. Food Agric. 85: 2067–2070.

Mollayusefian I, Ranaei V, Pilevar Z, Cabral-Pinto MMS, Rostami A, Nematolahi A, Khedher KM, Thai VN, Fakhri Y, Khaneghah AM (2021) Trends Food Sci. Technol. 115: 22–30.

Moretti A, Pascale M, Logrieco AF (2019) Trends Food Sci. Technol. 84: 38–40.

Murphy PA, Hendrich S, Landgren C, Bryant CM (2006) J. Food Sci. 71: 51–65.

Patyal A, Gill JPS, Bedi JS, Aulakh RS (2020) J. Environ. Sci. Health B 55: 827–834.

Pickova D, Ostry V, Toman J, Malir F (2021) Toxins 13: 399.

Pisoschi AM, Iordache F, Stanca L, Petcu AI, Purdoiu L, Geicu OI, Bilteanu L, Serban AI (2023) Microchem. J. 191: 108770.

Ramis-Ramos G, García-Álvarez-Coque M, Navarro-Huerta JA (2017) Liquid Chromatography (2nd ed.), 343–373. ISBN 978-0-12-805393-5.

Ribeiro TM, Brandão PRG (2017) Tecnol. Metal. Mater. Min. 14: 183–189.

Şenyuva HZ, Gilbert J (2010) J. Chromatogr. B 878: 115–132.

Shephard GS (2009) Anal. Bioanal. Chem. 395: 1215–1224.

Shuib NS, Makahleh A, Salhimi SM, Saad B (2017) J. Chromatogr. A 1510: 51–56.

Silva IMM, da Cruz AG, Ali S, Freire LGD, Fonseca LM, Rosim RE, Corassin CH, de Oliveira RBA, de Oliveira CAF (2023) Toxins 15: 182.

Šimko P, Kolarič L (2022) Toxins 14: 379.

Vaz A, Silva ACC, Rodrigues P, Venâncio A (2020) Microorganisms 8: 246.

Wang Y, Liu X, Xiao C, Wang Z, Wang J, Xiao H, Cui L, Xiang Q, Yue T (2012) Food Control 28: 131–134.

Comparison of gut resistomes in healthy individuals and patients with severe alcoholic hepatitis

Klára Cverenkárová[1], Petra Olejníková[2], Katarína Šoltys[3], Lucia Messingerová[2], Ľubomír Skladaný[4], and Lucia Bírošová[1]

[1]Department of Nutrition and Food Quality Assessment, Institute of Food Science and Nutrition,
Faculty of Chemical and Food Technology, Slovak University of Technology,
Radlinského 9, 81237 Bratislava, Slovakia
[2]Institute of Biochemistry and Microbiology, Faculty of Chemical and Food Technology,
Slovak University of Technology, Radlinského 9, 81237 Bratislava, Slovakia
[3]Department of Microbiology and Virology, Faculty of Natural Sciences, Comenius University,
Mlynská dolina, Ilkovičova 6, 842 15 Bratislava 4, Slovakia
[4]HEGITO (Div Hepatology, Gastroenterology and Liver Transplantation),
Dept Internal Medicine 2 of the Slovak Medical University, F.D. Roosevelt University Hospital
of Banská Bystrica, Námestie L. Svobodu 1, 97401 Banská Bystrica, Slovakia
klara.cverenkarova@stuba.sk

Abstract: Human gut microbiota has been in the centre of scientific interest for a long period of time. Overall health status of an individual has a great impact on the composition of gut microbiota; however, gut microbiota can affect human health. Antibiotic resistance genes (ARGs) are often a part of human gut microbiome. In this paper, total genomic DNA was extracted from stool samples of 147 healthy individuals and of 45 patients with severe alcoholic hepatitis. The presence of six common ARGs (bla_{TEM}, bla_{SHV}, bla_{OXA}, *vanA, tet*(A), *tet*(E)) was analysed in the genomic DNA by end-point PCR. The results show significantly higher occurrence of ARGs in the DNA samples from patients ($p = 0.0001$) showing multiple ARGs significantly more often than in healthy individuals ($p = 0.00003$). Antibiotic treatment in patients strongly correlated with the occurrence of ARGs ($p = 0.0038$). Nutrition and sex of healthy individuals did not have significant effect on the occurrence of ARGs ($p = 0.156$; $p = 0.456$). ARGs' occurrence in healthy individuals was the highest in the oldest age group, but the age of individuals and ARGs' occurrence were not related ($p = 0.617$). In conclusion, the results underline the importance of health for normal functioning of gut microbiota. Antibiotic resistance represents a challenge in the treatment of patients with liver diseases.

Keywords: alcoholic hepatitis, antibiotic resistance, gut, microbiome, resistomer

Introduction

Gut microbiota is the set of all microorganisms colonising the human gastrointestinal (GI) tract. The set of genetic material of the gut microbiota is referred to as gut microbiome. Healthy gut microbiota has a health positive effect but changes in its composition and imbalance can also cause a change in health status (Doré and Corthier, 2010). However, pathological state can lead to changes in the microbiota through various mechanisms, such as change in eating habits, functioning of the intestinal tract, or the use of drugs, e.g. antibiotics (ATB) (Shreiner et al., 2015). Differences in the diversity, composition, and functionality of microbiota have been associated with Crohn's disease, ulcerative colitis, obesity, type 2 diabetes, depression, and colon cancer (Falony et al., 2019). Imbalance in the gut microbiota is also associated with a number of liver diseases. There is increasing evidence that the pathophysiology and treatment of a wide range of liver diseases is strongly influenced by the nature/behaviour of gut microbiota. Disruption of microbial and intestinal homeostasis is related to chronic liver diseases — non-alcoholic fatty liver disease (NAFLD), non-alcoholic steatohepatitis (NASH), and alcoholic liver disease (ALD) (Xie et al., 2016; Tilg et al., 2016). Severe alcoholic hepatitis is the most serious form of ALD (Li et al., 2019; Hartmann et al., 2015). ALD includes several stages, such as fatty liver (steatosis), steatohepatitis, fibrosis, cirrhosis, and even liver cancer (Li et al., 2019). In general, alcohol abuse causes small intestinal bacterial overgrowth (Hartmann et al., 2015; Vassallo et al., 2015; Kwong and Puri, 2021). Cirrhotic patients usually have reduced abundance of beneficial microorganisms, such as families *Lachnospiraceae*, *Ruminococcaceae* and *Clostridiales* Family XIV *Incertae Sedis* (Hartmann et al., 2015) while families *Enterobacterales* (and *E. coli*), *Enterococcaceae* (genus *Enterococcus* spp.), *Fusobacteriaceae*, *Staphylococcaceae* (genus *Staphylococcus*) are often present in higher counts (Hartmann et al., 2015). Gut microbiome of patients with alcoholic hepatitis is often linked with increased abundance of families *Enterobacterales* and *Streptococcaceae* (Bajaj, 2019), and genus *Veilonella* and *Enterococcus* (Lang et al., 2020). Genus *Akkermansia*, especially species *Akkermansia muciniphila* is reported in significantly lower abundance in patients with alcoholic hepatitis (Lang et al., 2020; Bajaj, 2019). The abundance of phylum *Bacteroidetes* in cirrhotic patients or patients with alcoholic hepatitis is decreased while abundance of *Actinobacteria* and *Proteobacteria* is increased in their gut microbiome (Bajaj, 2019; Kwong and Puri, 2021). Increased abundance of *Candida* species is reported in alcoholics and patients with alcoholic hepatitis, with species *Candida albicans* contributing the most to the alteration (Li et al., 2019; Kwong and Puri, 2021). Counts of *Epicoccum*, *Galactomyces* and *Debaryomyces* were also decreased in alcoholics (Li et al., 2019). Viruses are minor part of the gut microbiome and there are few studies describing their role in the gut microbiome of patients with alcoholic hepatitis. According to Jiang et al. (2000), patients with alcoholic hepatitis showed significantly higher occurrence of viruses in their faecal microbiota in comparison with healthy individuals. Patients with alcoholic hepatitis showed higher occurrence of *Escherichia*-, *Enterobacteria*-, and *Enterococcus* phages. From mammalian viruses, occurrence of *Parvoviridae* and *Herpesviridae* was significantly increased in these patients (Jiang et al., 2020).

Dysbiosis of gut microbiota caused by chronic alcohol abuse leads to increased levels of *Proteobacteria* and then to intestinal mucosal inflammation. Moreover, alcohol abuse causes bacterial overgrowth and increases gut permeability. These factors contribute to the transfer of bacteria from gut to portal blood and expose liver cells to lipopolysaccharides (LPS). LPS trigger immune response and cause release of pro-inflammatory mediators, which are responsible for liver damage and long term inflammation in alcoholics and patients with different stages of ALD (Hartmann et al., 2015; Minemura, 2015; Vassallo et al., 2015). Therefore, restoring the balance in gut microbiota of these patients is one of the possible treatment approaches. Administration of probiotics, prebiotics, and antibiotics, or faecal microbiota transplantation are commonly used in patients with ALD (Li et al., 2019; Bajaj, 2019).

There are differences in the intestinal microbiota between vegans/vegetarians and omnivores. Changes in its composition can be caused directly by the content of bacteria in the food, differences in the food consumed, the length of time the food passes through the GI tract, pH, host excretion dependent on the way of eating and regulation of the expression of the genes of host/its microbiota (Tomova et al., 2019).

Bacteria present in the gut microbiota can also be carriers of antibiotic resistance genes (ARGs) (Penders et al., 2013). In addition to the most dominant representatives of the human gut microbiota – phyla *Bacteroidetes* and *Firmicutes*, facultative anaerobic bacteria, such as family *Enterobacterales* or *Enterococcaceae* (about 100 times less) are a part of human gut microbiota. Gut microbiota can serve as a reservoir for opportunistic pathogens from these families, which can cause problems especially for immunocompromised individuals. ATB treatment can subsequently create selection pressure for the emergence of microbial resistance (van Schaik, 2015).

Many representatives of *Enterobacterales* family belong to pathogenic microorganisms and are frequent carriers of antibiotic resistance genes. As beta-lactam ATBs are among the most important and widely used in human medicine, extended-spectrum beta-lactamases (ESBLs) represent a major problem, and it is highly likely that the genes encoding them are part of the intestinal resistome. These enzymes are capable to hydrolyze broad-spectrum beta-lactam antibiotics (oxyiminocephalosporins – 3rd and 4th generation, monobactams). They are divided into several groups according to the target substrate. Among the most widespread types are TEM, SHV and CTX-M. Another important representative of this group is the OXA type (Ur Rahman et al., 2018). Genus *Enterococcus* is an important part of human and animal intestinal microbiota. *E. faecalis* and *E. faecium* are most commonly found in the human GI tract. Enterococci are the most serious nosocomial pathogens because they are naturally resistant to several ATBs and easily become virulent and acquire multidrug resistance (even to the ATBs of last choice for glycopeptide resistance). The emergence of vancomycin-resistant enterococci (VRE), which cause infections and persistent colonisation, has major health and economic impacts (Ahmed and Baptiste, 2018). Resistance to vancomycin is caused by *Enterococcus* spp. Van operon, which can be part of a chromosome or a plasmid. It consists of *vanS/R* – response regulator, *vanH* – D-lactate dehydrogenase, *vanX* – D-Ala-D-Ala dehydrogenase and variable ligase, of which a total of nine have been identified – *vanA*, *vanB*, *vanC*, *vanD*, *vanE*, *vanG*, *vanL*, *vanM* and *vanN*. These genes encode the variable ligase that determines the level of vancomycin resistance (low, medium or high). VanA phenotype is plasmid mediated and causes high resistance to glycopeptides. The emergence of resistance occurs due to the substitution of the terminal peptide D-Ala-D-Ala on the subunits of N-acetylmuramic acid with high affinity to vancomycin to the sequence D-Ala-D-Lac.

This leads to a 1000-fold reduction in the affinity of the pentapeptide to vancomycin. Due to the presence of the *vanZ* gene on the *vanA* operon, strains expressing VanA are also teicoplanin resistant. This phenotype is most often found in *E. faecalis* and *E. faecium* and is the most widespread worldwide (Faron et al., 2016).

Resistance genes labeled *tet* and *otr* are classified as genes for acquired resistance to tetracycline and oxytetracycline. Currently, 38 *tet* and *otr* genes encoding different mechanisms of tetracycline resistance are known (energy-dependent efflux pumps, ribosomal protection proteins, and inactivating enzymes). The most common mechanism of tetracycline resistance is efflux pump that transports tetracycline out of the cell; *tet*(A) and *tet*(E) genes are included in this group (Roberts, 2005).

ESBL-producing *Enterobacterales* and VRE are listed as serious threat in the AR Threats Report by Centers for Disease Control and Prevention in 2019 (CDC, 2019). Bacteria from family *Enterobacterales* and *Enterococcaceae* belong to frequent inhabitants of the GI tract, and high occurrence of genes encoding resistance to beta-lactams and vancomycin is expected. Tetracycline resistance genes are also frequently detected in the gut microbiome of humans.

The use of ATB has a significant effect on the formation of gut resistome. During the treatment, all bacteria in the human body are exposed to their selection pressure. The selection of antibiotic resistant strains can lead to horizontal gene transfer between other susceptible strains in the intestinal tract. Meat from farm animals contaminated with ARGs also represents a source of ARGs in human gut resistome (Schjørring and Krogfelt, 2011).

The main aim of this paper was to compare and analyse gut resistomes of healthy individuals and patients with severe alcoholic hepatitis. Samples of total DNA extracted from stools of subjects were analysed with end-point PCR for the detection of selected ARGs and their occurrence was compared in healthy individuals and patients based on the sex, nutrition, and age of the subjects.

Materials and Methods

Characteristics of stool samples

Healthy individuals

A group of 147 healthy individuals from Bratislava, Slovakia, and surrounding areas were randomly included into the study. According to diet, the group was divided into vegetarians and meat-eaters. Based on their sex, the group consisted of women and men. The main condition for the participation in the study was the subjective health of the individual (without cardiovascular disease, cancer, diabetes, kidney disease, gastrointestinal tract disease or thyroid disease). All the individuals were non-smokers. All volunteers were healthy and had not undergone antibiotic or other medical therapy for more than six months. All subjects signed informed consent. The main characteristics and numbers of individuals in each group are stated in Tab. 1 (Kudláčková (Krajčovičová) et al., 2012).

Tab. 1. Numbers and characteristics of healthy individuals (Kudláčková (Krajčovičová) et al., 2012).

	Vegetarians	**Meat-eaters**
n	79	68
Men	39	34
Women	40	34
Age span (y)	20–60	20–60
Average age (y)	40.33	40.87

The study was realised in spring (April, May) 2010. The samples of morning stool were immediately lyophilised and stored at –80 °C.

Patients with severe alcoholic hepatitis

A group of 35 patients with severe alcoholic hepatitis was randomly included into the study. All patients suffered from ALD, some in combination with NASH (n = 3) or hepatitis B virus (n = 1) and were treated at the 2nd SMU Department of Internal Medicine of F.D. Roosevelt General Hospital in Banská Bystrica (FDRH), Slovakia. One of the patients (male) suffered from clostridial colitis. A total number of 45 stool samples were collected from the patients. Thirteen patients underwent faecal microbiota transplant (FMT) as a form of treatment, therefore multiple stool samples before and after the procedure were sampled. Two of the individuals were donors of faecal microbiota for the procedure. Several patients were given non-specified antibiotic treatment during their hospitalisation. All patients were meat-eaters. The information about patients is provided in Table 2.

Tab. 2. Numbers and characteristics of patients.

	Patients	**ATB treatment**
n	35	20
Men	23	15
Women	12	5
Age span (y)	19–66	
Average age (y)	46.83	

Collection of morning stool samples was performed from September 2016 to January 2020. Samples were stored at –80 °C.

Extraction of total genomic DNA from stool samples

DNA extraction was performed with GenElute™ Stool DNA Isolation Kit (Sigma Aldrich, USA). Maximum of 200 mg of stool were weighed and processed according to the manufacturer's instructions. Concentration of genomic DNA was evaluated with a Nanodrop 2000 Spectrophotometer (Thermo Fisher Scientific, USA). Samples of genomic DNA were stored at –40 °C until further analysis.

Detection of antibiotic resistance genes
in total genomic DNA by PCR

The presence of antibiotic resistance genes in DNA samples was evaluated by simple or multiplex end-point PCR. Six common ARGs were chosen for the gut resistome analysis: ARGs responsible for extended spectrum betalactamases (ESBL) production in *Enterobacterales* (bla_{TEM}, bla_{SHV}, bla_{OXA}), vancomycin resistance gene in genus *Enterococcus vanA,* and two tetracycline resistance genes: *tet*(A) and *tet*(E). Sequences of the primers are listed in Tab. 3.

PCR mix for simple PCR (bla_{TEM}, *vanA*) of 50 µL total volume consisted of: PCR buffer, 1.5—2 mM $MgCl_2$, 200 µM dNTP Mix, 0.5—1 µM of both primers, 2 µL of total DNA, variable volume of DNase, RNase, and protease, free water, and 2.5 U of Hot Start Taq DNA Polymerase (Biotechrabbit, Germany). PCR mix for Multiplex PCR (Multiplex 1, *tet* Multiplex) of 50 µL total volume consisted of: 0.5—1 µM of both pairs of primers, 2 µL of total DNA, DNase, RNase, and protease, free water, and Multiplex PCR Master Mix (Biotechrabbit, Germany). PCRs were carried out in a Mastercycler gradient (Eppendorf, Germany) as follows: initial denaturation at 94 °C for 20 min, 30 cycles of 94 °C for 40 s, 60.5 °C for 1 min (bla_{TEM}, bla_{SHV}, bla_{OXA}), or 65 °C for 30 s (*vanA*), 72 °C for 1—1.5 min, and final elongation at 72 °C for 10 min. PCR program for *tet* Multiplex was: initial denaturation at 94 °C for 20 min, 72 °C for 30 s, 35 cycles of 94 °C for 1 min, 55.4 °C for 1 min, 72 °C for 1.5 min, and final elongation at 72 °C for 10 min. PCR products were separated by gel electrophoresis in 1.5 % agarose gel with TAE at 100 V for 1:40 h. Additional staining with Gel Red™ Nucleic Acid Gel Stain (Biotium, USA) was performed to visualise the products. For DNA bands identification, 100 bp DNA ladder (Biotechrabbit, Germany) was used as a size standard. For each ARG a sequenced PCR product was used as a positive control. Random PCR products of each ARG were sequenced for confirmation.

Statistical analysis

The occurrence of ARGs was expressed as total numbers of detected genes or as a ratio of detected ARGs to number of samples in the particular group in percent (%). The occurrence of ARGs in different groups was visualised in bar plots as percentage. To determine whether there is a significant difference in ARGs' occurrence between different groups of individuals, the Chi-squared (χ^2) test was performed with the significance set to $p < 0.05$.

Results

Presence of ARGs in gut microbiota of healthy people

A set of 147 samples of total genomic DNA from stools of healthy individuals was tested for the presence of six ARGs. Together, 94 ARGs were detected in the samples. The most common ARG was bla_{TEM} gene, which was present in 28.6 % of the

Tab. 3. Names and sequences of used primers.

ARG	**Primers**	**Primer sequence (5´ — 3´)**	**Product size**
vanA **(Depardieu et al., 2004)**	EA1 (+)	GGGAAAACGACAATTGC	732 bp
	EA2 (–)	GTACAATGCGGCCGTTA	
Multiplex 1 **(bla_{SHV}, bla_{OXA})** **(Dallenne et al., 2010)**	MultiTSO-S_for	AGCCGCTTGAGCAAATTAAAC	713 bp
	MultiTSO-S_rev	ATCCCGCAGATAAATCACCAC	
	MultiTSO-O_for	GGCACCAGATTCAACTTTCAAG	564 bp
	MultiTSO-O_rev	GACCCCAAGTTTCCTGTAAGTG	
bla_{TEM} **(Dallenne et al., 2010)**	MultiTSO-T_for	CATTTCCGTGTCGCCCTTATTC	800 bp
	MultiTSO-T_rev	CGTTCATCCATAGTTGCCTGAC	
***tet* Multiplex** **(*tet*(A, E))** **(Ng et al., 2001)**	*tet*(A)	GCTACATCCTGCTTGCCTTC	210 bp
		CATAGATCGCCGTGAAGAGG	
	tet(E)	AAACCACATCCTCCATACGC	278 bp
		AAATAGGCCACAACCGTCAG	

samples, followed by *vanA* (23.1 %), bla_{OXA} (10.2 %), *tet*(A) (1.4 %) and bla_{SHV} (0.7 %). Gene *tet*(E) was not detected in any of the samples. The most common resistance genes were the group of ESBL encoding genes bla_{TEM}, bla_{SHV}, and bla_{OXA}. Total number of positive individuals (with at least 1 ARG) was 72 (49.0 %) which means that some of the individuals were carriers of multiple resistance genes. The majority of positive samples carried only single resistance gene (75.0 %). In 19.4 % of individuals, two ARGs and in 5.6 % of samples, three ARGs were detected simultaneously.

Comparison of gut resistomes based on the sex of individuals

The group of healthy individuals consisted of 74 women and 73 men. In the female part of the group, the presence of 49 ARGs was detected while 45 ARGs were detected in the male group.

The occurrence of ARGs in the two groups is shown in Fig. 1. Based on the overall results, the most common ARGs in both sexes are bla_{TEM} and *vanA* with slight dominance in women. Gene bla_{OXA} was more prevalent in men. Genes *tet*(A) and bla_{SHV} were detected only in women and *tet*(E) gene was not identified in healthy individuals. The differences in ARGs' occurrence between both sexes are minor with exception of the bla_{OXA} gene (Fig. 1). The occurrence of ARGs and the sex of healthy individuals did not show significant relationship ($p = 0.456$).

The presence of multiple ARGs in both sexes was detected. The total numbers of positive women and men was 38 and 34, respectively. Majority (76.3 % of positive women, 73.5 % of positive men) carried single resistance gene, 18.4 % of women and 20.6 % of men carried two ARGs, and in the total DNA of 5.3 % of women and 5.9 % of men, three ARGs were detected. The detected numbers of ARGs did not depend on the sex of individuals ($p = 0.938$).

Comparison of gut resistomes based on the nutrition of individuals

Based on the preferred diet habits, healthy individuals were divided into two groups: vegetarians and meat-eaters. The vegetarian group consisted of 79 individuals and meat-eater group of 68 individuals. As shown in Fig. 2, the most prevalent resistance gene in the vegetarians group was *vanA* gene (29.1 %), followed by bla_{TEM} and bla_{OXA} gene. Genes *tet*(A) and bla_{SHV} were detected only in a couple of cases in vegetarian total genomic DNA. On the contrary, the most prevalent resistance gene in meat-eaters was bla_{TEM}, followed by *vanA* and bla_{OXA}. With the exception of bla_{TEM} genes, all resistance genes were more prevalent in the vegetarian group. Differences between vegetarians and meat-eaters were clear mainly with *vanA* and bla_{OXA} genes. Although differences were detected in the ARGs' occurrence between vegetarians and meat-eaters, statistical analysis did not prove significant relationship of nutrition style and ARGs' occurrence in healthy individuals ($p = 0.156$).

In addition, vegetarians showed higher occurrence of multiple ARGs in one sample. Together, ARGs were detected in 40 vegetarians and 32 meat-eaters. In both groups, the majority of samples showed the presence of only one resistance gene (65.0 % positive vegetarians, 87.5 % positive meat-eaters). On the contrary, two ARGs were present in 27.5 % of vegetarian total DNA compared to 9.4 % of

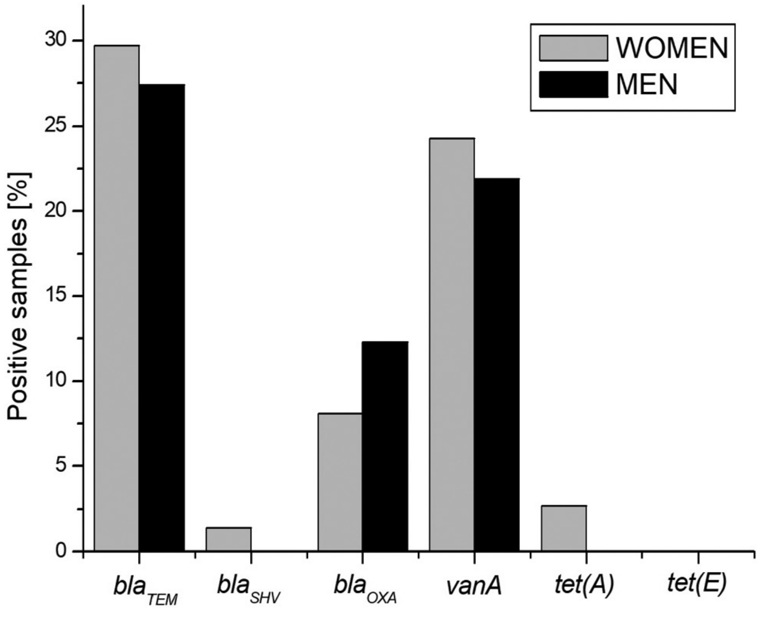

Fig. 1. Occurrence of ARGs in healthy men and women.

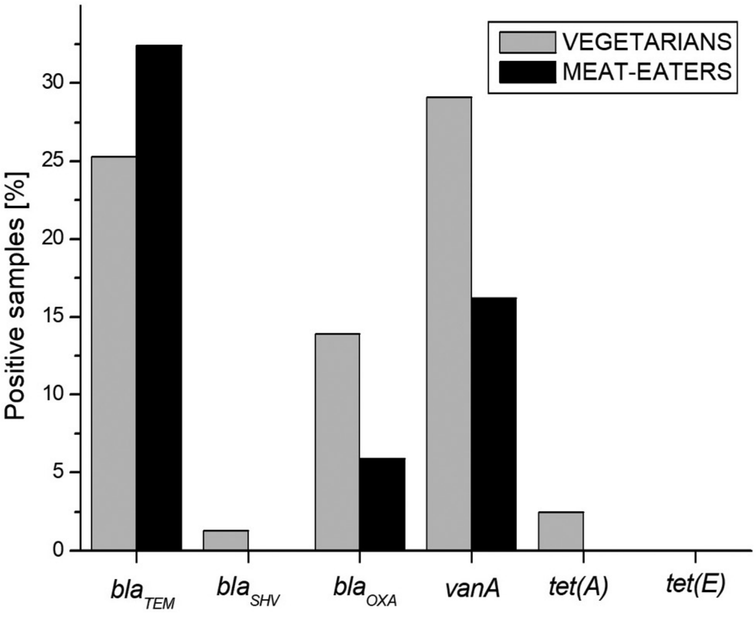

Fig. 2. Occurrence of ARGs in healthy vegetarians and meat-eaters.

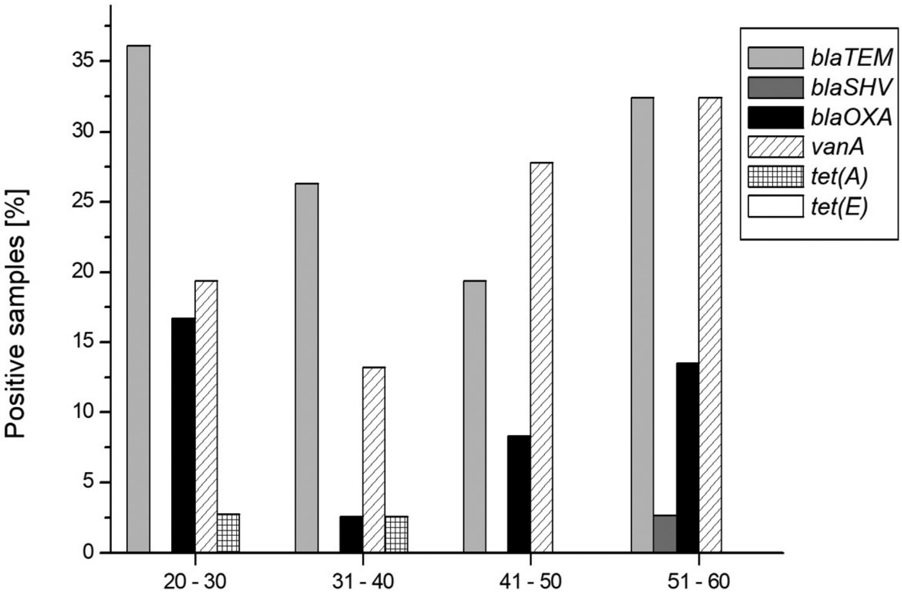

Fig. 3. Occurrence of ARGs in different age groups of healthy individuals.

meat-eaters. Three ARGs were detected in 7.5 % of vegetarians and in 3.1 % of meat-eaters. The numbers of ARGs in one individual did not relate to the nutrition type of the individual ($p = 0.174$).

Comparison of gut resistomes based on the age of individuals

The age span of the healthy individuals ranged from 20 to 60 years. Therefore, the group was divided into four groups according to age: 20–30 (n = 36), 31–40 (n = 38), 41–50 (n = 36), and 51–60 years old (n = 37). Based on the overall results shown in Fig. 3, the most prevalent ARGs in each age group were *bla*$_{TEM}$ or *vanA* genes, *bla*$_{TEM}$, *bla*$_{OXA}$ and *vanA* were present in all age groups. One case of *bla*$_{SHV}$ gene was detected only in the eldest individuals, and two cases of *tet*(A) genes only in 20–30 and 31–40 years old individuals. Absolute numbers show that the highest number of ARGs (30) was detected in 51–60 years old (81.1 %), 27 ARGs in 20–30 years old (75.0 %), 20 ARGs in 41–50 years old (55.6 %) and the lowest number of ARGs was present in 31–40 years old (17; 44.7 %) individuals. The Chi-squared test did not confirm any significant relationship between the ARGs' occurrence and the age of the individuals ($p = 0.617$).

From the positive samples of all age groups, multiple ARGs (9.5 % 3 ARGs, 23.8 % 2 ARGs, 66.7 %

1 ARG) were most often found in 51–60 years old individuals. The best results were obtained for the group of 31–40 years old individuals, where no triple occurrence of ARGs was detected, 13.3 % of positive individuals carried two ARGs, and 86.7 % carried one ARG. Distribution of ARGs was not affected by the age of individuals ($p = 0.674$).

Presence of ARGs in gut microbiota of patients

A total number of 45 DNA samples was recovered from the stool samples of patients with severe alcoholic hepatitis. After PCR detection, 59 ARGs were detected in the DNA samples with *vanA* gene as the most prevalent in 46.7 % of the samples, followed by bla_{TEM} and bla_{OXA} (24.4 % and 22.2 %). Interestingly, *tet(A)* occurrence reached 20.0 % and bla_{SHV} only 13.3 %. Also, the *tet*(E) gene was detected in 4.4 % of the samples. Percentage of positive samples (with min. one ARG) was 77.8 %. In 65.7 % of positive samples only a single ARG was detected. Two ARGs were detected in 31.4 %, three ARGs in 14.3 %, and four ARGs in 5.7 % of the positive samples. In addition, there was a sample with five ARGs detected. Since all patients belonged to the group of meat-eaters, ARGs' occurrence was compared between groups divided according to age and sex.

Comparison of gut resistome based on the sex of patients

Thirty-one samples of total genomic DNA originated from men and 14 samples from women. Fig. 4 shows a comparison of ARGs' occurrence in both sexes. In total, 23 ARGs were present in female samples and 36 ARGs in male samples. The most evident difference was detected in the occurrence of *vanA* and bla_{TEM} genes as *vanA* genes were more prevalent in men and bla_{TEM} in women. Also, *tet*(E) genes were present only in the DNA samples of women. Statistical analysis did not confirm any significant relationship between sex of the patients and ARGs occurrence ($p = 0.130$).

Comparison of gut resistomes based on the age of patients

Patients' age ranged from 19 to 66 years. The group was divided similarly as the group of healthy individuals – 19–30 (n = 4), 31–40 (n = 11), 41–50 (n = 11), 51–66 (n = 19). The results are shown in Fig. 5. Gene *vanA* was the most prevalent ARG in the groups of 51–66 and 31–40 years old patients. The highest number of ARGs to the number of samples was detected in the group of 31–40 years old patients (20 ARGs). This means that patients in this group were also the most frequent carriers of multiple ARGs with 182 % occurrence of ARGs (ratio of detected genes to the number of patients in the age group). Statistical analysis did not show any significant relationship between age of the patients and the ARGs' occurrence ($p = 0.755$).

Effect of antibiotic treatment on the gut resistomes of patients

From 45 samples, 28 were gathered from patients on antibiotic treatment. ARGs' presence was confirmed in 78.6 % of these samples. The occurrence of ARGs in samples from patients without antibiotic treatment was 76.5 %. In one case, five ARGs were detected in the sample from a 36-year-old woman

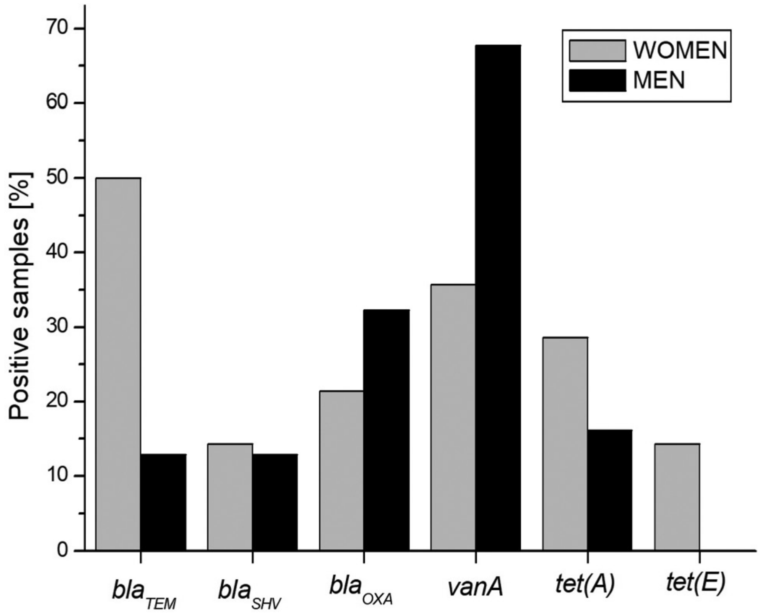

Fig. 4. Occurrence of ARGs in patients based on their sex.

who did not receive antibiotic treatment. Although relative occurrence of ARGs was similar in both groups of patients, results of the Chi-squared test show significant relationship between the antibiotic treatment and ARGs' occurrence in patients ($p = 0.0038$).

Comparison of gut resistomes of healthy individuals and patients with severe alcoholic hepatitis

One of the most important characteristics is the comparison between the two groups of subjects. In general, the positivity for ARGs in healthy individuals was 49.0 %, while in patients it was 77.8 %. The distribution of ARG types is shown in Fig. 6. Gene *vanA* was the most prevalent gene in patients, with double occurrence in comparison with healthy individuals. Except for bla_{TEM}, all monitored ARGs were more prevalent in patients. Gene *tet*(E) was detected only in the genomic DNA of patients, *tet*(A) and bla_{SHV} genes occurred also in some healthy individuals.

The occurrence of ARGs in healthy individuals and patients strongly correlates with the health status of the tested individuals (p = 0.0001).

The comparison of patients and healthy individuals based on sex is shown in Fig. 7. The variety of ARGs in patients is wider than in the healthy individuals. Also, higher percentage of ARGs was detected in

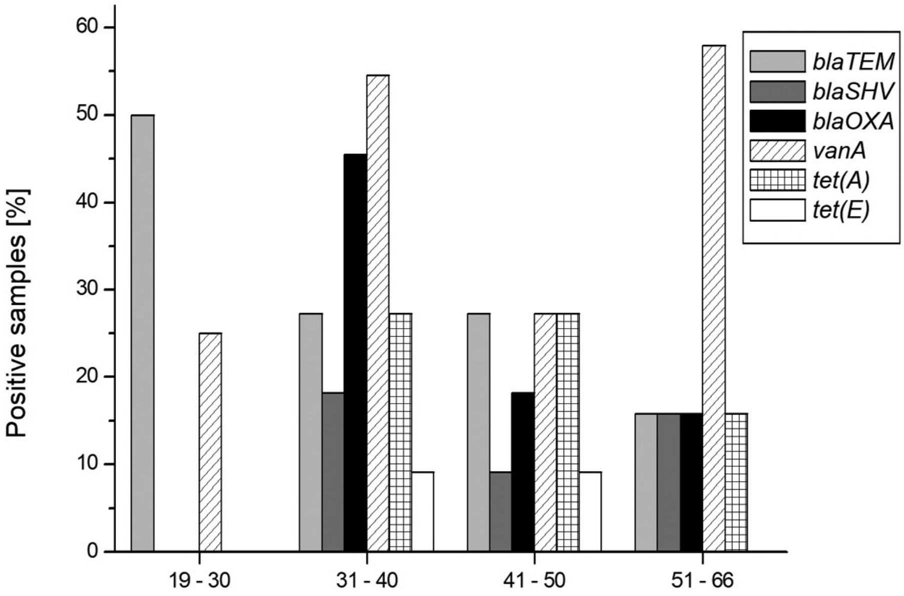

Fig. 5. Occurrence of ARGs in patients based on their age.

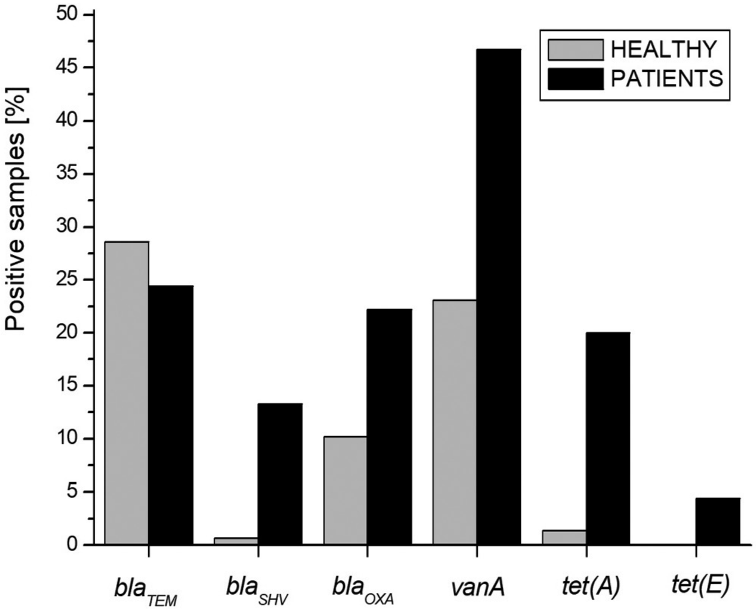

Fig. 6. Occurrence of ARGs in healthy individuals and patients.

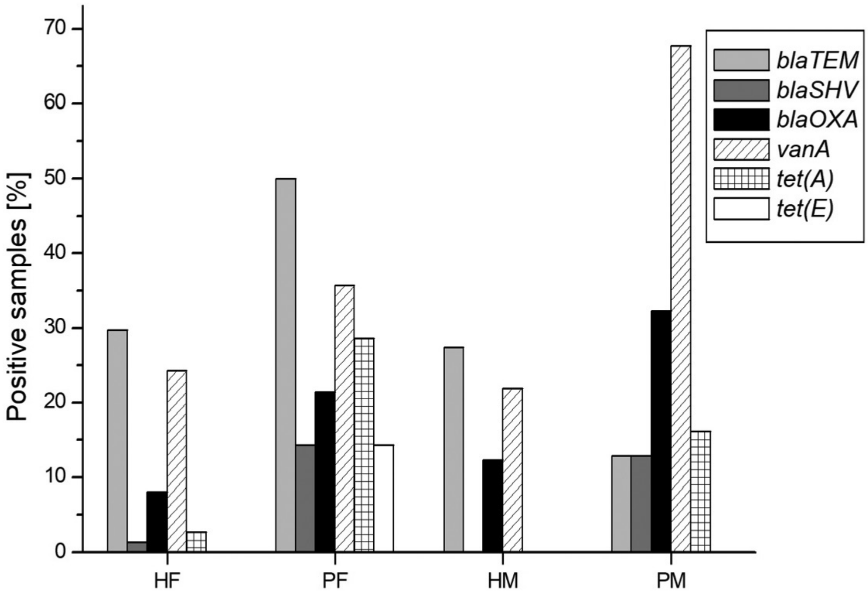

Fig. 7. Occurrence of ARGs in healthy individuals and patients based on the sex (HF — healthy female; PF — patient female; HM — healthy male; PM — patient male).

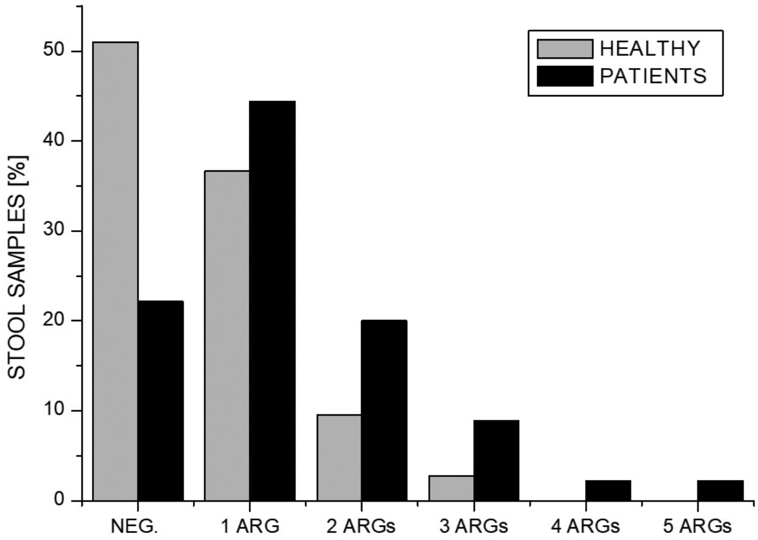

Fig. 8. Numbers of ARGs [%] detected in healthy individuals and patients.

patients. The occurrence of the *vanA* gene was the highest in male patients. In female patients, bla_{TEM} was the most frequently observed ARG. The distribution of ARGs in healthy individuals is more balanced and on a very similar level in both sexes. The statistical analysis showed significant relationship between the sex, health status, and the occurrence of ARGs ($p = 0.0005$).

The last comparison is the number of ARGs detected in samples (Fig. 8). Genomic DNA from patients' stools contained multiple ARGs more often than that from healthy individuals. The number of ARGs detected in one sample strongly correlated with the health status of tested individuals ($p = 0.00003$).

Discussion

Resistome analysis of healthy individuals showed the presence of maximum three ESBL-encoding genes in total. Similar results were observed in a study performed at a California university campus. Authors detected bla_{TEM} in 55 % of bacterial isolates from 102 stool samples of healthy individuals. They also registered bla_{SHV} in 18 % and bla_{OXA} type in 1 % of isolates (Rubin et al., 2020).

Sinha et al. (2019) analysed the gut microbiota composition of 1135 individuals based on sex and resistome profiling in a cohort study concluding that the resistomes of women and men differ in their richness. Females showed higher prevalence of resistance genes than males and a higher number of gene families. The biggest difference between women and men was manifested in the family of genes encoding lincosamide nucleotidyltransferases: 85.98 % in women and 79.07 % in men. The gene cluster for glycopeptide resistance was detected in 39.45 % of women and 31.29 % of men. The gene family encoding ESBLs was detected in 7.70 % of women and 4.44 % of men (Sinha et al., 2019). The results of this study point to a similar trend as our results, a higher number of resistance genes in women. The difference was evident mainly in case of female patients with multiple ARGs' occurrence in one sample. On the contrary, no significant differences were found in the ARGs' occurrence between healthy men and women ($p = 0.456$).

An important period for a person is their early age when the foundations of the gut microbiota are formed. However, the emergence of resistance to ATB in this period has not yet been mapped. We assumed the highest number of resistance genes in the oldest age group. Similarly Lu et al. (2014) reported the accumulation of resistance genes from childhood to adulthood. This phenomenon may be due to older people being usually exposed to higher impact of ATB during their entire lives and them being exposed to several types of antibiotics. Tavella et al. (2021) reported accumulation of ARGs with increasing age with some ARGs present in all age groups and creating a core gut resistome. These assumptions were confirmed in case of healthy individuals where the eldest individuals were the most frequent ARGs carriers. In patients, ARGs occurred the most in the age group of 31—40 years old individuals. An interesting finding, however, is the second highest number of genes detected in the youngest age group of healthy individuals — 21 to 30 years. However, such a result is no exception. Ohashi and Fujisawa (2017) studied the prevalence of ARGs in the total DNA extracted from the stools of young Japanese women aged from 21 to 22 years monitoring ARGs to tetracyclines, macrolides, chloramphenicol, betalactams (*bla_{TEM}*, *bla_{SHV}*, *bla_{OXA}*, *$bla_{CTX\text{-}M}$*), fluoroquinolone, ampicillin, meticillin, streptomycin, sulfonamide, and vancomycin (*vanA*, *vanB* and *vanC1*). Gene *bla_{TEM}* was detected in 62.5 %, *bla_{SHV}* in 21.9 %, *$bla_{CTX\text{-}M}$* in 6.3 % and *bla_{OXA}* in 3.1 % of subjects. From vancomycin resistance genes, only *vanC*1 gene was detected in 6.3 % of cases (Ohashi and Fujisawa, 2017). The genes of beta-lactam resistance were most commonly represented by the *bla_{TEM}* gene in the group of 21—30 years old, but also in the groups of 31—40 years old, and 51—60 years old healthy individuals (in this case at the same level with *vanA*). This study did not find any significant differences in ARGs' occurrence between the groups with different age ($p = 0.617$).

Differences in the occurrence of resistance genes between vegetarians, vegans, and meat-eaters were discussed by Losasso et al. (2018). In fecal DNA samples from 101 people divided according to the type of diet, the presence of four resistance genes: *sul2*, *tet*(A), *bla_{TEM}* and *strB* was determined using qPCR. Vegans had the lowest number of resistance genes, however, when comparing the relative representation of individual genes between the three groups, no major differences were found. The results suggest that conventional and vegetarian diets (intake of animal products) promote the accumulation of resistance (Losasso et al., 2018). Milanović et al. (2017) observed the effects of long-term general, ovo-lacto vegetarian, and vegan diet on the occurrence of 12 resistance genes in 144 people who came from the Italian cities of Turin, Bari, Bologna, and Parma. Between the analysed genes were *erm(A), erm(B), erm(C), blaZ, tet(M), tet(O), tet(K), tet(S), tet(W), mecA, vanA* and *vanB*. The most commonly found genes were *erm* and *tet* genes, which occurred in almost all samples. The *vanA* gene occurred in 17 % of omnivores, 25 % of vegans, and 21 % ovolactovegetarians. The *blaZ* gene, which encodes resistance to beta-lactam antibiotics, was detected in 65 % of omnivores, 48 % of vegans, and 58 % ovolactovegetarians (Milanović et al., 2017). When comparing the results of their study with our results, it can be stated that the numbers of ESBL genes are almost balanced between the two groups of healthy individuals, the only noticeable difference is in case of *bla_{OXA}*. With the *vanA* gene, the trend is similar as in the aforementioned study, higher occurrence of this gene in vegetarians was observed compared to omnivores. Although diet has a major influence on the gut microbiota, very little is known about its impact on the gut resistome and this area requires further research (Milanović et al., 2019). Food chain represents a route of transmission for antibiotic resistant bacteria from food to people. Therefore, the spread of antibiotic resistance is greatly influenced by food safety and food hygiene (World Health Organization, 2011). Stege et al. (2022) compared ARGs' abundance between four different nutrition types (omnivores, pescatarians, vegetarians, and vegans) in Dutch population using metagenomic shotgun sequencing but found no significant differences in abundance of ARGs between the groups. Based on their data, ARGs represent a very small part of all genetic information found in gut microbiota and long-term dietary habits do not influence resistomes in a specific way (Stege et al., 2022). This study confirms our results that there is no correlation between the diet of healthy individuals and ARGs' occurrence ($p = 0.174$).

Several liver diseases are linked with changes and dysbiosis of gut microbiota (Minemura, 2015). Antibiotic treatment causes profound changes in the gut microbiota, it can selectively increase the spectrum of resistant microorganisms leading to higher prevalence of resistance genes and increased likelihood of their spread through horizontal gene transfer (Sommer and Dantas, 2011). The significant difference observed in the occurrence of *vanA* genes in patients is most likely caused by the disruption of their gut microbiota. According to non-published data from the sequencing analysis of total DNA samples from patients and controls (healthy individuals), the composition of gut microbiota of patients and controls significantly differed in the presence of genus *Enterococcus*, with major occurrence in patients (Supplementary material). This shift in the gut microbiota composition and combination with ATB treatment can lead to high occurrence of the *vanA* gene. Higher occurrence of genus *Enterococcus* (besides *Clostridium* spp.) in the gut microbiome of cirrhotic patients was reported in literature (Hartmann et al., 2015; Lang et al., 2020). The results also show significant differences in ARGs' occurrence between patients with and without ATB treatment ($p = 0.0038$). Antibiotic treatment is important for patients with ALD, mainly for those in the end stage of the disease. However, antibiotics cause antimicrobial resistance to some enteric pathogens and change the microbial community in the gut and its function (Yan, 2012). The appearance of stool samples from patients was unusual in colour, shape, and consistency which also supports the assumption of gut microbiome disruption. Shamsaddini et al. (2021) reported higher abundance of ARGs from beta-lactamases, vancomycin, and quinolone resistance groups in patients with cirrhosis. These patients also had higher abundance of bacteria from families *Enterobacterales*, *Streptococcus* spp., and *Enterococcus* spp. (Shamsaddini et al., 2021; Pan et al., 2022). Patients with liver disease are also prone to bacterial infections, for example Merli et al. (2010) describe hospital acquired infections in cirrhotic patients, of which 64 % are caused by antibiotic resistant pathogens. Cirrhotic patients frequently suffer from multidrug resistant infections (Vergis et al., 2020). Acute-on-chronic liver failure (ACLF) describes health condition of patients with liver cirrhosis and is defined by organ failure. This syndrome is characterised by high mortality (15 %) within 28 days. Based on the number of organ failures, the severity of the syndrome is divided into three grades: ACLF-1(a/b), ACLF-2, and ACLF-3(a/b). Grade 1 is characterised by one organ failure (kidney or another organ). In grade 2, two organ failures occur, and in grade 3, three to six organs fail (Kumar et al., 2020). In our group of patients, ten patients did not have any symptoms of ACLF (28.6 %), seven patients were in grade 1 (20.0 %), 12 patients in grade 2 (34.3 %), and three patients suffered grade 3 ACLF (8.6 %). ACLF disease was not present in three patients (two were controls and one patient had clostridial colitis). Due to the high mortality of this disease, health condition of the patients was very serious. Although 28.6 % of patients did not show the ACLF syndrome, Kumar et al. (2020) reported 28-day mortality of 4.4 % without organ failure and 6.3 % in case of failure of one organ (except for kidneys) in the absence of ACLF.

The analysis of ARGs occurrence based on age and sex of patients showed similar results as in case of healthy individuals. There was no correlation in ARGs occurrence between female and male patients ($p = 0.130$) or between the age groups of patients ($p = 0.755$). The effect of nutrition in patients was not assessed since all of the patients were meat-eaters.

The most significant results were obtained by comparing the numbers of detected ARGs in both groups: healthy individuals and patients. There was a strong correlation between the ARGs' occurrence and health status of the individuals (p = 0.0001). Furthermore, statistical analysis of healthy individuals and patients divided by the sex showed a relationship between the health status and the ARGs' occurrence ($p = 0.0005$). The detected numbers of ARGs in the stool samples from healthy individuals and patients were significantly different ($p = 0.00003$). In the group of healthy individuals, a higher number of negative individuals (75 vs. 65 expected) as well as of individuals with two resistance genes (4 vs. 10 expected) were present compared to the expected values. On the other hand, in the group of patients, the number of negative samples was lower than expected (10 vs. 20 expected) and that of samples with one ARG (20 vs. 17 expected) and two ARGs was higher (9 vs. 3 expected).

Gut microbiome is a reservoir of ARGs, even in healthy individuals. Therefore, the impact of antibiotic resistant microorganisms on immunocompromised individuals, such as patients with severe alcoholic hepatitis, is more serious. The diversity of gut microbiota in patients is disrupted by dysbiosis caused by alcohol abuse and antibiotic treatment. The presence of antibiotic resistant pathogens can lead to pathogen invasion and colonisation. Some promising solutions are faecal microbiota transplantation, and the use of probiotics (Lamberte and van Schaik, 2022; Anthony et al., 2021).

Conclusion

The results of our study show differences in the ARGs' occurrence in healthy individuals and patients with severe alcoholic hepatitis. The analysis of the healthy individuals based on their diet style and sex did not show significant differences between the groups. The main differences in ARGs' occurrence were observed between groups of healthy individuals and patients. These results show that the overall health and healthy gut microbiome play an important role in the occurrence of ARGs. Actual trends in research of resistomes show the importance of metagenomics and sequencing and allow detection of many ARGs.

Acknowledgement
This research was funded by the Scientific Grant Agency VEGA under the contract 1/0464/21, the Slovak Research and Development Agency under the contracts APVV-16-0171 and APVV-19-0094, the STU Grant scheme for Support of Young Researchers, and by the Operational Program Integrated Infrastructure for the project: "Strategic research in the field of SMART monitoring, treatment and preventive protection against coronavirus (SARS-CoV-2)", Project no. 313011ASS8, and research project ITMS:26240220022 both co-financed by the European Regional Development Fund. This study was co-funded by the Department of Internal Medicine and HEGITO (Hepatology, Gastroenterology and Liver Transplantation), F.D. Roosevelt University Hospital, Slovakia, and managed by Sanitas Slovaca – agency for health development in Slovakia.

Supplementary Materials
Tab. S1. Significant differences in composition of gut microbiome on genus level in patients with severe alcoholic hepatitis and selected healthy individuals as controls.
Fig. S1. Distribution of genus *Enterococcus* in patients with severe alcoholic hepatitis and healthy individuals.

Informed Consent Statement
Informed consent was obtained from all subjects involved in the study.

Institutional Review Board Statement
The study was conducted in accordance with the Declaration of Helsinki and approved by the Ethics Committee of F. D. Roosevelt Hospital, Banská Bystrica, Slovakia (9/2018, 17th April 2018).

References

Ahmed MO, Baptiste KE (2018) Microb Drug Resist. 24(5): 590–606.

Anthony WE, Burnham CD, Dantas G, Kwon JH (2021) J. Infect. Dis. 223: 209–213.

Bajaj JS (2019) Nat. Rev. Gastroenterol. Hepatol. 16(4): 235–246.

CDC (2019) Atlanta, GA: U.S. Department of Health and Human Services, CDC.

Dallenne C, Da Costa A, Decré D, Favier C, Arlet G (2010) J. Antimicrob. Chemother. 65(3): 490–495.

Depardieu F, Perichon B, Courvalin P (2004) J. Clin. Microbiol. 42(12): 5857–5860.

Doré J, Corthier G (2010) Gastroentérologie Clin. Biol. 34: 7–15.

Falony G, Vandeputte D, Caenepeel C, Vieira-Silva S, Daryoush T, Vermeire S, Raes J (2019) Acta Clin. Belg. 74(2): 53–64.

Faron ML, Ledeboer NA, Buchan BW (2016) J Clin Microbiol. 54(10): 2436–2447.

Hartmann P, Seebauer CT, Schnabl B (2015) Alcohol. Clin. Exp. Res. 39(5): 763–775.

Lu J, Lang S, Duan Y, Zhang X, Gao B, Chopyk J, Schwanemann LK et al. (2020) Hepatology 72(6): 2182–2196.

Kudláčková (Krajčovičová) M, Valachovičová M, Bírošová L (2012) Bratislava, Slovakia: Slovenská zdravotnícka univerzita.

Kumar R, Mehta G, Jalan R (2020) Clin Med (Lond). 20(5): 501–504.

Kwong EK, Puri P (2021) Transl. Gastroenterol. Hepatol. 6: 3.

Lamberte LE, van Schaik W (2022) Curr. Opin. Microbiol. 68: 102150.

Lang S, Fairfied B, Gao B, Duan Y, Zhang X, Fouts De, Schnabl B (2020) Gut Microbes 12(1): 1785251.

Li F, McClain CJ, Feng W (2019) Liver Res. 3(3–4): 218–226.

Losasso C, Di Cesare A, Mastrorilli E, Patuzzi I, Cibin V, Eckert EM, Fontaneto D, Vanzo A, Ricci A, Corno G (2018) Int. J. Antimicrob. Agents 52(5): 702–705.

Lu N, Hu Y, Zhu L, Yang X, Yin Y, Lei F, Zhu Y (2014) Sci. Rep. 4(1): 4302.

Merli M, Lucidi C, Giannelli V, Giusto M, Riggio O, Falcone M, Ridola L, Attili AF, Venditti M (2010) Clin. Gastroenterol. Hepatol. 8(11): 979–985.

Milanović V, Osimani A, Aquilanti L, Tavoletti S, Garofalo C, Polverigiani S, Litta-Mulondo A et al. (2017) Mol. Nutr. Food Res. 61(9): 1601098.

Milanović V, Osimani A, Cardinali F, Litta-Mulondo A, Vignaroli C, Citterio B, Mangiaterra G et al. (2019) PLoS One 14(8): e0220549.

Minemura M (2015) World J. Gastroenterol. 21(6): 1691.

Ng LK, Martin I, Alfa M, Mulvey M (2001) 15(4): 209–215.

Ohashi Y, Fujisawa T (2017) Biosci. Microbiota, Food Heal. 36(4): 151–154.

Pan X, Zhou Z, Liu B, Wu Z (2022) Front. Microbiol. 13.

Penders J, Stobberingh EE, Savelkoul PHM, Wolffs PFG (2013) Front. Microbiol. 4.

Roberts MC (2005) FEMS Microbiol Lett 245(2): 195–203.

Rubin J, Mussio K, Xu Y, Suh J, Riley LW (2020) Microb. Drug Resist. 26(10): 1227–1235.

Van Schaik W (2015) Philos. Trans. R. Soc. B Biol. Sci. 370(1670): 20140087.

Schjørring S, Krogfelt KA (2011) Int. J. Microbiol. 2011: 1–10.

Shamsaddini A, Gillevet PM, Acharya C, Fagan A, Gavis E, Sikaroodi M, McGeorge S et al. (2021) Gastroenterology 161(2): 508–521.e7.

Shreiner AB, Kao JY, Young VB (2015) Curr. Opin. Microbiol. 31(1): 69–75.

Sinha T, Vich Vila A, Garmaeva S, Jankipersadsing SA, Imhann F, Collij V, Bonder MJ et al. (2019) Gut Microbes 10(3): 358–366.

Sommer MOA, Dantas G (2011) Curr. Opin. Microbiol. 14(5): 556–563.

Stege PB, Hordijk J, Shetty SA, Visser M, Viveen MC, Rogers MRC, Gijsbers E et al. (2022) Sci. Rep. 12(1): 1892.

Tavella T, Turroni S, Brigidi P, Candela M, Rampelli S (2021) mSphere 6(5): e00691-21.

Tilg H, Cani PD, Mayer EA (2016) Gut 65(12): 2035–2044.

Tomova A, Bukovsky I, Rembert E, Yonas W, Alwarith J, Barnard ND, Kahleova H (2019) Front. Nutr. 6.

Ur Rahman S, Ali T, Ali I, Khan NA, Han B, Gao J (2018) Biomed Res Int. 26: 9519718.

Vassallo G, Mirijello A, Ferrulli A, Antonelli M, Landolfi R, Gasbarrini A, Addolorato G (2015) Aliment. Pharmacol. Ther. 41(10): 917–927.

Vergis N, Atkinson SR, Thursz MR (2020) Semin. Liver Dis. 40(1): 11–19.

World Health Organization (2011) Copenhagen: World Health Organization.

Xie G, Wang X, Liu P, Wei R, Chen W, Rajani C, Hernandez BY et al. (2016) Oncotarget 7(15): 19355–19366.

Yan AW (2012) World J. Hepatol. 4(4): 110.